Yulia Grebenyuk

Experimental and Theoretical Investigations of Wicking in Porous Media

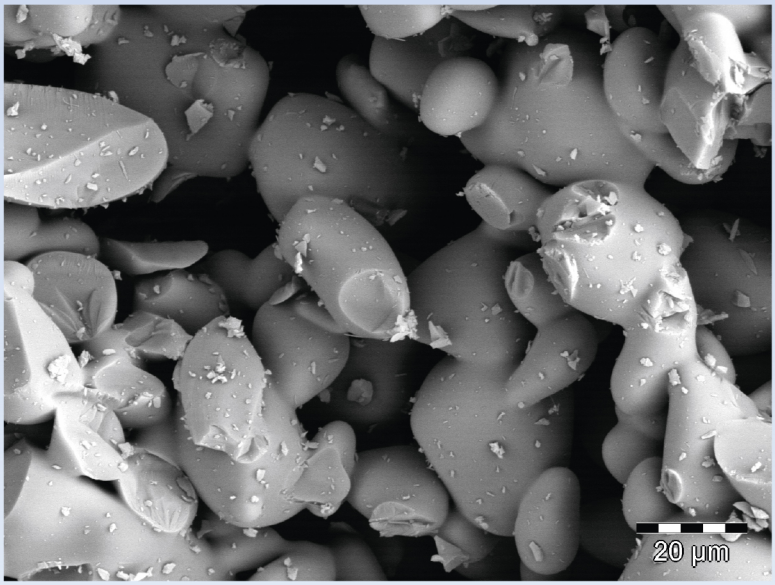

Cuvillier Verlag Göttingen
Internationaler wissenschaftlicher Fachverlag

Experimental and Theoretical Investigations of Wicking in Porous Media

Experimental and Theoretical Investigations of Wicking in Porous Media

Vom Fachbereich Produktionstechnik

der

UNIVERSITÄT BREMEN

zur Erlangung des Grades

Doktor-Ingenieur

genehmigte

Dissertation

von

M. Sc. Yulia Grebenyuk

Gutachter: Prof. Dr.-Ing. Michael Dreyer

Apl. Prof. Dr. Sc. Tatiana Gambaryan-Roisman, TU Darmstadt

Tag der mündlichen Prüfung: 1. Dezember 2017

Bibliografische Information der Deutschen Nationalbibliothek
Die Deutsche Nationalbibliothek verzeichnet diese Publikation in der Deutschen Nationalbibliografie; detaillierte bibliografische Daten sind im Internet über http://dnb.d-nb.de abrufbar.

1. Aufl. - Göttingen: Cuvillier, 2018
Zugl.: Bremen, Univ., Diss., 2017

Nonnenstieg 8, 37075 Göttingen
Telefon: 0551-54724-0
Telefax: 0551-54724-21
www.cuvillier.de

1. Auflage, 2018
Gedruckt auf umweltfreundlichem, säurefreiem Papier aus nachhaltiger Forstwirtschaft

ISBN 978-3-7369-9727-1
eISBN 978-3-7369-8727-2

Abstract

This work is aimed to advance the existing knowledge on the behavior of fluids in porous materials. In the spaceflight community such materials are applied for phase separation and transport of storable and cryogenic propellants. For that purpose propellant management devices (PMD) can be implemented inside propellant tanks. Wicking, or the capillary pressure driven flow in porous elements of PMDs ensures vapor-free propellant delivery to spacecraft engines. For high performance propulsion systems cryogenic liquids, such as liquid oxygen and hydrogen, are used. However, evaporation of cryogenic liquids in porous elements of PMDs can significantly diminish their performance or even lead to the operation failure. On that account, a special attention was paid in this work to the investigation of wicking of a cryogenic liquid (cryo-wicking) subjected to evaporation.

Two one-dimensional theoretical models were proposed to predict vertical wicking of a cryogenic liquid at saturation temperature into superheated porous media. Both macroscopic models account for the evaporation caused by the heat transfer at the wicking front. The influence of the vapor flow created due to evaporation was particularly taken into consideration in the second model. For both models the dimensionless form was deduced. Cryo-wicking experiments were performed in a one-species system under pre-defined non-isothermal conditions using a novel test facility. The test facility configuration enabled to define the sample superheat by its initial position in a stratified nitrogen vapor environment inside the cryostat. Simultaneous sample weight and temperature measurements indicated the wicking front propagation during the imbibition. To the author's extent of knowledge these are the first wicking experiments performed with cryogenic fluids subjected to evaporation using the weight-time measurement technique. The mass of the imbibed liquid nitrogen was determined varying the sample superheat, geometry and porous structure. It was observed that the increase of the sample superheats leads to the wicking rate decrease. The results also revealed that the wicking rate can be greatly affected by the vapor flow created due to evaporation. The proposed theoretical model qualitatively described the experiment data. In order to investigate the impact of the vapor flow,

cryo-wicking experiments were performed with sealed samples. The sealing was applied at lateral sides of the samples. Thus, the vapor created at the wicking front could only escape through the sample top. A significant temperature decrease of the solid structure above the wicking front was observed during the imbibition. That was explained by the influence of the created cold vapor pushed along the sample height due to the sealing. The imbibition rate of the sealed samples decreased greatly. A good agreement was observed between the experiment data and the prediction via the proposed model in case of low sample superheat. However, for high sample superheat the model significantly underestimates the results.

In the second part of this work, the capillary transport abilities of porous polymer-ceramic samples were studied. Along with such properties, as the high specific surface area, the chemical stability and the thermal stability, the pore size range and porosity of porous ceramics can be adjusted using different fabrication techniques. This has already made porous ceramics an important material for the heat and mass transfer applications. Besides that for the spaceflight community a substantial benefit is the relatively light weight of porous ceramics compared to metallic elements used nowadays. For this study the silicon oxycarbide samples were fabricated by the freeze-casting method in the Advanced Ceramic Group of the University of Bremen. The samples were of similar porosity but different pore size and revealed an axial anisotropy. Vertical wicking experiments were performed applying the sample weight measurement method and using the FC-72 liquid as a test liquid. The permeability of the structures was determined from the wicking results at the viscous-dominated stage. The obtained values were found to vary for different sample orientations that quantified the impact of the axial anisotropy. Furthermore, the imbibition results at both sample orientations showed a good agreement with a prediction via the Lucas-Washburn equation with gravity effects. This demonstrated that the macroscopic approach describes the wicking behavior in some anisotropic structures reasonably well, providing a simple tool for further porous material investigations.

In the third part, the capillary transport properties of porous media and the wicking process were investigated using the computational fluid dynamics (CFD) software. Microscopic simulations allowed to provide the information on macroscopic parameters (porosity, permeability, and static pore radius) of a real porous structure. For that a 3D-image of the structure was obtained via X-ray tomography and imported into the CFD software. The steady fluid flow simulation was performed to determine the permeability and porosity. The software also enabled to conduct the wicking simulation on a pore level. The results were used to estimate the static pore radius of the structure. The wicking simulation data was analyzed and compared to the theoretical prediction via the Lucas-Washburn model with gravity effects. Furthermore,

macroscopic wicking simulation was performed using the porous media model available in the CFD software. The model allows to predict wicking result for lab-scale samples with pre-defined macroscopic parameters. The simulation results were found to be in a good agreement with the experiment data and the Lucas-Washburn model with the gravity effects. The results may serve as a foundation for further numerical research of flow problems in porous media at microscopic and macroscopic scales.

Zusammenfassung

Diese Arbeit dient der weiteren Vertiefung des Wissens über das Verhalten von Flüssigkeiten in porösen Materialien. In der Raumfahrt werden diese Werkstoffe zum Transport und zur Phasentrennung von kryogenen Flüssigkeiten, wie zum Beispiel von Treibstoff, verwendet. Zu diesem Zweck werden Treibstoff-Management-Systeme (auf englisch propellant management device, PMD) innerhalb von Treibstoff-Tanks verwendet. Die Dochtwirkung (auf englisch wicking), eine durch den Kapillardruck induzierte Flüssigkeitsbewegung in porösen Materialien, ist eine Teilfunktion, die für die blasenfreie Treibstoffversorgung des Antriebssystemen gewährleistet sein muss. Für Hochleistungs-Antriebssysteme werden kryogene Flüssigkeiten wie flüssiger Sauerstoff und flüssiger Wasserstoff verwendet. Dabei kann die Verdampfung dieser Flüssigkeiten in den porösen Strukturen die Leistung dieser Antriebe signifikant verringern oder den Betrieb unterbrechen. Vor diesem Hintergrund liegt ein besonderer Fokus dieser Arbeit auf der Erforschung der Dochtwirkung einer kryogenen Flüssigkeit unter nicht-isothermen Bedingungen, die zur Verdampfung führen können.

Zwei eindimensionale theoretische Modelle sollen den vertikalen Transport einer kryogenen Flüssigkeit bei Sättigungstemperatur in einem überhitzten porösem Material berechnen. Beide makroskopischen Modelle beinhalten die Verdampfung, die durch die Wärmeübertragung von der porösen Struktur auf die aufsteigende Flüssigkeit entsteht. Die Wirkung des Dampfflusses, welcher infolge der Verdampfung entsteht, wird besonders in dem zweiten Modell berücksichtigt. Beide Modelle werden auch in dimensionsloser Form dargestellt. Die Versuche zum Transport einer kryogenen Flüssigkeit in porösen Materialien wurden in einem Stickstoffsystem unter vordefinierten, nicht-isothermen Bedingungen in einer neuartigen Versuchsanlage durchgeführt. Die Konfiguration der Versuchsanlage ermöglicht die Überhitzung der Probe in ihrer initialen Position in einer geschichteten Stickstoffdampf-Umgebung innerhalb des Kryostaten. Gewichts- und Temperaturmessungen der verwendeten Proben über der Zeit ermöglichten die Bestimmung der durchschnittlichen Höhe der angesaugten Flüssigkeit. Nach dem aktuellen Wissensstand des Autors sind dies die ersten Versuche zum Kapillartrans-

port von kryogenen Medien bei Sättigungstemperatur unter Anwendung der Gewichtsmessung über der Zeit. Die Masse des aufgenommenen flüssigen Stickstoffs wurde anhand von unterschiedlichen Überhitzungen, Geometrien und porösen Strukturen der Proben ermittelt. Es wurde festgestellt, dass eine Erhöhung der Überhitzungstemperatur der Probe zu einer Abnahme der Eindringgeschwindigkeit führt. Aus den Ergebnissen geht zusätzlich hervor, dass die Eindringgeschwindigkeit durch den Dampffluss infolge der Verdampfung stark beeinflusst wird. Das vorgeschlagene theoretische Modell beschreibt die Versuchsdaten qualitativ.
Um die Wirkung des Dampfflusses genauer zu bestimmen, wurden die Versuche zum Kapillartransport von flüssigem Stickstoff mit Proben durchgeführt, die seitlich entlang der Vertikalachse versiegelt wurden. Infolgedessen musste der Dampf durch die Oberseite der Probe entweichen. Hierbei wurde eine signifikante Abnahme der Temperatur in Bereichen der Probe festgestellt, die noch nicht von der Flüssigkeit erreicht wurden. Der Einfluss des kalten Dampfes entlang der Probenhöhe infolge der Versiegelung erklärt diesen Zustand. Die Eindringgeschwindigkeit in die versiegelten Proben wurde im Vergleich zu den nicht versiegelten Proben deutlich verringert. Bei geringer Überhitzung der Proben wurde eine Übereinstimmung zwischen den Daten aus dem Versuch und dem theoretischen Modell festgestellt. Bei einer starken Überhitzung der Probe liegen die Vorhersagen aus dem theoretischen Modell weit unter den Ergebnissen aus den Versuchen.
Im zweiten Teil dieser Arbeit wurden die kapillaren Transporteigenschaften von porösen Keramiken untersucht. Neben den physikalischen Eigenschaften, wie der hohen spezifischen Oberfläche oder der chemischen und thermischen Stabilität, können die Porengrößen und die Porösität der keramischen Werkstoffe mit unterschiedlichen Herstellungsverfahren genau definiert werden. Somit sind die porösen Keramiken bereits ein wichtiger Werkstoff für Anwendungen im Bereich der Wärme- und Stoffübertragung. In dieser Arbeit wurden Silizium-Oxy-Carbid Proben mit dem Freeze-Casting-Verfahren (gerichtetes Einfrieren von Partikelsuspensionen) in Kooperation mit der Advanced Ceramics Group an der Universität Bremen hergestellt. Sie zeichnen sich durch eine ähnliche Porosität bei unterschiedlicher Porengröße und eine axiale Anisotropie aus. Vertikale Eindringexperimente wurden mit einer Testflüssigkeit (FC-72) bei Raumtemperatur bei gleichzeitiger Messung des Probengewichts durchgeführt. Die Permeabilität der Struktur wurde aus der viskos-dominierten Phase der Dochtwirkung ermittelt. Die Permeabilität variierte bei unterschiedlichen Orientierungen der Probe. Dieses Ergebnis quantifiziert den Einfluss der axialen Anisotropie. Die Messungen zum Eindringverhalten bei beiden Orientierungen der Proben zeigen eine hohe Übereinstimmung mit den Vorhersagen aus der Lucas-Washburn Gleichung unter Berücksichtigung der Gravitation. Es zeigt sich,

dass die makroskopische Annäherung des Kapillartransportverhaltens in anisotropen Strukturen den Vorgang angemessen beschreibt. Somit steht ein vergleichsweise einfaches Verfahren für zukünftige Untersuchungen an porösen Materialien zur Verfügung.
Im dritten Teil dieser Arbeit wurden die Kapillartransport-Eigenschaften von porösen keramischen Materialien und das Eindringverhalten mit Mitteln der numerischen Strömungsmechanik (CFD, computational fluid dynamics) untersucht. Simulationen auf mikroskopischer Skala ergaben Informationen zu den makroskopischen Parametern (Porosität, Permeabilität und statische Porenradien) einer realen porösen Struktur. Hierzu wurde eine dreidimensionale (3D) Röntgen-Aufnahme einer Struktur erstellt und in die CFD-Software importiert. Die Permeabilität und Porosität wurde anhand der Simulation von stationären Durchströmungsverhältnissen ermittelt. Die Software hat es zusätzlich ermöglicht, die Simulation des Eindringverhaltens auszuführen sowie die statische Porengröße der Struktur zu bestimmen. Anschließend wurden die Einströmergebnisse analysiert und mit den theoretischen Vorhersagen des Lucas-Washburn-Modells unter Berücksichtigung der Gravitation verglichen. Weiterführend wurden makroskopische Simulationen zu porösen Medien anhand der in der CFD-Software verfügbaren Modelle durchgeführt. Diese Modelle ermöglicht es, Voraussagen zu kapillaren Eindringen bei Proben mit vordefinierten makroskopischen Parametern zu treffen. Die Simulationsergebnisse ergaben eine hohe Übereinstimmung mit den Versuchsergebnissen und den Daten aus dem Lucas-Washburn- Modell. Diese Ergebnisse könnten als Grundlage für zukünftige strömungstechnische Fragestellungen in der numerischen Untersuchung von porösen Materialen dienen.

Acknowledgment

This work evolved from my employment as a research associate in the Multiphase Flow Group at the Center of Applied Space Technology and Microgravity (ZARM) at the University of Bremen and as a member of the Research Training Group GRK 1860 “Micro-, meso- and macroporous nonmetallic Materials: Fundamentals and Applications” (MIMENIMA) from 2013 to 2016.

First of all, I would like to acknowledge and to express my sincere gratitude to my supervisor and the first reviewer of this thesis Prof. Dr.-Ing. Michael E. Dreyer. His guidance, scientific expertise, encouragement and continuous support contributed to the development and finalization of this work. Secondly, I would like to gratefully acknowledge Apl. Prof. Dr. Sc. Tatiana Gambaryan-Roisman from the University of Darmstadt for being the second reviewer of this thesis. My gratitude goes also to the executive director of the Center of Applied Space Technology and Microgravity Prof. Dr. Marc Avila.

Furthermore, I would like to thank Prof. Dr.-Ing. Kurosch Rezwan, the chairman of the Research Training Group GRK 1860 MIMENIMA. Due to his work I could be a member of the team of young researchers that continuously inspired me throughout the development of my project. Special thanks go also to the coordinator of the Research Training Group GRK 1860 MIMENIMA Dr.-Ing. Michaela Wilhelm, who successfully organized all the internal events and ensured the implementation of the study program.

My gratitude goes to the ZARM’s technicians Peter Prengel, Frank Ciecior, and Holger Faust who provided a great support in designing the test facility and in carrying out the experiments for this work. I would like to thank all my former colleagues Dr-Ing. Diana Gaulke, Peter Canfield, Dr-Ing. Max Bronowicki, Dr-Ing. Sebastian Schmitt, Wilhelm Raider, Dr-Ing. Yvonne Chen, Ronald Mairose, Peter Friese, Andre Pingel, Dr-Ing. Michael Conrath, Dr. rer. nat. Kerstin Avila, Anna Guseva, Paul Ritter, Carlos Plana Turmo and Dr. rer. nat. Baofang Song for fruitful discussions and nice working atmosphere. Here special thanks go to Diana Gaulke who also voluntarily became my first German teacher. Moreover, I thank the first generation of MIMENIMA students for sharing the experience of starting and developing a research project,

for research collaborations, and for mutual support. Herewith I would specially like to thank Huixing Zhang and Laura Luhede. My gratitude goes also to my student assistants Fabian Teschner and Yulia Smiyukha for developing the software to control the test facility and for the help in processing of the experimental data. For the administrative support I would like to thank Stephanie Dackow, Andrea Baitz, and Sabrine Vogelsang.

My deepest gratitude goes to my family and especially to my mom Nadejda Grebenyuk, my brother Sergei Grebenyuk, my grandfather Zavodov Vladimir Petrovich and my grandmother Zavodova Lyudmila Danilovna. This time I have been even more far away from you, but 2500 km is nothing for your love and care. Thank you for always giving me freedom and emotional support to follow my challenges. Ya vas ochen lyublyu.

I dedicate this work to my soulmate and my love Christof Riemann. Thank you.

Hamburg 2017

Contents

Nomenclature

Roman symbols

A	[m^2]	cross section area
A	[-]	FLOW-3D: fractional area open to flow
a	[m]	length of the side of a sample volume
a_F	[s^{-1}]	FLOW-3D: coefficient, see Eq. 7.28
a_i	[-]	coefficient, see Eq. 4.6
b	[s m^{-2}]	parameter, see Table 3.1
b	[-]	FLOW-3D: parameter, see Eq. 7.27
C19	[-]	cylindrical sample
C12	[-]	cylindrical sample
C^*	[-]	geometric constant, see Eq. 2.71
CA	[m^2]	control surface
CV	[m^3]	control volume
c_P	[J kg^{-1} K^{-1}]	specific heat capacity at constant pressure
c_S	[J kg^{-1} K^{-1}]	specific heat capacity of solid
c_V	[J kg^{-1} K^{-1}]	specific heat capacity at constant volume
c	[m^{-1}]	parameter, see Table 3.1
c	[-]	Kozeny constant, see Eq. 2.72
D_m	[m^2 s^{-1}]	mass diffusivity coefficient
d	[m]	diameter
F	[-]	FLOW-3D: volume fraction of fluid
F_d	[s^{-1}]	FLOW-3D: drag coefficient, see Eq. 7.27
FUX	[m s^{-2}]	FLOW-3D: u-velocity flux in x-direction
FUY	[m s^{-2}]	FLOW-3D: u-velocity flux in y-direction
FUZ	[m s^{-2}]	FLOW-3D: u-velocity flux in z-direction
f	[m s^{-2}]	FLOW-3D: viscous acceleration

G	[m s^{-2}]	FLOW-3D: body acceleration
g	[m s^{-2}]	gravitational acceleration
g	[m^3]	local hydraulic throat conductance
h	[m]	height
j	[kg s^{-1} m^{-2}]	mass flux
K	[m^2]	permeability
L	[m]	distance
L	[m]	sample height
L	[m]	thickness
L_e	[m]	actual length of fluid flow path
l	[m]	length
m	[kg]	mass
N_c	[-]	number of equivalent cylindrical capillaries
N_cell	[-]	number of mesh cells
N_F	[-]	FLOW-3D: cell flag
$\boldsymbol{n}$	[m]	normal
n_1	[-]	parameter, see Table 3.1
n_2	[m^{-1}]	parameter, see Table 3.1
P	[N]	weight
p	[Pa]	pressure
Q	[m^3 s^{-1}]	volumetric flow rate
q	[J]	heat
S	[-]	saturation
S	[m^2]	surface area
S	[N]	FLOW-3D: surface tension force
s	[m^2 kg^{-1}]	specific surface area per unit mass
s_v	[m^{-1}]	specific surface area per unit volume
R	[m]	radius
$\Re$	[J kg^{-1} K^{-1}]	specific gas constant
R19	[-]	rectangular sample
R12	[-]	rectangular sample
R12T	[-]	rectangular sample with temperature sensors
r	[m]	radius
T	[K]	temperature

t	[s]	time
$\boldsymbol{t}$	[m]	tangential vector to interface
u	[m s^{-1}]	velocity in x-direction
V	[m^3]	volume
V_{F}	[-]	FLOW-3D: volume fraction
$\boldsymbol{v}$	[m s^{-1}]	velocity vector
v	[m s^{-1}]	velocity in y-direction
w	[m]	width
w	[m s^{-1}]	velocity in z-direction
wsx	[Pa m^{-1}]	FLOW-3D: wall shear stress gradient in case of velocity in x-direction
wsy	[Pa m^{-1}]	FLOW-3D: wall shear stress gradient in case of velocity in y-direction
wsz	[Pa m^{-1}]	FLOW-3D: wall shear stress gradient in case of velocity in z-direction
X	[m]	FLOW-3D: boundary function for free surface
x	[m]	x-direction
Y	[m]	FLOW-3D: boundary function for free surface
y	[m]	y-direction
Z	[m]	distance
Z	[m]	FLOW-3D: boundary function for free surface
z	[m]	z-direction

Greek symbols

α	[m^2 s^{-1}]	thermal diffusivity
α	[-]	FLOW-3D: parameter, see Eq. 7.13
β_{F}	[m^{-1}]	inertia parameter, see Eq. 2.70
$\triangle$	[-]	difference
$\triangle h_{\mathrm{v}}$	[J kg^{-1}]	latent heat of evaporation
δ	[m]	fiber diameter
δt	[s]	FLOW-3D: time increment
δx	[m]	FLOW-3D: cell width
δy	[m]	FLOW-3D: cell depth
δz	[m]	FLOW-3D: cell height
δ_{T}	[m]	thermal boundary layer thickness
δ_{W}	[m]	mass diffusion length

ϵ	[-]	parameter, see Table 3.1
θ	[°]	static contact angle
θ_c	[°]	apparent contact angle in the Cassie model
θ_d	[°]	dynamic contact angle
θ_w	[°]	apparent contact angle in the Wenzel's model
λ	[W m^{-1} K^{-1}]	thermal conductivity
μ	[Pa s]	dynamic viscosity
Π^*	[-]	parameter, see Eq. 3.28
π	[-]	circle constant
π	[-]	parameter, see systems 3.17 and 3.49
ρ	[kg m^{-3}]	density
σ	[N m^{-1}]	surface tension
τ	[-]	tortuosity
τ	[Pa]	shear stress
ϕ	[-]	porosity
ϕ_g	[-]	area fraction of a surface filled with gas
Ω_1	[-]	parameter, see Eq. 3.29
Ω_2	[-]	parameter, see Eq. 3.32

Subscripts and superscripts

0	initial at a sample bottom
a	ambient
av	average
b	bubble point
c	capillary
e	effective
ev	evaporation
eq	equilibrium
F	fluid
f	fluid
g	gravity
H	hydraulic

i	counter in x-direction
j	counter in y-direction
k	counter in z-direction
L	liquid
LN_2	liquid nitrogen
lp	lower boundary
m	meniscus
m	mean
max	maximum
merc	mercury
min	minimum
N_2	nitrogen
n	time step
rel	relative
S	solid
SG	solid gas
SL	sample top
SL	solid liquid
s	static
s	superficial
solid	solid
total	total
up	upper boundary
V	vapor
vis	viscous
void	void
x	x-component
y	y-component
z	z-component
$+z$	“bottom to top” sample orientation
$-z$	“top to bottom” sample orientation
*	dimensionless

Dimensionless numbers

Bo	Bond number	$\frac{\rho g R^2}{\sigma}$
Ca	Capillary number	$\frac{\mu u}{\sigma} \sim \frac{\mu R}{\sigma t}$
Eu	Euler number	$\frac{\triangle p}{\rho u^2}$
Hg	Hagen number	$-\frac{\mathrm{d}p}{\mathrm{d}z}\frac{\rho D^3}{\mu^2}$
Ja	Jakob number	$\frac{c_{\mathrm{PL}} \triangle T}{\triangle h_{\mathrm{v}}}$
Le	Lewis number	$\frac{\alpha_{\mathrm{S}}}{D_{\mathrm{m}}}$
Re	Reynolds number	$\frac{\rho u D}{\mu}$

Operators

∇	Nabla
$\sum$	summation
$\frac{\mathrm{D}}{\mathrm{D}t}$	total derivative
$\frac{\partial}{\partial x}$	partial derivative
$\frac{\mathrm{d}}{\mathrm{d}t}$	derivative

Abbreviations

CFD	Computational Fluid Dynamics
GMRES	Generalized Minimum RESidual method
H44	methyl phenyl polysiloxane derived filler
LAD	Liquid Acquisition Device

LN2	Liquid Nitrogen
PMD	Propellant Management Device
REV	Representative Elementary Volume
SEM	Scanning Electron Microscopy
1D	one-Dimensional
2D	two-Dimensional
3D	three-Dimensional

Chapter 1

Introduction

1.1 Motivation

This section is based on the publications "Wicking of liquid nitrogen into superheated porous structure"[1] by Y. Grebenyuk and M.E. Dreyer [34] and "Wicking into porous polymer-derived ceramic monoliths fabricated by freeze-casting"[2] by Y. Grebenyuk et al. [160].

Porous materials have found a wide range of applications in a variety of industry branches. Due to the high specific surface area and the ability to conduct a fluid flow, such materials became an effective tool to implement the heat and mass transfer processes. This is of particular interest, for example, in heat pipes technologies [18, 19, 26] and catalyst support in chemical reactors [20, 21, 22]. Mass transport and structure characteristics of porous materials are essential for filtration technologies [23, 24, 25] and textile production [27, 28, 78].

Moreover, porous materials are applied in the space industry for phase separation and transport of storable and cryogenic fluids. Vapor-free propellant delivery to the engines is of importance for all space mission stages. In the absence of gravity, however, liquid-gas separation becomes challenging. For that reason, propellant management devices (PMD) can be implemented inside propellant tanks. Capillary pressure driven flow is an effective solution to enable vapor-free liquid delivery. Based on this principle, PMDs with porous screen elements [118, 119, 146] were designed. A screen PMD, or a screen channel liquid acquisition device (LAD), includes several porous elements that get saturated with a liquid and ensure the liquid transport through

[1] Reprinted from Cryogenics, Vol. 78, Y. Grebenyuk, M.E. Dreyer, Wicking of liquid nitrogen into superheated porous structures, Pages No. 27-39, Copyright (2017), with permission from Elsevier.

[2] Reprinted from Journal of the European Ceramic Society, Vol. 37, Y. Grebenyuk, H.X. Zhang, M. Wilhelm, K. Rezwan, M.E. Dreyer, Wicking into porous polymer-derived ceramic monoliths fabricated by freeze-casting, Pages No. 1993-2000, Copyright (2017), with permission from Elsevier.

them due to the capillary pressure. Vapor ingestion is blocked until the screen bubble point pressure is not exceeded. An influence of the screen parameters on the LAD performance was investigated in [120, 121, 122]. Furthermore, venting might be necessary during ballistic flight phases which could lead to liquid expulsion via the gas ports of upper stage propellant tanks. A gas phase port separator was designed to prevent this undesired effect [123]. The device includes double porous screen elements which shall avoid the expulsion of liquid propellant during venting. A double porous screen element concept and a theoretical model are given in [72].

Evaporation in porous elements can diminish the performance of liquid-vapor separation devices or even lead to their operation failure. Some studies were performed to investigate this effect for storable liquids [125, 126]. Meanwhile, cryogenic fluids are widely used in the spaceflight community for high performance propulsion systems. Liquid oxygen and hydrogen are the most common cryogenic propellants. Such liquids are characterized by low surface tension values and low normal boiling point temperature. For that reason the capillary transport of cryogenic liquids subjected to evaporation requires a thorough investigation and analysis.

The application of porous ceramics for transport of cryogenic liquids may increase technical efficiency and reduce production and maintenance costs. Properties of porous ceramics including high specific surface area, chemical and thermal stability, corrosion resistance and controllable surface characteristics can be adjusted by applying different techniques, like sacrificial templating, direct foaming or freeze casting method, which give different structures and pore size ranges [150, 25, 151]. For the spaceflight community a substantial benefit is the relatively light weight of porous ceramics compared to metallic elements used nowadays. However, porous ceramics have to fulfil the requirements of the aerospace industry concerning mechanical integrity and cleanliness. A special attention has recently been drawn to anisotropic porous materials [147, 148, 149]. The properties of these materials are directionally dependent. That allows to adjust porous structures to particular needs of certain devices and to improve their performance.

The aim of this work is to advance the knowledge on the behavior of fluids in porous materials. The wicking process was investigated. Wicking, or imbibition, is a spontaneous penetration of liquid into porous media driven by capillary forces. Due to the challenges of the capillary transport of cryogenic liquids described above, the wicking of liquid nitrogen subjected to evaporation was of a special interest for this research. For that, a novel test facility was built to perform wicking experiments in a one-species system under pre-defined non-isothermal conditions. Two one-dimensional macroscopic wicking models were proposed to evaluate the

impact of the porous sample superheat, geometrical and structural characteristics as well as the impact of the vapor flow created due to evaporation. In the second part of this work, the capillary transport abilities of porous ceramic monoliths of an anisotropic structure were investigated. The polymer-derived ceramic samples fabricated via freeze-casting method were characterized via vertical wicking tests. In the third part, the capillary transport properties of porous media and the wicking process were studied using the computational fluid dynamics software. The results of benchmark microscopic and macroscopic simulations of fluid flow problems in porous media were discussed.

1.2 Outline

This work is divided into eight chapters. The theoretical background necessary for the understanding of the investigated problems and the state of the art are given in chapter 2.
Chapter 3 describes the macroscopic approach applied in this study for modeling of the wicking process. It also presents the derivation of governing equations for the proposed one-dimensional theoretical models. The models account for evaporation occurring at the wicking front due to the heat transfer between superheated porous media and cryogenic liquid at saturation temperature. The dimensionless scaling of the model variables and parameters is shown.
Chapter 4 provides information on the experimental apparatus as well as the experiment preparation and methodology for wicking tests with liquid nitrogen (cryo-wicking) and superheated porous samples. The analysis of the experiment data and its comparison with the theoretical model predictions are discussed. The results are presented in dimensionless form.
In chapter 5 the results of wicking experiments with liquid nitrogen and sealed superheated porous samples are summarized. The sealing was applied in order to investigate the influence on the imbibition process of the vapor flow created due to the heat transfer at the wicking front. The experiment data were compared to the results for the samples with no sealing. The theoretical model prediction is given. The dimensionless form of the results is discussed.
Chapter 6 describes the findings of the investigation of the capillary transport abilities of porous polymer-derived ceramic monoliths. The monoliths revealed an anisotropic structure and were characterized using vertical wicking experiments at different sample orientation.
The study of the capillary transport properties of porous media and the wicking process performed using the computational fluid dynamics software FLOW-3D is described in chapter 7. The chapter provides information on the computation approach, relevant equations and numerical approximations applied for fluid flow simulations. The microscopic simulations were

performed for the steady fluid flow and the wicking process in porous media. The macroscopic wicking simulation was conducted. The analysis of the simulation results and their comparison with the theoretical model prediction and experiment data are shown.
Chapter 8 provides a conclusion based on the results obtained in this study.

Chapter 2

Theoretical background and state of the art

This chapter provides the theoretical background required for the understanding of the phenomena studied in this work and describes the state of the art on the characterization of porous media and the wicking process. The latter is a spontaneous penetration of liquid into porous media due to capillary forces. An overview of the theoretical approaches and experimental investigations of wicking is given. The application of computational fluid dynamics software for wicking simulations is discussed.

2.1 Surface tension

If a liquid is unable to expand freely, an interface is formed with a second fluid phase [4]. This phenomenon is due to the fact that the molecules at the interfacial surface are unbalanced and attract to each other by van der Waals forces. It results in an effect that the surface is in tension. If an element dl is defined on the interfacial surface between the liquid and gas, then this element is excerted to a force $\sigma \mathrm{d}l$ which is tangential to the surface. The coefficient σ is called the surface tension of the liquid. The free surface tends to minimize. Therefore, a certain amount of work $\sigma \mathrm{d}A$ is required to be done in order to increase the surface [4]. This is an alternative approach to introduce the concept of the surface tension.

Generally the surface tension of liquids decreases with an increasing pressure and temperature and is equal to zero at the critical point [4].

The most common methods to determine the surface tension of liquids are the ring method [8, 9], the maximum bubble pressure method [10, 11], the drop-weight-method [12, 13] and the Wilhelmy plate method [14, 15, 16].

2.2 Contact angle

Wicking process in porous media always involves a solid and at least two fluid phases. A drop of liquid placed on a smooth, plain solid surface in a gaseous environment is depicted on Fig. 2.1. Here three different interfaces are present: liquid-gas, solid-gas and liquid-solid. These three interfaces meet in a contact line (a contact point for two-dimensional case). Fig. 2.1 displays the directions of the interfacial forces, where σ is the surface tension of the liquid, σ_{SG} is the interfacial tension between the solid and gas (or the surface tension of the solid), and σ_{SL} is the interfacial tension between the liquid and solid. In fact, each interface is characterized by the interfacial tension. However, the determination of the interfacial tension between the solid and gas σ_{SG} and between the solid and liquid σ_{SL} is much more complicated than the determination of the surface tension for liquids σ [29, 30]. If the drop is in equilibrium, a finite angle θ is formed between the liquid-gas and solid-liquid interfaces. The angle θ is called the static contact angle. The balance of the interfacial forces parallel to the solid surface yields the Young equation [1]

$$\sigma \cos\theta = \sigma_{\mathrm{SG}} - \sigma_{\mathrm{SL}}. \tag{2.1}$$

Depending on the value of the static contact angle θ, the liquid is referred to as perfectly wetting, wetting and non-wetting. A perfectly wetting liquid has a zero static contact angle,

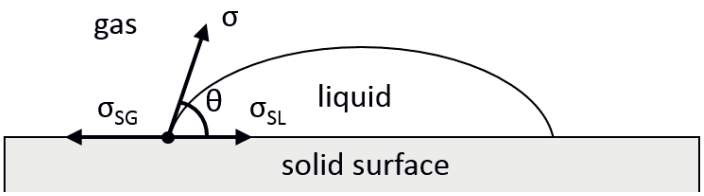

Figure 2.1: A drop of liquid placed on a smooth, plain solid surface in a gaseous environment. The directions of the interfacial tensions are shown via the arrows: σ is the surface tension of the liquid, σ_{SG} is the interfacial tension between the solid and gas (or the surface tension of the solid), and σ_{SL} is the interfacial tension between the liquid and solid. A finite angle θ formed between the liquid-gas and solid-liquid interfaces is the static contact angle.

i.e. $\theta = 0°$. For $0° < \theta < 90°$ the liquid is referred to as wetting. For $90° \leq \theta < 180°$ it is referred to as the non-wetting liquid. In this work wicking in porous media has been studied for a cryogenic liquid (nitrogen) and FC-72 liquid. Both, cryogenic liquids and the FC-72 liquid are identified as perfectly-wetting with a variety of materials [31, 32, 33, 34, 36, 126, 38, 39, 40]. On the actual geometry of a rough solid surface the contact angle may significantly differ from the one given by the Young equation. A relation between the Young static contact angle θ and the apparent contact angle θ^*_{w} observed on the rough surface can be expressed by the Wenzel's equation [35]

$$\cos\theta^*_{\mathrm{w}} = r\cos\theta, \tag{2.2}$$

where $r = A/A_0$ is the roughness of the surface given as a ratio of the real surface area A to the projected surface area A_0. In this model it is assumed that the liquid conforms the solid topography. However, in case of very rough and hydrophobic surfaces a gas can be trapped in the interstices on the solid surface [35]. This effect is implemented in the Cassie model that defines a relation between the Young static contact angle θ and the apparent contact angle θ^*_{c} as [35]

$$\cos\theta^*_{\mathrm{c}} = (1 - \phi_{\mathrm{g}})\cos\theta - \phi_{\mathrm{g}}, \tag{2.3}$$

where ϕ_{g} is the area fraction of the surface filled with the gas. The effect of the rough surfaces is not considered in this work.

If the contact line moves, the contact angle changes and is referred to as the dynamic contact angle θ_{d}. For the advancing and receding contact lines one should also distinguish between the advancing and receding contact angles [1, 35, 16]. The dynamic contact angle θ_{d} changes with the contact line velocity u parallel to the solid surface. Therefore, it can be connected to the capillary number given as

$$\mathrm{Ca} = \frac{\mu_{\mathrm{L}} u}{\sigma}, \tag{2.4}$$

where μ_{L} is the dynamic viscosity of the liquid. Some empirical correlations were proposed to state a relation between the capillary number, the dynamic and static contact angles [41, 42, 43]. For the advancing contact line formed with a perfectly-wetting liquid and for $\mathrm{Ca} < 0.1$ the dynamic contact angle can be calculated as [44, 45]

$$\theta_{\mathrm{d}} = 4.54\ \mathrm{Ca}^{0.353}. \tag{2.5}$$

In this study the wicking phenomena occurred at small capillary numbers ($\mathrm{Ca} < 2 \cdot 10^{-4}$, see sections 4.4.5 and 5.4.4). The calculation of the dynamic contact angle for such capillary numbers via Eq. 2.5 gives some insignificant deviations from zero. Therefore, in this work the contact angle was taken as $\theta_{\mathrm{d}} = \theta = 0°$.

2.3 Young-Laplace equation

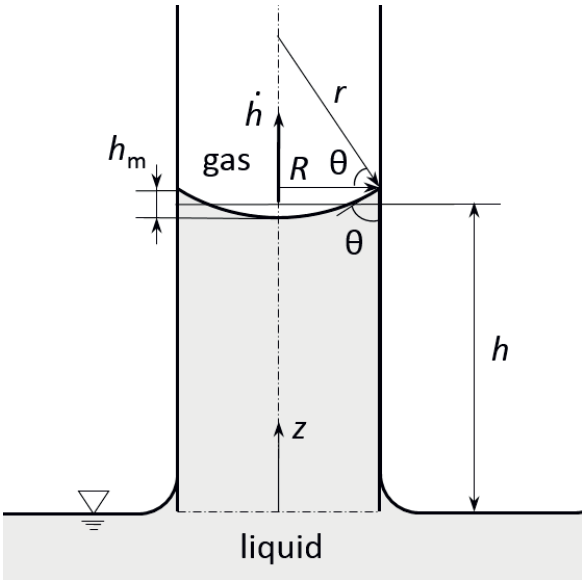

Figure 2.2: The liquid rise in the capillary of an internal radius R. The spherical meniscus of a principal radius of curvature $r = R/\cos\theta$ is formed between the liquid, the gaseous phase and the solid walls of the capillary. h_{m} is the height of the meniscus. The angle formed between the walls of the capillary and the liquid-gas interface is the contact angle θ. h is the liquid height that relates the total volume of liquid in the tube and the volume of a liquid column with a flat surface. $\dot{h}$ is the meniscus velocity.

In case of a curved free interface, there is a pressure difference between the liquid and the second fluid phase. The pressure is higher on a concave side of the interface. For an arbitrary interface with principal radii of curvature r_1 and r_2, this pressure difference $\triangle p$ is given by the Young-Laplace equation [1]

$$\triangle p = \sigma \left(\frac{1}{r_1} + \frac{1}{r_2} \right), \tag{2.6}$$

where for the liquid-gas interface σ is the surface tension of the liquid. The derivation of the Young-Laplace equation is shown, for example, by Dullien [1].

Wicking into a pore is often implied to be analogous to the liquid rise in a small circular capillary. Fig. 1 displays a liquid rise in the capillary of an internal radius R. An interface formed between the liquid, the gaseous phase and the solid walls of the capillary is called the meniscus. The angle formed between the walls of the capillary and the liquid-gas interface is the contact angle θ, see Fig. 1. The Bond number Bo characterizes the ratio of the gravitational force to the surface tension and given as

$$\mathrm{Bo} = \frac{\rho_{\mathrm{L}} g R^2}{\sigma}, \tag{2.7}$$

where ρ_{L} is the density of liquid and g is the gravitational acceleration. In case of a small capillary, Bo $<<$ 1 and the meniscus of a spherical shape can be assumed. Therefore, the principal radii of curvature for the interface are $r_1 = r_2 = R/\cos\theta$. Thus, applying the Young-Laplace equation for a circular capillary, one obtains

$$\triangle p = \frac{2\sigma\cos\theta}{R}, \tag{2.8}$$

where the pressure difference $\triangle p$ is also called the capillary pressure.
The height of a spherical meniscus can be calculated as [46]

$$h_{\mathrm{m}} = R\left(\frac{1}{\cos\theta} - \tan\theta\right). \tag{2.9}$$

2.4 Conservation equations

2.4.1 Control volume

To describe fluid motion the basic equations of mass, linear momentum and energy conservation can be written for an infinitesimally small control volume. A control volume of a infinitesimal size dx, dy and dz in x-,y- and z-directions, respectively, was defined in the Cartesian coordinates (x, y, z). Such an approach provides differential equations of fluid motion.

2.4.2 Mass conservation

The mass conservation equation for an infinitesimal control volume defined in the Cartesian coordinates (x, y, z) yields [4]

$$\frac{\partial\rho}{\partial t} + \frac{\partial}{\partial x}(\rho u) + \frac{\partial}{\partial y}(\rho v) + \frac{\partial}{\partial z}(\rho w) = 0, \tag{2.10}$$

where t is time, ρ is the density of fluid, u, v and w are the velocity components in x-,y- and z-directions, respectively.
For the incompressible fluid Eq. 2.10 reduces to

$$\frac{\partial u}{\partial x} + \frac{\partial v}{\partial y} + \frac{\partial w}{\partial z} = 0. \tag{2.11}$$

Using the Nabla operator ∇ given with unit vectors $\mathbf{i}$, $\mathbf{j}$, and $\mathbf{k}$ as

$$\nabla = \mathbf{i}\frac{\partial}{\partial x} + \mathbf{j}\frac{\partial}{\partial y} + \mathbf{k}\frac{\partial}{\partial z}, \tag{2.12}$$

Eqs. 2.10 and 2.11 can be written in a compact form as

$$\frac{\partial \rho}{\partial t} + \nabla \cdot (\rho \boldsymbol{v}) = 0, \tag{2.13}$$

$$\nabla \cdot \boldsymbol{v} = 0, \tag{2.14}$$

respectively. The vector $\boldsymbol{v}$ in Eqs. 2.13 and 2.14 is the velocity vector given as

$$\boldsymbol{v} = \mathbf{i}u(x, y, z, t) + \mathbf{j}v(x, y, z, t) + \mathbf{k}w(x, y, z, t). \tag{2.15}$$

2.4.3 Linear momentum conservation

The momentum conservation equations for an infinitesimal control volume defined in the Cartesian coordinates (x, y, z) yield [4]

$$\rho\left(\frac{\partial u}{\partial t} + u\frac{\partial u}{\partial x} + v\frac{\partial u}{\partial y} + w\frac{\partial u}{\partial z}\right) = -\frac{\partial p}{\partial x} + \frac{\partial \tau_{xx}}{\partial x} + \frac{\partial \tau_{yx}}{\partial y} + \frac{\partial \tau_{zx}}{\partial z} + \rho G_x, \tag{2.16}$$

$$\rho\left(\frac{\partial v}{\partial t} + u\frac{\partial v}{\partial x} + v\frac{\partial v}{\partial y} + w\frac{\partial v}{\partial z}\right) = -\frac{\partial p}{\partial y} + \frac{\partial \tau_{xy}}{\partial x} + \frac{\partial \tau_{yy}}{\partial y} + \frac{\partial \tau_{zy}}{\partial z} + \rho G_y, \tag{2.17}$$

$$\rho\left(\frac{\partial w}{\partial t} + u\frac{\partial w}{\partial x} + v\frac{\partial w}{\partial y} + w\frac{\partial w}{\partial z}\right) = -\frac{\partial p}{\partial z} + \frac{\partial \tau_{xz}}{\partial x} + \frac{\partial \tau_{yz}}{\partial y} + \frac{\partial \tau_{zz}}{\partial z} + \rho G_z, \tag{2.18}$$

where μ is the dynamic viscosity of fluid, G_x, G_y and G_z are the body accelerations in x-,y- and z-directions, respectively. The components τ_{xx}, τ_{yy}, τ_{zz}, τ_{xy}, τ_{xz}, τ_{yz} τ_{zx}, τ_{yx} and τ_{zy} in Eqs. 2.16, 2.17 and 2.18 are the shear stresses given for Newtonian fluid as

$$\tau_{xx} = 2\mu\frac{\partial u}{\partial x} - \frac{2}{3}\mu\left(\frac{\partial u}{\partial x} + \frac{\partial v}{\partial y} + \frac{\partial w}{\partial z}\right), \tag{2.19}$$

$$\tau_{yy} = 2\mu\frac{\partial v}{\partial y} - \frac{2}{3}\mu\left(\frac{\partial u}{\partial x} + \frac{\partial v}{\partial y} + \frac{\partial w}{\partial z}\right), \tag{2.20}$$

$$\tau_{zz} = 2\mu\frac{\partial w}{\partial z} - \frac{2}{3}\mu\left(\frac{\partial u}{\partial x} + \frac{\partial v}{\partial y} + \frac{\partial w}{\partial z}\right), \tag{2.21}$$

$$\tau_{xy} = \tau_{yx} = \mu\left(\frac{\partial v}{\partial x} + \frac{\partial u}{\partial y}\right), \tag{2.22}$$

$$\tau_{xz} = \tau_{zx} = \mu\left(\frac{\partial u}{\partial z} + \frac{\partial w}{\partial x}\right), \tag{2.23}$$

$$\tau_{yz} = \tau_{zy} = \mu\left(\frac{\partial v}{\partial z} + \frac{\partial w}{\partial y}\right). \tag{2.24}$$

For an incompressible fluid the components τ_{xx}, τ_{yy} and τ_{zz} (see Eqs. 2.19, 2.20 and 2.21) transform to

$$\tau_{xx} = 2\mu\frac{\partial u}{\partial x}, \tag{2.25}$$

$$\tau_{yy} = 2\mu\frac{\partial v}{\partial y}, \tag{2.26}$$

$$\tau_{zz} = 2\mu\frac{\partial w}{\partial z}. \tag{2.27}$$

Substituting Eqs. 2.22, 2.23, 2.24, 2.25, 2.26 and 2.27 to Eqs. 2.16, 2.17 and 2.18, one obtains the momentum conservation equations for an incompressible fluid as

$$\rho\left(\frac{\partial u}{\partial t} + u\frac{\partial u}{\partial x} + v\frac{\partial u}{\partial y} + w\frac{\partial u}{\partial z}\right) = -\frac{\partial p}{\partial x} + \mu\left(\frac{\partial^2 u}{\partial x^2} + \frac{\partial^2 u}{\partial y^2} + \frac{\partial^2 u}{\partial z^2}\right) + \rho G_x, \tag{2.28}$$

$$\rho\left(\frac{\partial v}{\partial t} + u\frac{\partial v}{\partial x} + v\frac{\partial v}{\partial y} + w\frac{\partial v}{\partial z}\right) = -\frac{\partial p}{\partial y} + \mu\left(\frac{\partial^2 v}{\partial x} + \frac{\partial^2 v}{\partial y^2} + \frac{\partial^2 v}{\partial z^2}\right) + \rho G_y, \tag{2.29}$$

$$\rho\left(\frac{\partial w}{\partial t} + u\frac{\partial w}{\partial x} + v\frac{\partial w}{\partial y} + w\frac{\partial w}{\partial z}\right) = -\frac{\partial p}{\partial z} + \mu\left(\frac{\partial^2 w}{\partial x^2} + \frac{\partial^2 w}{\partial y^2} + \frac{\partial^2 w}{\partial z^2}\right) + \rho G_z. \tag{2.30}$$

Here the dynamic viscosity μ of fluid is assumed being constant.

In a compact form the linear momentum conservation equation can be written as

$$\rho\frac{\mathrm{D}\boldsymbol{v}}{\mathrm{D}t} = -\nabla p + \nabla\cdot\boldsymbol{\tau} + \rho\mathbf{G}, \tag{2.31}$$

where $\boldsymbol{\tau}_{i,j}$ is the shear stress tensor given as

$$\boldsymbol{\tau} = \begin{pmatrix} \tau_{xx} & \tau_{yx} & \tau_{zx} \\ \tau_{xy} & \tau_{yy} & \tau_{zy} \\ \tau_{xz} & \tau_{yz} & \tau_{zz} \end{pmatrix}. \tag{2.32}$$

2.4.4 Energy conservation

The energy conservation equation of Newtonian fluid motion with no internal heat sources can be written in a compact form as [4]

$$\rho\frac{\mathrm{D}\tilde{u}}{\mathrm{D}t} + p(\nabla\cdot\boldsymbol{v}) = \nabla\cdot\mathbf{q} + \Phi, \tag{2.33}$$

where $\tilde{u}$ is the internal energy, $\mathbf{q}$ is the heat flux and Φ is the viscous-dissipation function given in the Cartesian coordinates (x, y, z) as Eq. 2.38 and 2.40. To simplify Eq. 2.33, one can make the following approximations

$$c_\mathrm{V}, c_\mathrm{P}, \mu, \lambda = \mathrm{const}, \tag{2.34}$$

$$\mathrm{d}\tilde{u} \approx c_\mathrm{V}\mathrm{d}T, \tag{2.35}$$

where c_V and c_P are the specific heat capacity at constant volume and at constant pressure, respectively, λ is the thermal conductivity of fluid and T is the temperature. For incompressible fluids one can also assume the equality of c_V and c_P.

Eq. 2.35 refer to compressible and incompressible fluids, respectively.

If the heat is transferred by conduction, the heat flux $\mathbf{q}$ can be described by Fourier's law as

$$\mathbf{q} = -\lambda \nabla T, \tag{2.36}$$

where ∇T is the temperature gradient.

Substituting Eqs. 2.35 and 2.36 to Eq. 2.33 and applying the Cartesian coordinates (x, y, z), one obtains the energy conservation equation as [17]

$$\rho c_{\mathrm{V}} \left(\frac{\partial T}{\partial t} + u\frac{\partial T}{\partial x} + v\frac{\partial T}{\partial y} + w\frac{\partial T}{\partial z} \right) = \lambda \left(\frac{\partial^2 T}{\partial x^2} + \frac{\partial^2 T}{\partial y^2} + \frac{\partial^2 T}{\partial z^2} \right) - p \left(\frac{\partial u}{\partial x} + \frac{\partial v}{\partial y} + \frac{\partial w}{\partial z} \right) + \Phi, \tag{2.37}$$

where the viscous-dissipation function Φ is given as

$$\Phi = \mu \left[2\left(\frac{\partial u}{\partial x}\right)^2 + 2\left(\frac{\partial v}{\partial y}\right)^2 + 2\left(\frac{\partial w}{\partial z}\right)^2 + \left(\frac{\partial u}{\partial y} + \frac{\partial v}{\partial x}\right)^2 + \left(\frac{\partial v}{\partial z} + \frac{\partial w}{\partial y}\right)^2 + \left(\frac{\partial w}{\partial x} + \frac{\partial u}{\partial z}\right)^2 - \frac{2}{3}\left(\frac{\partial u}{\partial x} + \frac{\partial v}{\partial y} + \frac{\partial w}{\partial z}\right)^2 \right]. \tag{2.38}$$

In the case of incompressible fluid, Eqs. 2.37 and 2.38 reduce to [4, 17]

$$\rho c_{\mathrm{P}} \left(\frac{\partial T}{\partial t} + u\frac{\partial T}{\partial x} + v\frac{\partial T}{\partial y} + w\frac{\partial T}{\partial z} \right) = \lambda \left(\frac{\partial^2 T}{\partial x^2} + \frac{\partial^2 T}{\partial y^2} + \frac{\partial^2 T}{\partial z^2} \right) + \Phi, \tag{2.39}$$

$$\Phi = \mu \left[2\left(\frac{\partial u}{\partial x}\right)^2 + 2\left(\frac{\partial v}{\partial y}\right)^2 + 2\left(\frac{\partial w}{\partial z}\right)^2 + \left(\frac{\partial u}{\partial y} + \frac{\partial v}{\partial x}\right)^2 + \left(\frac{\partial v}{\partial z} + \frac{\partial w}{\partial y}\right)^2 + \left(\frac{\partial w}{\partial x} + \frac{\partial u}{\partial z}\right)^2 \right], \tag{2.40}$$

respectively.

2.4.5 Boundary conditions

The system of the mass (see Eq. 2.13 and 2.14), momentum (see Eq. 2.31) and energy (see Eq. 2.33) conservation equations contains five variables, which are ρ, $\boldsymbol{v}$, p, $\tilde{u}$, and T. The approximation for the internal energy $\tilde{u}$ was given as Eqs. 2.35 and **??**. Using this approximation as well as the corresponding initial and boundary conditions, one can solve the system of the conservation equations for the case of incompressible fluid. For the compressible fluid the equation of state $\rho = \rho(p, T)$ shall be provided. For the ideal gas one can use the ideal gas law given as [4]

$$p = \rho \Re T, \tag{2.41}$$

where $\Re$ is the specific gas constant.

As initial conditions the values of the variables ρ, $\boldsymbol{v}$, p, $\tilde{u}$, and T shall be defined at $t = 0$. On the fluid-solid interface and on the free surface, or the vapor-liquid interface, for all times one applies the boundary conditions.

Fluid-solid interface boundary conditions

The boundary conditions for the fluid-solid interface are in detail described in literature [4, 6, 7]. Here these boundary conditions are discussed only briefly.

At the fluid-solid interface, or at the wall, the no-slip condition can be defined by

$$\boldsymbol{v}_{\mathrm{w}} = \boldsymbol{v}^{\mathrm{f}}\Big|_{\mathrm{wall}}, \tag{2.42}$$

where $\boldsymbol{v}_{\mathrm{w}}$ and $\boldsymbol{v}^{\mathrm{f}}$ are the wall velocity and the fluid velocity, respectively.

The solid wall temperature T_{w} can be assumed the same as the fluid temperature T^{f} at the wall, i.e.

$$T_{\mathrm{w}} = T^{\mathrm{f}}\Big|_{\mathrm{wall}}. \tag{2.43}$$

The fluid-solid boundary condition can be also expressed with the heat flux over the interface by

$$\mathbf{q}_{\mathrm{S}}\Big|_{\mathrm{wall}} = \mathbf{q}^{\mathrm{f}}\Big|_{\mathrm{wall}}, \tag{2.44}$$

where $\mathbf{q}_{\mathrm{S}}$ and $\mathbf{q}^{\mathrm{f}}$ are the heat fluxes within the solid and the fluid, respectively.

Free surface or vapor-liquid interface boundary conditions

As discussed in section 2.1, the interface, or free surface, is formed between the vapor and liquid phase. For this study evaporation at the vapor-liquid interface is of interest. Therefore, the appropriate boundary conditions shall be given to account for the mass loss, linear momentum transfer and energy consumption. This is well described, for example, by Burelbach et al. [5]. The authors considered a thin layer of an incompressible Newtonian fluid (liquid) on a uniformly heated horizontal rigid plane. The liquid is evaporating in the direction normal to the interface formed between the liquid and its vapor. The normal and two tangent vectors to the interface are given as $\boldsymbol{n}$, $\boldsymbol{t}_1$, and $\boldsymbol{t}_2$, respectively. The components in normal and tangential directions are identified with the superscripts n, t_1, and t_2, respectively.

At the interface there are the vapor-liquid jump conditions for mass, momentum and energy. To simplify these conditions, we assume the following relations

$$\frac{\rho_{\mathrm{V}}}{\rho_{\mathrm{L}}} \longrightarrow 0, \; \frac{\mu_{\mathrm{V}}}{\mu_{\mathrm{L}}} \longrightarrow 0, \; \frac{\lambda_{\mathrm{V}}}{\lambda_{\mathrm{L}}} \longrightarrow 0, \tag{2.45}$$

where the subscripts L and V indicate the liquid and the vapor properties, respectively.
The jump mass balance is given as

$$j_{\mathrm{ev}} = \rho_{\mathrm{L}}(v_{\mathrm{L}}^n - v_{\mathrm{int}}^n) = \rho_{\mathrm{V}}(v_{\mathrm{V}}^n - v_{\mathrm{int}}^n), \tag{2.46}$$

where v_{L}^n and v_{V}^n are the velocities of liquid and vapor in the normal direction, respectively, v_{int}^n is the interface velocity and j_{ev} is the evaporative mass flux.
The jump momentum balance should be written for normal and tangential directions. The momentum balance in the normal direction can be expressed as

$$p_{\mathrm{L}} - p_{\mathrm{V}} = \sigma\left(\frac{1}{r_1} + \frac{1}{r_2}\right) - j_{\mathrm{ev}}(v_{\mathrm{L}}^n - v_{\mathrm{V}}^n) + (\boldsymbol{\tau}_{\mathrm{L}} - \boldsymbol{\tau}_{\mathrm{V}}) \cdot \boldsymbol{n} \cdot \boldsymbol{n}, \tag{2.47}$$

where r_1 and r_2 are the principal radii of the curvature of the free surface, $\boldsymbol{\tau}_{\mathrm{L}}$ and $\boldsymbol{\tau}_{\mathrm{V}}$ are the shear stresses of liquid and vapor, respectively. The second term on the right side of Eq. 2.47 is known as the vapor recoil [136]. It is a backward reaction on large accelerations of the vapor due to a large disparity in liquid and vapor densities, see Eq. 2.46. The pressure exerted by the vapor recoil on the interface is directed into the liquid phase. Ramon and Oron [136] showed that the vapor recoil is an important factor at high evaporation rates and for large capillary radii, especially under conditions of reduced pressure. Meanwhile, some authors claim the vapor recoil to be negligible for small capillary radii and porous media as well as for small capillary numbers [47, 48]. Neglecting the vapor recoil and the shear stress term in Eq. 2.47, one obtains the Young-Laplace equation given as Eq. 2.6.
The momentum balance in the tangential directions can be written as

$$(\boldsymbol{\tau}_{\mathrm{L}} - \boldsymbol{\tau}_{\mathrm{V}}) \cdot \boldsymbol{n} \cdot \boldsymbol{t}_1 - \frac{\partial \sigma}{\partial t_1} = j_{\mathrm{ev}}(v_{\mathrm{L}}^{t_1} - v_{\mathrm{V}}^{t_1}), \tag{2.48}$$

$$(\boldsymbol{\tau}_{\mathrm{L}} - \boldsymbol{\tau}_{\mathrm{V}}) \cdot \boldsymbol{n} \cdot \boldsymbol{t}_2 - \frac{\partial \sigma}{\partial t_2} = j_{\mathrm{ev}}(v_{\mathrm{L}}^{t_2} - v_{\mathrm{V}}^{t_2}), \tag{2.49}$$

where $v_{\mathrm{L}}^{t_1}$ and $v_{\mathrm{L}}^{t_2}$ are the liquid velocities in the tangential directions, $v_{\mathrm{V}}^{t_1}$ and $v_{\mathrm{V}}^{t_2}$ are the vapor velocities in the tangential directions. Assuming the surface tension being constant and applying the non-slip boundary condition $v_{\mathrm{L}}^{t_1} = v_{\mathrm{V}}^{t_1}$ and $v_{\mathrm{L}}^{t_2} = v_{\mathrm{V}}^{t_2}$, one obtains Eq. 2.48 and 2.49 as

$$\boldsymbol{\tau}_{\mathrm{L}} \cdot \boldsymbol{n} \cdot \boldsymbol{t}_1 = \boldsymbol{\tau}_{\mathrm{V}} \cdot \boldsymbol{n} \cdot \boldsymbol{t}_1, \tag{2.50}$$

$$\boldsymbol{\tau}_{\mathrm{L}} \cdot \boldsymbol{n} \cdot \boldsymbol{t}_2 = \boldsymbol{\tau}_{\mathrm{V}} \cdot \boldsymbol{n} \cdot \boldsymbol{t}_2. \tag{2.51}$$

For Newtonian fluids Eqs. 2.50 and 2.51 can be written as [17]

$$\mu_{\mathrm{L}}\left(\frac{\partial v_{\mathrm{L}}^n}{\partial t_1} + \frac{\partial v_{\mathrm{L}}^{t_1}}{\partial n}\right) = \mu_{\mathrm{V}}\left(\frac{\partial v_{\mathrm{V}}^n}{\partial t_1} + \frac{\partial v_{\mathrm{V}}^{t_1}}{\partial n}\right). \tag{2.52}$$

$$\mu_{\mathrm{L}} \left(\frac{\partial v_{\mathrm{L}}^{n}}{\partial t_2} + \frac{\partial v_{\mathrm{L}}^{t_2}}{\partial n} \right) = \mu_{\mathrm{V}} \left(\frac{\partial v_{\mathrm{V}}^{n}}{\partial t_2} + \frac{\partial v_{\mathrm{V}}^{t_2}}{\partial n} \right). \tag{2.53}$$

The jump energy balance can be given as [5]

$$j_{\mathrm{ev}} \left(\triangle h_{\mathrm{v}} + \frac{1}{2} \left(\frac{j_{\mathrm{ev}}}{\rho_{\mathrm{V}}} \right)^2 \right) = -\mathbf{q}_{\mathrm{L}} \cdot \boldsymbol{n}, \tag{2.54}$$

where $\mathbf{q}_{\mathrm{L}}$ is the heat flux, and $\triangle h_{\mathrm{v}}$ is the latent heat of evaporation.
Applying Fourier's law (see Eq. 2.36), one obtains Eq. 2.54 as

$$j_{\mathrm{ev}} \left(\triangle h_{\mathrm{v}} + \frac{1}{2} \left(\frac{j_{\mathrm{ev}}}{\rho_{\mathrm{V}}} \right)^2 \right) = \lambda_{\mathrm{L}} \nabla T \cdot \boldsymbol{n}. \tag{2.55}$$

If the vapor recoil is assumed to be negligible, the second term on the left side of Eqs. 2.54 and 2.55 can be omitted.

2.5 Porous media

Porous medium is defined as a medium constructed of the solid matrix and voids. In this section some parameters of a porous medium are discussed: the characteristic pore size and pore size distribution, porosity, specific surface area, tortuosity and permeability.

2.5.1 Pore size

The irregularity of pore shapes in real structures induces a problem in the definition of a characteristic pore size. Therefore, the term "pore" should be preliminary defined. Dullien [1] describes an approach to characterize a pore medium as being consisted of "pore bodies". Each pore body is defined by the solid surfaces and the imaginary planes erected at the local minima of the pore body, see Fig. 2.3. These imaginary cross-sections are called the "pore throats". Thus, a porous medium consists of a large number of pore bodies connected to each other with pore throats. The pore bodies can be then characterized using any arbitrary definition of size of an irregularly shaped object. Such an approach to describe a pore space is also known as the concept of the "void particles".
However, for the flow problems the determination of the pore throat size is as much essential as the determination of the pore body size. According to Scheidegger [2], in that case the pores should be visualized as "tube-shaped bodies".
As a measure of the pore throats the hydraulic radius R_{H} was introduced [1]. It follows the assumption that a porous medium is equivalent to a bundle of hypothetical channels. In case of the uniform cross-section channels the hydraulic radius is defined as

$$R_{\mathrm{H}} = \frac{V_{\mathrm{void}}}{S}. \tag{2.56}$$

where V_{void} is the volume of a pore space and S is the surface area of pores. R_{H} may be determined through its connection to the specific surface area and permeability of a porous medium, see sections 2.5.3 and 2.5.5.

Some measurement methods can be applied to determine the characteristic pore size and pore size distribution. The latter is a distribution of the pore volume with respect to the pore size. Nevertheless, one should take into account that these methods are indirect and always imply some assumptions made about the shape of the pores.

The most common method is the mercury intrusion technique, or the mercury porosimetry [52, 53, 54]. It requires the injection of mercury into a preliminary evacuated porous specimen. The varied injection pressure and the corresponding volume of mercury occupying the pore space are recorded. The pores are assumed to be cylindrical capillaries. Using the mercury injection pressure and applying the Young-Laplace's equation (Eq. 2.8) the pore diameters d are calculated as

$$d = \frac{4\sigma \cos\theta}{\triangle p_{\mathrm{merc}}}. \tag{2.57}$$

As a result, the pore size distribution in the specimen and its porosity (see section 2.5.2) can be obtained. From the pore size distribution the mean pore size can be calculated as the arithmetic mean value weighted by the number of pores. The median pore size can be estimated as the

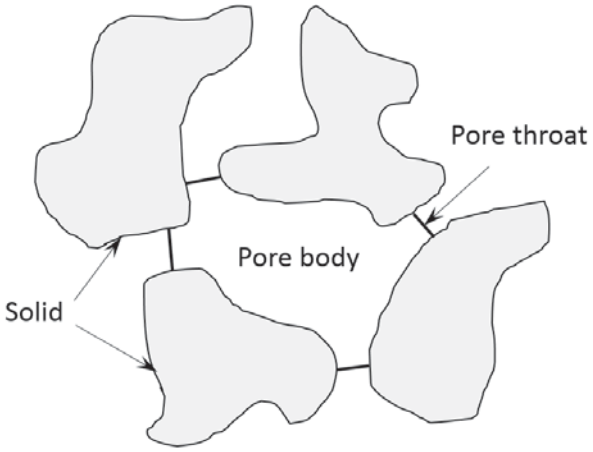

Figure 2.3: Two-dimensional (2D) representation of a porous medium using the concept of the "void particles". A porous medium consists of a large number of the pore bodies connected to each other with the pore throats.

pore size that is smaller or larger than 50% of the total number of pores of the specimen. The most frequent pore diameter in the specimen, or the modal pore size, can be determined.
The bubble point pressure method [55, 56] is based on measuring the differential pressure through a porous specimen, saturated with a wetted liquid, at which this specimen becomes gas permeable. The pressure is called the bubble point pressure, or the breakthrough pressure. It corresponds to the smallest cross-section of the largest pore in the specimen. The radius of this pore, or the bubble point radius R_b, is calculated via the Young-Laplace's equation for a cylindrical capillary (Eq. 2.8) as

$$R_\mathrm{b} = \frac{2\sigma\cos\theta}{\triangle p_\mathrm{b}}. \tag{2.58}$$

For homogeneous porous media the characteristic pore size can be experimentally determined using the hydrostatic equilibrium of a liquid in a vertically oriented porous sample [100, 126, 38]. The method requires an implementation of the vertical wicking process in a closed reservoir partly filled with some wetting liquid. At the end of wicking the capillary pressure given by the Young-Laplace equation (Eq. 2.8) is balanced by the hydrostatic pressure that yields

$$\frac{2\sigma\cos\theta}{R_\mathrm{s}} = \rho_\mathrm{L} g h_\mathrm{eq}, \tag{2.59}$$

where h_eq is the equilibrium wicking height that corresponds to a maximum achievable value of the wicking height for this porous structure. For homogeneous porous media h_eq is the same at each part of the specimen cross-section. Therefore, it can be determined optically or using the weight-time measurement technique. The characteristic pore size obtained by the hydrostatic equilibrium method R_s is called the static pore radius. From Eq. 2.59 it is given as

$$R_\mathrm{s} = \frac{2\sigma\cos\theta}{\rho_\mathrm{L} g h_\mathrm{eq}}. \tag{2.60}$$

The hydrostatic equilibrium method is based on the assumption of a porous media being equivalent to a bundle of cylindrical capillaries, see section 2.6.1.
Alternatively, the pore size distribution can be evaluated via the nitrogen adsorption technique [49, 50, 51] and X-ray tomography with a three-dimensional (3D) image analysis [57, 58, 59].

2.5.2 Porosity

The total porosity of a specimen is defined as a relation of the specimen volume occupied by pores, i.e. the void volume V_void, to the total volume V_total of the specimen

$$\phi = \frac{V_\mathrm{void}}{V_\mathrm{total}}, \tag{2.61}$$

where ϕ takes values between 0 and 1.

The total porosity takes into account all the pores of the specimen, including dead-end and isolated pores. However, for the flow problems the volume of the interconnected pores is of importance. Such pores form a network that contributes to the mass transport in a porous medium. The porosity accounting for the volume of the interconnected pores is called the effective porosity (or the open porosity). In this study ϕ is always referred to as the effective porosity of a specimen.

The most direct method for the porosity determination is based on a comparison of the bulk volume of a porous specimen with the volume of the specimen pieces compacted together [2]. It gives the total porosity. This method is a destructive one, and, therefore, it is not used extensively. The density (or weight) method [1, 2] can be applied to a specimen with a known density of the solid material. It also provides the total porosity value. Both, the total and effective porosities can be obtained applying X-ray tomography with a three-dimensional (3D) image analysis [57, 58, 59]. The imbibition method (or the soaking method) [1, 126, 38] is a non-destructive technique that provides the effective porosity. The method requires the weight measurements of the dry porous specimen and the specimen completely saturated with the imbibed liquid. For that one should ensure a negligibly low evaporation rate of the liquid. The effective porosity can be also determined using the mercury porosimetry, see 2.5.1. In this case the volume of the mercury intruded into a porous specimen is used for the calculation. The gas expansion method [1, 49] and the nitrogen adsorption method [49, 50] are widely applied and provide the effective porosity values.

2.5.3 Specific surface area

The specific surface area of a porous medium is defined as the interstitial surface area S of the pores per unit mass of the solid material

$$s = \frac{S}{m_{\text{solid}}}, \tag{2.62}$$

or per unit volume of the solid material

$$s_v = \frac{S}{V_{\text{solid}}}. \tag{2.63}$$

The specific surface area is commonly determined using the nitrogen adsorption method [49, 50, 51].

The concept of the surface area is used for the definition of the hydraulic radius, see section 2.5.1. The hydraulic radius theories were developed to describe the pressure losses of the flow

through porous media. These theories use the surface area and the specific surface area for the determination of the permeability K. The concept of the permeability is discussed in section 2.5.5. The relation between K, S and s_v is stated, for example, by the Kozeny and Carman-Kozeny equations given as Eq. 2.72 and 2.74, respectively.

2.5.4 Tortuosity

The tortuosity is defined as the ratio of the actual length L_e of a flow path of a fluid and the straight-line distance L between inflow and outflow [2, 60, 61]

$$\tau = \frac{L_\mathrm{e}}{L} \geqslant 1. \tag{2.64}$$

This definition of the tortuosity is also referred to as the hydraulic tortuosity [62, 63]. In order to account for the tortuous shape of pores, τ was included in the hydraulic radius theories of a fluid flow through porous media, see section 2.5.5. Some correlations of the tortuosity τ and the porosity ϕ were proposed [63, 64, 65, 66].

2.5.5 Permeability

The permeability is a property of a porous medium that characterizes its ability to conduct a fluid flow [1]. It is defined by Darcy's law. Darcy [3] experimentally investigated slow, unidirectional, steady liquid flow though homogeneous porous specimens. He stated that the viscous pressure loss $\triangle p$ through a specimen is linearly dependent on the flow rate. Darcy's law yields [2]

$$Q = \frac{KA}{\mu}\frac{\triangle p}{L}, \tag{2.65}$$

where Q is the volumetric flow rate, L and A are, respectively, the thickness of a porous specimen and the area of its cross-section perpendicular to the flow direction, μ is the dynamic viscosity of fluid, and K is the permeability. The permeability has dimensions of a length squared m^2. In some scientific communities, however, it is expressed in "Darcy" units. 1 Darcy is defined as approximately $9.87{\cdot}10^{-13}\mathrm{m}^2$. Using the superficial flow velocity (or the filter velocity) u_s, one-dimensional Darcy's equation can be expressed as

$$-\frac{\mathrm{d}p}{\mathrm{d}z} = \frac{\mu}{K}u_\mathrm{s}, \tag{2.66}$$

where z is the axis in the direction of the superficial flow velocity u_s.

In case of anisotropic porous media the permeability tensor $\mathbf{K}$ is introduced as [67, 68]

$$\mathbf{K} = \begin{pmatrix} K_{xx} & K_{yx} & K_{zx} \\ K_{yx} & K_{yy} & K_{zy} \\ K_{xz} & K_{yz} & K_{zz} \end{pmatrix}. \tag{2.67}$$

Darcy's law with the permeability tensor $\mathbf{K}$ and the pressure gradient ∇p is given as

$$\mathbf{u}_\mathrm{s} = -\frac{\mathbf{K}}{\mu} \cdot \nabla p. \tag{2.68}$$

The methods of the permeability determination are based on measurements of the pressure drop of a fluid flow through a porous medium, from which K is calculated with Darcy's law. The experiments are usually performed at various low flow rates. The pressure drop is then plotted versus the flow rates and a straight line is fitted to the data points. Both liquid and gas flows can be used for the measurements. The most common configuration of the setup for the permeability determination is the falling head permeater. Its principle is described, for example, in [2, 104].

At high velocity the pressure drop through a porous medium deviates from Darcy's law predictions. Many attempts were undertaken to determine the critical Reynolds number for porous media. The Reynolds number characterizes the ratio of the inertia forces to viscous forces and can be expressed as

$$\mathrm{Re} = \frac{\rho u D}{\mu}, \tag{2.69}$$

where D is a characteristic pore diameter and u is the interstitial velocity of fluid. The relation between the interstitial velocity u and the superficial velocity u_s can be given via the Dupuit-Forchheimer assumption, see Eq. 2.93. The latter is discussed in section 2.6.1. The critical Reynolds number would characterize the transition from the Darcy to the non-Darcy flow regime. That was based on the analogy of the flow through porous media to the flow in tubes, where the critical Reynolds number characterizes the transition from the laminar to the turbulent regime.

However, the results reveal a high uncertainty in the critical Reynolds numbers for different porous materials. The values deviate from 0.1 to 75 [2]. Such a discrepancy may be stipulated on the one hand by the difficulty in definition of the characteristic pore size and on the other hand by the ineligibility of the "flow in tubes" analogy to some irregular and complex porous structures. In order to account for the pressure drop deviations from Darcy's law at high velocities, Forchheimer suggested the following modification [2]

$$-\frac{\mathrm{d}p}{\mathrm{d}z} = \frac{\mu}{K} u_\mathrm{s} + \beta_\mathrm{F} \rho u_\mathrm{s}^2. \tag{2.70}$$

The first term of Eq. 2.70 describes the viscous flow effects expressed by the Darcy's flow, while the second term with an empirical parameter β_{F} serves to correlate the pressure drop with the experimental data and, thus, to account for the high velocity effects. The parameter β_{F} is called the inertia parameter. Besides the limitation at high flow rates, the deviations from Darcy's law might occur due to molecular effects such as gas slippage, adsorption, capillary condensation, etc. [2].

In order to describe the viscous pressure loss in porous media, the hydraulic radius theories were developed. The hydraulic radius concept was given in section 2.5.1. These theories assume a relation between the permeability K and hydraulic radius R_{H} as [2]

$$K = \frac{C^*}{\phi R_{\mathrm{H}}^2}, \tag{2.71}$$

where C^* is some geometric constant. The first hydraulic radius theory was developed by Kozeny [2]. The Kozeny theory states an expression for the permeability K in terms of the surface area S of a porous medium as [2, 69]

$$K = \frac{c\phi^3}{S^2}, \tag{2.72}$$

where c is the Kozeny constant that varies slightly for different pore geometries ($c = 0.5$ for a circle, $c = 0.516$ for a square, and $c = 0.5974$ for an equilateral triangle). The relation between the surface area and the hydraulic radius is discussed in section 2.5.1. To take into account the tortuous shape of pores, the Kozeny equation was modified as follows [2, 61, 69]

$$K = \frac{c\phi^3}{\tau^2 S^2}, \tag{2.73}$$

where τ is the tortuosity of a porous medium, see section 2.5.4. Carman found that the Kozeny equation gives a better agreement with experiments if $c = 1/5$. He also included the specific surface area s into Eq. 2.72. The Carman-Kozeny equation yields the permeability K as [2, 70, 71]

$$K = \frac{\phi^3}{5(1-\phi)^2 s^2}. \tag{2.74}$$

The "drag" theories of permeability provides a different approach to give a physical explanation to K. In these theories the walls of the pores are treated as the obstacles on the way of the straight flow of some viscous fluid [2]. The Navier-Stokes equations are used to estimate the drag of the fluid on the walls. The sum of these drugs represents the resistance of the porous medium to the flow. There are two main types of the "drag" theories. Depending on the

geometry of the obstacles, one distinguishes the fiber and the spherical obstacles theories. The fiber theory gives the permeability K as [2]

$$K = \frac{3}{16}\frac{\phi\delta^2}{1-\phi}\frac{2-\ln[\delta Q\rho/(\mu\phi)]}{4-\ln[\delta Q\rho/(\mu\phi)]}, \tag{2.75}$$

where δ is the fiber diameter, Q is the flow rate, ρ is the density of fluid, μ is the dynamic viscosity of fluid. In contrast to the Darcy's concept, the permeability in Eq. 2.75 is not constant. It varies slowly with the flow rate. The spherical obstacle theory was extensively developed by Brinkman. He deduced the expression for the permeability K as [2]

$$K = \frac{R^2}{18}\left(3+\frac{4}{1-\phi}-3\sqrt{\frac{8}{1-\phi}-3}\right), \tag{2.76}$$

where R is the radius of a sphere.

2.6 Theoretical investigations of wicking

This section provides an overview of the theoretical investigations performed to study a spontaneous penetration of liquid into porous media, or wicking.

2.6.1 Bundle of capillaries models

A traditional approach to model the wicking process implies the analogy of the flow through a porous medium to the flow through a bundle of capillaries. This approach combines the one-dimensional (1D) mathematical description of the liquid rise in a capillary tube and the averaging of a porous medium via macroscopic parameters. Therefore, the mass and linear momentum conservation equations shall be first written for a liquid rise into a small single capillary.

Control volume

In section 2.4 the mass, linear momentum and energy conservation equations were written for a control volume of an infinitesimal size ("differential" approach). These equations can be also derived for large scale fixed or deformable control volumes. For that the Reynolds transport theorem should be applied to the differential conservation equations. Such an approach is known as an "integral" approach. The derivation of the conservation equations for fixed or deformable control volumes is in detail described, for example, in [4]. Here we focus on the mass and linear momentum conservation equations for a deformable control volume of the liquid

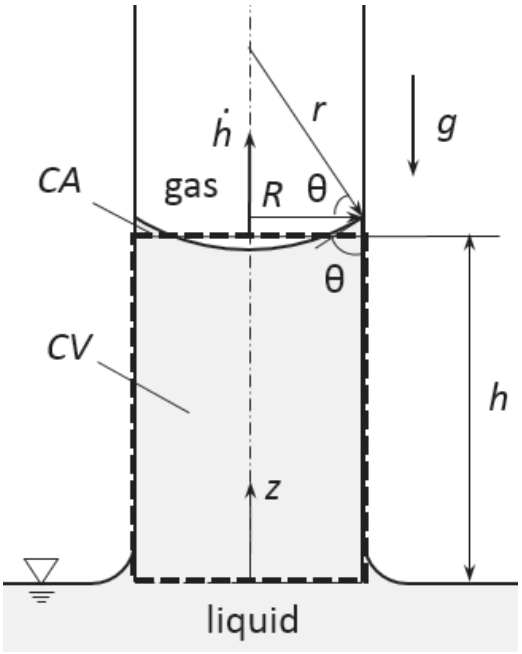

Figure 2.4: The liquid rise in the capillary of a radius R. The deformable control volume CV and the moving control surface CA are assigned for the rising liquid. h is the height of the liquid column in the tube and θ is the contact angle.

rising in a capillary tube. A deformable control volume CV and a moving control surface CA were assigned for a liquid rising in the tube of a radius R as shown on Fig. 2.4.

Mass conservation

The mass conservation equation for a deformable control volume CV with a control surface CA as a moving boundary is given as [4]

$$0 = \frac{\mathrm{d}m}{\mathrm{d}t} = \frac{\mathrm{d}}{\mathrm{d}t}\left(\int_{CV} \rho_\mathrm{L} dV\right) + \int_{CA} \rho_\mathrm{L}(\boldsymbol{v}_\mathrm{rel} \cdot \boldsymbol{n})\mathrm{d}A, \tag{2.77}$$

where $\boldsymbol{v}_\mathrm{rel}$ is the relative velocity with respect to a moving control surface CA and $\boldsymbol{n}$ is the normal to the plane of CA. The latter term in Eq. 2.77 denotes outflow if it is positive and inflow if negative.

For the capillary rise depicted on Fig. 2.4 Eq. 2.77 transforms into

$$0 = \frac{\mathrm{d}}{\mathrm{d}t}\left(\int_0^h \rho_\mathrm{L}\pi R^2 dz\right) - \rho_\mathrm{L}\pi R^2 u_\mathrm{rel}, \tag{2.78}$$

where the last term refers to the inflow and h is the height of the liquid column in the tube. The movement of the upper boundary is assumed to be defined with a meniscus velocity $\dot{h}$ that

in porous media corresponds to the wicking front velocity. Thus, the relative velocity at the upper boundary turns to zero. For an incompressible fluid Eq. 2.78 yields

$$0 = \rho_{\mathrm{L}} \pi R^2 \dot{h} - \rho_{\mathrm{L}} \pi R^2 u_{\mathrm{rel}}. \tag{2.79}$$

From Eq. 2.79 the inflow velocity is defined by the meniscus velocity $\dot{h}$.

Linear momentum conservation

The linear momentum conservation equation for a deformable control volume CV with a control surface CA is given as [4]

$$\sum \mathbf{F} = \frac{\mathrm{d}}{\mathrm{d}t}(m\boldsymbol{v}) = \frac{\mathrm{d}}{\mathrm{d}t}\left(\int_{CV} \rho_{\mathrm{L}} \boldsymbol{v} dV\right) + \int_{CA} \rho_{\mathrm{L}} \boldsymbol{v}(\boldsymbol{v}_{\mathrm{rel}} \cdot \boldsymbol{n})\mathrm{d}A. \tag{2.80}$$

For the capillary rise depicted on Fig. 2.4, Eq. 2.80 can be written as

$$\sum \mathbf{F}_z = \frac{\mathrm{d}}{\mathrm{d}t}\left(\int_0^h \rho_{\mathrm{L}} \pi R^2 \dot{h} dh\right) - \rho_{\mathrm{L}} \pi R^2 \dot{h} u_{\mathrm{rel}}. \tag{2.81}$$

Rearranging Eq. 2.81 and taking into account Eq. 2.79, for an incompressible fluid one obtains

$$\sum \mathbf{F}_z = \left(\rho_{\mathrm{L}} \pi R^2 h\ddot{h} + \rho_{\mathrm{L}} \pi R^2 \dot{h}^2\right) - \rho_{\mathrm{L}} \pi R^2 \dot{h}^2 = \rho_{\mathrm{L}} \pi R^2 h\ddot{h} \tag{2.82}$$

The left part of Eq. 2.82 corresponds to the sum of the following forces

$$\sum \mathbf{F}_z = F_{\mathrm{up}} + F_{\mathrm{lp}} + F_{\mathrm{vis}} + F_{\mathrm{g}}, \tag{2.83}$$

where F_{up} and F_{lp} are the total pressure force at the upper and lower boundary, respectively, F_{vis} is the viscous pressure loss and F_{g} is the gravity force. The total pressure force at the upper boundary is given as

$$F_{\mathrm{up}} = -\pi R^2 (p_{\mathrm{a}} - \triangle p) = -\pi R^2 \left(p_{\mathrm{a}} - \frac{2\sigma \cos\theta}{R}\right), \tag{2.84}$$

where p_{a} is the ambient pressure and $\triangle p$ is the capillary pressure given by the Young-Laplace equation, see section 2.3. As shown by Stange [115] and Fries [46], the local acceleration of liquid and viscous loss below the tube can be neglected for small capillaries and porous media. Thus, the total pressure force at the upper boundary can be written as

$$F_{\mathrm{lp}} = \pi R^2 (p_{\mathrm{a}} - \rho_{\mathrm{L}} \dot{h}^2), \tag{2.85}$$

where the last term corresponds to the convective acceleration losses given by Stange [115] (the coefficient 23/24 is omitted here).

The viscous pressure loss is given by the Hagen-Poiseuille equation [4]

$$F_{\mathrm{vis}} = -\pi R^2 \frac{8\mu_{\mathrm{L}} h\dot{h}}{R^2}, \tag{2.86}$$

where μ_{L} is the dynamic viscosity of liquid. The gravity force acting on a liquid in the capillary can be written as

$$F_{\mathrm{g}} = -\int_0^h \rho_{\mathrm{L}} g \pi R^2 \mathrm{d}z = -\pi R^2 \rho_{\mathrm{L}} g h, \tag{2.87}$$

where g is the gravitational acceleration. Substituting Eqs. 2.84, 2.85, 2.86 and 2.87 into Eq. 2.82, one obtains

$$\rho_{\mathrm{L}} \pi R^2 h\ddot{h} = -\pi R^2 \left(p_{\mathrm{a}} - \frac{2\sigma\cos\theta}{R} \right) + \pi R^2 p_{\mathrm{a}} - \pi R^2 \rho_{\mathrm{L}} \dot{h}^2 - \pi R^2 \frac{8\mu_{\mathrm{L}} h\dot{h}}{R^2} - \pi R^2 \rho_{\mathrm{L}} g h \tag{2.88}$$

Rearranging Eq. 2.88, one can write the linear momentum conservation equation for the capillary rise in a small tube as

$$\underbrace{\frac{2\sigma\cos\theta}{R}}_{\text{capillary pressure}} = \underbrace{\rho_{\mathrm{L}} \frac{\mathrm{d}(h\dot{h})}{\mathrm{d}t}}_{\text{inertia}} + \underbrace{\frac{8\mu_{\mathrm{L}} h\dot{h}}{R^2}}_{\text{viscous drag}} + \underbrace{\rho_{\mathrm{L}} g h}_{\text{hydrostatic pressure}}. \tag{2.89}$$

A good overview of the capillary rise stages and dominant forces at the stages is given by Stange et al. [115]. Fries and Dreyer [116] predicted the transition times between the stages. As shown in these papers, the purely inertial stage is relevant for early times. In case of small capillaries, for later times the inertia effect vanishes. Therefore, for the capillary transport in porous media many authors neglect inertia and focus on the viscous and gravitational stages. Lucas [94] and Washburn [93] were the first, who applied the bundle of capillaries analogy for modeling of the wicking process. They independently studied the penetration of liquids into a single cylindrical capillary and a porous medium. The porous medium was implied to be an assemblage of small parallel capillary tubes of uniform circular cross-section. The liquid rise was driven by the capillary pressure given by the Young-Laplace equation (see Eq. 2.8) and influenced by the viscous pressure losses given by the Hagen-Poiseuille equation (see Eq. 2.86). The impact of the inertia and gravity on the liquid rise was neglected. The obtained equation is known as the Lucas-Washburn equation and is given as

$$\frac{2\sigma\cos\theta}{R} = \frac{8\mu_{\mathrm{L}} h\dot{h}}{R^2}. \tag{2.90}$$

For this flow regime Lucas [94] and Washburn [93] proposed an analytic solution that stated the propagation $h(t)$ of the liquid meniscus in a capillary being proportional to the squared root of time $\sqrt{t}$.

Washburn [93] extended the model including the gravity term. Thus, Eq. 2.90 was transformed into

$$\frac{2\sigma\cos\theta}{R} = \frac{8\mu_{\mathrm{L}}h\dot{h}}{R^2} + \rho_{\mathrm{L}}gh. \tag{2.91}$$

An analytic solution for the extended model in terms of $t(h)$ was given by Washburn [93] as well as by Lukas and Soukupova [95]. Zhmund et al. [96] deduced a long-time asymptotic solution for this model in terms of $h(t)$. Fries and Dreyer [97] deduced an analytic solution in terms of $h(t)$ using the Lambert function. The viscous-gravitational capillary rise in porous media under isothermal conditions was also investigated in [101, 117].

Hamraoui and Nylander [98] and Martic et al. [99] modified the Lucas-Washburn equation with gravity effects to account for the dynamic contact angle θ_{d}. The concept of the dynamic contact angle was discussed in section 2.2.

Aiming to account for the irregularity of pores in real porous media, several models for non-uniform capillaries were proposed. For example, Young [169] analyzed the liquid rise in a tube constructed of a few circular capillaries of a different size. Staples and Shaffer [171] and Patro et al. [172] investigated imbibition into sinusoidal capillaries.

Hydraulic diameter approach

Applying the Lucas-Washburn equation with gravity effects, Fries et al. [36] and Masoodi et al. [100, 101] distinguished between the capillary diameter D_{c} for the computation of the capillary pressure and the hydraulic diameter D_{H} for the viscous pressure losses. In their works it was also shown that these two diameters are connected and the effective diameter D_{e} was introduced as

$$D_{\mathrm{e}} = \frac{D_{\mathrm{H}}^2}{D_{\mathrm{c}}}. \tag{2.92}$$

D_{H} in Eq. 2.92 accounted for the effect of the arbitrary shaped pores.

Darcy's law approach

Many authors substitute the viscous pressure term in the Lucas-Washburn equation (or its extended form) with Darcy's law (Eq. 2.66). The viscous pressure term in the Lucas-Washburn equation was originally given with the Hagen-Poiseuille equation (see Eq. 2.90 and 2.91). Darcy's law includes the permeability K of a porous medium. The concept of the permeability was discussed in section 2.5.5. Since the permeabilty can be determined experimentally, this allows to connect the bundle of the capillaries model to the structure characteristics of the real porous medium. Such an approach was used, for example, by Symons [125], Marmur [173],

Fries et al. [126, 38] and Masoodi et. al [100, 101]. Here, however, one should take into account that the bundle of capillaries model describes the wicking process using an interstitial velocity of liquid u_{L} in the capillary (microscopic velocity). Meanwhile, Darcy's law includes the filter or the superficial velocity u_{s} (macroscopic velocity), which is calculated on the basis of the bulk volume of the porous medium. A commonly accepted hypotheses that connects these two velocities is the Dupuit-Forchheimer assumption [2]. It states the relation between u_{L} and u_{s} as

$$u_{\mathrm{L}} = \frac{u_{\mathrm{s}}}{\phi}, \tag{2.93}$$

where ϕ is the porosity of a porous medium. The interstitial velocity of a liquid u_{L} is always larger than the superficial velocity u_{s} due to the reduced space available for the fluid to flow. Nevertheless, u_{L} should not be confused with an actual pore velocity that is in fact expected to fluctuate along the interconnected irregular pore channels.

Applying Darcy's law (Eq. 2.66) and the Dupuit-Forchheimer assumption (Eq. 2.93) to Eq. 2.89, one obtains the momentum balance for isothermal wicking in porous media as

$$\underbrace{\frac{2\sigma\cos\theta}{R_{\mathrm{s}}}}_{\text{capillary pressure}} = \underbrace{\rho_{\mathrm{L}}\frac{\mathrm{d}(h\dot{h})}{\mathrm{d}t}}_{\text{inertia}} + \underbrace{\frac{\phi\mu_{\mathrm{L}}\dot{h}h}{K}}_{\text{viscous drag}} + \underbrace{\rho_{\mathrm{L}}gh}_{\text{hydrostatic pressure}}, \tag{2.94}$$

where ϕ is the porosity and K is the permeability of a porous medium. The capillary pressure in Eq. 2.94 is given using the static pore radius R_{s}, see section 2.5.1.

Neglecting the inertia term in Eq. 2.94, one obtains the Lucas-Washburn equation with gravity effects as

$$\frac{2\sigma\cos\theta}{R_{\mathrm{s}}} = \frac{\phi\mu_{\mathrm{L}}h\dot{h}}{K} + \rho_{\mathrm{L}}gh. \tag{2.95}$$

For purely viscous flow Eq. 2.94 transforms into the Lucas-Washburn equation given as

$$\frac{2\sigma\cos\theta}{R_{\mathrm{s}}} = \frac{\phi\mu_{\mathrm{L}}h\dot{h}}{K}. \tag{2.96}$$

The bundle of capillaries models significantly simplify the representation of a porous medium. The flow in these models is inherently one-dimensional that makes it impossible to apply them for complicated heterogeneous geometries. The structure properties (characteristic pore size, permeability and porosity) are assumed to be equal to some values averaged for the bulk volume of the porous medium. The tortuous flow of liquid through interconnected pores in real structures is substituted with the flow along not-interconnected capillaries [104]. In addition, the bundle of capillaries models do not account for the variability of saturation of the porous medium with liquid. In fact, here only two states of saturation are valid: when the porous

medium is completely saturated with liquid or when it is completely dry. The latter makes these models inapplicable for the prediction of wicking in soils and some natural porous media where the saturation issues are of importance.

Despite the described above disadvantages the bundle of capillaries models are extensively used in the porous media community. They proved to be a simple and reliable tool for the capillary transport prediction in homogeneous porous structures. These models require minimum computational power and, thus, are applicable to perform predictions for lab-scale samples and industrial porous elements [34].

The theoretical models proposed in this work for the prediction of cryo-wicking are based on the bundle of capillaries approach. The models include the Lucas-Washburn equation with gravity effects combined with Darcy's law. The derivation of the governing equations for the models is given in chapter 3.

2.6.2 Pore network models

In pore network models the pore space is represented as a network of pore bodies connected by throats. The principle of this approach for the prediction of wicking is explained, for example, by Masoodi and Pillai [104].

In a simplest case the pores can form a square network. The pore bodies are spheres of a uniform diameter and the pore throats are identical cylindrical tubes. Each pore body is connected to four neighboring bodies. The mass conservation for each pore body yields

$$\sum_i Q_{i,j} = 0, \tag{2.97}$$

where $Q_{i,j}$ is the volumetric flow rate between two pores i and j given as

$$Q_{i,j} = \frac{g_{i,j}}{\mu_{\mathrm{L}}}(p_i - p_j). \tag{2.98}$$

$g_{i,j}$ in Eq. 2.98 is the local hydraulic throat conductance expressed using the Hagen-Poiseuille equation as

$$g_{i,j} = \frac{\pi d_{i,j}^4}{128 d_{\mathrm{l}}}, \tag{2.99}$$

where $d_{i,j}$ is the tube diameter and d_{l} is the distance between two pore bodies.

The flow rate at the pore throat with a liquid-gas interface is given as

$$Q_{i,j} = \frac{g_{i,j}}{\mu_{\mathrm{L}}}(p_i + \triangle p_{i,j}), \tag{2.100}$$

where $\triangle p_{i,j}$ is the capillary pressure expressed using the Young-Laplace equation (Eq. 2.8) as

$$\triangle p_{i,j} = \frac{4\sigma \cos\theta}{d_{i,j}}. \tag{2.101}$$

Due to the capillary pressure the liquid invasion into an empty adjacent pore j occurs. The time for filling t_j of this pore is calculated as

$$t_j = V_j(1 - S_j) \sum_i Q_{i,j}, \tag{2.102}$$

where V_j is the pore volume and S_j is the saturation of the pore with the liquid.

The computation of the system of such equations for a perfectly ordered structure (uniform pore body size and uniform throat size) results in a flat wicking front as for the bundle of capillaries models, see section 2.6.1. However, the advantage of the pore network approach is in a possibility to define the diameters of pore bodies and throats as randomly distributed in a given range of values. In this case the deviations from the averaged wicking front can be captured. Pore network models are preferable for heterogeneous porous media, where such deviations are significant.

A good overview of pore network models is given by Blunt [86]. Joekar-Niasar et al. [87] investigated various shapes of pore throat cross-sections. Prat [134] and Figus et al. [89] studied evaporation induced by external heating of a porous structure. The drying process in saturated porous structures was investigated by Segura [90] and Yiotis [91, 92]. Nevertheless, the pore network approach is considered to be a promising tool only for relatively small systems [134]. The influence of large scale heterogeneities, for example, in natural systems cannot be estimated using such models.

Pore network models were not applied in this study. Theoretical prediction of wicking was performed using the macroscopic approach, see section 2.6.1.

2.7 Experimental investigations of wicking

This section is based on the publications "Wicking of liquid nitrogen into superheated porous structure"[1] by Y. Grebenyuk and M.E. Dreyer [34] and "Wicking into porous polymer-derived

[1]Reprinted from Cryogenics, Vol. 78, Y. Grebenyuk, M.E. Dreyer, Wicking of liquid nitrogen into superheated porous structures, Pages No. 27-39, Copyright (2017), with permission from Elsevier.

ceramic monoliths fabricated by freeze-casting"[2] by Y. Grebenyuk et al. [160]. It provides an overview of the experimental investigations performed to study the wicking process.

There are two main methods that are usually applied for wicking experiments: the optical and the weight measurement method.

The optical method combines video recording of the wicking process and image processing. For example, Conrath et al. [72] investigated radial capillary transport into various filter papers. The authors recorded radially outward and inward wicking into a specimen via a digital video camera and processed the obtained images to obtain the propagation of the radius of the wetted spot in time. Some theoretical models were proposed to describe the results. Morent et al. [73] experimentally studied horizontal wicking into textile specimens. The authors compared different image processing algorithms for the analysis of the increase of the wetted area. Vertical wicking experiments using the optical methods were performed, for example, by Lago and Araujo [117] and Fries et al. [36, 126, 38]. In case of vertical wicking the increase of the wicking height in time is studied. Lago and Araujo [117] investigated the capillary rise in glass beds and sandstones. The authors observed the Lucas-Washburn behavior (see section 2.6.1) of wicking and the deviations from it for different time-scales and porous structures. Fries et al. [36] performed vertical wicking experimens to extract macroscopic parameters of metallic screen meshes. The authors studied the effect of evaporation of the liquid from the saturated structure on the imbibition rate and proposed a theoretical model to account for that [126, 38]. For the experiments, however, both, the optical and the weight measurements methods were applied. The weight measurement method is based on recording the weight change of a sample or a liquid reservoir during the imbibition. The mass of the imbibed liquid can be extracted from the measurements. For homogeneous structures the wicking height can be calculated from the mass of the imbibed liquid. The weight measurement method was also applied in the wicking experiments conducted by Masoodi et al [101, 102]. The authors used the results of the imbibition into polymer wicks to validate various theoretical models. Galet et al. [75] applied the weight measurement method for the characterization of the wettability of powders. They determined the contact angle from the capillary rise tests with powder beds and different test liquids. Liu et al. [148] determined the mass of the imbibed liquid to study the influence of evaporation in wicking experiments with filter papers. The imbibition into swelling porous

[2]Reprinted from Journal of the European Ceramic Society, Vol. 37, Y. Grebenyuk, H.X. Zhang, M. Wilhelm, K. Rezwan, M.E. Dreyer, Wicking into porous polymer-derived ceramic monoliths fabricated by freeze-casting, Pages No. 1993-2000, Copyright (2017), with permission from Elsevier.

media was extensively studied by Hong and Kim [78], Pucci et al. [77], Stuart et al. [79] and Masoodi et al. [80, 81].

Some authors performed experiments to investigate the heat transfer in porous structures. Hanlon and Ma [82] studied the effect of the thin-film evaporation on the heat transport behavior of the horizontal wick structure saturated with liquid. The authors showed that the thin-film evaporation occurs at the top surface of the wick and plays an important role in the enhancement of evaporating heat transfer. Hanlon and Ma [82] showed that the maximum dry-out heat flux greatly depends on the wick thickness. The evaporation from the heated horizontal porous structures was also studied by Li et al. [83, 107]. The authors observed the dependence of the critical heat flux on the thickness, pore size and porosity of specimens. Similar studies with vertically oriented porous structures were conducted by Brautsch and Kew [85]. Nevertheless, a key wicking parameter, the imbibition rate, was not assessed in these works.

Few studies have been done to understand the behavior of cryogenic fluids in porous structures. Zhang et al. [127] demonstrated wicking of liquid nitrogen with a sintered, multi-layer, porous lamination of metal wire in an open cryogenic chamber. Local temperatures of porous and non-porous samples identical in geometry and material were measured by sensors allocated along the sample height. The saturation of the porous sample with liquid nitrogen changed its temperature response to external heating at the sample top. That indicated the liquid presence in the porous structure. Choi et al. [128] studied the flow phenomena of liquid nitrogen subjected to evaporation in glass wool porous media. Experiments were performed to obtain temperature and pressure distributions in the specimens and, thus, to evaluate the tendency of propagation of the liquid-saturated region in porous media. Some numerical simulation was conducted and compared to the experimental results. A series of experiments with liquid hydrogen, oxygen and nitrogen was performed by Hartwig et al. [144, 129, 130] to determine the bubble point pressure of metallic screen meshes. The authors investigated the impact of a screen mesh type, liquid temperature and pressure, and type of pressurization gas.

Few works have been done to examine wicking in porous ceramics. Einset [152] analyzed the capillary rise of organic liquids into a porous medium fabricated of consolidated particles of C and SiC via the tape casting method. The author optically measured the penetration heights as a function of time and determined the corresponding infiltration rates. Kumar et al. [153] investigated organic liquid infiltration in porous carbon-carbon preforms. The authors applied optical measurements to determine penetration heights and estimated the flow rate of water through porous media to characterize permeability. In a second paper, Kumar et al. [154] studied the infiltration rates of silicone in porous carbon-carbon preforms. Okada et al. [155]

estimated capillary rise properties of porous mullite ceramics prepared by an extrusion method. The capillary rise height in experiments with water was determined by visual observation. Okada et al. [156] also examined the imbibition into porous geopolymers prepared by an extrusion method.

In this study wicking experiments were performed using the weight measurement method. The imbibition tests were conducted with commercially obtained porous samples made of sintered glass frits and ceramic samples supplied by the Advanced Ceramics Group of the University of Bremen. Liquid nitrogen and FC-72 liquid were used as test liquids.

2.8 Numerical simulations of fluid flow in porous media

Computational fluid dynamics (CFD) has recently become a commonly used tool for the investigation of fluid flow problems. It is based on numerical approximation and computation of equations governing a fluid flow. A computation domain is discretized using two- or three-dimensional elements (cells). Some boundary and initial conditions are applied to the domain. A range of CFD software packages is available to perform simulations of a fluid flow in porous media.

Ranut et al. [105] studied the laminar steady flow regime in metal foams using the commercial software Ansys CFX. The flow was simulated with 3D-images of the porous structures obtained via X-ray tomography. The pressure drop of the flow through the porous medium was computed. The permeability of the metal foams was estimated via Darcy's law (see section 2.5.5) and found to be in a good agreement with experimentally determined values. Li et al. [106, 107] applied Ansys CFX to investigate the pressure drop of the flow through foam corrugated sheets. The authors applied the computer aided design tools to construct a representative volume of a solid structure used for simulations. Boccardo et al. [108] used similar approach to estimate the pressure drop of the flow through packings of spheres and trilobes from the steady flow simulations performed via Ansys Fluent. Meinicke et al. [109, 110] studied single-phase hydrodynamics in glass sponges using OpenFOAM. Narsilio et al. [111] and Fourie et al. [112] estimated the permeability of glass beads packings and soil specimens, respectively, from the steady flow simulations performed using COMSOL.

In this work the commercial CFD software FLOW-3D was used for benchmark microscopic (pore level) and macroscopic simulations of a flow in porous media. The computation approach, governing equations and numerical approximations applied for these simulations are described in section 7.2. Some studies with porous media and FLOW-3D has been conducted. Fries et

al. [36] performed a macroscopic wicking simulation for a geometry element having properties of a metallic mesh. The authors applied the porous media model available in FLOW-3D and validated it with the Lucas-Washburn equation (see section 2.6.1). Zhang [113] applied this model for simulations of radial outward wicking in filter papers. The porous media model is described in section 7.4.1. In this study macroscopic wicking simulations were conducted for sample of various geometries and properties and were validated with experiment results. Using the steady flow simulations in FLOW-3D, Zhang [113] investigated the pressure losses for various sphere packings. He also performed such simulations using a 3D-image of a porous structure obtained via X-ray tomography. The capillary rise simulation was conducted to estimate the static pore radius of the porous structure. Zhang [113] performed simulations for the porous structure made of sintered glass frits. A similar structure of smaller pore size was studied in this work. The microscopic simulation of the steady one fluid flow was performed to estimate the porosity and permeability. The microscopic wicking simulation was conducted. The settings of macroscopic and microscopic simulations and the analysis of the results are described in chapter 7.

2.9 Aims of this work

The motivation for this work was discussed in section 1.1. Here the aims of the study derived from the analysis of the state of the art are described.

The state of the art showed that there is a lack of experiment data for wicking of a cryogenic liquid subjected to evaporation, see section 2.7. For this reason, cryo-wicking tests should be performed. In order to provide reliable results, it is essential to ensure a one-species system in the vessel containing the cryogenic liquid and the porous structure. A setup configuration should enable a sample superheat with regard to the liquid temperature to ensure the evaporation effect. The non-isothermal conditions should be predefined to allow the validation of theoretical predictions with the experiment results. However, no theoretical model was found in the literature to describe wicking of a cryogenic liquid subjected to evaporation due to the heat transfer with a superheated porous structure. Therefore, such a theoretical model should be developed.

Only few works devoted to the investigations of the capillary transport characteristics of porous ceramics were found in the literature, see section 2.7. Meanwhile, as discussed in chapter 1.1, porous ceramics is a promising material for mass transport applications. For that reason, wicking experiments should be performed for such porous structures. A special attention should

be drawn to anisotropic porous structures that provide additional benefits for mass transport processes, see section 1.1. To the author's extent of knowledge no experiments have been carried out to investigate the capillary transport abilities of anisotropic porous ceramics.

The literature research revealed a wide range of studies on the fluid flow problems in porous media conducted using a computational fluid software, see section 2.8. However, only some of them focus on the investigation of wicking in porous media. In the works of Fries [36] and Zhang [113] the computational fluid software FLOW-3D was identified as a possible tool to perform wicking simulations on macroscopic and microscopic (pore size) scales. Nonetheless, the feasibility of this software to simulate wicking in porous media of various geometries and properties should be investigated in more detail. The simulation results should be validated with experiment data.

Chapter 3

1D theoretical models for cryo-wicking

This chapter is based on the publication "Wicking of liquid nitrogen into superheated porous structures"[1] by Y. Grebenyuk and M.E. Dreyer [34].
Macroscopic or continuum wicking models proved to be a simple and reliable tool for the capillary transport prediction in homogeneous porous media under isothermal conditions. They require minimum computational power and are applicable to perform predictions for lab-scale samples and industrial porous elements. These models are based on averaging of porous media via the introduction of macroscopic parameters: porosity, characteristic pore size and permeability. We propose macroscopic models for non-isothermal wicking that account for evaporation occurring at the wicking front due to the heat transfer between superheated porous media and cryogenic liquid at saturation temperature. The analogy of the flow through porous media to the flow through a bundle of capillary tubes is assumed. Such an analogy is inherent to the bundle of capillary tubes macroscopic models, see section 2.6.1.

3.1 Wicking of a cryogenic liquid into superheated porous structures

3.1.1 1D theoretical model

We study the non-isothermal imbibition of a cryogenic liquid at saturation temperature into a porous sample. The dry solid structure of the vertically oriented sample (in z-direction) is superheated with regard to the liquid temperature. The superheat is in accordance with a

[1] Reprinted from Cryogenics, Vol. 78, Y. Grebenyuk, M.E. Dreyer, Wicking of liquid nitrogen into superheated porous structures, Pages No. 27-39, Copyright (2017), with permission from Elsevier.

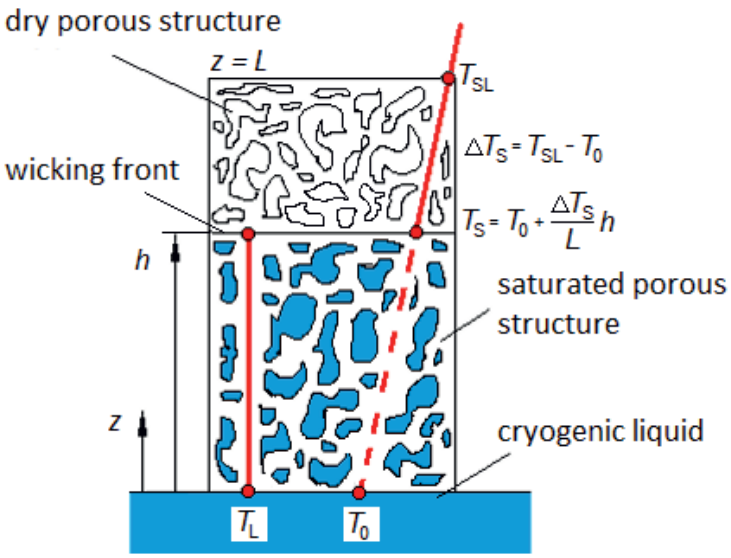

Figure 3.1: Vertical wicking of a cryogenic liquid at saturation temperature T_L into the superheated porous sample of a height L. The local temperature of the dry solid structure T_S is defined by the linear temperature gradient $\triangle T_\mathrm{S}/L$ and the initial temperature at the sample bottom T_0. T_SL is the initial temperature of the dry solid structure at the sample top.

linear temperature gradient along the sample height. The imbibition into a porous sample is schematically shown in Fig. 3.1. The local temperature of the dry solid structure T_S is defined by the temperature gradient $\triangle T_\mathrm{S}/L$ and the initial temperature at the sample bottom T_0 as

$$T_\mathrm{S} = T_0 + \frac{\triangle T_\mathrm{S}}{L} z. \tag{3.1}$$

Due to the heat transfer between superheated porous structure and cryogenic liquid, a certain amount of liquid evaporates at the wicking front ($z = h$). We assume that the vapor created due to evaporation escapes through the lateral sides of the porous sample and, therefore, has no influence on the wicking process. Therefore, the momentum balance for the capillary rise of a liquid evaporating in porous media states

$$\underbrace{\frac{2\sigma\cos\theta}{R_\mathrm{s}}}_{\text{capillary pressure}} = \underbrace{\frac{\phi\mu_\mathrm{L}}{K} h u_\mathrm{L}}_{\text{viscous drag}} + \underbrace{\rho_\mathrm{L} g h}_{\text{hydrostatic pressure}}, \tag{3.2}$$

where u_L is the interstitial velocity of the liquid. Evaporation changes the relationship between u_L and the imbibition rate $\dot{h}$ that were equal to each other in the isothermal case in Eq. 2.94. The mass balance gives this relationship for the case with evaporation at the wicking front ($z = h$) as follows (see Eq. 2.46)

$$\rho_\mathrm{L}\left(u_\mathrm{L} - \frac{\mathrm{d}h}{\mathrm{d}t}\right) = \rho_\mathrm{V}\left(u_\mathrm{V} - \frac{\mathrm{d}h}{\mathrm{d}t}\right) = j_\mathrm{ev}, \tag{3.3}$$

where j_{ev} is the evaporative mass flux. From Eq. 3.3 the interstitial velocity of liquid is given by

$$u_{\mathrm{L}} = \dot{h} + \frac{j_{\mathrm{ev}}}{\rho_{\mathrm{L}}}. \tag{3.4}$$

In [136, 137] the similar approach is described for the capillary rise in a tube.

To evaluate the evaporative mass flux, we assume that the heat needed to cool down the superheated solid structure is taken from the latent heat of evaporation. Thus, the heat removal rate needed to cool an infinitely slim layer dh of the solid structure from its local temperature T_{S} at the wicking front to the saturation temperature of liquid T_{L} is

$$\frac{\mathrm{d}q}{\mathrm{d}t} = \rho_{\mathrm{S}} c_{\mathrm{S}} (T_{\mathrm{S}} - T_{\mathrm{L}})(1-\phi) A \frac{\mathrm{d}h}{\mathrm{d}t}. \tag{3.5}$$

The rate of heat absorption due to evaporation (see Eq. 2.54) is

$$\frac{\mathrm{d}q}{\mathrm{d}t} = \triangle h_{\mathrm{v}} \phi A j_{\mathrm{ev}}, \tag{3.6}$$

where $\triangle h_{\mathrm{v}}$ is the specific latent heat of evaporation.

Rearranging Eq. 3.5 and Eq. 3.6, one obtains the evaporative mass flux as follows

$$j_{\mathrm{ev}} = \frac{\rho_{\mathrm{S}} c_{\mathrm{S}} (T_{\mathrm{S}} - T_{\mathrm{L}})(1-\phi)}{\phi \triangle h_{\mathrm{v}}} \frac{\mathrm{d}h}{\mathrm{d}t}. \tag{3.7}$$

We neglect the heat conduction in the solid structure and the heat exchange between the saturated vapor and the solid structure. The local temperature of the dry solid structure T_{S} at $z = h$ is assumed to be as given in Eq. 3.1.

In order to simplify the equations, we introduce the parameters summarized in Table 3.1. Using these parameters and substituting Eq. 3.7 to Eq. 3.4, one obtains the interstitial velocity of liquid as

$$u_{\mathrm{L}} = \dot{h} + \epsilon n_1 \dot{h} + \epsilon n_2 h \dot{h}. \tag{3.8}$$

The momentum balance Eq. 3.2 with the parameters introduced in Table 3.1 transforms into

$$1 = ch + bhu_{\mathrm{L}}. \tag{3.9}$$

Substituting Eq. 3.8 to Eq. 3.9, one obtains the final equation for the capillary rise of a cryogenic liquid in superheated porous media with evaporation at the wicking front as

$$1 = ch + bh\dot{h}(1 + \epsilon(n_1 + n_2 h)). \tag{3.10}$$

Integrating Eq. 3.10 yields the analytic solution in implicit form as follows

$$t(h) = -\frac{b\epsilon n_2}{2c} h^2 - \frac{b}{c}\left(1 + \epsilon\left(n_1 + \frac{n_2}{c}\right)\right)\left(h + \frac{1}{c}\ln(1-ch)\right). \tag{3.11}$$

Table 3.1: List of the parameters of Eq. 3.11.

Parameter	Equation	Physical meaning
ϵ	$\frac{1-\phi}{\phi}$	-
b	$\frac{\phi R_\mathrm{s}}{K}\frac{\mu_\mathrm{L}}{2\sigma\cos\theta}$	$\frac{\text{viscous forces}}{\text{capillary pressure}}$
c	$R_\mathrm{s}\frac{\rho_\mathrm{L} g}{2\sigma\cos\theta}$	$\frac{\text{gravity}}{\text{capillary pressure}}$
n_1	$\frac{\rho_\mathrm{S}}{\rho_\mathrm{L}}\frac{c_\mathrm{S}(T_0-T_\mathrm{L})}{\triangle h_\mathrm{v}}$	$\frac{\text{sensible heat}}{\text{latent heat of evaporation}}$
n_2	$\frac{\rho_\mathrm{S}}{\rho_\mathrm{L}}\frac{c_\mathrm{S}}{\triangle h_\mathrm{v}}\frac{\triangle T_\mathrm{S}}{L}$	temperature gradient impact

More details on the derivation of Eq. 3.11 are provided in the Appendix A.1.
Eq. 3.11 with $n_1 = n_2 = 0$ represents a solution for the viscous-gravitational capillary rise in porous media under isothermal conditions given in [93, 95]

$$t(h) = -\frac{b}{c}\left(h + \frac{1}{c}\ln(1-ch)\right). \tag{3.12}$$

Heat conduction in solid structure

The proposed wicking model was derived neglecting the heat transfer by conduction in solid structure of a porous sample. In this section an approach to estimate its significance for the wicking process is described.
The thermal diffusivity α_S of a solid is defined as

$$\alpha_\mathrm{S} = \frac{\lambda_\mathrm{S}}{\rho_\mathrm{S} c_\mathrm{S}}, \tag{3.13}$$

where λ_S is the thermal conductivity of solid, ρ_S and c_S are the density and the specific heat capacity of solid, respectively. The diffusion of the thermal energy by conduction can be scaled by the boundary layer thickness δ_T given as

$$\delta_\mathrm{T} = \sqrt{\frac{\lambda_\mathrm{S} t}{\rho_\mathrm{S} c_\mathrm{S}}} = \sqrt{\alpha_\mathrm{S} t}. \tag{3.14}$$

Meanwhile, the imbibition of a wetting liquid into an unsaturated porous structure can be seen as the mass diffusion. The proposed wicking model is based on the bundle of capillary tubes

approach, see section 2.6.1. Therefore, neglecting the gravity and evaporation effects, one can describe the mass diffusion of the imbibing liquid by the Lucas-Washburn equation (see Eq. 2.96) written as

$$\delta_{\mathrm{W}} = \sqrt{\frac{4\sigma \cos\theta K t}{R_{\mathrm{s}} \phi \mu_{\mathrm{L}}}} = \sqrt{\frac{2t}{b}} = \sqrt{D_{\mathrm{m}} t}, \tag{3.15}$$

where D_{m} is the mass diffusion coefficient. The ratio of the thermal diffusivity to the mass diffusion coefficient leads to the dimensionless Lewis number given as

$$\mathrm{Le} = \frac{\alpha_{\mathrm{S}}}{D_{\mathrm{m}}}. \tag{3.16}$$

Thus, the Lewis number can serve to estimate the significance of the heat conduction in solid for the imbibition into a porous sample.

Chapters 4 and 5 describe cryo-wicking experiments with liquid nitrogen and porous samples made of glass filter elements (borosilicate glass). The thermal diffusivity α_{S} of solid, the mass diffusivity D_{m}, and the Lewis number were computed via Eqs. 3.13, 3.15, and 3.16, respectively, using the thermophysical properties of liquid nitrogen at 77.355 K and 101325 Pa (see Table 4.6), of borosilicate glass at 77.355 K and at 300 K (see Table 4.1), and the macroscopic parameters of the porous samples (see Table 4.4). The obtained values were summarized in Table 3.2. From the comparison of α_{S} with D_{m} and the Lewis number values, the heat conduction in solid structure can be assumed negligible for the imbibition of liquid nitrogen into the test samples. However, the Lucas-Washburn equation taken for the calculation of D_{m} is valid only for the viscous-dominated stage of the wicking process, see section 2.6.1. Further the gravity effects significantly slow down the wicking front propagation. This is shown, for example, in [97]. According to Fries and Dreyer [126, 97], one can apply the Lucas-Washburn equation up to 10 % of the equilibrium wicking height h_{eq}, when accepting an error of 3.7 %. The term of the equilibrium wicking height was discussed in section 2.5.1. Using Eq. 2.59, $0.1h_{\mathrm{eq}}$ was calculated for the imbibition of liquid nitrogen into each test sample, see Table 3.2. As shown in Table 4.2, the test samples for the cryo-wicking experiments were of 0.08 m height, which is larger than $0.1h_{\mathrm{eq}}$. For $h > 0.1h_{\mathrm{eq}}$ the imbibition (i.e. the mass diffusion) was additionally counteracted by the gravity effects. According to the proposed model, the cryogenic liquid evaporates during the wicking process due to the heat transfer with the superheated porous structure. As discussed in chapters 4 and 5, this effect as well leads to the decrease of the wicking rate (i.e. the mass diffusion rate). Therefore, due to the influence of the hydrostatic pressure and the evaporation on the wicking process the thermal diffusion and mass diffusion rates may become comparable.

Table 3.2: The mass diffusion coefficient D_{m}, thermal diffusivity α_{S} of solid and the Lewis number Le computed via Eqs. 3.15, 3.13, and 3.16, respectively, for liquid nitrogen at saturation temperature at 101325 Pa (77.355 K) and porous samples R19, R12, R12T, C19 and C12. The subscripts 1 and 2 refer to the values calculated via thermophysical properties of borosilicate glass at 300 K and 77.355 K, respectively. h_{eq} refers to the equilibrium wicking height (see Eq. 2.59).

Sample	D_{m} ($\mathrm{m^2\ s^{-1}}$) 10^{-5}	α_{S1} ($\mathrm{m^2\ s^{-1}}$) 10^{-7}	α_{S2} ($\mathrm{m^2\ s^{-1}}$) 10^{-7}	Le_1 (-) 10^{-2}	Le_2 (-) 10^{-2}	$0.1h_{\mathrm{eq}}$ (m) 10^{-2}
R19	4.26	6.33	8.97	1.49	2.11	1.14
R12	3.72	6.33	8.97	1.70	2.41	1.83
R12T	3.72	6.33	8.97	1.70	2.41	1.83
C19	4.07	6.33	8.97	1.56	2.21	1.14
C12	1.97	6.33	8.97	3.22	4.56	1.83

Nevertheless, for simplification purposes the heat conduction in solid structure was neglected for the proposed wicking model.

3.1.2 Dimensionless formulation

To non-dimensionalize the final equation for the capillary rise of a cryogenic liquid in superheated porous media with evaporation at the wicking front (Eq. 3.10) and its analytic solution (Eq. 3.11), we apply the Buckingham π theorem. Such an approach was used by Fries [114] for dimensionless scaling of the capillary rise in a tube or porous media under isothermal conditions.

In Eqs. 3.10 and 3.11 one finds five (5) dimensional units b [s $\mathrm{m^{-2}}$], c [$\mathrm{m^{-1}}$], n_2 [$\mathrm{m^{-1}}$], h [m],

Table 3.3: The dimensional and fundamental units in Eqs. 3.10 and 3.11.

	b	c	n_2	h	t
s	1	0	0	0	1
m	-2	-1	-1	1	0

and t [s], and two (2) fundamental units *time* [s] and *length* [m]. The table of dimensional and fundamental units of the system is given in Table 3.3. Thus, one obtains 5-2=3 dimensionless π-parameters that characterize the problem.

According to the Buckingham π theorem, the system of equations evolves as follows

$$\begin{pmatrix} 1 & 0 & 0 & 0 & 1 \\ -2 & -1 & -1 & 1 & 0 \end{pmatrix} \cdot \begin{pmatrix} \pi_{1b} & \pi_{2b} & \pi_{3b} \\ \pi_{1c} & \pi_{2c} & \pi_{3c} \\ \pi_{1n_2} & \pi_{2n_2} & \pi_{3n_2} \\ \pi_{1h} & \pi_{2h} & \pi_{3h} \\ \pi_{1t} & \pi_{2t} & \pi_{3t} \end{pmatrix} = \begin{pmatrix} 0 & 0 & 0 \\ 0 & 0 & 0 \end{pmatrix} \tag{3.17}$$

This system is under-determined, and one is allowed to choose three (3) dimensional parameters in each π-vector.

We choose n_2 as a basic parameter, while b and c as scaling parameters. Then for h-scaling one can set $\pi_{1n_2} = 0$, $\pi_{1h} = 1$ and $\pi_{1t} = 0$. For t-scaling one can set $\pi_{2n_2} = 0$, $\pi_{2h} = 0$ and $\pi_{2t} = 1$. To find the basic parameter n_2, one can set $\pi_{3n_2} = 1$, $\pi_{3h} = 0$ and $\pi_{3t} = 0$. Taking into account the settings made above, one can solve the system 3.17 and obtain

$$\begin{pmatrix} \pi_{1b} & \pi_{2b} & \pi_{3b} \\ \pi_{1c} & \pi_{2c} & \pi_{3c} \\ \pi_{1n_2} & \pi_{2n_2} & \pi_{3n_2} \\ \pi_{1h} & \pi_{2h} & \pi_{3h} \\ \pi_{1t} & \pi_{2t} & \pi_{3t} \end{pmatrix} = \begin{pmatrix} 0 & -1 & 0 \\ 1 & 2 & -1 \\ 0 & 0 & 1 \\ 1 & 0 & 0 \\ 0 & 1 & 0 \end{pmatrix}. \tag{3.18}$$

Thereby, the Buckingham π theorem provides

$$\pi_1^* = b^0 c^1 n_2^0 h^1 t^0 = ch = h^*, \tag{3.19}$$

$$\pi_2^* = b^{-1} c^2 n_2^0 h^0 t^1 = \frac{c^2 t}{b} = t^*, \tag{3.20}$$

$$\pi_3^* = b^0 c^{-1} n_2^1 h^0 t^0 = \frac{n_2}{c} = \Omega_2. \tag{3.21}$$

Introducing the dimensionless parameter $\Omega_1 = n_1$ and taking into account the dimensionless parameter ϵ from Table 3.1, one obtains Eq. 3.10 in dimensionless form as follows

$$1 = h^* + h^* \dot{h}^* (1 + \epsilon(\Omega_1 + \Omega_2 h^*)). \tag{3.22}$$

With $\Omega_1 = \Omega_1 = 0$ Eq. 3.22 transfers into the dimensionless form of the Lucas-Washburn equation with gravity effects (Eq. 2.95) given as

$$1 = h^* + h^* \dot{h}^*. \tag{3.23}$$

An analytic solution for Eq. 3.22 can be obtained as

$$t^*(h^*) = -\frac{\epsilon\Omega_2}{2}h^{*2} - (1 + \epsilon(\Omega_1 + \Omega_2))(h^* + \ln(1 - h^*)). \tag{3.24}$$

Eq. 3.24 is also the dimensionless form of Eq. 3.11.
An analytic solution for the dimensionless form of the Lucas-Washburn equation with gravity effects (Eq. 3.23) yields

$$t^*(h^*) = -h^* - \ln(1 - h^*)). \tag{3.25}$$

The dimensionless variables and parameters h^* , t^*, Ω_1 and Ω_2 include the dimensionless numbers relevant for wicking, see Table 3.4.

Table 3.4: List of the dimensionless numbers relevant for wicking .

Abbreviation	Name	Equation	Forces
Bo	Bond number	$\frac{\rho g R_s^2}{\sigma}$	$\frac{\text{gravity}}{\text{surface tension}}$
Ca	Capillary number	$\frac{\mu u}{\sigma} \sim \frac{\mu R_s}{\sigma t}$	$\frac{\text{viscous}}{\text{surface tension}}$
Re	Reynolds number	$\frac{2\rho u R_s}{\mu}$	$\frac{\text{inertia}}{\text{viscous}}$
Ja_1	Jakob number	$\frac{c_{PL}(T_0 - T_L)}{\triangle h_v}$	$\frac{\text{sensible heat}}{\text{latent heat of evaporation}}$
Ja_2	Jakob number	$\frac{c_{PL}(T_{SL} - T_0)}{\triangle h_v}$	$\frac{\text{sensible heat}}{\text{latent heat of evaporation}}$

The variable h^* can be represented as

$$h^* = ch = \frac{h}{h_{eq}} = R_s\frac{\rho_L g}{2\sigma\cos\theta}h \sim \frac{\text{Bo}}{2\cos\theta}, \tag{3.26}$$

where Bo is the Bond number. Eq. 3.26 shows that h^* is defined as a ratio of the wicking height to the equilibrium wicking height h_{eq} that is the maximum achievable wicking height for a porous structure. Thus, the value of the dimensionless variable h^* indicates which part of the maximum wicking height was achieved at the time t^*.

The variable t^* can be represented as

$$t^* = \frac{c^2 t}{b} = \left(R_\mathrm{s}\frac{\rho_\mathrm{L} g}{2\sigma\cos\theta}\right)^2 t\frac{K}{\phi R_\mathrm{s}}\frac{2\sigma\cos\theta}{\mu_\mathrm{L}} = \\ = \frac{1}{2\cos\theta}\frac{\rho_\mathrm{L} g R_\mathrm{s}^2}{\sigma}\frac{\rho_\mathrm{L} g}{\sigma}\frac{K}{\phi R_\mathrm{s}}\frac{\sigma t}{\mu_\mathrm{L}}\frac{R_\mathrm{s}^2}{R_\mathrm{s}^2} = \\ = \frac{\mathrm{Bo}}{2\cos\theta}\frac{\rho_\mathrm{L} g R_\mathrm{s}^2}{\sigma}\frac{\sigma t}{\mu_\mathrm{L} R_\mathrm{s}}\frac{K}{\phi R_\mathrm{s}^2} = \frac{\mathrm{Bo}^2}{\mathrm{Ca}}\frac{1}{2\Pi^*\cos\theta}, \tag{3.27}$$

where Bo is the Bond number, Ca is the capillary number and Π^* is the dimensionless macroscopic parameter of the porous structure given as

$$\Pi^* = \frac{\phi R_\mathrm{s}^2}{K}. \tag{3.28}$$

The parameter Ω_1 can be represented as

$$\Omega_1 = n_1 = \frac{\rho_\mathrm{S}}{\rho_\mathrm{L}}\frac{c_\mathrm{S}(T_0 - T_\mathrm{L})}{\triangle h_\mathrm{v}} = \rho^*\frac{c_\mathrm{S}}{c_\mathrm{PL}}\frac{c_\mathrm{PL}(T_0 - T_\mathrm{L})}{\triangle h_\mathrm{v}} = \mathrm{Ja}_1\rho^* c_\mathrm{P}^*, \tag{3.29}$$

where Ja_1 is the Jakob number. ρ^* and c_P^* in Eq. 3.29 are defined as ratios of densities and specific heat capacities of solid and liquid, respectively, and given as

$$\rho^* = \frac{\rho_\mathrm{S}}{\rho_\mathrm{L}} \tag{3.30}$$

and

$$c_\mathrm{P}^* = \frac{c_\mathrm{S}}{c_\mathrm{PL}}. \tag{3.31}$$

The parameter Ω_2 can be represented as

$$\Omega_2 = \frac{n_2}{c} = \frac{\rho_\mathrm{S}}{\rho_\mathrm{L}}\frac{c_\mathrm{S}}{\triangle h_\mathrm{v}}\frac{\triangle T_\mathrm{S}}{L}\frac{2\sigma\cos\theta}{\rho_\mathrm{L} g R_\mathrm{s}} = \rho^*\frac{c_\mathrm{S}}{c_\mathrm{PL}}\frac{c_\mathrm{PL}(T_\mathrm{SL} - T_0)}{\triangle h_\mathrm{v}}\frac{\sigma}{\rho_\mathrm{L} g R_\mathrm{s} L}2\cos\theta \sim \frac{2\cos\theta}{\mathrm{Bo}}\mathrm{Ja}_2\rho^* c_\mathrm{P}^*, \tag{3.32}$$

where Ja_2 is the Jakob number and Bo is the Bond number.

3.2 Wicking of a cryogenic liquid into superheated porous structures: accounting for vapor flow

3.2.1 1D theoretical model

We study the non-isothermal imbibition of a cryogenic liquid into a vertically oriented porous sample with evaporation occuring at the wicking front due to the heat transfer between the superheated porous media and the cryogenic liquid at saturation temperature. We assume that

the vapor created due to evaporation cannot escape through the lateral sides of the porous sample and, therefore, influences the wicking front propagation. In analogy to the theoretical model described in section 3.1.1, we use the bundle of capillary tubes approach and propose a macroscopic wicking model. The imbibition into a vertically oriented (in z-direction) porous sample was schematically shown in Fig. 3.1. The momentum balance for the capillary rise of a liquid evaporating in porous media reads as the interaction of the capillary pressure, inertia, viscous forces for liquid and vapor and hydrostatic pressure

$$\underbrace{\frac{2\sigma\cos\theta}{R_\mathrm{s}}}_{\text{capillary pressure}} = \underbrace{\rho_\mathrm{L}\frac{\mathrm{d}(hu_\mathrm{L})}{\mathrm{d}t}}_{\text{inertia}} + \underbrace{\frac{\phi\mu_\mathrm{L}}{K}hu_\mathrm{L}}_{\text{viscous drag (liquid)}} + \underbrace{\frac{\phi\mu_\mathrm{V}}{K}(L-h)u_\mathrm{V}}_{\text{viscous drag (vapour)}} + \underbrace{\rho_\mathrm{L}gh}_{\text{hydrostatic pressure}}, \tag{3.33}$$

where u_L and u_V are the interstitial velocity of liquid and the interstitial velocity of vapor, respectively, L is the sample height, and h is the averaged height of the liquid column in porous media (wicking height).

We focus on the viscous-gravitational stage of the wicking process. Hence, Eq. 3.33 simplifies to

$$\underbrace{\frac{2\sigma\cos\theta}{R_\mathrm{s}}}_{\text{capillary pressure}} = \underbrace{\frac{\phi\mu_\mathrm{L}}{K}hu_\mathrm{L}}_{\text{viscous drag (liquid)}} + \underbrace{\frac{\phi\mu_\mathrm{V}}{K}(L-h)u_\mathrm{V}}_{\text{viscous drag (vapour)}} + \underbrace{\rho_\mathrm{L}gh}_{\text{hydrostatic pressure}}. \tag{3.34}$$

The dry solid structure of the sample is supposed to be superheated with regard to the liquid temperature. The superheat is in accordance with a linear temperature gradient along the sample height so that the local temperature of the dry solid structure T_S is defined as

$$T_\mathrm{S} = T_0 + \frac{\triangle T_\mathrm{S}}{L}z, \tag{3.35}$$

where $\triangle T_\mathrm{S}/L$ is the temperature gradient and T_0 is the initial temperature at the sample bottom.

The mass balance at the wicking front ($z = h$) yields the relationship between the imbibition rate $\dot{h}$ and the interstitial velocities of liquid and vapor as follows (see Eq. 2.46)

$$\rho_\mathrm{L}\left(u_\mathrm{L} - \frac{\mathrm{d}h}{\mathrm{d}t}\right) = \rho_\mathrm{V}\left(u_\mathrm{V} - \frac{\mathrm{d}h}{\mathrm{d}t}\right) = j_\mathrm{ev}, \tag{3.36}$$

where j_ev is the evaporative mass flux. From Eq. 3.36 the interstitial velocities of liquid and vapor are given as

$$u_\mathrm{L} = \dot{h} + \frac{j_\mathrm{ev}}{\rho_\mathrm{L}}, \tag{3.37}$$

$$u_\mathrm{V} = \dot{h} + \frac{j_\mathrm{ev}}{\rho_\mathrm{V}}. \tag{3.38}$$

In analogy to the theoretical model described in section 3.1.1, to evaluate the evaporative mass flux, we suppose that the heat needed to cool down the superheated solid structure is taken from the latent heat of evaporation. Thus, the heat removal rate needed to cool an infinitely slim layer dh of the solid structure from its local temperature T_S at the wicking front to the saturation temperature of liquid T_L is

$$\frac{\mathrm{d}q}{\mathrm{d}t} = \rho_\mathrm{S} c_\mathrm{S} (T_\mathrm{S} - T_\mathrm{L})(1-\phi) A \frac{\mathrm{d}h}{\mathrm{d}t}. \tag{3.39}$$

The rate of heat absorption due to evaporation (see Eq. 2.54) is

$$\frac{\mathrm{d}q}{\mathrm{d}t} = \triangle h_\mathrm{v} \phi A j_\mathrm{ev}. \tag{3.40}$$

where $\triangle h_\mathrm{v}$ is the specific latent heat of evaporation.

Rearranging Eq. 3.39 and Eq. 3.40, one obtains the evaporative mass flux as follows

$$j_\mathrm{ev} = \frac{\rho_\mathrm{S} c_\mathrm{S} (T_\mathrm{S} - T_\mathrm{L})(1-\phi)}{\phi \triangle h_\mathrm{v}} \frac{\mathrm{d}h}{\mathrm{d}t}. \tag{3.41}$$

We neglect the heat conduction in the solid structure and the heat exchange between the saturated vapor and the solid structure. The local temperature of the dry solid structure T_S at $z = h$ is assumed to be as given in Eq. 3.35. The argumentation used to neglect the heat conduction in solid structure for the wicking process was given in section 3.1.1.

In order to simplify the equations, we introduce the parameters summarized in Table 3.1 and the dimensionless parameters ρ_F^* and μ_F^*. The latter are defined as ratios of densities and dynamic viscosities of liquid and vapor and given as

$$\rho_\mathrm{F}^* = \frac{\rho_\mathrm{V}}{\rho_\mathrm{L}}, \tag{3.42}$$

and

$$\mu_\mathrm{F}^* = \frac{\mu_\mathrm{V}}{\mu_\mathrm{L}}, \tag{3.43}$$

respectively.

Using these parameters and substituting Eq. 3.41 to Eq. 3.37 and 3.38, one obtains the interstitial velocities of liquid and vapor as

$$u_\mathrm{L} = \dot{h} + \epsilon n_1 \dot{h} + \epsilon n_2 h \dot{h}, \tag{3.44}$$

$$u_\mathrm{V} = \dot{h} + \frac{\epsilon n_1}{\rho_\mathrm{F}^*} \dot{h} + \frac{\epsilon n_2}{\rho_\mathrm{F}^*} h \dot{h}. \tag{3.45}$$

The momentum balance Eq. 3.34 with the parameters introduced in Table 3.1 and Eq. 3.42 and 3.43 transforms into

$$1 = ch + bhu_\mathrm{L} + \mu_\mathrm{F}^* b (L-h) u_\mathrm{V}. \tag{3.46}$$

Substituting Eq. 3.44 and 3.45 to Eq. 3.46, one obtains the final equation for the capillary rise of a cryogenic liquid in superheated porous media with evaporation at the wicking front and the influence of the created vapor on the wicking front propagation as

$$1 = ch + bh\dot{h}(1 + \epsilon(n_1 + n_2 h)) + \mu_{\mathrm{F}}^* b\dot{h}(L - h)\left(1 + \frac{\epsilon}{\rho_{\mathrm{F}}^*}(n_1 + n_2 h)\right). \tag{3.47}$$

Integrating Eq. 3.47 yields the analytic solution in implicit form as follows

$$\begin{aligned} t(h) = -\frac{b\epsilon n_2}{c}\left[\frac{\mu_{\mathrm{F}}^*}{\rho_{\mathrm{F}}^*}Lh + \left(1 - \frac{\mu_{\mathrm{F}}^*}{\rho_{\mathrm{F}}^*}\right)\frac{h^2}{2}\right] - \mu_{\mathrm{F}}^* L\frac{b}{c}\left[1 + \frac{\epsilon}{\rho_{\mathrm{F}}^*}\left(n_1 + \frac{n_2}{c}\right)\right]\ln(1 - ch) - \\ -\frac{b}{c}\left[1 - \mu_{\mathrm{F}}^* + \epsilon\left(1 - \frac{\mu_{\mathrm{F}}^*}{\rho_{\mathrm{F}}^*}\right)\left(n_1 + \frac{n_2}{c}\right)\right]\left(h + \frac{1}{c}\ln(1 - ch)\right). \end{aligned} \tag{3.48}$$

More details on the derivation of Eq. 3.48 are provided in the Appendix A.2.

3.2.2 Dimensionless formulation

To non-dimensionalize the final equation for the capillary rise of a cryogenic liquid in superheated porous media with evaporation at the wicking front and the influence of the created vapor on the wicking front propagation (Eq. 3.47) and its analytic solution (Eq. 3.48), we apply the Buckingham π theorem. Such an approach was also described in section 3.1.2.
In Eqs. 3.47 and 3.48 one finds six (6) dimensional units b [s m^{-2}], c [m^{-1}], n_2 [m^{-1}], h [m], L [m], and t [s], and two (2) fundamental units *time* [s] and *length* [m]. The table of dimensional and fundamental units of the system is given in Table 3.5. Thus, one obtains 6-2=4 dimensionless π-parameters that characterize the problem.

Table 3.5: The dimensional and fundamental units in Eqs. 3.47 and 3.48.

	b	c	n_2	L	h	t
s	1	0	0	0	0	1
m	-2	-1	-1	1	1	0

According to the Buckingham π theorem, the system of equations evolves as follows

$$\begin{pmatrix} 1 & 0 & 0 & 0 & 0 & 1 \\ -2 & -1 & -1 & 1 & 1 & 0 \end{pmatrix} \cdot \begin{pmatrix} \pi_{1b} & \pi_{2b} & \pi_{3b} & \pi_{4b} \\ \pi_{1c} & \pi_{2c} & \pi_{3c} & \pi_{4c} \\ \pi_{1n_2} & \pi_{2n_2} & \pi_{3n_2} & \pi_{4n_2} \\ \pi_{1L} & \pi_{2L} & \pi_{3L} & \pi_{4L} \\ \pi_{1h} & \pi_{2h} & \pi_{3h} & \pi_{4h} \\ \pi_{1t} & \pi_{2t} & \pi_{3t} & \pi_{4t} \end{pmatrix} = \begin{pmatrix} 0 & 0 & 0 & 0 \\ 0 & 0 & 0 & 0 \end{pmatrix}. \tag{3.49}$$

This system is under-determined, and one is allowed to choose four (4) dimensional parameters in each π-vector.

We choose n_2 as a basic parameter, while b and c as scaling parameters.Then for h-scaling one can set $\pi_{1n_2} = 0$, $\pi_{1L} = 0$, $\pi_{1h} = 1$ and $\pi_{1t} = 0$. For t-scaling one can set $\pi_{2n_2} = 0$, $\pi_{2L} = 0$, $\pi_{2h} = 0$ and $\pi_{2t} = 1$. To find the basic parameter n_2, one can set $\pi_{3n_2} = 1$, $\pi_{3L} = 0$, $\pi_{3h} = 0$ and $\pi_{3t} = 0$. To find the basic parameter L, one can set $\pi_{4n_2} = 0$, $\pi_{4L} = 1$, $\pi_{4h} = 0$ and $\pi_{4t} = 0$. Taking into account the settings made above, one can solve the system 3.49 and obtain

$$\begin{pmatrix} \pi_{1b} & \pi_{2b} & \pi_{3b} & \pi_{4b} \\ \pi_{1c} & \pi_{2c} & \pi_{3c} & \pi_{4c} \\ \pi_{1n_2} & \pi_{2n_2} & \pi_{3n_2} & \pi_{4n_2} \\ \pi_{1L} & \pi_{2L} & \pi_{3L} & \pi_{4L} \\ \pi_{1h} & \pi_{2h} & \pi_{3h} & \pi_{4h} \\ \pi_{1t} & \pi_{2t} & \pi_{3t} & \pi_{4t} \end{pmatrix} = \begin{pmatrix} 0 & -1 & 0 & 0 \\ 1 & 2 & -1 & 1 \\ 0 & 0 & 1 & 0 \\ 0 & 0 & 0 & 1 \\ 1 & 0 & 0 & 0 \\ 0 & 1 & 0 & 0 \end{pmatrix}. \tag{3.50}$$

Thus, the Buckingham π theorem provides

$$\pi_1^* = b^0 c^1 n_2^0 L^0 h^1 t^0 = ch = h^*, \tag{3.51}$$

$$\pi_2^* = b^{-1} c^2 n_2^0 L^0 h^0 t^1 = \frac{c^2 t}{b} = t^*, \tag{3.52}$$

$$\pi_3^* = b^0 c^{-1} n_2^1 L^0 h^0 t^0 = \frac{n_2}{c} = \Omega_2, \tag{3.53}$$

$$\pi_4^* = b^0 c^1 n_2^0 L^{-1} h^0 t^0 = cL = L^*. \tag{3.54}$$

Introducing the dimensionless parameter $\Omega_1 = n_1$ and taking into account the dimensionless parameter ϵ from Table 3.1, one obtains Eq. 3.47 in dimensionless form as follows

$$1 = h^* + h^* \dot{h}^* (1 + \epsilon(\Omega_1 + \Omega_2 h^*)) + \mu_{\mathrm{F}}^* \dot{h}^* (L^* - h^*) \left(1 + \frac{\epsilon}{\rho_{\mathrm{F}}^*} (\Omega_1 + \Omega_2 h)\right). \tag{3.55}$$

An analytic solution for Eq. 3.55 can be obtained as

$$\begin{aligned} t^*(h^*) = -\epsilon\Omega_2 \left[\frac{\mu_{\mathrm{F}}^*}{\rho_{\mathrm{F}}^*} L^* h^* + \left(1 - \frac{\mu_{\mathrm{F}}^*}{\rho_{\mathrm{F}}^*}\right) h^{*2}\right] - \mu_{\mathrm{F}}^* L^* \left(1 + \frac{\epsilon}{\rho_{\mathrm{F}}^*}(\Omega_1 + \Omega_2)\right) \ln(1 - h^*) - \\ - \left[1 - \mu_{\mathrm{F}}^* + \epsilon \left(1 - \frac{\mu_{\mathrm{F}}^*}{\rho_{\mathrm{F}}^*}\right)(\Omega_1 + \Omega_2)\right] (h^* + \ln(1 - h^*)). \end{aligned} \tag{3.56}$$

Eq. 3.56 is also the dimensionless form of Eq. 3.48.

The connection between the dimensionless variables and parameters h^* , t^*, Ω_1 and Ω_2 and the dimensionless numbers relevant for wicking from Table 3.4 is shown in Eq. 3.26, 3.27, 3.29 and 3.32, correspondingly. The parameter L^* can be represented as

$$L^* = cL = \frac{L}{h_{\mathrm{eq}}} = R_{\mathrm{s}} \frac{\rho_{\mathrm{L}} g}{2\sigma \cos\theta} L \sim \frac{\mathrm{Bo}}{2\cos\theta}, \tag{3.57}$$

where Bo is the Bond number. Eq. 3.57 shows that the variable L^* is defined as a ratio of the sample height to the equilibrium wicking height h_{eq} that is the maximum achievable wicking height for a porous structure. Thus, the value of the dimensionless variable L^* indicates which part of the maximum wicking height can be achieved at the given sample height.

Chapter 4

Experimental investigation of wicking of liquid nitrogen into superheated porous structures

The following chapter is based on the publication "Wicking of liquid nitrogen into superheated porous structures"[1] by Y. Grebenyuk and M.E. Dreyer [34]. This chapter describes the results of cryo-wicking experiments with liquid nitrogen and superheated porous samples. The results were compared to the theoretical prediction via the macroscopic model described in section 3.1.

4.1 Materials

This section provides the information about porous structures and a solid material of the experimental samples. It also describes the methodology for the determination of the macroscopic parameters of porous structures. In order to validate the applicability of the macroscopic approach for the description of the vertical wicking, the results of wicking experiments with no sample superheat were compared to the theoretical prediction given via the Lucas-Washburn equation with gravity effects (Eq. 2.95).

[1]Reprinted from Cryogenics, Vol. 78, Y. Grebenyuk, M.E. Dreyer, Wicking of liquid nitrogen into superheated porous structures, Pages No. 27-39, Copyright (2017), with permission from Elsevier.

4.1.1 Porous media

Experiments were performed with sintered glassfilter elements of porous structures (ROBU Glasfilter-Geraete, Germany). The solid material of the structures was specified as boroslicate glass 3.3. Some thermophysical properties of borosilicate glass are summarized in Table 4.1. Samples of two geometries were chosen: cylindrical samples of a larger cross-section area and rectangular samples of a smaller cross-section area. That was done in order to investigate a possible impact of the vapour flow created above the wicking front in experiments with liquid nitrogen. Geometrical characteristics of the samples are summarized in Table 4.2.

Table 4.1: Thermophysical properties of borosilicate glass at room temperature (from ROBU Glasfilter-Geraete, Germany) and saturation temperature of nitrogen at 101325 Pa [142].

T (K)	ρ_S ($kg\,m^{-3}$) 10^3	c_S ($J\,kg^{-1}\,K^{-1}$) 10^3	λ_S ($W\,m^{-1}\,K^{-1}$)
300	2.23	0.8	1.13
77.355	2.23	0.25	0.5

Table 4.2: Geometrical characteristics of the porous samples commercially obtained from ROBU Glasfilter-Geraete, Germany. w_1 and w_2 are referred to as the length and widths of the rectangular samples, respectively. d is referred to as the diameter of the cylindrical samples. A is the area of the sample cross section that is perpendicular to the direction of the wicking front propagation. L is referred to as the sample height. The sample R12T was used for the simultaneous sample weight and temperature measurements, see section 4.4.2.

Sample	ROBU class	w_1 (m) 10^{-3}	w_2 (m) 10^{-3}	d (m) 10^{-3}	A (m^2) 10^{-6}	L (m) 10^{-3}
R19	P3	15	8	-	120	80
R12	P4	15	10	-	150	80
R12T	P4	15	10	-	150	80
C19	P3	-	-	30	706.5	50
C12	P4	-	-	30	706.5	50

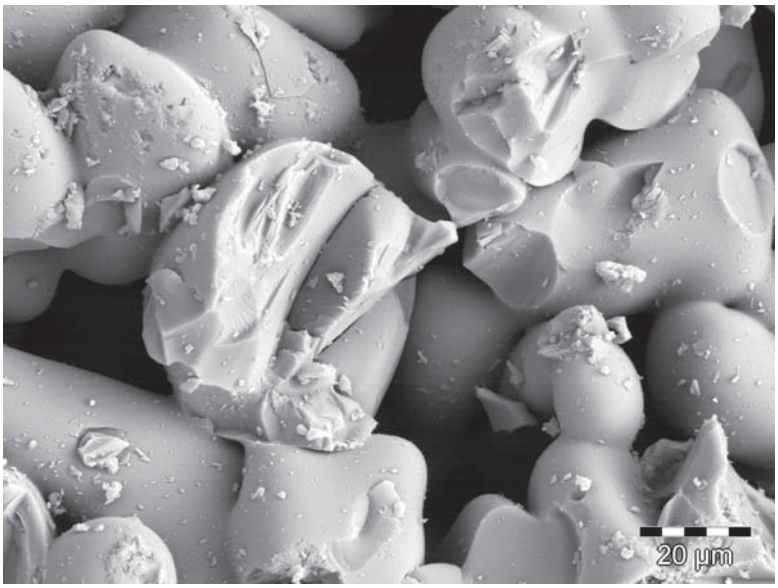

Figure 4.1: SEM image for the R19 sample.

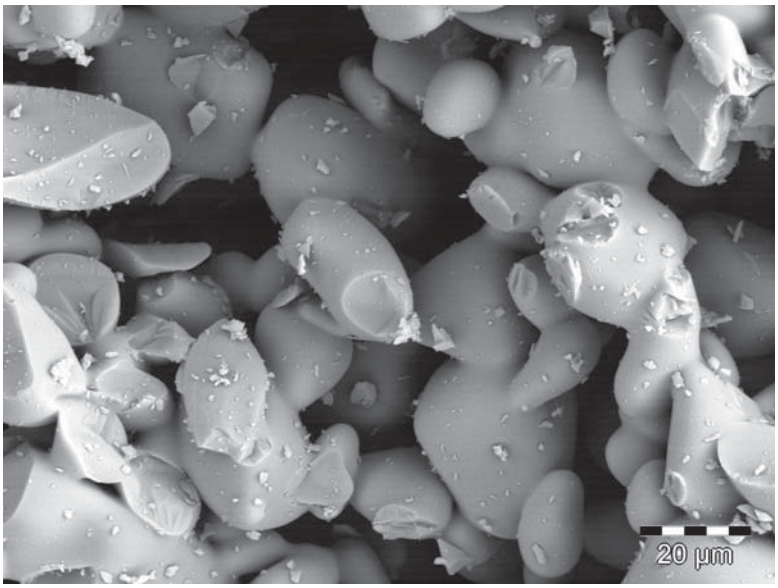

Figure 4.2: SEM image for the R12 sample.

The porous structures were of two different characteristic pore sizes. In further experiments the static pore radius was determined. Samples with the static pore radius of $19.7{\cdot}10^{-6}$ m are referred to as R19 or C19, where R stands for rectangular and C for cylindrical samples. Correspondingly, samples with the static pore radius of $12.3{\cdot}10^{-6}$ m are referred to as R12 or C12. R12T is referred to a rectangular sample with the static pore radius of $12.3{\cdot}10^{-6}$ m that was used for temperature measurements. The morphology of the samples of each pore size group was obtained via Scanning Electron Microscopy (SEM, CamScan Ltd.). The samples

were first sputtered with gold to enable the scanning (K550, Emitech, Judges Scientific plc.). SEM images for R19 and R12 samples are presented on Fig. 4.1 and 4.2, respectively.

4.1.2 Macroscopic parameters

The open (effective) porosity, static pore radius and permeability of the samples were determined under isothermal conditions in experiments with the FC-72 liquid, see Table 4.3. A schematic image of the setup is shown on Fig 4.3. The electronic high precision balance (LA310S-0CE, Sartorius) with an accuracy of ± 0.0001 g was fixed on a height-adjustable platform and served to measure the sample weight. The sample was located in a closed vessel of 0.095 m diameter partly filled with the experimental liquid. The platform was driven via two stepper motors (VRDM566/50, Berger Lahr/Schneider Electric) with a velocity of 0.38 mm/s to bring the sample into the contact with the liquid surface.

The choice of the liquid is explained by the perfect wetting characteristics of FC-72 with a variety of materials [36, 126, 38, 39, 40]. The static contact angle θ with borosilicate glass was assumed to be zero. Due to its high density the FC-72 liquid was also preferable for the static pore radius determination. Some thermophysical properties of FC-72 liquid are summarized in Table 4.3.

The open porosity characterizes a volume of interconnected pores in a porous structure. This macroscopic parameter was determined using the weight measurements applied to a dry and a

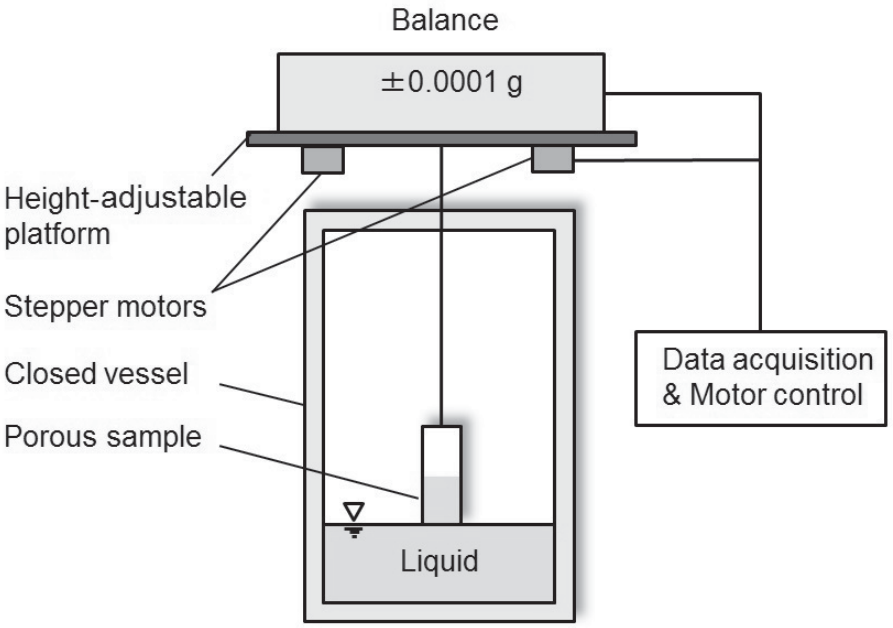

Figure 4.3: Schematic image of the setup for isothermal wicking experiments.

Table 4.3: Thermophysical properties of FC-72 liquid at 101325 Pa and 298.15 K.

ρ_L	μ_L	σ
$(\mathrm{kg\,m^{-3}})$	$(\mathrm{Pa\,s})$	$(\mathrm{N\,m^{-1}})$
	10^{-6}	10^{-3}
1690	709.8	12

saturated porous sample. The obtained mass of the imbibed liquid was used to calculate the open porosity as

$$\phi = \frac{V_{\mathrm{void}}}{V_{\mathrm{total}}} = \frac{m/\rho_L}{V_{\mathrm{total}}}. \tag{4.1}$$

The static pore radius R_s that indicates a characteristic pore size of a porous structure was determined using the weight of the imbibed liquid corresponding to the equilibrium wicking height h_{eq}

$$P_{\mathrm{eq}} = \phi A \rho_L g h_{\mathrm{eq}}. \tag{4.2}$$

The equilibrium wicking height is a maximum achievable wicking height, when the capillary pressure is balanced by the hydrostatic pressure

$$h_{\mathrm{eq}} = \frac{2\sigma\cos\theta}{\rho_L g R_s}. \tag{4.3}$$

This method of the static pore radius determination was also applied by Fries et al. in [126]. In their experiments, Masoodi et al. [100] refer to this value as to the capillary radius. In order to obtain R_s for the chosen porous structures, the samples of a bigger height should be used. Therefore, rectangular samples were tested that had initially a height of 0.15 m. Due to hardware limitations for experiments with liquid nitrogen the samples were cut to 0.08 m as shown in Table 4.2.

The permeability K characterizes the ability of a porous structure to conduct a flow through it. To determine this macroscopic parameter, we performed sample weight measurements during the imbibition and calculated the mass of the imbibed liquid. Then the squared mass was plotted versus time for smaller times of the viscous-dominated stage. In this domain governed by the Lucas-Washburn equation (see Eq. 2.96) the linear regression of the experimental data had a constant slope

$$\frac{m^2}{t} = \frac{4\sigma\cos\theta\rho_L^2 A^2 \phi}{\mu_L}\frac{K}{R_s}. \tag{4.4}$$

From this slope the relation K/R_s was obtained and, knowing R_s, the permeability was determined. More details on the applied method are provided in [126].

Table 4.4: Macroscopic parameters of the porous samples.

Sample	ϕ (-)	R_s (m) 10^{-6}	K (m^2) 10^{-12}
R19	0.40 ± 0.02	19.7 ± 0.4	1.52 ± 0.06
R12	0.44 ± 0.02	12.3 ± 0.3	0.91 ± 0.04
R12T	0.44 ± 0.02	12.3 ± 0.3	0.91 ± 0.04
C19	0.35 ± 0.02	19.7 ± 0.4	1.27 ± 0.12
C12	0.31 ± 0.02	12.3 ± 0.3	0.34 ± 0.06

The obtained values of the macroscopic parameters for the experimental samples are summarized in Table 4.2. The values for each sample are shown with a standard deviation for three test runs.

4.2 Wicking experiment (no sample superheat)

Fig. 4.4 shows the results of wicking of the FC-72 liquid into the samples R19, R12, C19 and C12 (no sample superheat). A theoretical prediction was performed using the Lucas-Washburn equation with gravity effects (Eq. 2.95) and macroscopic parameters from Table 4.4. The increase of the wicking height $h(t)$ obtained via Eq. 2.95 was recalculated into the mass increase $m(t)$ of the imbibed liquid as follows

$$m(t) = \rho_L \phi A h(t). \tag{4.5}$$

According to Quintard and Whitaker [138] and Lasseux et al. [139], a porous medium is homogeneous with respect to a given process and a given averaging volume when the effective transport coefficients in the volume-averaged transport equations are independent of position. In our case such transport coefficients are the macroscopic parameters in Eq. 3.12 that were taken constant for the whole process. A good agreement between the theory and experiment indicates the homogeneity of the porous structures with respect to vertical wicking and the accurate determination of the macroscopic parameters.

Due to the application of the sample weight measurement technique some corrections were required to account for the buoyancy effect and the surface tension effect on the outer circumference of the samples. More details are provided in section 4.3.3. The sample weight

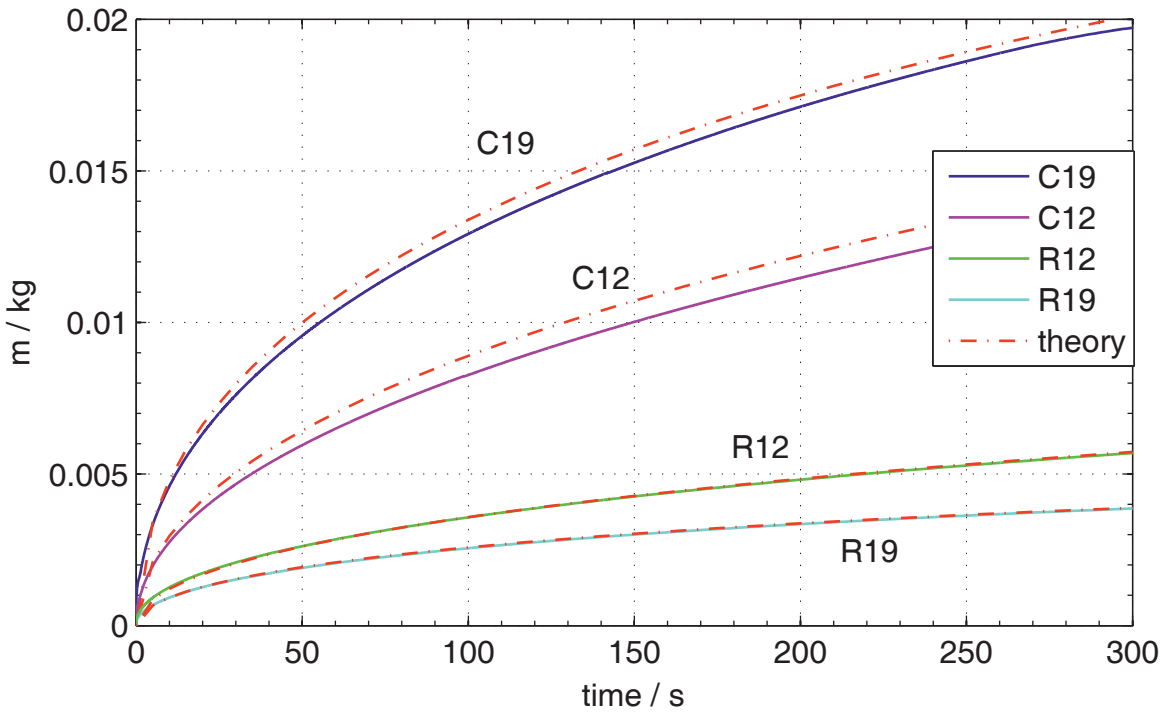

Figure 4.4: Wicking of the FC-72 liquid into the samples R19, R12, C19 and C12 (no sample superheat). The theoretical prediction computed with the Lucas-Washburn equation with gravity effects (Eq. 2.95) is in good agreement with the experiment data.

measurement technique was also used for wicking experiments with liquid nitrogen. As opposed to liquid nitrogen experiments, the evaporation of the bulk FC-72 liquid was negligible. However, due to a smaller diameter of the experimental vessel we had to account for a liquid level decrease resulted from the imbibition of the liquid contained in the vessel into the samples. The correction of the mass of the imbibed liquid was found to be up to 1.9 % for R19 sample, 2.4 % for R12 and R12T samples and up to 11.1 % for cylindrical samples.

4.3 Cryo-wicking experiment

4.3.1 Experimental apparatus

A setup was designed to investigate non-isothermal wicking of liquid nitrogen into a superheated porous sample. A schematic image of the setup is depicted on Fig. 4.5.

The stainless steel cylindrical cryostat of 394 mm diameter and 725 mm height and total internal volume of 43 liters was facing ambient conditions with $T_a \approx 300$ K at $p_a \approx 101325$ Pa. The

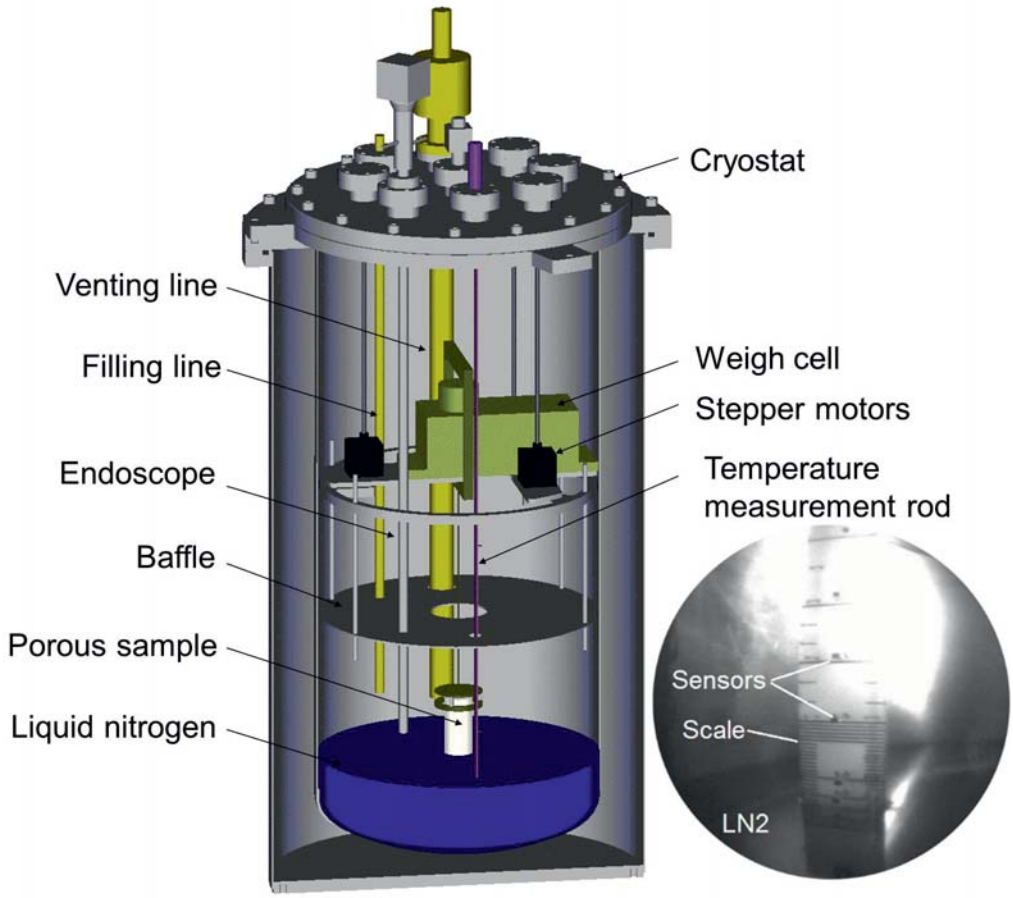

Figure 4.5: Schematic image of the setup for non-isothermal wicking experiments with liquid nitrogen.

inner tank of the cryostat was evacuated and partly filled with liquid nitrogen at saturation conditions ($T_{\mathrm{LN_2}} \approx 77.355$ K at $p_{\mathrm{N_2}} \approx p_{\mathrm{a}}$). This ensured having a one-species system (liquid nitrogen in a pure nitrogen vapor) in the cryostat. Thermophysical properties of nitrogen are summarized in Table 4.6. For better insulation the inner tank was placed in a vacuum casing. The thermally non-insulated lid conducted a heat flux from the ambient at the top of the cryostat. This caused the establishment of a temperature stratification in the nitrogen vapor. Thus, the required non-isothermal conditions for wicking experiments were created.

In order to measure the weight of a porous sample, a weigh cell (WZA1203-N, Sartorius) with an accuracy of ± 0.001 g and capacity of 1200 g was placed inside the cryostat. The weigh cell was fixed on a height adjustable supporting platform driven via three stepper motors (L3518S1204-T6x1, NanoTec). The motors lifted the platform up and down with a velocity of 2 mm/s. A baffle was allocated at 465 mm from the lid. The baffle and the venting line served

Table 4.5: The distances from the lid of the cryostat to the location of the temperature sensors T1 to T10.

Z_1 (m)	Z_2 (m)	Z_3 (m)	Z_4 (m)	Z_5 (m)	Z_6 (m)	Z_7 (m)	Z_8 (m)	Z_9 (m)	Z_{10} (m)
0.595	0.590	0.585	0.580	0.565	0.550	0.535	0.430	0.385	0.340

to protect the weigh cell from over-cooling with nitrogen vapor created during the filling stage. The venting and filling lines were used during the filling and warming up stages. The venting line was kept closed during the wicking experiments, whereas the filling line was kept open.

A temperature measurement rod was designed and implemented vertically in the cryostat to determine the temperature distribution in nitrogen vapor and liquid. The measurement rod consisted of an epoxy glass plate and ten temperature sensors allocated along its length. The sensors were silicon diodes DT-670A manufactured by LakeShore for cryogenic conditions. They had an accuracy of $\pm$ 0.25 K at temperatures from 2 K to 100 K and $\pm$ 0.5 K at temperatures from 100 K to 305 K. The thermal dissipation of the sensors was given as $10{\cdot}10^{-6}$ W at 77 K and $5{\cdot}10^{-6}$ W at 305 K. Their response time to a temperature change was specified as 100 ms at 77 K and 200 ms at 300 K. The measurement rod was fixed on the lid to ensure the same location of the temperature sensors in the cryostat for each experiment. The distances from the lid to each sensor location are summarized in Table 4.5. In the vicinity of the liquid level the plate of the measurement rod was scaled. The optical access to the scale, provided via an endoscope, enabled the liquid level determination. A snapshot of the temperature measurement rod obtained with the endoscope is presented on Fig 4.5.

A pressure sensor (Sensotec TJE-1256-30) with an accuracy of $\pm$ 0.2 kPa measured a nitrogen vapor pressure in the ullage of the cryostat.

Weight, temperature and pressure measurements were recorded simultaneously with a sampling rate of 20 Hz.

4.3.2 Experiment preparation and methodology

The heat flux from the ambient through the lid of the cryostat caused evaporation of nitrogen from the liquid surface. This resulted in a constant liquid level decrease of approximately 3

Table 4.6: The thermophysical properties of saturated nitrogen (liquid and vapor) at 101325 Pa and 77.355 K [141]. The static contact angle of liquid nitrogen with borosilicate glass is taken as zero.

Fluid	ρ	μ	λ	c_P	c_V	σ	$\triangle h_\mathrm{v}$
	$(\mathrm{kg\,m^{-3}})$	$(\mathrm{Pa\,s})$	$(\mathrm{W\,m^{-1}\,K^{-1}})$	$(\mathrm{J\,kg^{-1}\,K^{-1}})$	$(\mathrm{J\,kg^{-1}\,K^{-1}})$	$(\mathrm{N\,m^{-1}})$	$(\mathrm{J\,kg^{-1}})$
		10^{-6}	10^{-3}	10^{3}	10^{3}	10^{-3}	10^{3}
Liquid	806.08	160.66	144.77	2.0415	1.0841	8.8748	199.18
Vapor	4.6121	5.4440	7.1876	1.1239	0.77128	-	-

mm/hour. It greatly affected the vapor temperature during the preparation stage that defined the initial temperature distribution for the experiments.

Fig. 4.6 plots the temperature evolution inside the cryostat during and after the filling with liquid nitrogen. At the end of the filling the sensors T1, T2, T3, T5, T6 and T7 are submerged in the liquid, while the sensors T8, T9 and T10 measure local temperatures in nitrogen vapor. A stable temperature stratification in nitrogen vapor established in approximately 8 h. Due to the liquid level decrease the sensors initially submerged in liquid nitrogen sequentially emerge and start measuring local vapor temperatures. As shown on Fig. 4.6, after 18 h only sensors T1, T2, T3 and T4 are still in the liquid.

To determine the liquid level for each wicking experiment, we ensured first that the liquid level was between two pairs of neighbouring temperature sensors T1 and T2 or T3 and T4. The neighbouring sensors were spaced out at 5 mm distance from each other, see Table 4.5. When the liquid level was in between the sensors, the lower sensor showed the liquid nitrogen temperature, while the higher sensor showed the local vapour temperature. The spacing of 5 mm between temperature sensors is sufficient. A closer spacing would not increase the accuracy due to the fact that liquid nitrogen perfectly wets the sensors and forms a meniscus of approximately 1.5 mm height. Using the optical access to the scaled plate provided via the endoscope, it was possible to estimate the liquid level in the cryostat with an uncertainty of 1 mm.

A first wicking experiment for each sample was started when the liquid level was between the sensors T3 and T4 at approximately 582 mm from the lid of the cryostat. In this case the initial sample location was at a maximum distance from the liquid surface. The distance from the sample bottom to the liquid surface was 140 mm for rectangular and 167 mm for cylindrical samples. Due to the heat transfer with the surrounding nitrogen vapor, the sample was

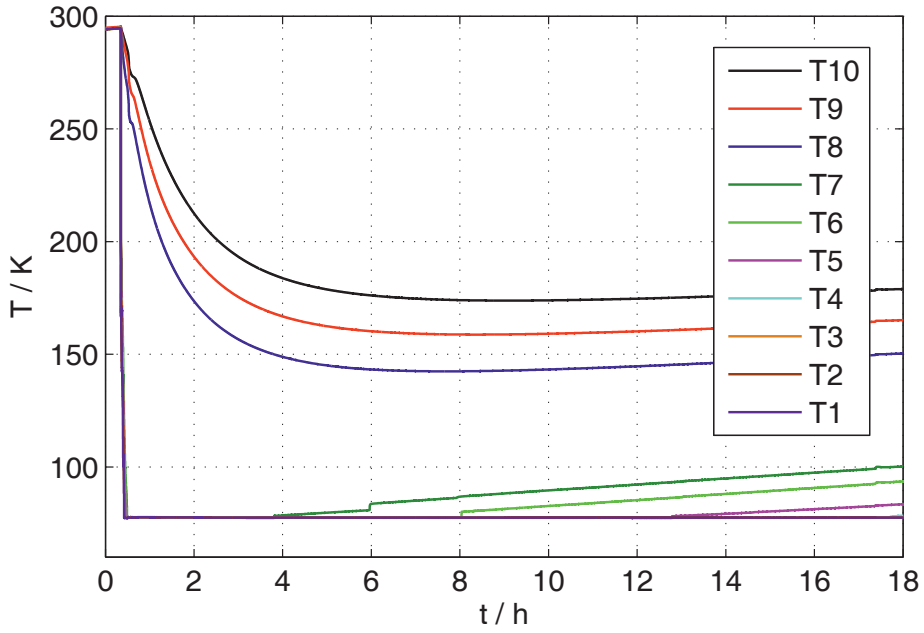

Figure 4.6: Temperature evolution inside the cryostat during and after the filling with liquid nitrogen. T1 to T10 sensors are allocated vertically along the cryostat height. A stable temperature stratification in the nitrogen vapor establishes after approximately 8 h.

superheated with regard to the liquid temperature. To perform the wicking experiment, the sample was driven down and partly submerged into the bulk liquid. The submersion depth was estimated to be between 1 mm and 2 mm. This deviation is explained by the uncertainty in the liquid level determination. The vertical wicking takes place into the unsaturated (not submerged) part of the porous sample. During the imbibition of liquid nitrogen into the porous structure the sample weight increased until a certain value and then stopped. Such an abrupt change of the imbibition behaviour corresponds to the moment when the wicking front reached the top of the sample. That was additionally verified by the fact that the final mass of the imbibed liquid nitrogen into each sample corresponds to the porosity value determined in preliminary wicking experiments with FC-72 liquid, see Table 4.2. Therefore, at the end of each wicking experiment the sample was completely saturated. After that, the sample was driven upwards for approximately 2 mm above the liquid level and kept in this location until the complete evaporation of the imbibed liquid nitrogen. The time to raise the sample from the bulk liquid was always set to 2 s using the motor control system. The actual time needed to detach the sample from the liquid surface was always smaller and was dependent on how deep the sample was submerged. This experiment case is referred to as Superheat 1.

A second wicking experiment was started at approximately 2.5 h from complete evaporation of the imbibed liquid nitrogen out of the sample. At that time the liquid level was between the sensors T1 and T2 at 592 mm from the lid. The distance from the sample bottom to the liquid surface was only 10 mm for all sample geometries. For that reason the sample superheat obtained through the heat transfer with the surrounding vapor was lower compared to the first experiment (Superheat 1). The sample was driven down to the liquid surface, partly submerged to measure the weight increase until the complete saturation, and then driven for approximately 2 mm above the liquid level to evaporate the imbibed liquid. The methodology for the second wicking experiment was the same as for the first one. This experiment case is referred further to as Superheat 2.

Three test runs were carried out for each experiment case and each porous sample. To guarantee the same temperature distribution for each experiment run, wicking was always initiated at the same liquid level in the cryostat: 582 mm for the first wicking experiment and 592 mm for the second (measured from the lid).

In addition, experiments were conducted to trace the sample temperature evolution. After the macroscopic parameters were determined for R12T, two elliptical holes of 2 mm and 3 mm diameters and 6 mm depth were drilled on its lateral side. The holes were located at 10 mm and 60 mm distance from the sample bottom. One temperature sensor (silicon diodes DT-670A, LakeShore) was inserted inside each hole. For these experiments no additional techniques were applied to fix the sensors inside the holes. The fixing of the sensors inside the sealed sample is described in section 5.1.2. Simultaneous sample weight and temperature measurements were performed in Superheat 1 and 2 experiment cases.

4.3.3 Correction of sample weight measurements

To initiate wicking, a porous sample was partly submerged into the bulk liquid. That induced some sample weight decrease due to buoyancy. Taking into account the uncertainty in the liquid level determination, the calculation of the buoyancy force would not be accurate. In section 4.3.2 we also mentioned that the heat flux from the ambient caused the evaporation of the bulk liquid in the cryostat. The corresponding liquid level decrease of 3 mm/h influenced the sample weight measurements during the imbibition. Using the liquid level decrease rate, we corrected the measurement data to eliminate the sample weight changes. For that we calculated the total sample weight increase due to the decrease of the buoyancy force acting on the partly submerged sample and the sample weight increase due to the weight of the imbibed liquid that

was brought above the decreased liquid level. Then the obtained value of the sample weight increase was subtracted from the measured data at each recorded time.

In addition to that, an outer meniscus forms at the sample perimeter upon contact of the sample with the liquid surface. This effect leads to some weight increase and is known as the Wilhelmy force. For non-porous samples it can be estimated using the Wilhelmy plate method [16, 140]. Nevertheless, due to the porous structure of the experimental samples the accurate determination of the Wilhelmy force was not possible.

The sample weight changes due to the buoyancy force, the Wilhelmy force and early wicking occur almost simultaneously and are difficult to separate. However, if the total weight change caused by the buoyancy force and the Wilhelmy force is constant, it can be found subtracting the final weight of a completely saturated but still partly submerged sample from the actual weight of the saturated sample. The actual weight of the saturated sample should be measured immediately when the sample is detached from the liquid surface, and before the evaporation reduces the weight. In such a way, the results of the sample weight measurements were corrected to account for the buoyancy and the surface tension effects. The total correction of the mass of the imbibed liquid was found to be up to 1.3% for R19 sample, 1.7% for R12 and R12T samples and up to 3.7% for cylindrical samples.

4.4 Results

This section is divided into four parts. In the first part, the experiment environment is analyzed using the nitrogen vapor temperature evolution during the imbibition and shortly before and after that. The second part presents results of simultaneous sample weight and temperature measurements with four identified experiment stages. In the third part, the influence of various porous structures, sample geometries and superheats on the mass of the imbibed liquid nitrogen is compared to theoretical predictions. In the forth part, the dimensionless formulation of the results is given.

4.4.1 Temperature evolution of nitrogen vapor

Fig. 4.7 depicts the temperature distribution in the cryostat before the first (Superheat 1) and second wicking experiment (Superheat 2). The circles in Fig. 4.7 indicate readings of the temperature sensors plotted versus their locations in the cryostat at the moment when the sample was driven to the liquid surface. The initial sample position for rectangular (R) and

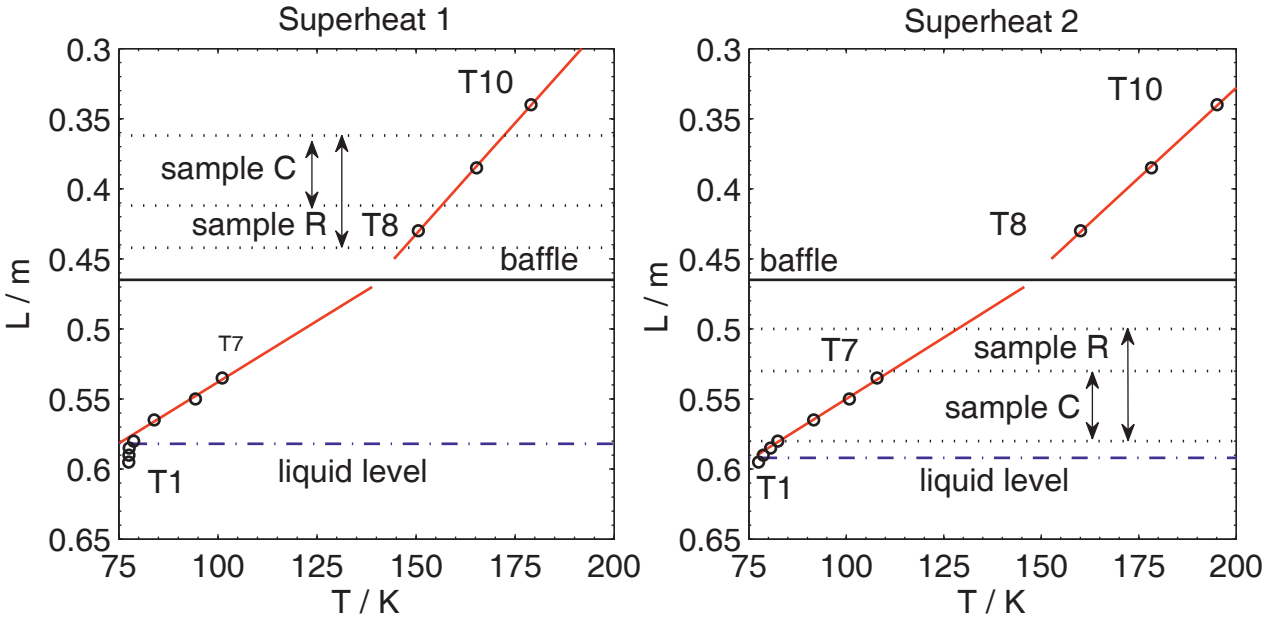

Figure 4.7: Temperature distribution in the cryostat before the first (Superheat 1) and second wicking experiment (Superheat 2). It illustrates the establishment of linear temperature gradients in a stratified nitrogen vapor environment below and above the baffle. The initial sample position for rectangular (R) and cylindrical samples (C) is shown via arrows and dotted lines. The liquid level displayed by the dot-dashed lines was slightly lower for Superheat 2 case resulting in higher temperature values of sensors T1 to T10.

cylindrical samples (C) is shown via arrows and dotted lines. The dot-dashed lines display the liquid level in the cryostat. For Superheat 1 case the initial sample position corresponds to a maximum achievable distance from the sample to the liquid surface. For Superheat 2 the sample is at a minimum distance.

Linear temperature gradients established in a stratified nitrogen vapor environment below and above the baffle. Above the baffle the gradient and absolute temperatures were of interest for Superheat 1, since it reflected vapor temperature distribution at the initial sample position and defined the superheat. The gradient and absolute temperatures below the baffle were of interest for Superheat 2. The average sample superheat values were higher at Superheat 1, however, temperature gradients for this case were smaller compared to Superheat 2. Assuming the same temperature distribution in the sample as in the surrounding vapor, the temperatures at the sample top and bottom were estimated. The obtained values are summarized in Table 4.7.

Furthermore, all the sensors display higher vapor temperatures in Superheat 2 case, see Fig. 4.7. This is substantiated by the liquid level decrease and the movement of the supporting

Table 4.7: Initial linear temperature gradient $\triangle T_S/L$ in a stratified nitrogen vapor environment along the sample height and calculated sample temperature at the bottom T_0 and top T_{SL}.

Sample	T_0 (K)	T_{SL} (K)	$\triangle T_S/L$ ($K\,m^{-1}$)
Superheat 1			
R19	146.9 ± 0.8	172.3 ± 0.8	316.9 ± 0.7
R12	146.9 ± 0.3	171.9 ± 0.3	313.5 ± 2.0
R12T	147.2 ± 0.3	172.6 ± 0.2	317.3 ± 1.4
C19	154.5 ± 1.2	170.6 ± 1.2	323.4 ± 1.7
C12	155.9 ± 2.0	172.0 ± 1.9	321.3 ± 2.1
Superheat 2			
R19	82.3 ± 0.3	127.9 ± 0.6	571.1 ± 4.2
R12	82.6 ± 0.3	127.7 ± 0.4	564.5 ± 1.3
R12T	83.0 ± 0.6	128.2 ± 0.4	565.7 ± 2.3
C19	82.1 ± 0.2	110.8 ± 0.5	573.9 ± 6.8
C12	81.6 ± 0.3	110.1 ± 0.4	569.6 ± 1.0

platform with the weigh cell and stepper motors from the warmer region close to the lid to the colder region of the baffle location. The influence of the platform movement is most pronounced for T8, T9 and T10 sensors allocated in the upper part of the cryostat.

T1, T2, T3, T4, T5, T6 and T7 sensors measure vapor and liquid temperatures at the wicking sample location. Fig. 4.8 and 4.9 demonstrates their temperature evolutions for each experiment. The first vertical line on each figure indicates the beginning of the wicking process. Particularly, $t = 0$ here and on all the further figures corresponds to the stop of the sample movement towards the bulk liquid. At that moment the sample was submerged at 1 to 2 mm and wicking into the upper not-submerged part of the sample occurred. The second vertical line depicts the moment of full saturation of the sample. The time period between these lines corresponds to the wicking time.

The vapor temperature changes during the experiments. It increases from the moment of the sample movement, reaches a maximum value during the wicking process and then again decreases to an approximately initial value. Such a behavior is caused by the heat transfer between the sample and the surrounding vapor. A vapor temperature increase is most pronounced for

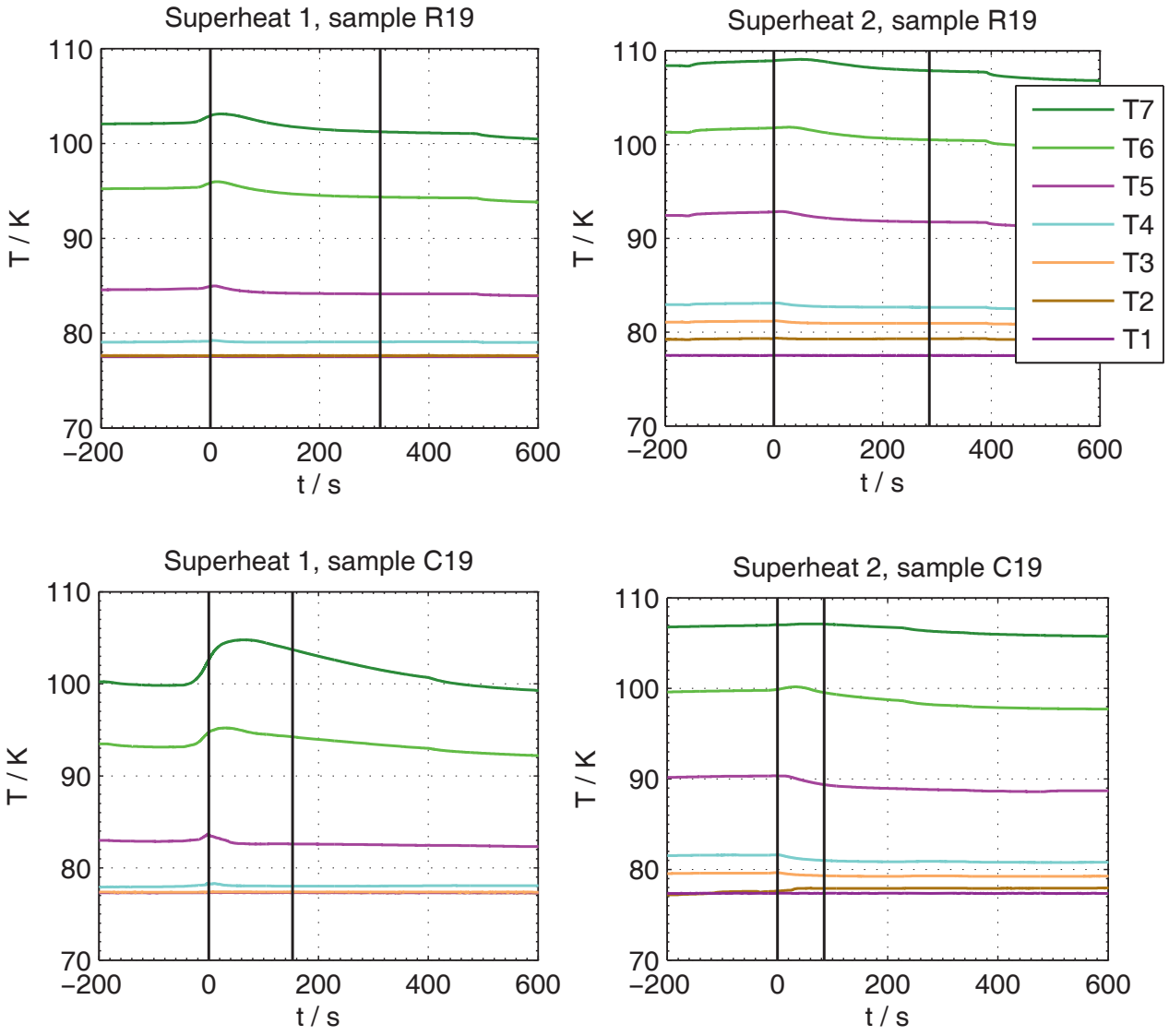

Figure 4.8: Vapor temperature evolution during the imbibtion of liquid nitrogen into the superheated porous samples R19 and C19.

Superheat 1 case due to higher values of the sample superheat. During the imbibition of liquid nitrogen the sample structure cools down and starts cooling the surrounding vapor. That is clearly seen for both experiment cases. One also notices that heating and cooling of the surrounding vapor are most pronounced for cylindrical samples that had larger mass and surface area per a sample height for the heat transfer.

Fig. 4.9 also shows that for each sample the wicking time was longer in the experiments with Superheat 1 than with Superheat 2. This indicates that higher superheats cause a wicking time increase. Comparing results for samples of identical geometry, one also observes that the

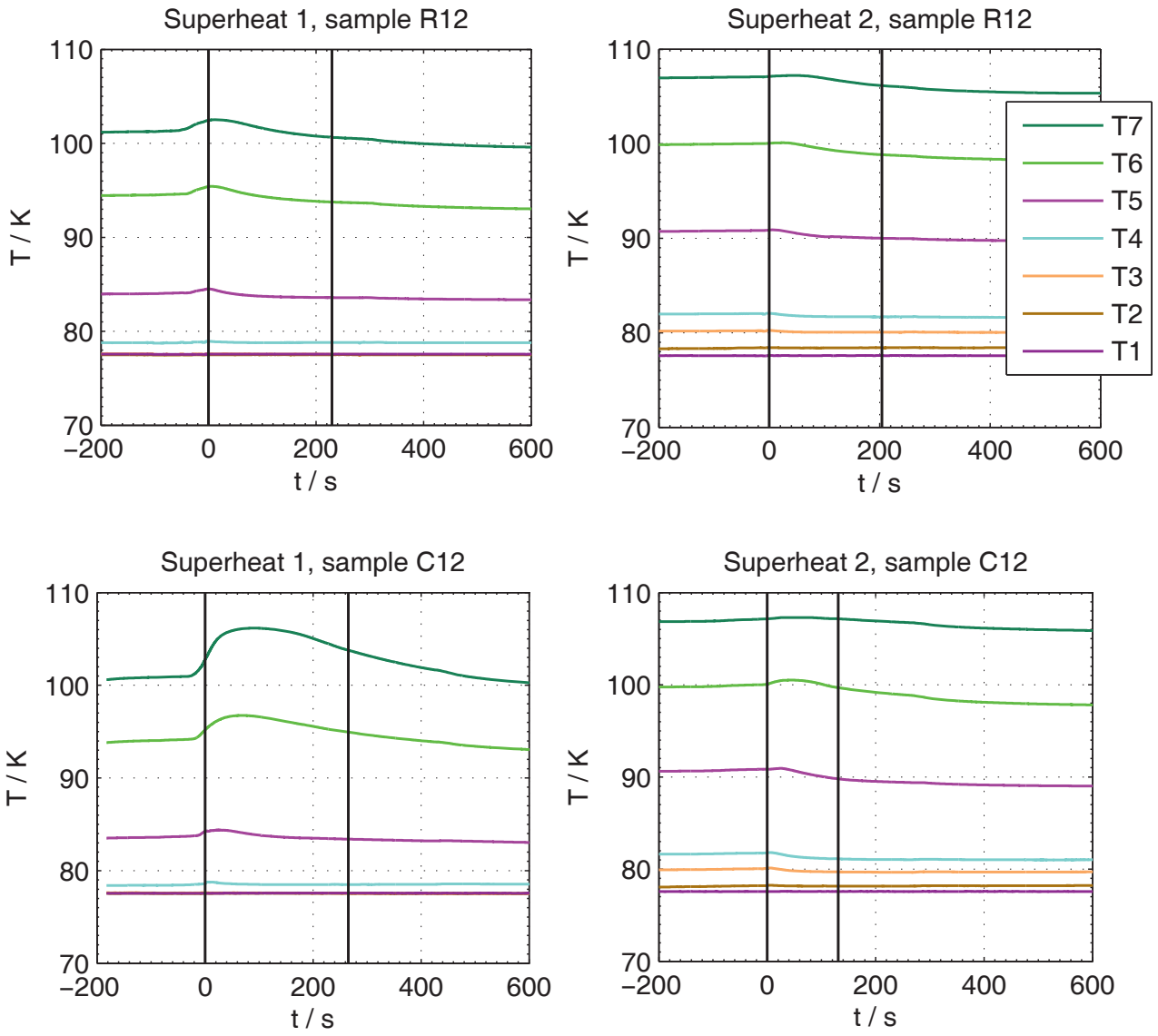

Figure 4.9: Vapor temperature evolution during the imbibtion of liquid nitrogen into the superheated porous samples R12 and C12.

wicking time is longer for samples of smaller permeability. For example, C12 sample needed approximately 130 s to get saturated with liquid nitrogen in Superheat 2 case, while C19 sample of much higher permeability needed only 80 s. The same trend holds for Superheat 1 runs.

4.4.2 Imbibed liquid mass and sample temperature

This part presents results of simultaneous sample weight and temperature measurements during the imbibtion of liquid nitrogen in R12T sample. Wicking experiments referred in previous sections as Superheat 1 and Superheat 2 were performed. The mass of the imbibed liquid was

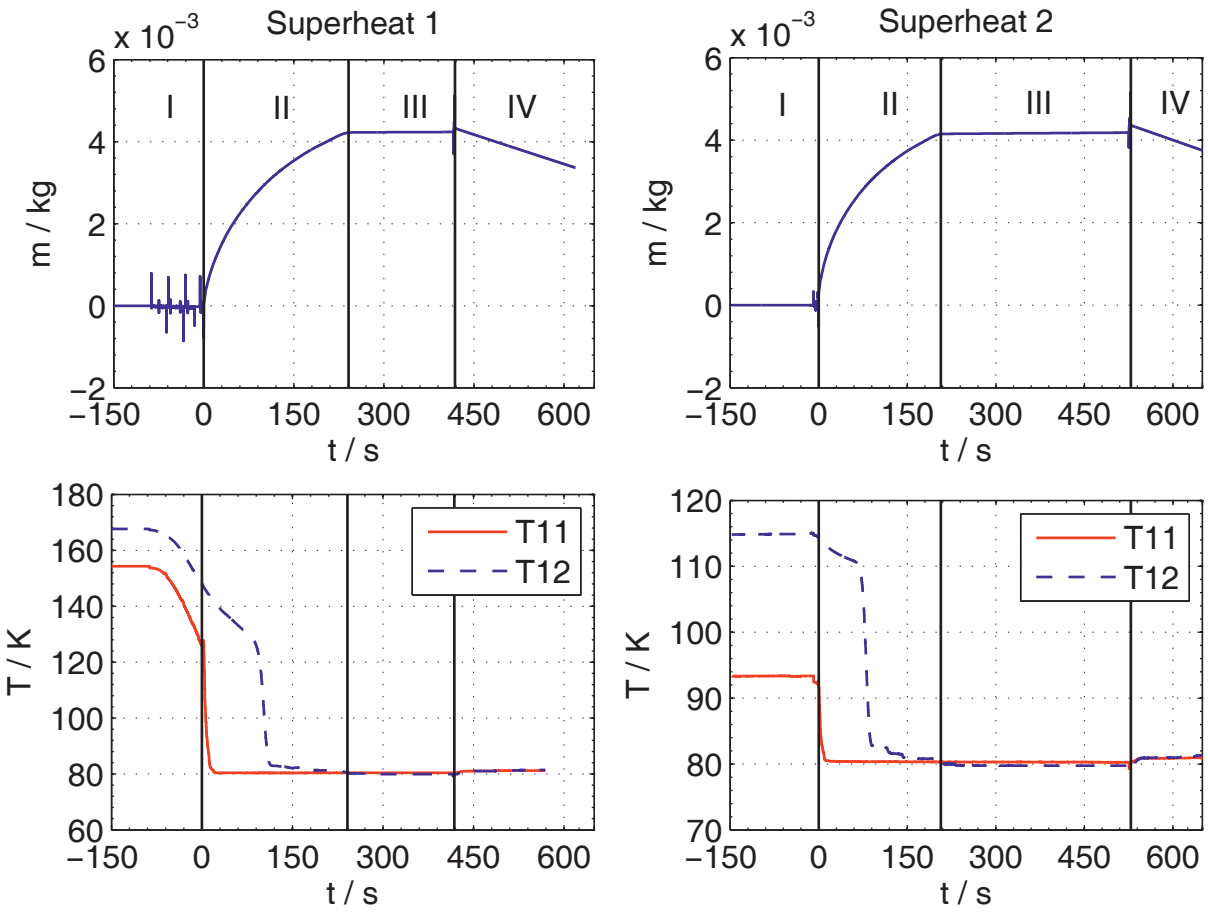

Figure 4.10: The mass of the imbibed liquid and sample temperature evolution obtained with T11 and T12 sensors during the imbibition of liquid nitrogen into superheated porous sample R12T. The vertical lines separate different stages of the experiment.

calculated using dry sample weight measurements and sample weight measurements during the imbibition.

Fig. 4.10 demonstrates the mass increase of the imibibed liquid nitrogen and simultaneous temperature evolution obtained with T11 and T12 sensors. These sensors were inserted into two holes along the sample height. More details on the sensor allocation is provided in section 4.3.2. The vertical lines on Fig. 4.10 separate different stages of the experiment.

During the stage I the sample was moved from its initial position to the liquid surface. The sample movement caused some sample weight perturbations recorded by the weigh cell and corresponded to the mass perturbations shown on Fig. 4.10. The perturbation time was smaller for Superheat 2 when the sample was moved at a smaller distance. Fig. 4.10 also shows that for Superheat 1 case the heat transfer between the sample and surrounding vapor led to

a significant sample temperature decrease. This is demonstrated by the change of T11 and T12 sensors readings from 154.3 K and 167.6 K at the initial sample position to approximately 125.9 K and 148.2 K, respectively, at the wicking start. In the case of Superheat 2 the sample movement caused a temperature change from 93.3 K and 114.9 K to approximately 92.1 K and 114.4 K for T11 and T12 sensors, respectively.

The stage II corresponds to the wicking process. The mass of the imbibed liquid increases in time. When the wicking front passes through the sensor location, the sensor reading decreases abruptly. Thus, the abrupt temperature decrease is a wicking front indicator. A smooth temperature decrease can be also seen for T12 sensor before the abrupt one. This is contributed by the heat conduction in the solid structure of the sample and the heat transfer between the solid structure and newly created vapor.

The constant liquid mass and sample temperature during the stage III on Fig. 4.10 indicate the saturation of the sample with liquid nitrogen. The temperature of the saturated sample is approximately 80 K that exceeds the liquid nitrogen temperature (77.355 K). Such a difference might be due to some imperfections in fixing of T11 and T12 sensors on the porous surface inside the holes. In fact, the sensors might partly measure the vapor temperature. Another possible explanation could be a creation of vapor pockets in the porous structure during the imbibition.

The stage IV starts at the moment when the sample is detached from the liquid surface. The mass decrease on Fig. 4.10 indicates evaporation of the imbibed liquid out of the sample. Due to the heat transfer with the surrounding vapor the sample temperature increases.

The mass increase $m(t)$ of the imbibed liquid nitrogen into the sample R12T can be connected to the wicking height $h(t)$ of liquid nitrogen via Eq. 4.5. Using the experimental data and Eq. 4.5, the propagation of the wicking front of liquid nitrogen was estimated. Fig. 4.11 shows the wicking height propagation in time obtained from the mass increase of the liquid nitrogen imbibed into the sample R12T for Superheat 1 and 2 cases (dotted and solid lines).

On the other hand, the abrupt temperature decreases of the sensors T11 and T12 allocated along the sample height was observed when the liquid nitrogen front was passing through the sensors locations, see Fig 4.10. Therefore, the wicking front propagation could be tracked using the sensors locations and the times corresponding to the temperature drops. These results for Superheat 1 and 2 cases are shown on Fig. 4.11 as the data points.

Hence, Fig. 4.11 presents the wicking front propagation during the imbibition of liquid nitrogen into the sample R12T determined with two different methods: using the mass increase of the

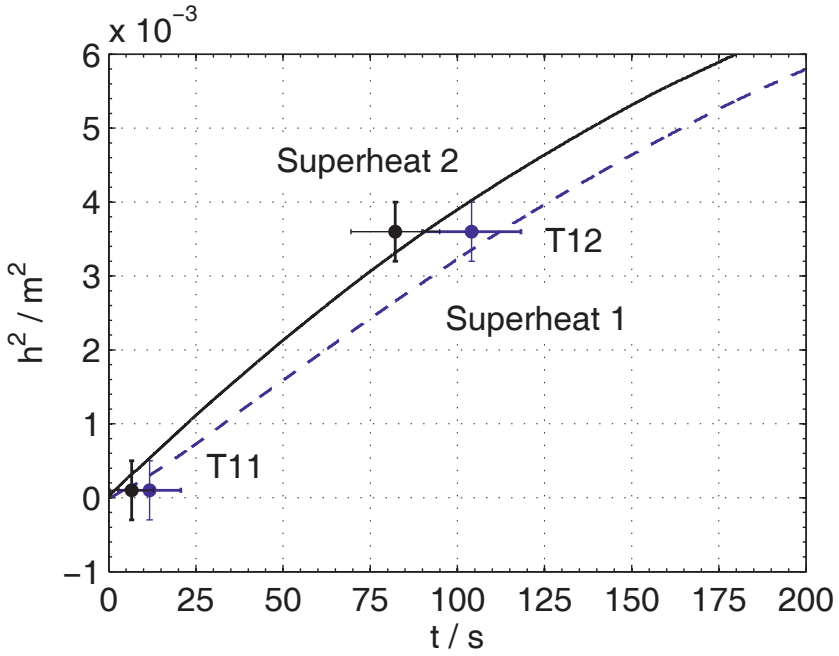

Figure 4.11: The wicking front propagation in time obtained from the mass increase of the liquid nitrogen imbibed into the sample R12T (dotted and solid lines) and from the temperature responses of the sensors T11 and T12 (data points) for Superheat 1 and 2.

imbibed liquid and using the temperature sensors responses. As shows Fig. 4.11, the results are in good agreement with each other.

4.4.3 Imbibed liquid mass at various porous structures, sample geometries and superheats

In this part, the experiment stage II that directly relates to the imbibition is under investigation for Superheat 1 and 2 cases. The sample weight measurements were conducted during wicking of liquid nitrogen into R19, R12, C19 and C12 samples to obtain the mass of the imbibed liquid. The measurements were corrected in accordance with the argumentation provided in section 4.3.3.

The theoretical prediction was performed using the proposed model with Eq. 3.11. The model predicts the imbibition in form of the wicking height increase in time. In order to compare it with experimental results, the wicking height was recalculated into the wicking mass using Eq. 4.5. In addition, the theoretical prediction for the isothermal case (no sample superheat) at saturation temperature of liquid nitrogen was performed with the Lucas-Washburn equation with gravity effects (Eq. 2.95). The solution of Eq. 2.95 was given as Eq. 3.12.

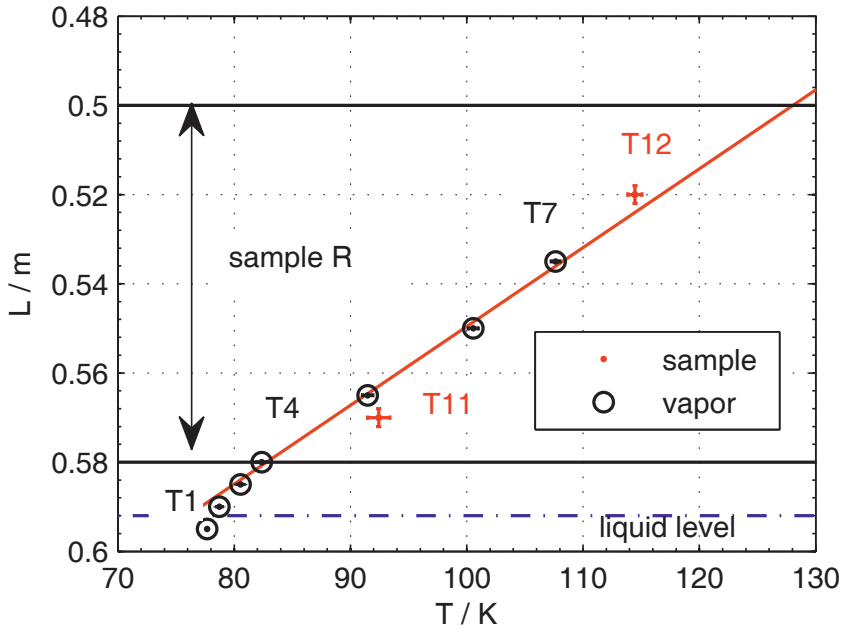

Figure 4.12: The sample (T11 and T12) and the vapor (T1 to T7) temperatures before the second wicking experiment (Superheat 2) for the sample R12T. Sample temperature deviates from the corresponding vapor temperature. The values are shown with a standard deviation for three experiment runs. The sample position is shown via arrows and solid black lines. The liquid level is displayed by a dot-dashed blue line.

The parameters of Eq. 3.11 and 3.12 were computed using thermophysical properties of liquid nitrogen at saturation temperature and borosilicate glass, sample geometrical characteristics and macroscopic parameters and sample temperatures. As shown in section 4.4.2, in Superheat 1 case the sample temperature decreases from its initial value during the sample movement to the liquid surface. Results of R12T sample temperature measurements were used to calculate sample temperatures at the wicking start. 122 K and 157 K were obtained for rectangular samples at the bottom and top, respectively, and 129 K and 151 K for cylindrical samples. In case of Superheat 2 no significant sample temperature decrease was observed due to the sample movement, therefore, the temperatures from Table 4.7 were taken as the sample temperature. However, some deviations were noticed for the sample temperature measured by the sensors T11 and T12 and the corresponding vapor temperatures. Fig. 4.12 shows sample and vapor temperatures before the sample R12T was moved to the liquid surface in Superheat 2 case. The sample top and bottom temperatures deviate up to 5 K, comparing the vapor and sample temperature measurement values. This might be stipulated by the fact that the solid porous structure with the vapor in its pores was located in the stratified bulk vapor environment

Table 4.8: List of the parameters of Eq. 3.11 and 3.12.

Sample	ϵ	b	c	n_1	n_2
	-	$(\mathrm{s\,m^{-2}})$	$(\mathrm{m^{-1}})$	(-)	$(\mathrm{m^{-1}})$
		10^4			
Superheat 1					
R19	1.50	4.70	8.76	0.26	1.81
R12	1.27	5.38	5.47	0.26	1.80
C19	1.89	4.92	8.76	0.30	1.90
C12	2.23	10.17	5.47	0.30	1.89
Superheat 2					
R19	1.50	4.70	8.76	0.022	2.49
R12	1.27	5.38	5.47	0.023	2.46
C19	1.89	4.92	8.76	0.019	2.27
C12	2.23	10.17	5.47	0.017	2.24

that was constantly influenced by the evaporation of the bulk liquid. Therefore, we took an uncertainty of ±5 K in the sample temperature determination and accounted for this in an error analysis for the theoretical model prediction, see in section 4.4.3.

Schnelle et al. [143] deduced a polynomial equation that describes the temperature dependence of the specific heat capacity of borosilicate glass 3.3 in the range from 48.2 K to 320 K

$$c_{\mathrm{S}}(T) = \exp\left[\sum a_i (\ln T)^i\right], \tag{4.6}$$

where a_i are empirical coefficients. Eq. 4.6 was used to calculate the specific heat capacity at average sample temperatures. The parameter values for all the samples are summarized in Table 4.8.

The parameters ϵ and b in Table 4.8 are different for the samples due to the fact that they include porosity and permeability values, which depend on a porous structure of each sample. The parameter c is equal for the samples of similar characteristic pore size. However, at both superheats the parameters n_1 and n_2, which include sample and liquid temperatures, deviate only slightly for samples of identical geometry. This indicates that tests were conducted under comparable conditions (with the same fluid and at approximately equal temperatures). The higher sample superheat, the bigger n_1 is. The parameter n_2 in its turn is higher for higher temperature gradients in porous structures.

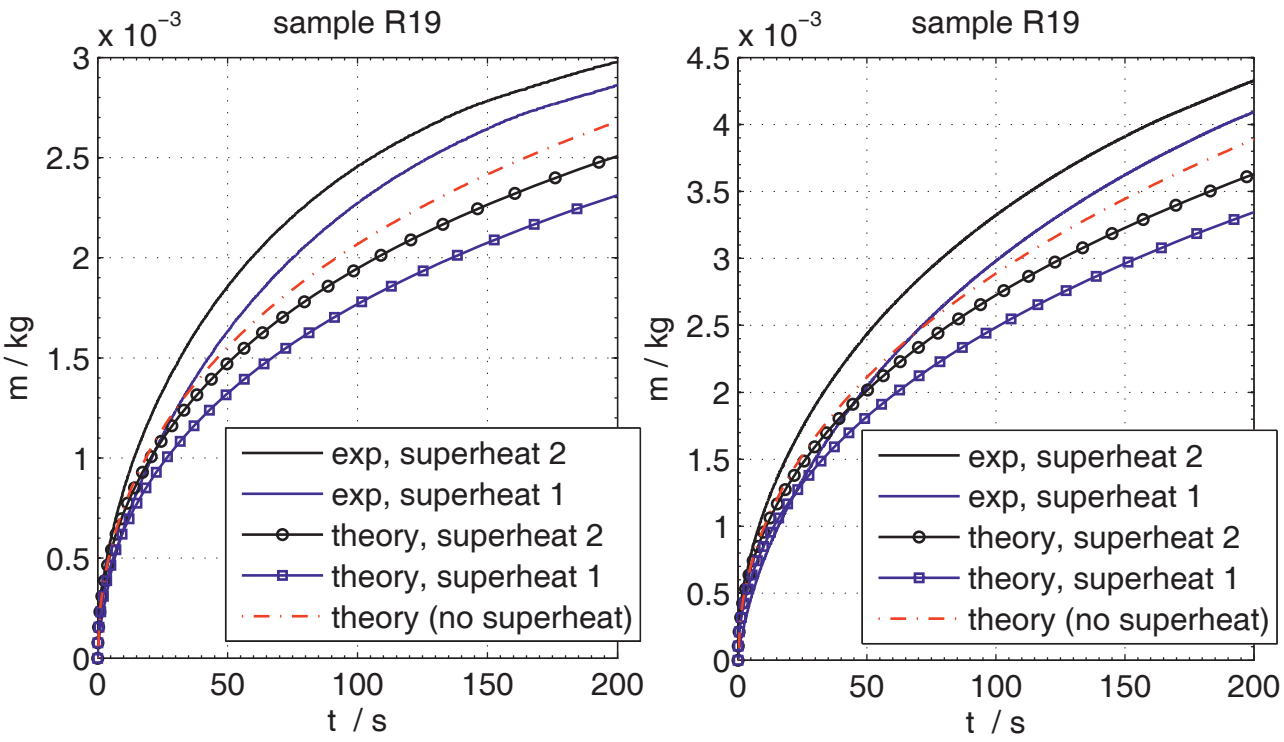

Figure 4.13: The mass of the imbibed liquid nitrogen during wicking in superheated porous samples R19 and R12. The theoretical prediction for the Superheat 1 and 2 cases was performed using the proposed model with Eq. 3.11. The theoretical prediction for the case of no sample superheat was computed with the Lucas-Washburn equation with gravity effects (Eq. 2.95). For both samples the relative decrease of the imbibition rate between two experimental curves at lower (2) and higher (1) sample superheats is in good agreement with predictions via Eq. 3.11. High sample superheat does not lead to a considerable decrease of the imbibition rate.

Fig. 4.13 shows experimental results and theoretical predictions for rectangular samples R19 and R12. A qualitative agreement between the theory and experiment was reached for both samples. Moreover, the relative decrease of the imbibition rate between two experimental curves at lower and higher sample superheats is in good quantitative agreement with predictions via Eq. 3.11. The experiment and theory also evidence that even for high sample superheat (122 K at the sample bottom) the results deviate only slightly from the results for much lower superheat (82 K at the sample bottom). Therefore, the liquid loss at the wicking front due to evaporation caused by the heat transfer between liquid nitrogen and superheated sample does not lead to a considerable decrease of the imbibition rate.

The predictions with Eq. 3.11 and 3.12 underestimate the imbibition rate. Such a result might be due to the assumptions made for the model derivation. The heat needed to cool down the

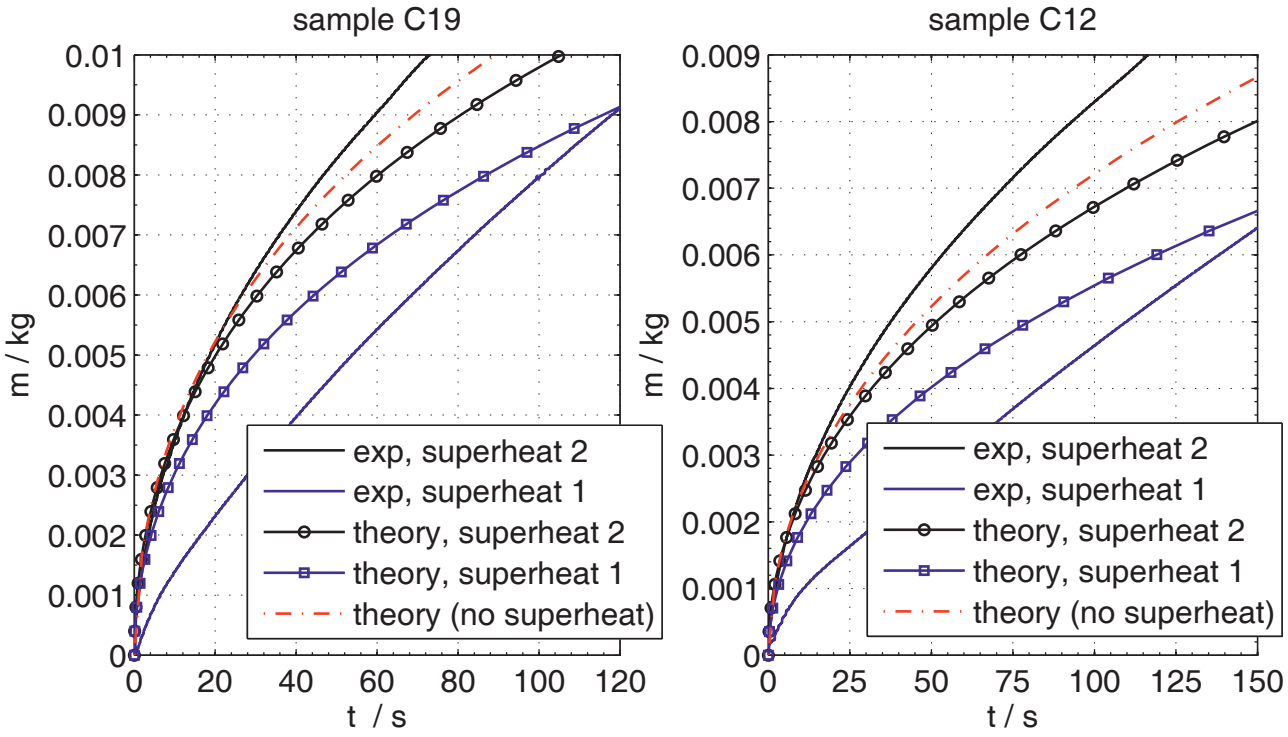

Figure 4.14: The mass of the imbibed liquid nitrogen into superheated porous samples C19 and C12. The theoretical prediction for the Superheat 1 and 2 cases was performed using the proposed model with Eq. 3.11. The theoretical prediction for the case of no sample superheat was computed with the Lucas-Washburn equation with gravity effects (Eq. 2.95). The vapor flow created due to evaporation in Superheat 1 case significantly slows down the imbibition rate and changes the wicking behavior. Eq. 3.11 neglecting the vapor flow impact provides a qualitative theoretical description only at smaller Superheat 2.

superheated solid structure above the wicking front was assumed to be entirely taken from the latent heat of evaporation of the liquid at saturation temperature. In fact, in the vicinity of the liquid-vapor interface heat transfer occurs between the rising liquid, the superheated porous structure, the newly created cold vapor and the superheated vapor initially contained in the structure. As a result the actual liquid-vapor interface temperature in the pores might differ from 77.355 K taken for calculations. Correspondingly, the thermophysical properties of the liquid taken for calculations will be affected. Especially, one should note here such a temperature dependent property as the surface tension that defines the capillary pressure for the imbibition. Hartwig et al. [144, 130, 145] observed the effect of evaporation and condensation measuring the liquid nitrogen, oxygen and methane bubble point pressures for steel meshes using non-condensable and autogenous pressurization schemes. The authors noted significant

differences between the bulk vapor and liquid temperatures and the corresponding screen side temperatures. The evaporation in experiments with a non-condensable pressurization led to the decrease of the interfacial temperature and, thus, to the increase of the local surface tension. The condensation in experiments with an autogenous pressurization caused the increase of the interfacial temperature and the decrease of the local surface tension.

Fig. 4.14 plots experimental data and theoretical predictions at two sample superheats for cylindrical samples C19 and C12. The theory describes results qualitatively for smaller Superheat 2. Meanwhile, results for higher Superheat 1 drastically deviate from the model predictions. Previous examination revealed that the liquid loss due to evaporation could not cause such deviations. Thereby, such a behavior might be stimulated by the vapor flow created due to evaporation. This vapor builds up an additional pressure in the pores above the rising liquid which slows down the imbibition rate. Due to relatively small cross-sections of R19 and R12 samples, the vapor could easily escape from the structures through their lateral sides, thus, its influence was negligible for wicking. However, in C19 and C12 samples the rising liquid pushes a larger amount of newly created vapor out of the structures along more complex and long trajectories. Moreover, the higher sample superheat, the more vapor is created. Therefore, the vapor flow effect is most pronounced for highly superheated samples of large cross-sections and may greatly slow down the imbibition rate. That is in conformity with results for C19 and C12 samples with Superheat 1.

Error analysis for theoretical model prediction

In this section an error analysis is given for the theoretical model prediction with Eq. 3.11. The model parameters contain macroscopic parameters of the samples and sample temperatures that are the error sources for the prediction, see Table 3.1. The deviations in the determination of the macroscopic parameters are presented Table 4.4. In consequence with the observed discrepancy of the results of sample and vapor temperature measurements, an error of ± 5 K was assumed for the sample temperatures determination. Table 4.9 summarizes results of the estimation of relative errors for the determined parameters of Eq. 3.11 and relative errors for the model prediction. A large discrepancy in the determination of n_1 for Superheat 2 case was caused by errors in the sample temperature determination. However, the absolute values of n_1 for Superheat 2 were relatively small compared to n_2/c and, therefore, only slightly influenced the final results. The relative errors for the model prediction of the mass of the imbibed liquid

Table 4.9: List of relative errors for determined parameters of Eq. 3.11 and relative errors for the model prediction.

Sample	$\delta\epsilon$ %	δb %	δc %	δn_1 %	δn_2 %	$\delta t(h)$ %	$\delta t(m)$ %
Superheat 1							
R19	8.33	6.69	2.03	11.2	28.9	9.26	12.7
R12	8.12	6.78	2.44	11.2	29.7	8.61	11.4
C19	8.79	11.2	2.03	8.67	27.5	12.6	14.0
C12	9.35	13.6	2.44	8.67	28.0	15.1	16.5
Superheat 2							
R19	8.33	6.69	2.03	101	20.6	8.60	12.2
R12	8.12	6.78	2.44	95.3	19.7	7.96	11.0
C19	8.79	11.2	2.03	105	21.0	12.0	13.4
C12	9.35	13.6	2.44	118	20.4	14.5	16.2

nitrogen versus time were estimated to be up to 12.7 % for rectangular and up to 16.5 % for cylindrical samples, see Table 4.9.

4.4.4 Wicking height of liquid nitrogen

Zhang et al. [127] performed experiments demonstrating the presence of liquid nitrogen in a metallic mesh due to wicking. The authors also reported that the height of the liquid column due to capillary effects is often used as a metric for wicking performance. The maximum height of the liquid column due to wicking, or the equilibrium wicking height, characterizes a balance between the capillary pressure and the hydrostatic pressure. It was also introduced in section 2.5.1, see Eq. 2.59. Zhang et al. [127] showed a prediction of the equilibrium wicking height for different effective radii of a porous structure and reported their experimentally determined wicking height for liquid nitrogen. The authors demonstrated a wicking height of 60 mm for a mesh structure with a pore size of approximately $5{\cdot}10^{-6}$ m. In this study the wicking height of 80 mm was achieved for sintered glass frits structures with a pore size of approximately $39.4{\cdot}10^{-6}$ m and $24.6{\cdot}10^{-6}$ m. The results are plotted together on Fig. 4.15. It should be mentioned that the obtained values [34] and the values reported by Zhang et al. [127] are not

claimed to be the equilibrium wicking height. However, these are the first reported values of the wicking height of liquid nitrogen.

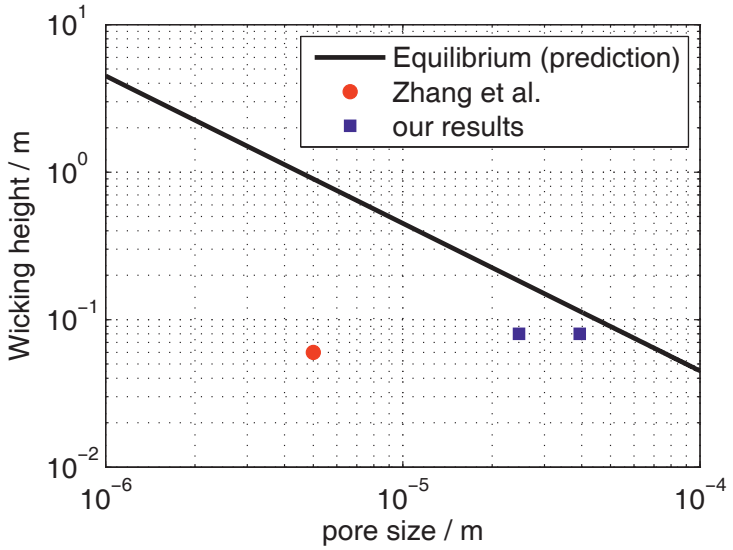

Figure 4.15: The wicking height of liquid nitrogen at different pore sizes. The equilibrium wicking height is predicted using Eq. 2.59 (no evaporation) and properties of liquid nitrogen at 101325 Pa and 77.355 K. The static contact angle is taken as zero. A red circle corresponds to a wicking height reported by Zhang et al. [127], blue squares correspond to the results obtained in this study [34].

4.4.5 Dimensionless analysis

The approach described in section 3.1.2 was used to non-dimensionalize the results. The wicking height and time were computed from the experiment data in dimensionless form using Eqs. 3.26 and 3.27, respectively.

Fig. 4.16 demonstrates the results of the isothermal wicking process (no sample superheat). The dimensionless wicking height obtained from the experiments with the FC-72 liquid and the samples R19, R12, C19, and C12, was plotted versus the dimensionless time. The experiment data were compared to the theoretical prediction performed via the dimensionless form of the Lucas-Washburn equation with gravity effects (Eq. 3.25). As shown in Fig. 4.16, the wicking results for different porous structures converge into one curve that was modeled via Eq. 3.25. The dimensionless wicking height increases with the dimensionless time until it approaches its maximum value equal to 1. Here the equilibrium wicking height is achieved, and the capillary pressure is balanced by the gravity. According to Eq. 3.25, wicking curves converge also for

different experiment liquids. In this case, however, the evaporation from the saturated porous structure into environment should be negligible, i.e. the surrounding gas should be saturated with the vapor of the experiment liquid. The influence of such evaporation on the wicking process has been studied by Fries et al. [126, 38].

In this work, the evaporation due to the sample superheat in one-species experiment environment was studied. The theoretical prediction via Eq. 3.24 for two sample superheats as well as the experiment results for wicking of liquid nitrogen into the superheated samples R19, R12, C19, and C12 are presented in dimensionless form on Fig. 4.17. The values of the dimensionless parameters and numbers for the theoretical prediction are summarized in Table 4.10. Here the Bond number was computed using the experimentally determined static pore radius as the characteristic length for each porous structure. In addition, the theoretical prediction for the case of no samples superheat performed via Eq. 3.25 is shown on each subplot of Fig. 4.17.

As for the dimensional wicking results described in section 4.4.3, the model prediction demonstrates the decrease of the dimensionless wicking rate with an increase of the sample superheat. The dimensionless wicking height h^* approaches its maximum value equal to 1 at larger t^* for the case of higher Superheat 1, see Fig. 4.17 (upper subplots). This is also in conformity with

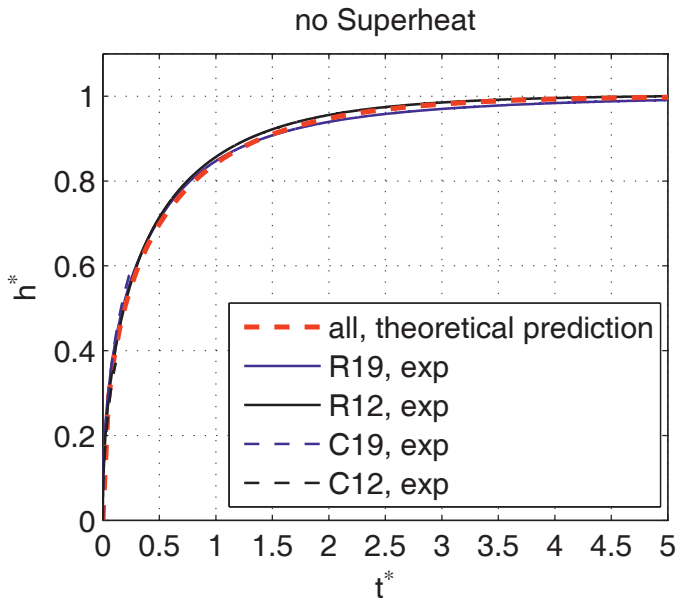

Figure 4.16: The dimensionless wicking height vs. the dimensionless time for the isothermal wicking into samples R19, R12, C19, and C12 (no sample superheat). The experiment data for wicking with the FC-72 liquid was recalculated using Eqs. 3.26 and 3.27. The theoretical prediction for the samples was performed using Eq. 3.25.

the experiment data (lower subplots). However, in comparison to the isothermal wicking results shown in Fig. 4.16, the predicted curves do not converge into the one curve even for similar superheats applied to the samples. This is due to the fact that the increase of h^* with the dimensionless time t^* depends in the model not only on the temperature conditions but also on the porous structure. The experiment data for the samples R19 and R12 indicate higher dimensionless wicking rates than it was predicted by the theoretical model, see Fig. 4.16. Such a result has been already shown in dimensional form and explained in section 4.4.3. The effect of the vapor flow that significantly decreased the wicking rates for the samples C19 and C12 at the high Superheat 1 has been discussed in section 4.4.3. However, the results in dimensionless form demonstrate that only a part of the equilibrium wicking height was achieved in the experiments. h^* did not reach its maximum value equal to 1. This is due to the sample size limited by the setup hardware. The maximum dimensionless wicking heights achieved in the experiments are different for the samples of the same geometry. That is due to the dependence of the equilibrium wicking height on the static pore radius, see Eq. 4.3, that varied for the samples.

The dimensionless theoretical model predicts the wicking process depending on the values of the parameters ϵ, Ω_1 and Ω_2. The parameter Ω_1 varies with a sample superheat. It includes

Table 4.10: List of the dimensionless parameters of Eq. 3.24 and relevant dimensionless numbers.

Sample	ϵ	Ω_1 10^{-1}	Ω_2 10^{-1}	Π^* 10^{2}	Bo 10^{-4}	Ja_1 10^{-1}	Ja_2 10^{-1}
Superheat 1							
R19	1.50	2.56	2.07	1.02	3.45	4.58	2.60
R12	1.28	2.56	3.28	0.73	1.35	4.58	2.57
C19	1.86	3.03	2.17	1.07	3.45	5.30	1.66
C12	2.23	3.03	3.45	1.38	1.35	5.30	1.65
Superheat 2							
R19	1.50	0.22	2.83	1.02	3.45	0.51	4.69
R12	1.28	0.23	4.49	0.73	1.35	0.54	4.63
C19	1.86	0.19	2.59	1.07	3.45	0.49	2.94
C12	2.23	0.17	4.09	1.38	1.35	0.44	2.92

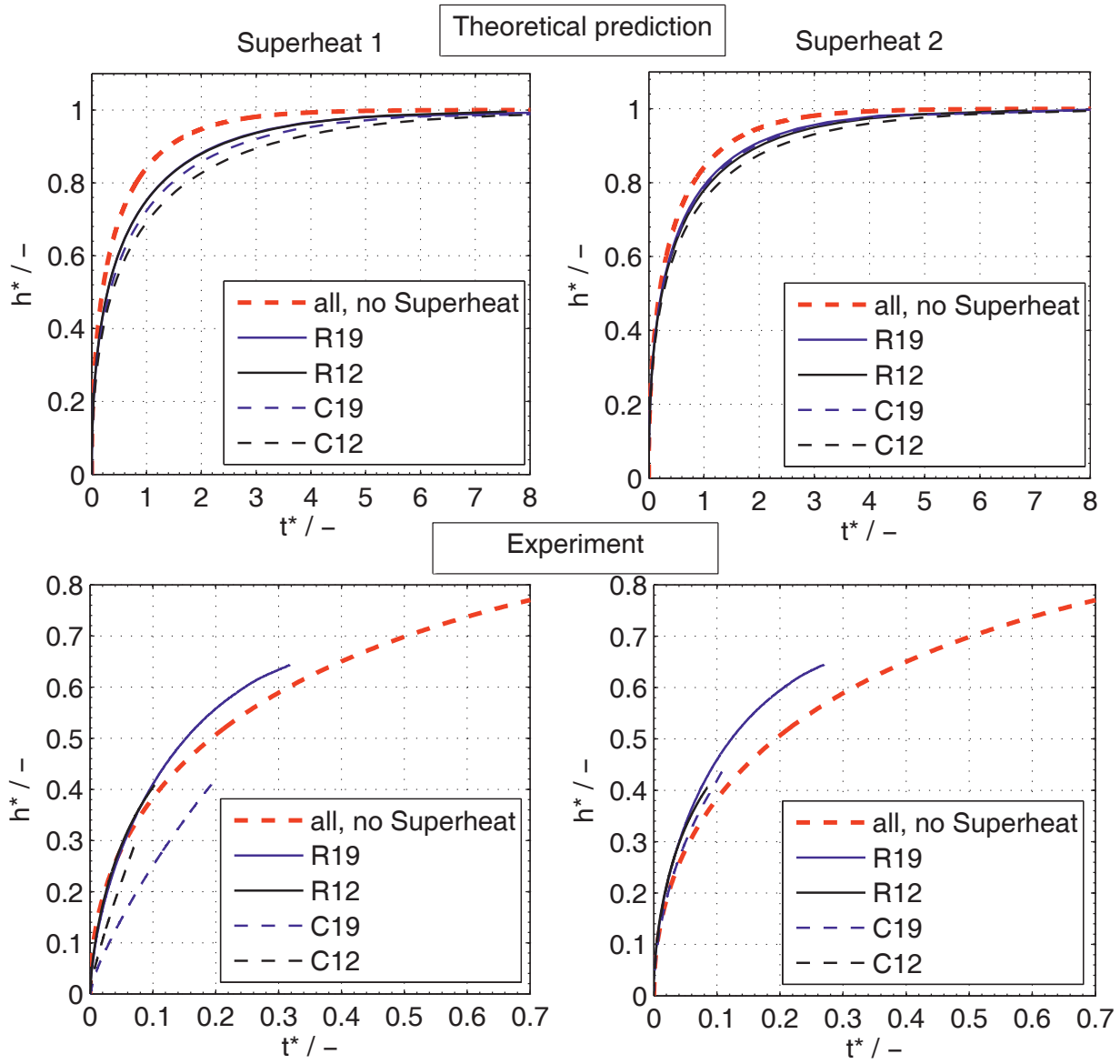

Figure 4.17: The dimensionless wicking height vs. the dimensionless time for the wicking of liquid nitrogen into the superheated porous samples R19, R12, C19, and C12. The theoretical prediction was performed for the Superheat 1 and 2 cases using Eq. 3.24 (upper subplots). The experiment wicking height was computed using the mass of the imbibed liquid and Eq. 4.5. The dimensionless wicking height and the dimensionless wicking time were recalculated from the experiment data with Eq. 3.26 and Eq. 3.27, respectively. The results are shown on lower subplots. The theoretical prediction for the case of no samples superheat was performed via Eq. 3.25.

the initial temperature at the bottom of the sample T_0, see Eq. 3.29. Fig. 4.18(a) shows that with an increase of Ω_1 due to the increase of T_0 the dimensionless wicking rate decreases. The

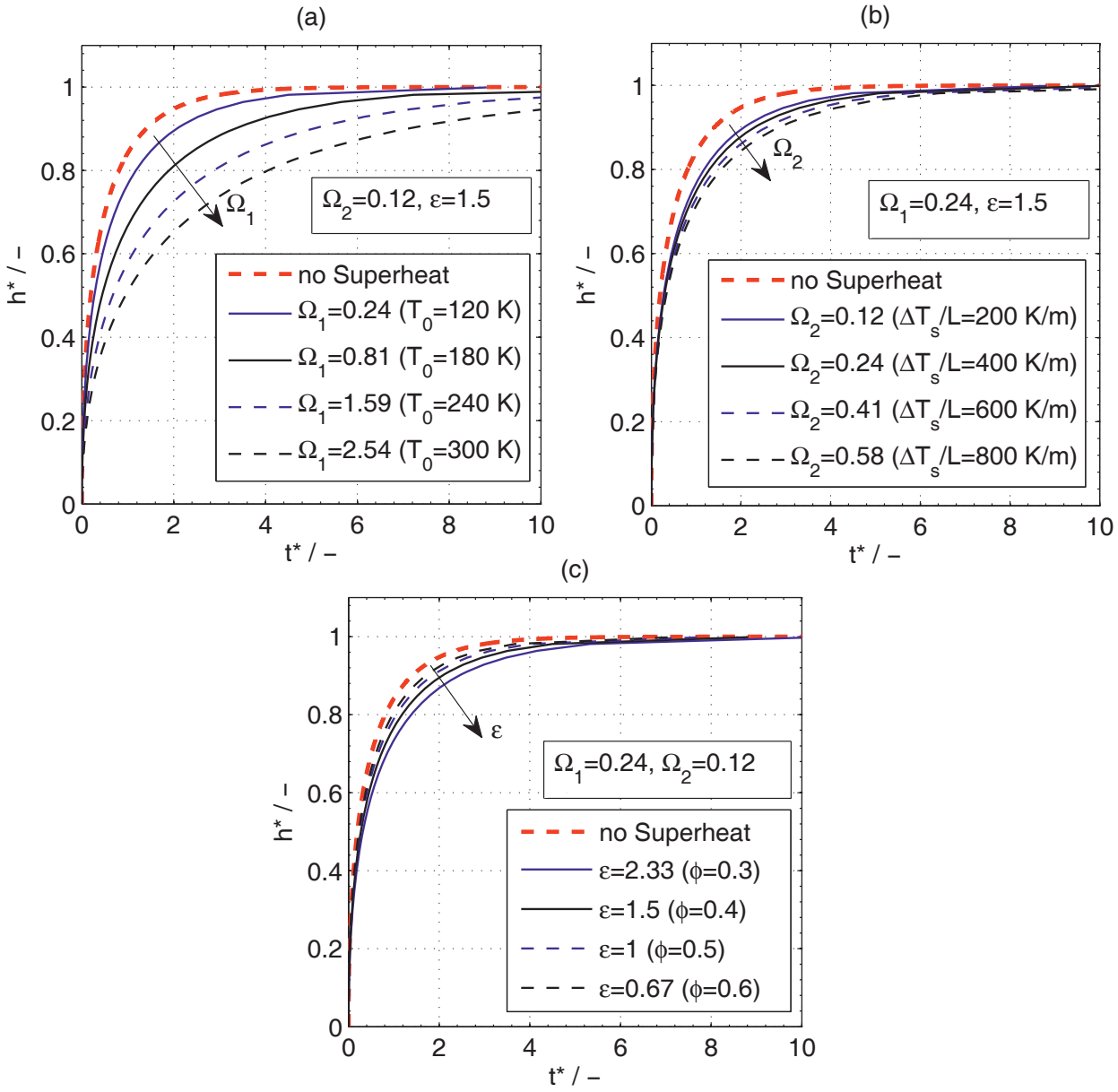

Figure 4.18: The dimensionless wicking height vs. the dimensionless time predicted via Eq. 3.24 varying the dimensionless parameters ϵ, Ω_1 and Ω_2. For the computations the thermophysical properties of liquid nitrogen and the macroscopic parameters of the sample R19 (by default) were used. The theoretical prediction for the case of no samples superheat was performed via Eq. 3.25. The increase of ϵ, Ω_1 and Ω_2 leads to the decrease of the dimensionless wicking rate.

parameter Ω_2 varies with an initial temperature gradient along the sample heights, see Eq. 3.32. Fig. 4.18(b) demonstrates that higher initial temperature gradients (larger Ω_2) lead to lower wicking rates. However, Ω_2 also includes the static pore radius of the structure R_s, and, thus, can also vary for different samples, see Table 4.10. The parameter ϵ is dependent only on the

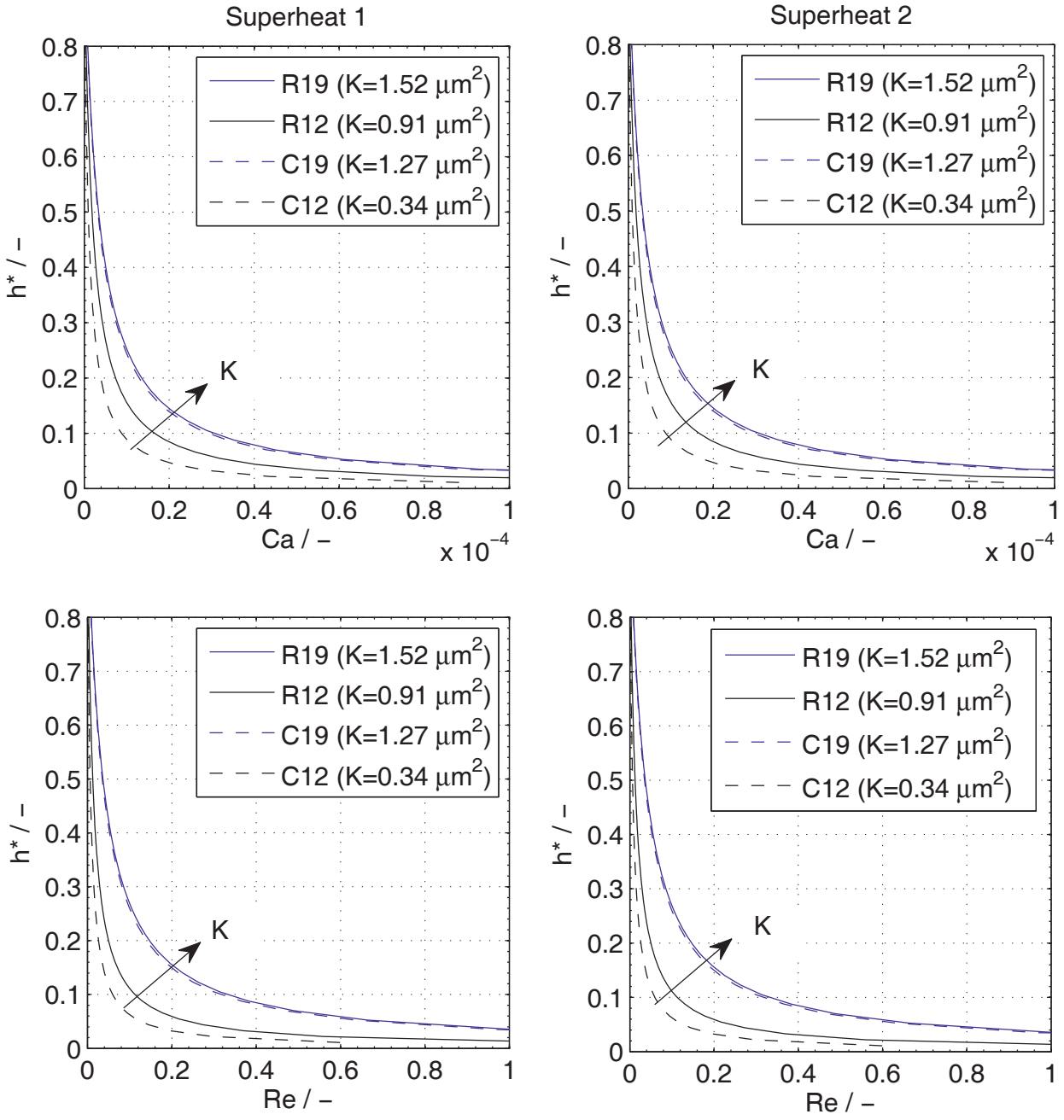

Figure 4.19: The dimensionless wicking height vs. the capillary (Ca) and Reynolds (Re) numbers during the imbibition process. Ca and Re numbers were computed using the thermophysical properties of liquid nitrogen and the interstitial velocity of liquid u_{L} predicted via Eq. 3.8. Ca and Re numbers are larger at the beginning of the imbibition ($h^* \to 0$) and decrease while the wicking front approaches the equilibrium wicking height ($h^* = 1$). At comparable superheats for the same h^* the samples of higher permeability K demonstrate higher u_{L} and, therefore, larger Ca and Re numbers.

porosity ϕ, see Table 3.1. It is larger for the samples of smaller porosity, when more superheated solid material is available for the heat transfer. Thus, with an increase of this parameter more liquid should evaporate resulting in the decrease of the wicking rate. On the other hand, lower porosity of the samples with same static pore radius supposes lower permeabilty that also leads to the decrease of the wicking rate This is in conformity with the prediction presented on Fig. 4.18(c).

The dimensionless capillary (Ca) and Reynolds (Re) numbers change during the imbibition process due to the change of the interstitial velocity of liquid u_{L}. The capillary number and Reynolds number were computed as

$$\mathrm{Ca} = \frac{\mu_{\mathrm{L}} u_{\mathrm{L}}}{\sigma}, \tag{4.7}$$

$$\mathrm{Re} = \frac{2\rho_{\mathrm{L}} u_{\mathrm{L}} R_{\mathrm{s}}}{\mu_{\mathrm{L}}}, \tag{4.8}$$

respectively. The thermophysical properties of liquid nitrogen and u_{L} predicted via Eq. 3.8 were substituted into Eqs. 4.7 and 4.7. Fig. 4.19 shows the change of Ca and Re numbers with an increase of the dimensionless wicking height. u_{L} and, correspondingly, Ca and Re numbers are larger at the beginning of the imbibition ($h^* \to 0$) and decrease while the wicking front approaches the equilibrium wicking height ($h^* = 1$). Moreover, at comparable superheats for the same h^* the samples of higher permeability K demonstrate higher u_{L} and, therefore, larger Ca and Re numbers, see Fig. 4.19. The values of Ca and Re numbers obtained in this study are typical for the capillary rise in porous media. The values of Re number indicate the laminar flow regime.

4.5 Summary

Wicking of liquid nitrogen at saturation temperature into vertical superheated porous structures was studied. Experiments were performed in a one-species system under pre-defined non-isothermal conditions to determine the mass of the imbibed liquid nitrogen measuring a sample weight increase during the imbibition. The setup configuration enabled to define a sample superheat by its initial position in a stratified vapor environment inside the cryostat. To the author's extent of knowledge these are the first wicking experiments performed with a cryogenic fluid subjected to evaporation using the weight-time measurement technique.

Two experimental cases with regard to a sample superheat value were examined. The vapor temperature distribution with established linear gradients in the initial and the wicking sample location was determined in the cryostat. The vapor temperature evolution demonstrated the

interaction of superheated porous structures with the surrounding vapor. Simultaneous sample weight and temperature measurements were conducted. Four experiment stages were identified in accordance with the weight and temperature responses. During the imbibition stage these responses indicated the wicking front propagation. The temperature decrease due to the heat conduction within the solid structure, and heat transfer between the solid structure and surrounding vapor was observed.

The impact of the porous sample superheat, structural and geometrical characteristics on the imbibition rate was investigated. Experimental and theoretical results are in a qualitative agreement and revealed that the liquid loss at the wicking front due to evaporation caused by the heat transfer between liquid nitrogen and superheated sample does not lead to a significant decrease of the imbibition rate. Only a slight decrease of the imbibition rate was observed for highly superheated samples of small cross-sections. In this case a good quantitative agreement between the experiment and theory was found for the relative decrease of the imbibition rate at two sample superheats. However, results of wicking with samples of larger cross-sections showed that the imbibition rate can be greatly affected by the vapor flow. The vapor created above the wicking front due to the heat transfer of the liquid with superheated porous structure counteracts the wicking front propagation and significantly slows down the process. Due to a larger amount of the created vapor and a more complex trajectory to escape of the porous structure, this effect is most pronounced for highly superheated samples of large cross-sections. The wicking results were studied in dimensionless form using the approach described in section 3.1.2. The increase of the dimensionless wicking height (h^*) with the dimensionless time (t^*) was investigated depending on the model parameters ϵ, Ω_1 and Ω_1 that characterize the sample superheat and porous structure peculiarities. The increase of these dimensionless parameters leads to the decrease of the dimensionless wicking rate. The capillary and Reynolds numbers decrease when the wicking front approaches the equilibrium wicking height.

Chapter 5

Experimental investigation of wicking of liquid nitrogen into sealed superheated porous structures

The following chapter describes the results of cryo-wicking experiments with liquid nitrogen and sealed superheated porous samples. The sample sealing was applied to enhance and study an influence on the imbibition rate of the vapor flow created due to the heat transfer at the wicking front. The results were compared to the theoretical prediction via the macroscopic model described in section 3.2.

5.1 Materials

The rectangular porous samples R19, R12 and R12T with no sealing have been tested in the cryo-wicking experiments described in chapter 4. Due to the geometry of these samples the imbibition into not-sealed porous structures was only slightly affected by the flow of the newly created vapor, see section 4.4.3. For this reason the samples R19, R12 and R12T were selected to be sealed for the following experiments and, thus, to demonstrate an influence of the vapor flow partly blocked inside the sealed structure.

5.1.1 Porous media

The porous structure of the samples R19, R12 and R12T made of sintered glassfilter elements have been described in section 4.1.1. The morphology was obtained via Scanning Electron Microscopy (SEM). The SEM images of the structures are presented on Figs. 4.1 and 4.2.

Some thermophysical properties of the solid material of the structures (borosilicate glass 3.3), are provided in Table 4.1. The geometrical characteristics of the samples are summarized in Table 4.2.

5.1.2 Sample sealing

In order to enhance the impact of the newly created vapor flow on the wicking process, lateral sides of the samples were treated with an adhesive sealing. An acrylat based adhesive film was obtained commercially (3M^{TM}). Two layer of the adhesive film were put on each lateral side of each sample resulting in the sealing of approximately 0.34 mm thickness, see Fig. 5.1. Thus, during the vertical wicking initiated at the bottom of the sample the newly created vapour could only escape through the sample top. Some additional handling was required to ensure the sealing of the temperature sensors allocated on the sample R12T. Three elliptical holes of 2 mm and 3 mm diameters and 6 mm depth were drilled on a smallest lateral side of the porous structure at 10 mm, 35 mm and 60 mm distance from the bottom of the sample. Three temperature sensors T11, T12 and T13 (silicon diodes DT-670A, LakeShore) were placed inside the holes. The latter were filled with a dust of borosilicate glass obtained from drilling of the sample material, and then sealed with several layers of the adhesive film. The film was partly attached to the connecting wires of the silicon diodes.

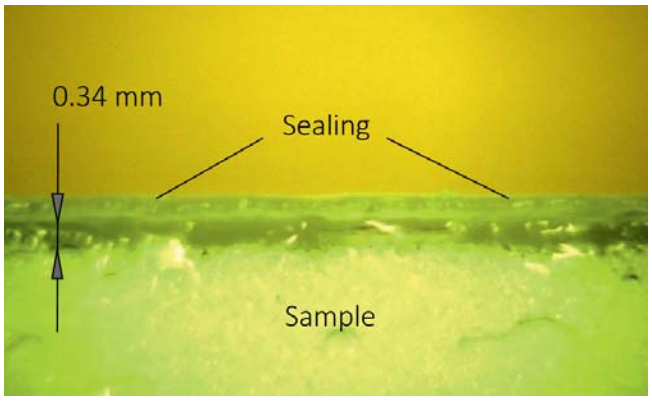

Figure 5.1: The sealing via an adhesive film attached to the sample.

5.1.3 Macroscopic parameters

The determination of the macroscopic parameters of the samples R19, R12 and R12T is described in section 4.1.2. The values of the open porosity, static pore radius and permeability

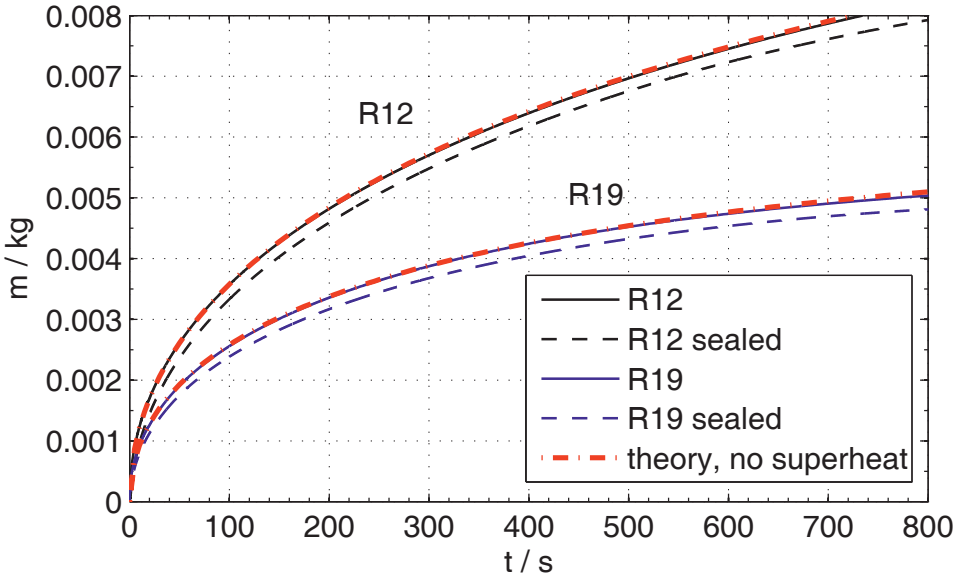

Figure 5.2: The mass increase of the imbibed FC-72 liquid into the sealed and not-sealed samples R19 and R12. The theoretical prediction was computed for the isothermal case (no sample superheat) via the Lucas-Washburn equation with gravity effects (Eq. 2.95). The sealing of the samples did not cause significant changes of the wicking rates.

were obtained in wicking experiments with the FC-72 liquid and summarized in Table 4.4. Some thermophysical properties of the FC-72 liquid are provided in Table 4.3.

5.2 Wicking experiment (no sample superheat)

Wicking experiments were performed with the FC-72 liquid and the sealed samples R19 and R12 using the setup described in section 4.1.2. The sealed sample R12T has not been tested on this setup due to some hardware limitations caused by the attached sensors and the connecting wires. However, the overall dimensions and macroscopic parameters of the sample R12T are similar to the overall dimensions and macroscopic parameters of the sample R12, see Tables 4.2 and 4.4. Thus, for these samples one might assume similar imbibition rates.

Wicking results for the sealed samples R19 and R12 were compared to the results for the not-sealed samples R19 and R12, respectively, see Fig. 5.2. The sealing of the samples did not cause significant changes of the wicking rates. The slight differences in the wicking rate shown on Fig. 5.2 are within 5% deviation for six test runs with the sealed and not-sealed samples.

A theoretical prediction was computed for the isothermal case (no sample superheat) using the Lucas-Washburn equation with gravity effects (Eq. 2.95). The thermophysical properties of

the FC-72 liquid (Table 4.3) and the macroscopic parameters of the samples (Table 4.4) were used for the computations. The increase of the wicking height $h(t)$ obtained via Eq. 2.95 was recalculated into the mass increase $m(t)$ via Eq. 4.5. A good agreement between the theoretical prediction and experiment data indicates the homogeneity of the porous structures with respect to the vertical wicking, see section 4.2.

5.3 Cryo-wicking experiment

Cryo-wicking experiments were conducted with liquid nitrogen and the sealed samples R19, R12 and R12T. The experiment apparatus has been described in section 4.3.1. Some thermophysical properties of saturated nitrogen (liquid and vapor) have been summarized in Table 4.6. The preparation and methodology of the experiment has been described in section 4.3.2.
Two wicking experiments ensuring different sample superheats (Superheat 1 and 2) were performed with each sample. In order to compare results with the results of the wicking experiments with the not-sealed samples R19, R12 and R12T (see chapter 4), similar sample superheat was ensured for each experiment case. For that the same temperature distribution in the cryostat was guaranteed by setting the same liquid level for the start of the corresponding experiment (582 mm for the Superheat 1 and 592 mm for the Superheat 2 cases). The initial position of the samples was also chosen to be the same. The distance from the sample bottom to the liquid surface was 140 mm and 10 mm for the Superheat 1 and 2 cases, respectively.
The sample weight measurement was applied during the imbibition into a superheated porous structure. The bulk vapor and liquid temperatures were recorded before, during and shortly after each test. The weight and temperature of the sample R12T were measured simultaneously. Three test runs have been conducted for each porous sample at each experiment case.
The sample weight measurements required a correction to account for buoyancy, the Wilhelmy force and the effect of a liquid level decrease in the cryostat. The method described in section 4.3.3 has been applied to the measurement data resulting in a correction of the mass of the imbibed liquid up to 1.3% for R19 and 1.7% for the samples R12 and R12T.

5.4 Results

The first part of this section provides the analysis of the experiment environment via the temperature evolution of the bulk vapor and liquid nitrogen. The second part summarizes the results of the simultaneous sample weight and temperature measurements. In the third part, the

impact of a porous structure and sample superheats on the mass of the imbibed liquid nitrogen are compared for sealed and not-sealed samples. The vapor flow influence on the imbibition is investigated. The theoretical prediction of wicking is performed via the macroscopic model described in section 3.2.1. In the fourth part, the dimensionless formulation of the results is given.

5.4.1 Temperature evolution of nitrogen vapor

Temperature distribution in the cryostat before the first (Superheat 1) and the second wicking experiment (Superheat 2) is presented on Fig. 5.3. Temperature values are plotted versus locations of the sensors in the cryostat at the moment when the sample was driven to the liquid surface. The initial sample position of the rectangular samples (R) is shown on Fig. 5.3 via arrows and dotted lines. The liquid level in the cryostat is indicated via a dot-dashed line.
Fig. 5.3 demonstrates the establishment of linear temperature gradients in a stratified nitrogen vapor environment below and above the baffle. This has been also observed in the cryo-wicking experiments with not-sealed samples described in chapter 4. The temperatures at the top and bottom of each sample were estimated using the temperature distribution in bulk vapor. Table

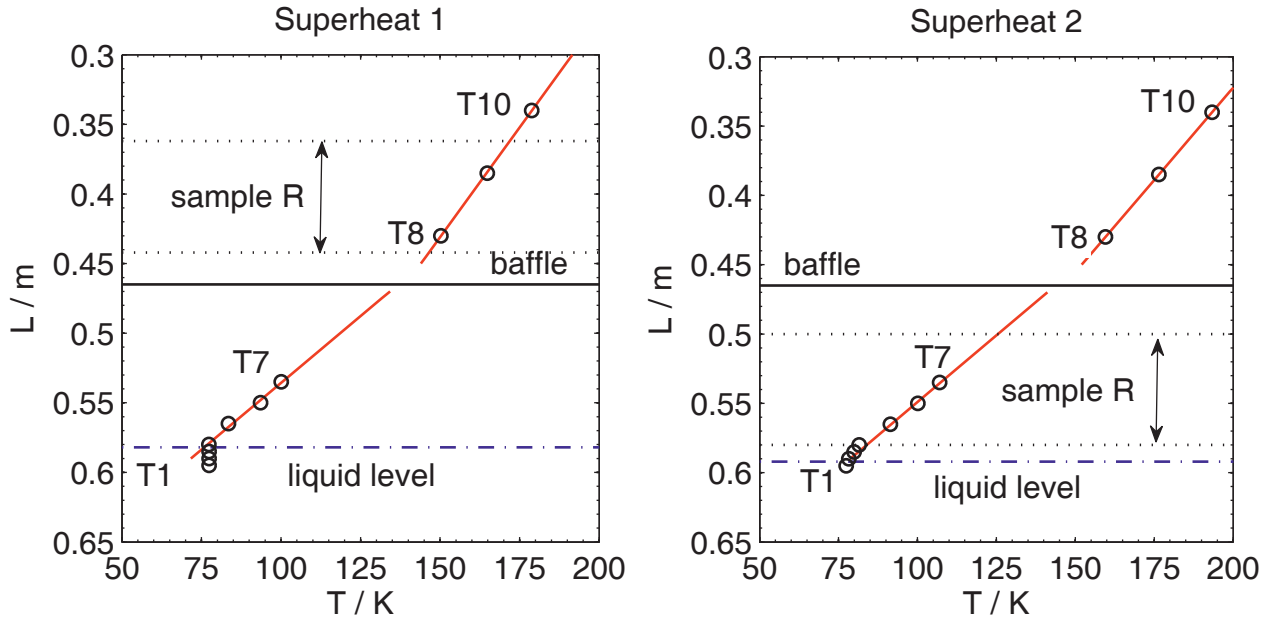

Figure 5.3: Temperature distribution in the cryostat before the first (Superheat 1) and second wicking experiment (Superheat 2). It illustrates the establishment of linear temperature gradients in a stratified nitrogen vapor environment below and above the baffle. The initial position for sealed rectangular (R) samples is shown via arrows and dotted lines.

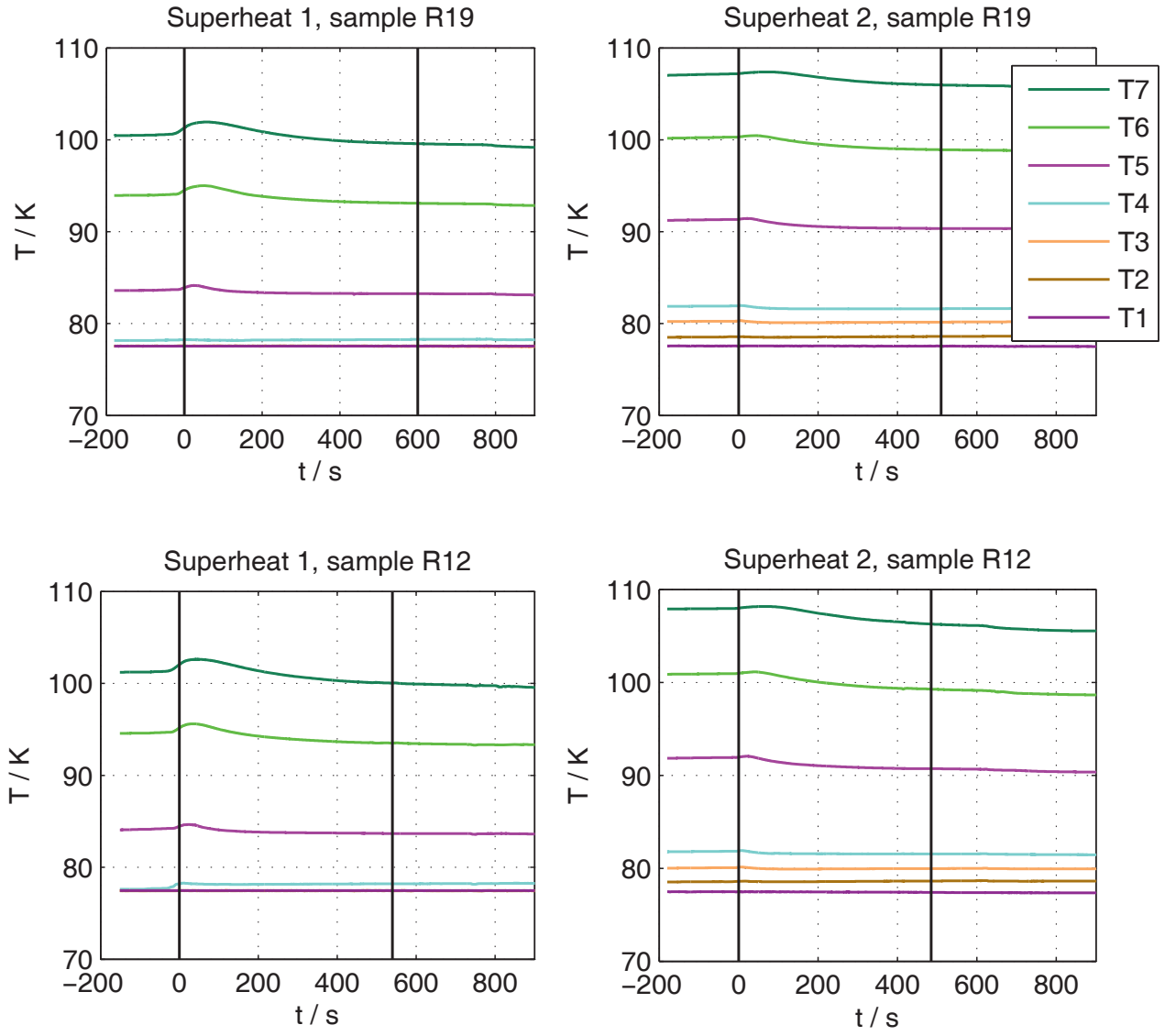

Figure 5.4: Vapor temperature evolution during the imbibtion of liquid nitrogen into the sealed porous samples R19 and R12 at Superheat 1 and 2.

5.1 summarizes the temperature gradients in bulk vapor and computed sample temperatures for each experiment case. The results are similar to the temperature distribution in the cryo-wicking experiment with not-sealed samples, see Table 4.7. This ensured comparable conditions for the determination of wicking rates into the samples with and without the sealing.

Fig. 5.4 presents temperature evolution in bulk vapor and liquid nitrogen recorded via the sensors T1 to T7 during the wicking experiment with the sealed samples R19 and R12 as well as shortly before and after that. Two vertical lines on each figure indicate the beginning of the wicking process and the moment of full saturation of the sample, respectively. $t = 0$ corresponds

Table 5.1: Initial linear temperature gradient in a stratified nitrogen vapor environment along the sample height $\triangle T_S/L$ and calculated temperature at the bottom T_0 and top T_{SL} of the sealed samples at Superheat 1 and 2.

Sample	T_0 (K)	T_{SL} (K)	$\triangle T_S/L$ ($K\,m^{-1}$)
Superheat 1			
R19 sealed	146.6 ± 0.2	171.8 ± 0.2	315.2 ± 0.9
R12 sealed	147.2 ± 0.6	172.6 ± 0.8	317.9 ± 2.3
R12T sealed	146.2 ± 0.8	171.6 ± 0.7	317.2 ± 0.9
Superheat 2			
R19 sealed	84.0 ± 0.2	128.5 ± 0.2	556.4 ± 0.8
R12 sealed	83.5 ± 0.4	129.2 ± 0.7	571.5 ± 6.5
R12T sealed	83.3 ± 0.1	127.4 ± 0.3	551.4 ± 2.6

to the stop of the sample movement towards the bulk liquid. At this moment the sample was submerged at 1 to 2 mm into the bulk liquid and wicking into the upper not-submerged part of the sample occurred. The results depicted on Fig. 5.4 are similar to the temperature evolution in bulk vapor and liquid nitrogen for cryo-wicking experiments with not-sealed samples shown in Figs. 4.8 and 4.8. This has been described in section 4.4.1.

5.4.2 Imbibed liquid mass and sample temperature

The sample weight and temperature measurements via the sensors T11, T12 and T13 were performed during the imbibition of liquid nitrogen into the sample R12T. Using the weight of a dry sample and the sample weight increase during the wicking process, the mass of the imbibed liquid was calculated. Fig. 5.5 demonstrates the results for the Superheat 1 and 2 cases. A similar experiment has been conducted with the not-sealed sample R12T. The results of this experiment have been described in section 4.4.2. In this section only the experiment stages shortly before and during the imbibition of liquid nitrogen are studied.

A vertical line with $t = 0$ on Fig. 5.5 indicates the beginning of the wicking process. The results before the vertical line correspond to the stage I when the sample was moved from its initial position towards the liquid surface. Due to the sample movement some sample weight perturbations were recorded by the weigh cell. This could be seen as the mass perturbations on

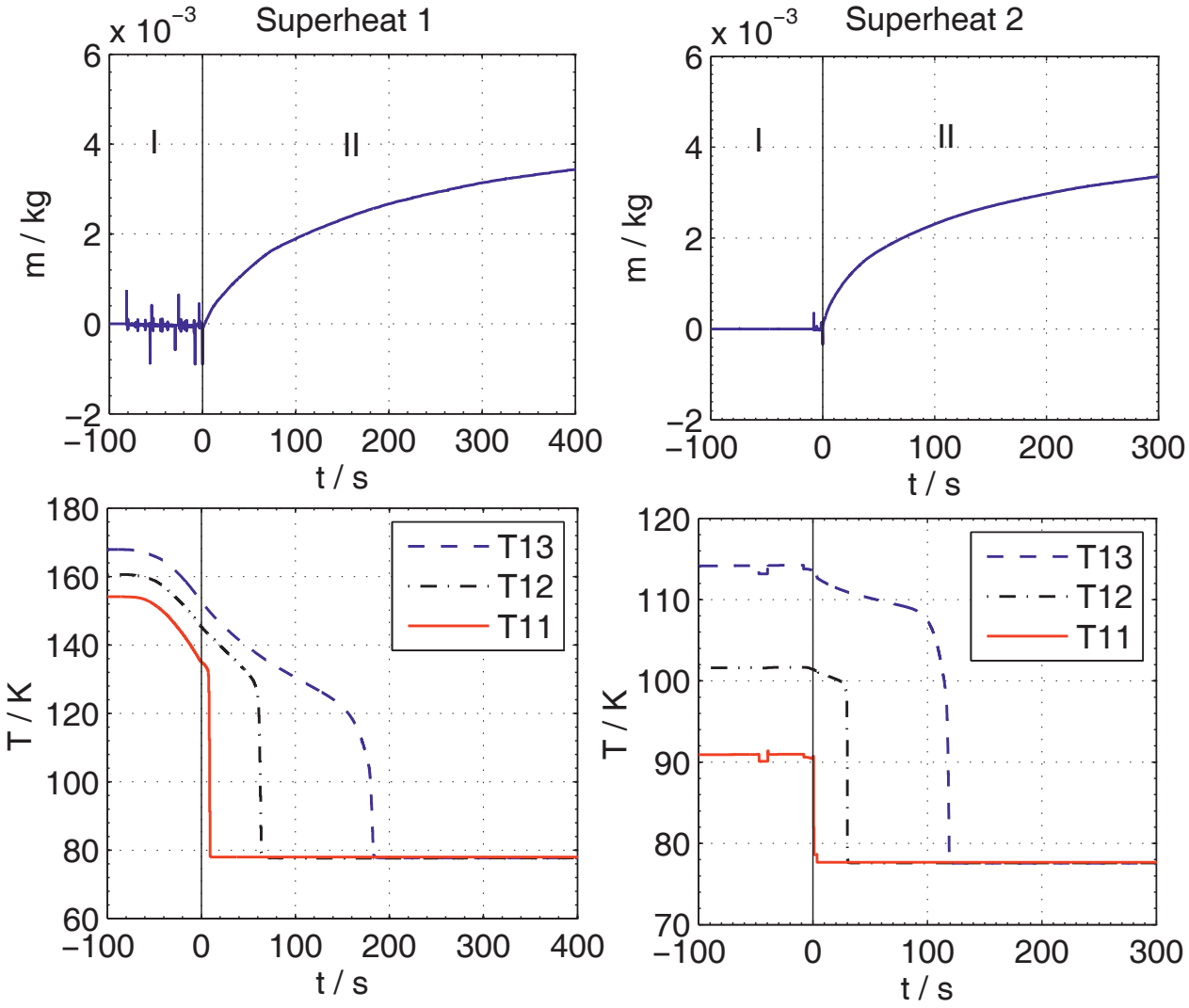

Figure 5.5: The mass of the imbibed liquid and sample temperature evolution obtained with the sensors T11, T12 and T13 during the imbibition of liquid nitrogen into the sealed superheated porous sample R12T.

Fig. 5.5. The sample was moved at a smaller distance in the Superheat 2 experiment. Hence, the perturbation time is smaller for this case. Due to the heat transfer with the surrounding vapor the sample temperature decreases during the sample movement. It is most pronounced for the Superheat 1 case with larger initial distance from the sample bottom to the liquid surface, see section 5.3. The temperatures T11, T12 and T13 decreased from 154.1 K, 160.6 K and 167.9 K down to 135.1 K, 145.3 K and 153.1 K, respectively. Moreover, the temperature decrease for the sensors T11 and T13 was found to be smaller at approximately 9.2 K and 4.2 K, respectively, compared to the results for the sample with no sealing, see section 4.4.2. (The sensors T11 and T13 correspond to T11 and T12 in the cryo-wicking experiment with the not-sealed sample.)

Thus, the sealing could reduce the heat exchange of the sample with the surrounding vapor. Nevertheless, some imperfections in fixing of the sensors on the porous surface (especially for the not-sealed sample) might also contribute to such temperature differences. In the Superheat 2 experiment the temperatures T11, T12 and T13 decreased from 90.9 K, 101.7 K and 114.2 K only at less than 0.5 K. Some short temperature drops and jumps at the stage I recorded by the sensors T11 and T13 were induced by the electronics disturbances and do not reflect any physical temperature changes .

At the beginning of the stage II the sample was submerged at 1 to 2 mm into the bulk liquid nitrogen and the vertical wicking into the upper (not-submerged) part of the sample started. The mass of the imbibed liquid increases in time. The temperatures recorded by the sensors T11, T12 and T13 decrease first smoothly and then abruptly to approximately 77.5 K. This minimum sample temperature within the sensors accuracy corresponds to the temperature of nitrogen at saturation. It could not be reached in the experiment with the not-sealed sample when the minimum sample temperature of only 80 K was recorded, see section 4.4.2. Thus, the insulation of the sensors due to the sealing allowed to detect the expected sample temperature drop. The smooth temperature decrease during the stage II could be stipulated by the heat transfer between the solid structure and newly created vapor as well as the heat conduction in solid.

On Fig. 5.6 the times of the abrupt temperature drops down to approximately 77.5 K are plotted versus the squared distances of the sensors locations from the sample bottom. The wicking front propagation in time was computed using Eq. 4.5 and the mass of the imbibed liquid nitrogen obtained from the weight increase of the sealed sample R12T. Fig. 5.6 demonstrates that for both experiment cases the temperature drops down to 77.5 K earlier than the sample weight measurement indicates the arrival of the liquid front to the sensor locations. Such a result could be caused by an influence of the vapor newly created in the structure and pushed towards the sample top by the rising liquid. Due to the sample sealing the vapor could only escape through the sample top and, thus, cooled down the solid structure above the wicking front to the temperature of nitrogen at saturation T_{L}. Meanwhile, in the cryo-wicking experiments with the not-sealed sample R12T both measurement approaches demonstrated a good agreement in detection of the wicking front propagation, see section 4.4.2. In that case the heat exchange of the newly created vapor with the solid structure above the wicking front was negligible and the local temperature of the solid structure dropped down to T_{L} only when the liquid nitrogen raised up to the sensor location.

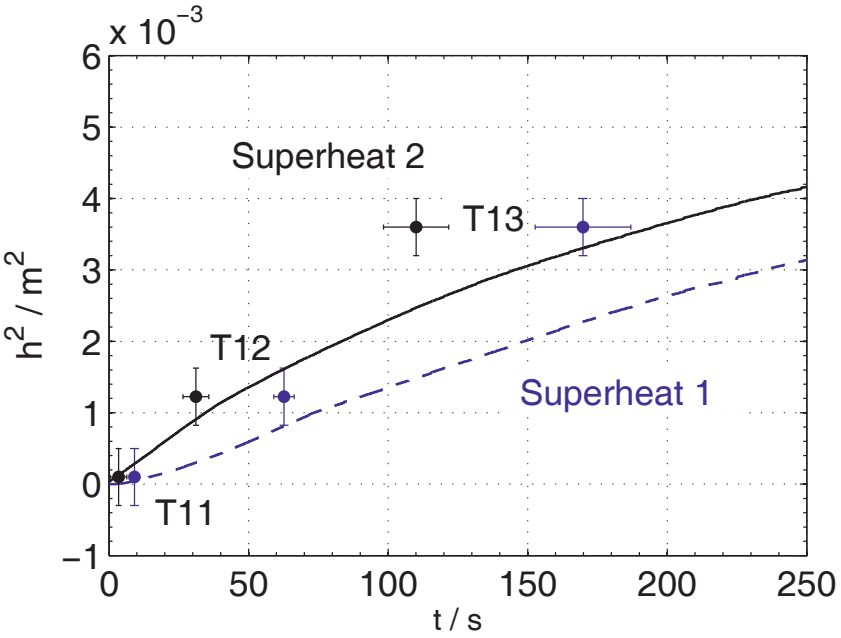

Figure 5.6: The times of the temperature drops of the sensors T11, T12 and T13 down to the temperature of nitrogen at saturation T_L during the wicking into the sealed sample R12T are plotted versus the squared distances of the sensors locations from the sample bottom for the Superheat 1 and 2 cases (data points). The wicking front propagation in time obtained from the sample weight measurement is plotted via dotted and solid lines for the Superheat 1 and 2 cases, respectively. For both experiment cases the sensors T11, T12 and T13 drops down to T_L earlier than the sample weight measurement indicates the arrival of the liquid front to the sensor locations. This implies that the nitrogen vapor cools down the solid structure above the wicking front.

5.4.3 Imbibed liquid mass at various porous structures and superheats

In this part the sample weight measurements results for the sealed samples R19 and R12 at the stage II are studied for the Superheat 1 and 2 cases. The stage II corresponds to the imbibition of liquid nitrogen. The mass of the imbibed liquid versus time is plotted on Fig. 5.7 (dashed lines). The cryo-wicking results obtained at comparable conditions for the not-sealed samples R19 and R12 are shown on Fig. 5.7 with a solid line.

Fig. 5.7 demonstrates that the imbibition rate greatly decreases compared to the structures with no sealing. For the Superheat 1 case a relative decrease of approximately 37.2 % and 32.4 % in the mass of the imbibed liquid nitrogen was observed in 200 s after the wicking start for the sample R19 and R12, respectively. For the Superheat 2 case these values correspond to

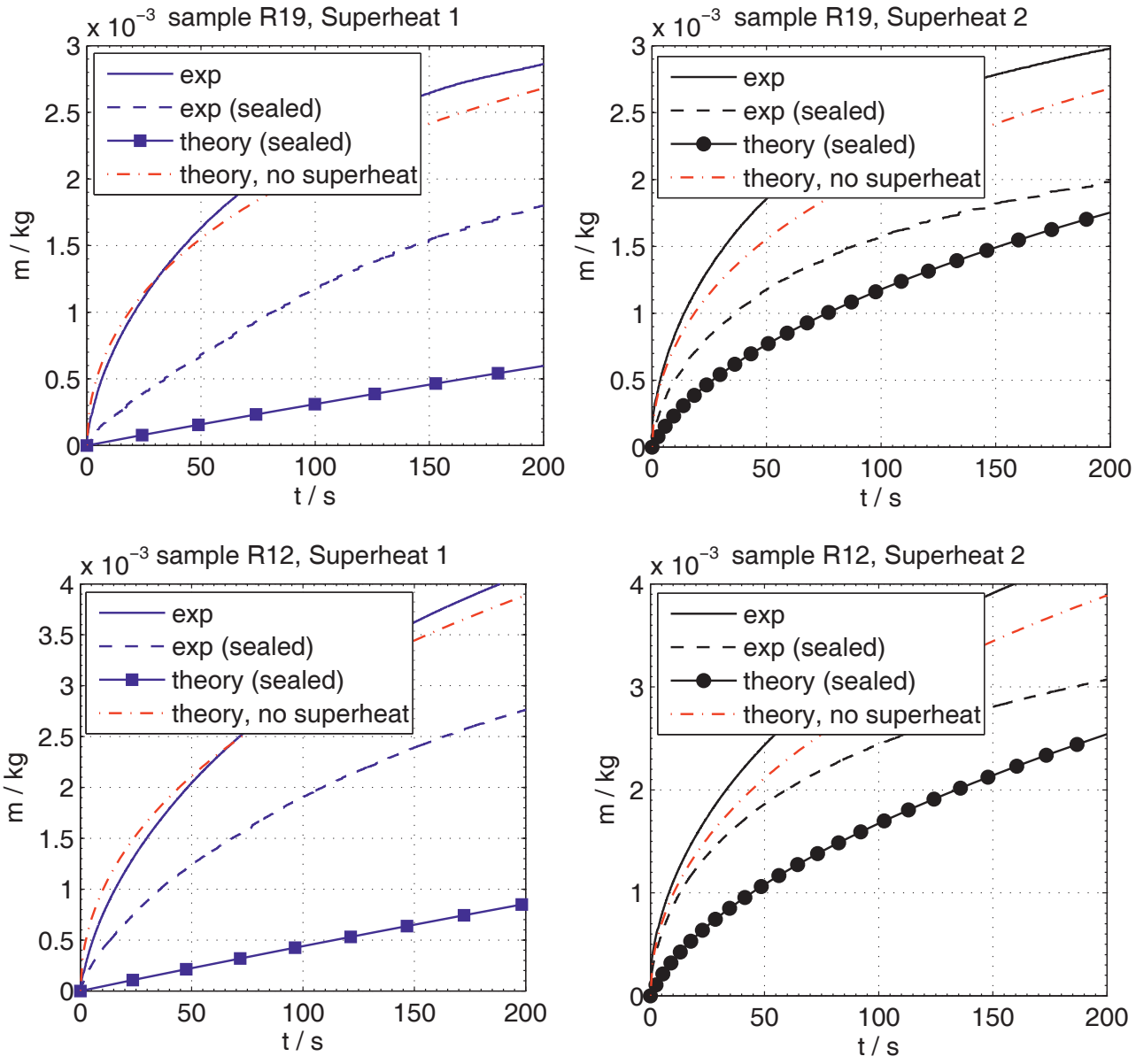

Figure 5.7: The mass of the imbibed liquid nitrogen during wicking into the sealed and not-sealed superheated porous samples R19 and R12. The imbibition rates greatly decrease due to the resistance of the vapor blocked in the sealed porous structure. The theoretical prediction for wicking into the sealed and not-sealed superheated porous samples at Superheat 1 and 2 was performed via Eqs. 3.48 and 3.11, respectively. The theoretical prediction for the isothermal case (no sample superheat) at saturation temperature of liquid nitrogen was performed with the Lucas-Washburn equation with gravity effects (Eq. 2.95).

33.3 % and 29.3 %, respectively. Such a result could be explained by an impact of the vapor created due to the heat transfer between superheated porous structure and liquid nitrogen. As

discussed in section 5.4.2, the vapor is partly blocked inside the porous structure due to the sealing and can escape only through the sample top. Thus, it creates an additional pressure above the liquid rising in pores that counteracts the wicking front propagation and causes the reduction of the imbibition rate.

Nevertheless, the relative decrease of the wicking rate caused by the sample sealing differs only slightly in the Superheat 1 and 2 cases. Due to higher initial sample superheat more vapor is produced in the beginning of the wicking process in the Superheat 1 case. This vapor, however, cools down the superheated solid structure above the wicking front, which further could lead to the production of the reduced amount of vapor. Thus, initially high sample superheat applied to the sealed porous structures does not necessarily cause stronger reduction of the imbibition rate compared to the results at lower sample superheat. This is in conformity with the experiment results, see Fig. 5.7. The heat transfer between the solid structure and large amount of the newly created vapor may lead to a great decrease of the sample temperature. The sample temperature decrease due to the heat transfer of the superheated solid structure and newly created vapor has been also discussed in section 5.4.2.

A theoretical prediction was performed using the macroscopic model described in section 3.2.1 (Eq. 3.48). The wicking height was recalculated into the wicking mass using Eq. 4.5. In addition, a theoretical prediction for the isothermal case (no sample superheat) at saturation temperature of liquid nitrogen was performed with the Lucas-Washburn equation with gravity effects (Eq. 2.95). The solution of Eq. 2.95 was given as Eq. 3.12. The parameters of Eqs. 3.48 and 3.12 were computed using thermophysical properties of nitrogen at saturation temperature and of borosilicate glass 3.3 given in Tables 4.6 and 4.1, respectively. The sample geometrical characteristics and macroscopic parameters were taken as given in Tables 4.2 and 4.4. The sample temperature at the moment before the wicking start obtained from the measurements with the sample R12T was used for calculations. In order to describe the temperature dependence of the specific heat capacity of borosilicate glass, a polynomial equation deduced by Schnelle et al. [143] was used. It is given as Eq. 4.6 in section 4.4.3. The calculated parameters are summarized in Table 5.2.

The values of the parameters ϵ, b and c are identical to the corresponding values presented in Table 4.8. This is due to the same porous structures and the same liquid used in the experiments. The parameters n_1 and n_2 include sample temperature and thermophysical properties of the solid, see Table 3.1. Their physical meaning has been discussed in section 4.4.3. n_1 and n_2 presented in Table 5.2 vary from the corresponding values listed in Table 4.8. As described in section 5.4.2, the sample sealing influenced the heat transfer between the solid structure and

Table 5.2: List of the parameters of Eq. 3.48 and 3.12.

Sample	ϵ (-)	b ($\mathrm{s\,m^{-2}}$) 10^4	c ($\mathrm{m^{-1}}$)	n_1 (-)	n_2 ($\mathrm{m^{-1}}$)	ρ_F^* (-) 10^{-3}	μ_F^* (-) 10^{-2}
Superheat 1							
R19 sealed	1.50	4.70	8.76	0.33	2.80	5.72	3.39
R12 sealed	1.27	5.38	5.47	0.33	2.80	5.72	3.39
Superheat 2							
R19 sealed	1.50	4.70	8.76	0.029	2.45	5.72	3.39
R12 sealed	1.27	5.38	5.47	0.027	2.52	5.72	3.39

the surrounding vapor in the cryostat, and led to slightly higher sample temperatures of the sealed samples at the wicking start. This explains slightly larger values of n_1 and n_2 for the experiments with the sealed samples. The parameters ρ_F^* and μ_F^* refer to the ratios of densities and dynamic viscosities of vapor and liquid nitrogen, respectively, see section 3.2.1.

The theoretical prediction via Eq. 3.48 underestimates the imbibition rate. The differences between the experiment data and the model prediction are larger at high sample superheat (Superheat 1). This can be explained by the fact that the theoretical model does not account for the sample temperature decrease during the imbibition. Therefore, it overestimates the amount of the vapor created at the wicking front that resists the liquid rise. Meanwhile, it was shown that the heat exchange between the superheated solid structure and the newly created cold vapor (as well as the heat conduction in solid) greatly reduces the sample temperature, see section 5.4.2. In addition, the assumptions made for the heat transfer at the vicinity of the liquid-vapor interface greatly simplified the description of the process, see section 4.4.3. Nevertheless, at low sample superheat (Superheat 2) the model provides a better agreement with the experiment results than the prediction for the isothermal case (no sample superheat) performed via the Lucas-Washburn equation.

5.4.4 Dimensionless analysis

The approach described in section 3.2.2 was used to non-dimensionalize the results. The wicking height and time were computed from the experiment data in dimensionless form using Eqs. 3.26 and 3.27, respectively.

Fig. 5.8 shows the dimensionless results for the wicking experiments with liquid nitrogen and the sealed and not-sealed samples R19 and R12 at Superheat 1 and 2 cases. The theoretical prediction for the wicking into the sealed samples was performed via Eq. 3.56. The values of the dimensionless parameters and numbers for the theoretical prediction are summarized in Table 5.3. Here the Bond number was computed using the experimentally determined static pore radius R_s as the characteristic length for each porous structure. In addition, the theoretical prediction for the case of no samples superheat performed via the dimensionless Lucas-Washburn equation with gravity effects (Eq. 3.25) is shown on each subplot of Fig. 5.8. As discussed for the dimensional form in section 5.4.3, the model prediction underestimates the experiment results. However, it demonstrates a better agreement for low Superheat 1 than the dimensionless Lucas-Washburn equation. It should be noted that the theoretical prediction given on Fig. 5.8 for the sealed superheated samples is only valid for $h^* \leqslant L^*$. As discussed in section 3.2.1, the dimensionless parameter L^* indicates which part of the maximum wicking height h_{eq} (or $h^* = 1$) can be achieved at the given sample height L (for $L < h_{eq}$). In comparison to the theoretical prediction for the not-sealed samples given in section 3.1.2, in this model the parameter L^* is included into the final equation and, thus, influences the predicted values. The sample height L used for the computations corresponds to the height of the experimental samples and was limited by the setup hardware. It resulted in $L^* < 1$. Thus, for $h^* > L^*$ Eq. 2.34 does not provide physical results and at some combination of the equation parameters may even diverge. The latter is presented on Fig. 5.8 for the sample R12 at $h^* > L^*$ (lower subplots).

Table 5.3: List of the dimensionless parameters of Eq. 3.56 and relevant dimensionless numbers.

Sample	ϵ	Ω_1	Ω_2	L^*	ρ_F^*	μ_F^*	Π^*	Bo	Ja_1	Ja_2
		10^{-1}	10^{-1}		10^{-3}	10^{-2}	10^{2}	10^{-4}	10^{-1}	10^{-1}
Superheat 1										
R19 sealed	1.50	3.31	3.19	0.70	5.72	3.39	1.02	3.45	5.47	3.69
R12 sealed	1.28	3.31	5.11	0.44	5.72	3.39	0.73	1.35	5.47	3.69
Superheat 2										
R19 sealed	1.50	0.29	2.80	0.70	5.72	3.39	1.02	3.45	0.68	4.57
R12 sealed	1.28	0.27	4.61	0.44	5.72	3.39	0.73	1.35	0.63	4.69

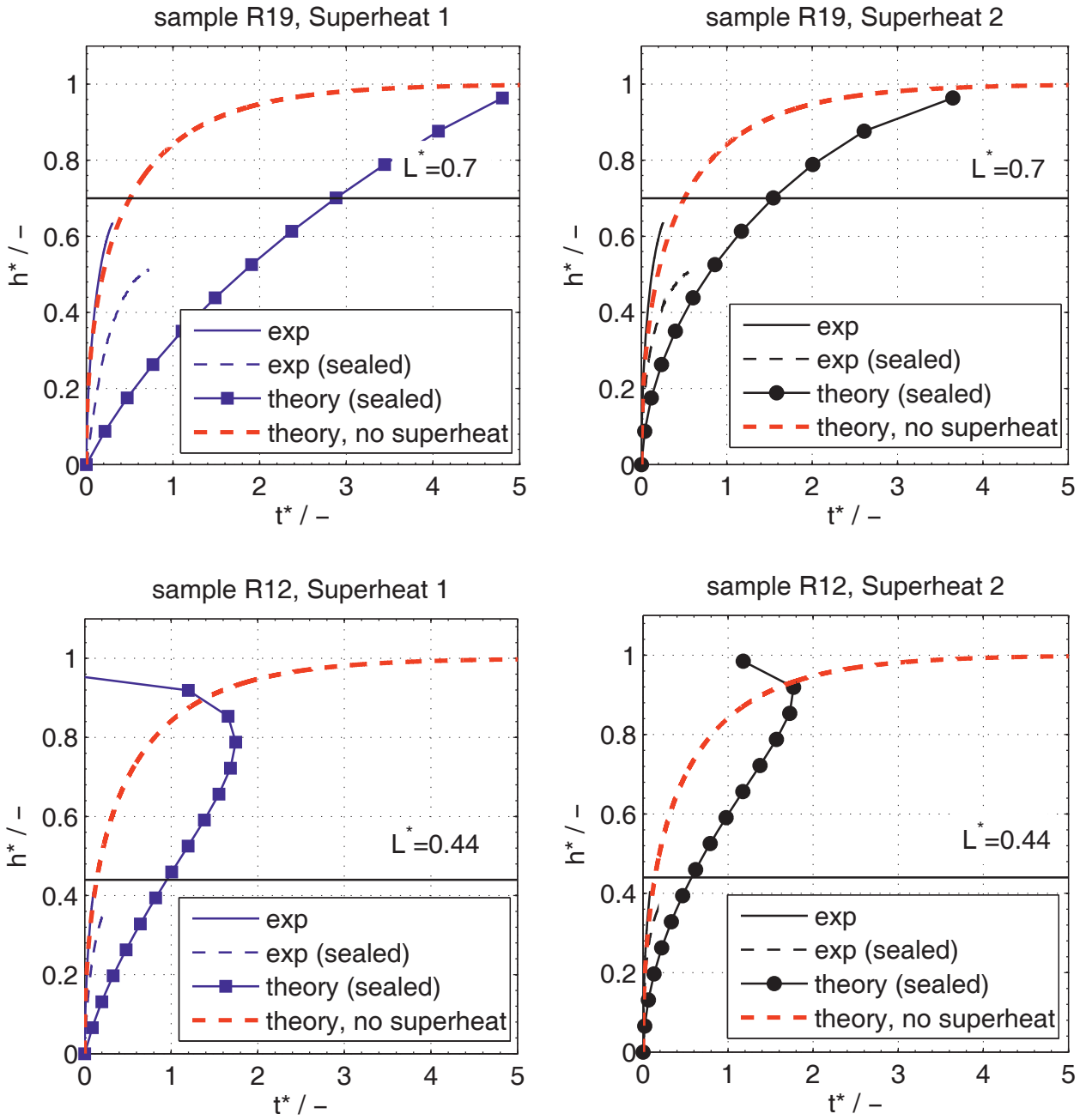

Figure 5.8: The dimensionless wicking height vs. the dimensionless time for the wicking of liquid nitrogen into the porous samples R19 and R12 at Superheat 1 and 2. The theoretical prediction for the sealed superheated samples was performed via Eq. 3.56 and is only valid for $h^* \leqslant L^*$. The theoretical prediction for the case of no samples superheat was performed via the dimensionless Lucas-Washburn equation with gravity effects (Eq. 3.25).

The dimensionless theoretical model predicts the wicking process depending on the values of the parameters ϵ, Ω_1, Ω_2, L^*, ρ_F^* and μ_F^*. The parameters Ω_1 and Ω_2 were given in Eqs. 3.29 and 3.32, respectively. Ω_1 and Ω_2 increase, correspondingly, with the initial temperature at the bottom of the sample T_0 and initial temperature gradient along the sample height $\triangle T_S/L$. Fig. 5.9(a-b) shows that the dimensionless wicking height achieves its maximum value L^* at larger t^* for higher Ω_1 and Ω_2. Thus, the increase of Ω_1 and Ω_2 results in the decrease of the dimensionless wicking rate. In section 4.4.5 the influence of Ω_1 and Ω_2 on the theoretical prediction given by the model not accounting for the vapor flow was studied. In that case the increase of these parameters also resulted in a decrease of the dimensionless wicking rate, however, not that greatly as it occurs here.

The parameter ϵ is dependent only on the porosity of the sample ϕ (larger ϵ at smaller ϕ), see Table 3.1. As for the results described in section 4.4.5, the increase of ϵ reduces the dimensionless wicking rate. The dimensionless wicking height h^* achieves L^* at larger t^* for the samples of larger ϵ, see Fig. 5.9(c). The samples of smaller porosity ϕ (larger ϵ) contain more superheated solid material available for the heat transfer. Thus, more liquid evaporates (liquid loss) and more vapor is produced and partly blocked in the pores (resistance to the liquid rise). This causes the decrease of the wicking rate. In addition, smaller ϕ of the samples with same static pore radius R_S supposes lower permeabilty K that also results in smaller wicking rates.

Fig. 5.9(d) shows that the dimensionless wicking rate decreases at larger values of the parameter L^*. The impact of the vapor created above the wicking front and resisting the liquid rise is more significant for the samples of larger height L (larger L^*). This is in conformity with the results presented on Fig. 5.9(d). Here, however, one should take into account that for $L^* < 1$ the maximum dimensionless wicking height is $h^* = L^*$, while for $L^* \geqslant 1$ it is $h^* = 1$.

The parameters ρ_F^* and μ_F^* given in Eqs. 3.42 and 3.43 are dependent on the thermophysical properties of liquid and vapor of the experimental fluid at saturation temperature. The choice of the fluid influences also the value of the parameter Ω_1, which includes the temperature of liquid at saturation T_L, see Eq. 3.29.

The dimensionless capillary (Ca) and Reynolds (Re) numbers change during the imbibition process due to the change of the interstitial velocity of liquid u_L. Ca and Re numbers were computed substituting the thermophysical properties of liquid nitrogen and u_L predicted via Eq. 3.44 into Eqs. 4.7 and 4.8. Since the model significantly underestimates the results for high Superheat 1 case, the computation of Ca and Re numbers was performed only for the low Superheat 2. Fig. 5.10 shows the change of Ca and Re numbers with an increase of the dimensionless wicking height for the samples R19 and R12. As it was also demonstrated for the

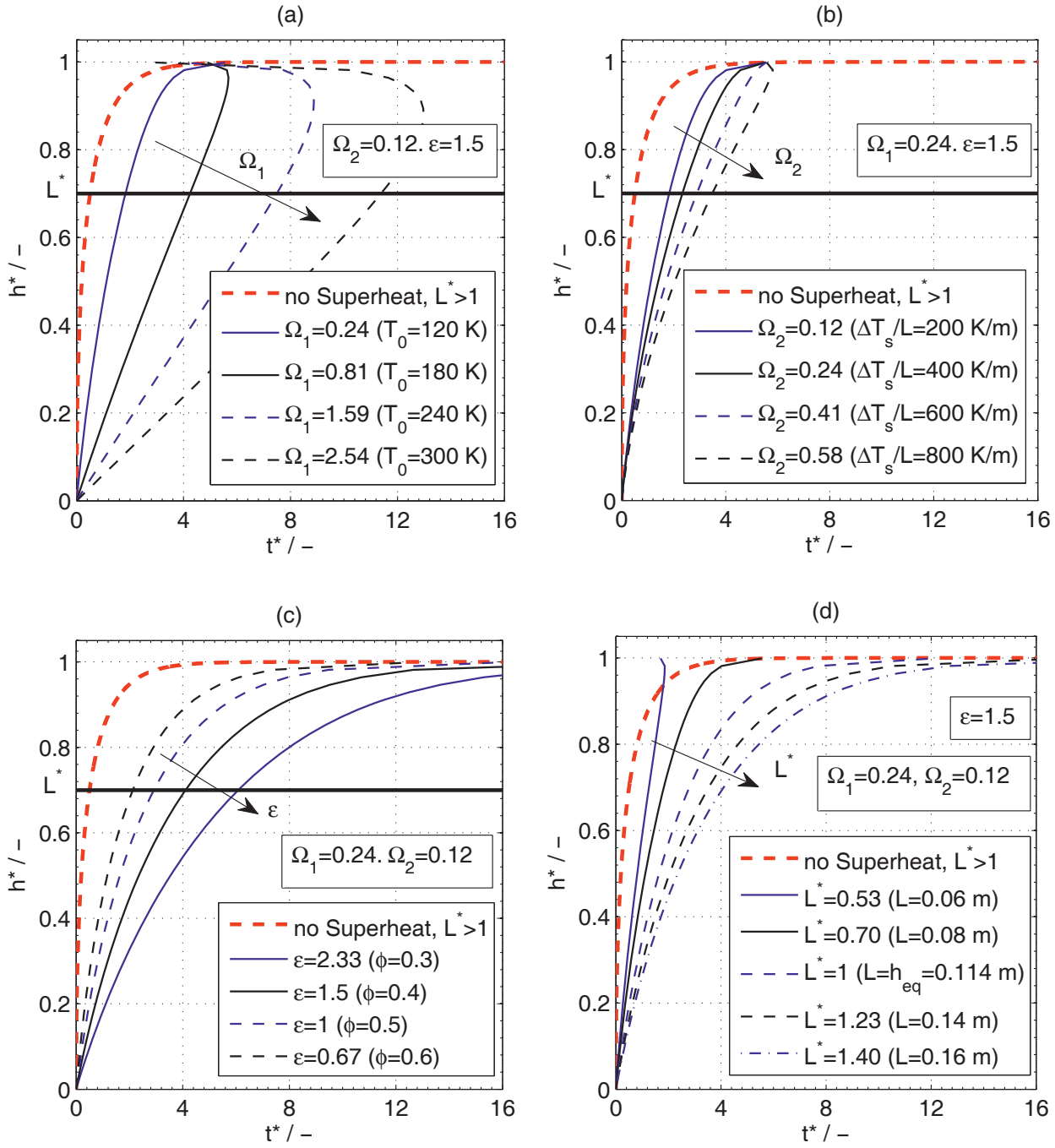

Figure 5.9: The dimensionless wicking height vs. the dimensionless time predicted via Eq. 3.56 at various parameters ϵ, Ω_1, Ω_2 and L^*. For the computations the thermophysical properties of liquid nitrogen and the macroscopic parameters of the sample R19 (by default) were used. For the subplots (a), (b) and (c) the sample height L was taken as $80{\cdot}10^{-3}$ m ($L^* = 0.7$) and the predicted curves are valid only for $h^* \leqslant L^*$. For the subplot (d) L^* is varied and the predicted curves are valid only for $h^* \leqslant L^*$ when $L^* \leqslant 1$ and for $h^* \leqslant 1$ when $L^* > 1$. The theoretical prediction for the case of no samples superheat was performed via the dimensionless Lucas-Washburn equation with gravity effects (Eq. 3.25).

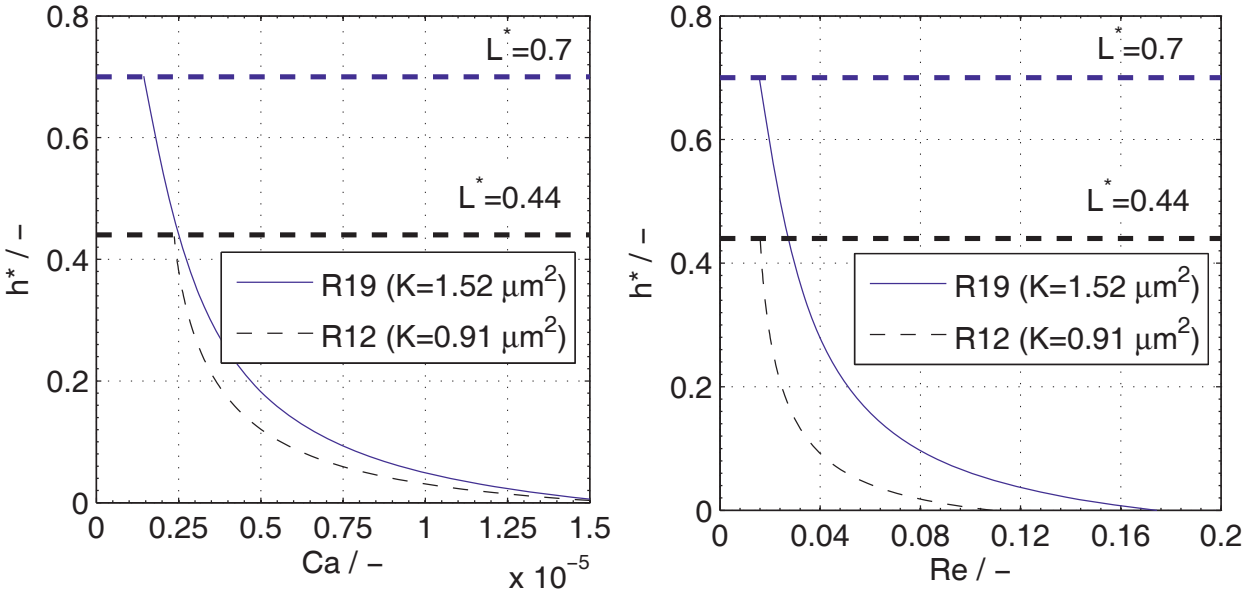

Figure 5.10: The dimensionless wicking height vs. the capillary (Ca) and Reynolds (Re) numbers during the imbibition process into the samples R19 and R12 at Superheat 2. Ca and Re numbers were computed using the thermophysical properties of liquid nitrogen and the interstitial velocity of liquid u_{L} predicted via Eq. 3.44. Ca and Re numbers are larger at the beginning of the imbibition ($h^* \to 0$) and decrease while the wicking front approaches the maximum dimensionless wicking height ($h^* = L^*$). For the same h^* the samples of higher permeability K demonstrate higher u_{L} and, therefore, larger Ca and Re numbers.

model not accounting for the vapor flow (see section 4.4.5), u_{L} and, correspondingly, Ca and Re numbers are larger at the beginning of the imbibition ($h^* \to 0$). However, they decrease while the wicking front approaches the maximum dimensionless wicking height ($h^* = L^*$). Moreover, for the same h^* the sample of higher permeability K (sample R12) demonstrate higher u_{L} and, therefore, larger Ca and Re numbers, see Fig. 5.10. The values of Ca and Re numbers obtained in this study are typical for the capillary rise in porous media. The values of Re number indicate the laminar flow regime.

5.5 Summary

Vertical wicking of liquid nitrogen at saturation temperature into sealed superheated porous structures was studied. Experiments were performed in a one-species system under pre-defined non-isothermal conditions with the porous samples used in the experiment described in chapter

4. The sample sealing was applied to enhance and study an influence on the imbibition rate of the vapor flow created due to the heat transfer at the wicking front.

For the experiments with no sample superheat the sealing showed no influence on the wicking rates of the samples. Two cryo-wicking experiments ensuring different sample superheats (Superheat 1 and 2) were performed with each sample. The experiment environment was analyzed using the temperature evolution of the bulk vapor and liquid nitrogen. The temperature conditions were found to be comparable with the temperature conditions in the cryo-wicking experiments with the not-sealed samples.

Simultaneous sample weight and temperature measurements were performed during the imbibition. The results reveal that the local temperature of solid structure decreases down to the saturation temperature of nitrogen T_{L} before it gets saturated with the liquid. Such a result was not observed for the same samples with no sealing. Therefore, the temperature decrease could be stipulated by the impact of the vapor created above the wicking front and pushed along the sample height due to the sample sealing. The minimum sample temperature of 77.5 K corresponding to the temperature of nitrogen at saturation was observed.

The impact of the sample sealing on the imbibition rate of the sealed samples was investigated at various sample superheat and structural characteristics. The mass of the imbibed liquid nitrogen was determined measuring a sample weight increase during the imbibition. The results demonstrated a significant decrease of the imbibition rates for the sealed samples compared to the same samples with no sealing. This could be also explained by the impact of the vapor created due to the heat transfer between the superheated solid and cold liquid. The vapor creates an additional pressure above the liquid rising in pores and counteracts the wicking front propagation. However, the relative decrease of the wicking rate caused by the sample sealing varied only slightly in the Superheat 1 and 2 cases. High sample superheat does not necessarily cause stronger reduction of the wicking rate compared to the results at low sample superheat. The sample temperature above the wicking front may significantly decrease due to the heat transfer between the superheated solid and the cold vapor pushed along the sample height. The theoretical prediction of wicking was performed via the macroscopic model described in section 3.2.1. The model significantly underestimates the imbibition rate at high sample superheat (Superheat 1) due to the fact that it does not account for the sample temperature decrease during the imbibition. Nevertheless, at low sample superheat (Superheat 2) the model provides a better agreement with the experiment data than the prediction for the isothermal case (no sample superheat) performed via the Lucas-Washburn equation.

The wicking results were studied in dimensionless form using the approach described in section 3.2.2. The increase of the dimensionless wicking height (h^*) with the dimensionless time (t^*) was investigated varying the model parameters ϵ, Ω_1, Ω_1, and L^*. These dimensionless parameters reflect the sample superheat, porous structure peculiarities, and the sample height. The results revealed that the increase of ϵ, Ω_1, Ω_1, and L^* leads to the decrease of the dimensionless wicking rate. The capillary (Ca) and Reynolds (Re) numbers were computed using the predicted interstitial velocity of liquid u_{L} for the case of low sample superheat (Superheat 2). Ca and Re numbers decrease when the dimensionless wicking front h^* approaches its maximum.

Chapter 6

Experimental investigation of wicking into porous polymer-derived ceramic monoliths

The following chapter is based on the publication "Wicking into porous polymer-derived ceramic monoliths fabricated by freeze-casting"[1] by Y. Grebenyuk et al. [160].
Wicking process was used to investigate capillary transport abilities of porous polymer-derived ceramic monoliths fabricated by freeze-casting. The monoliths were produced by H.X. Zhang in the Advanced Ceramics Group of the University of Bremen in the framework of the cooperation in the Research Training Group "MIMENIMA".

6.1 Materials

6.1.1 Preparation of porous ceramics

The porous monolith was prepared according to the method by Zhang et al. [157] with minor modification. The process scheme is shown in Fig. 6.1. The H44 (methyl phenyl polysiloxane) derived filler loading was 30% in weight. Silica sol worked as a binder as well as a water source. Cylindrical aluminum molds with a height of 60 mm, an inner diameter of 30 mm and a wall thickness of 2 mm were put on the bottom of the freezer at -80 °C or at -150 °C for 1 h. The freezing temperature was varied to obtain structures of different pore size distributions. After

[1]Reprinted from Journal of the European Ceramic Society, Vol. 37, Y. Grebenyuk, H.X. Zhang, M. Wilhelm, K. Rezwan, M.E. Dreyer, Wicking into porous polymer-derived ceramic monoliths fabricated by freeze-casting, Pages No. 1993-2000, Copyright (2017), with permission from Elsevier.

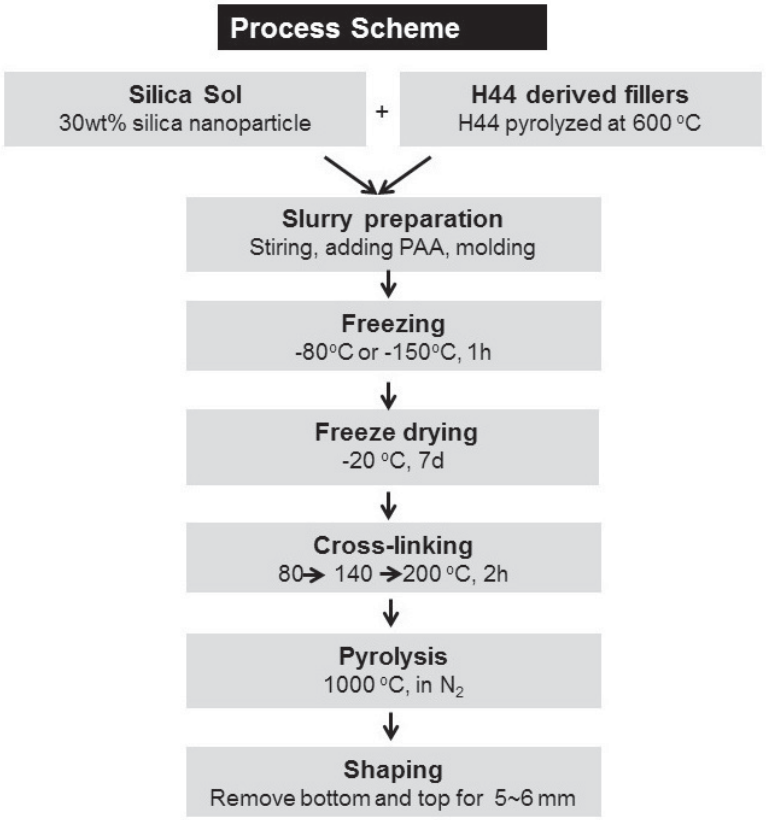

Figure 6.1: Preparation of the monolith by freeze casting method and shaping. Figure modified from [157]. H44 is referred to methyl phenyl polysiloxane.

the pyrolysis, 5-6 mm of the bottom and the top part of the monoliths were cut off to get a symmetric porous structure required for macroscopic modelling of the imbibition.
The details of the fabrication process can be found in [160].
In the following, the samples prepared at the freezing temperature of -80 °C are referred as to 80-1 and 80-2, while the samples prepared at -150 °C as to 150-1 and 150-2. The geometrical characteristics of the samples are summarized in Table 6.1.

6.1.2 Characterization

Methods

The particle size and pore morphology of the samples was analyzed via scanning electron microscopy (SEM, Camscan Series 2, Obducat CamScan Ltd.). The samples were sputtered with gold (K550, Emitech, Judges Scientific plc.) before the measurements. Mercury intrusion porosimetry (Pascal 140/440, POROTEC GmbH) was used to determine the macroporosities. For the pore size calculation, a cylindrical pore model was chosen. The average diameter was

Table 6.1: Geometrical characteristics of the porous samples. D and L are referred to as the overall diameter and height of the cylindrical monolith, respectively. d is referred to as the diameter of the cone area with upward oriented pores that is visible from the bottom of the monolith.

Sample	D (m) 10^{-3}	d (m) 10^{-3}	d/D (-)	L (m) 10^{-3}
80-1	30	21	0.70	42
80-2	30	19	0.63	42
150-1	30	21	0.70	42
150-2	30	15	0.50	42

Table 6.2: Macroscopic parameters of the porous samples. R_{av} and ϕ_{merc} are referred to as the average pore radius and the open porosity determined via the mercury intrusion porosimetry. The values of the open porosity ϕ and permeability $K_{\text{-z}}$ and $K_{\text{+z}}$ determined from imbibition experiments at $+z$ and $-z$ sample orientations are shown with a standard deviation for four test runs.

Sample	R_{av} (m) 10^{-6}	ϕ_{merc} (-)	ϕ (-)	$K_{\text{-z}}$ (m^2) 10^{-14}	$K_{\text{+z}}$ (m^2) 10^{-14}	$K_{\text{-z}}/K_{\text{+z}}$ (-)
80-1	8.35	0.532	0.466 ± 0.002	4.43 ± 0.10	3.65 ± 0.12	1.21
80-2	8.35	0.532	0.471 ± 0.003	5.00 ± 0.22	4.48 ± 0.12	1.12
150-1	1.57	0.548	0.516 ± 0.007	0.265 ± 0.003	0.177 ± 0.002	1.49
150-2	1.57	0.548	0.516 ± 0.005	0.368 ± 0.007	0.336 ± 0.002	1.10

calculated based on the derivative principle. The porosity range within which the porosimeter works was subdivided into 50 intervals, which determined the calculation sensitivity. The pore range to perform the measurement of the average radius was set from 0 to $200{\cdot}10^{-6}$ m. The derivative of the volume of mercury penetrated (namely the pores volume) versus the variation of the diameter for each of the selected intervals was performed by the instrument software. The interval with maximum penetration of mercury was selected, namely where the largest

volume of pores was located, and here the average radius was calculated within the selected range, see Table 6.2.

Macroporous structure

The macroporous structure of the monolith was determined by the temperature gradient during the freezing process. The freeze rate was controlled by applying different freezing temperatures. Water forms lamellar ice, which results in lamellar pores inside the ceramics after ice sublimation, resulting in an anisotropic porous structure of the material. Due to the cylindrical aluminum mold, the lamellar ice will grow from metal surface to the inner part. At the bottom part of the monolith, the ice grew upwards, forming a cone structure, which also happened at the top. However, the thermal conductivity of the solid in the freezing slurry was much lower than aluminum, therefore, the temperature gradient from the radial direction dominated in the

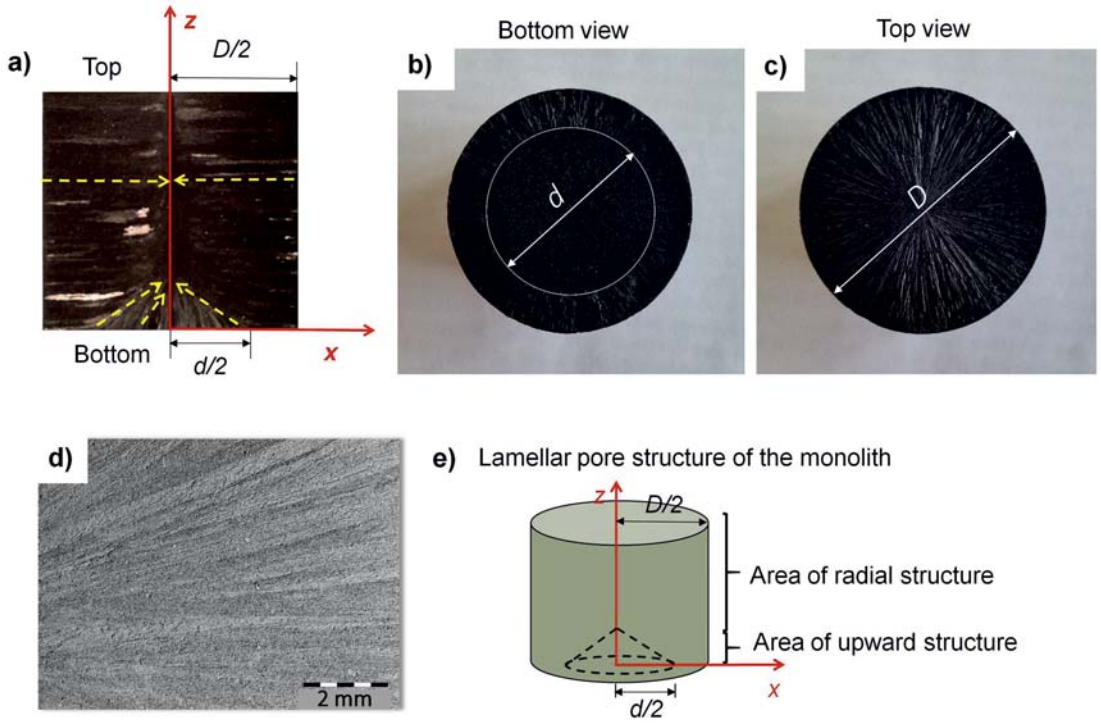

Figure 6.2: a) The side view of the longitudinal cross-section of the monolith. The yellow dash lines indicated the directions of the lamellar pores; b) the bottom view of the monolith; c) the top view of the monolith; d) the SEM of the transverse cross-section at the top; and e) the scheme of the anisotropic structure. D is referred as to the overall diameter of the cylindrical monolith and d is referred as to the diameter of the cone area with upward oriented pores that is visible from the bottom of the monolith.

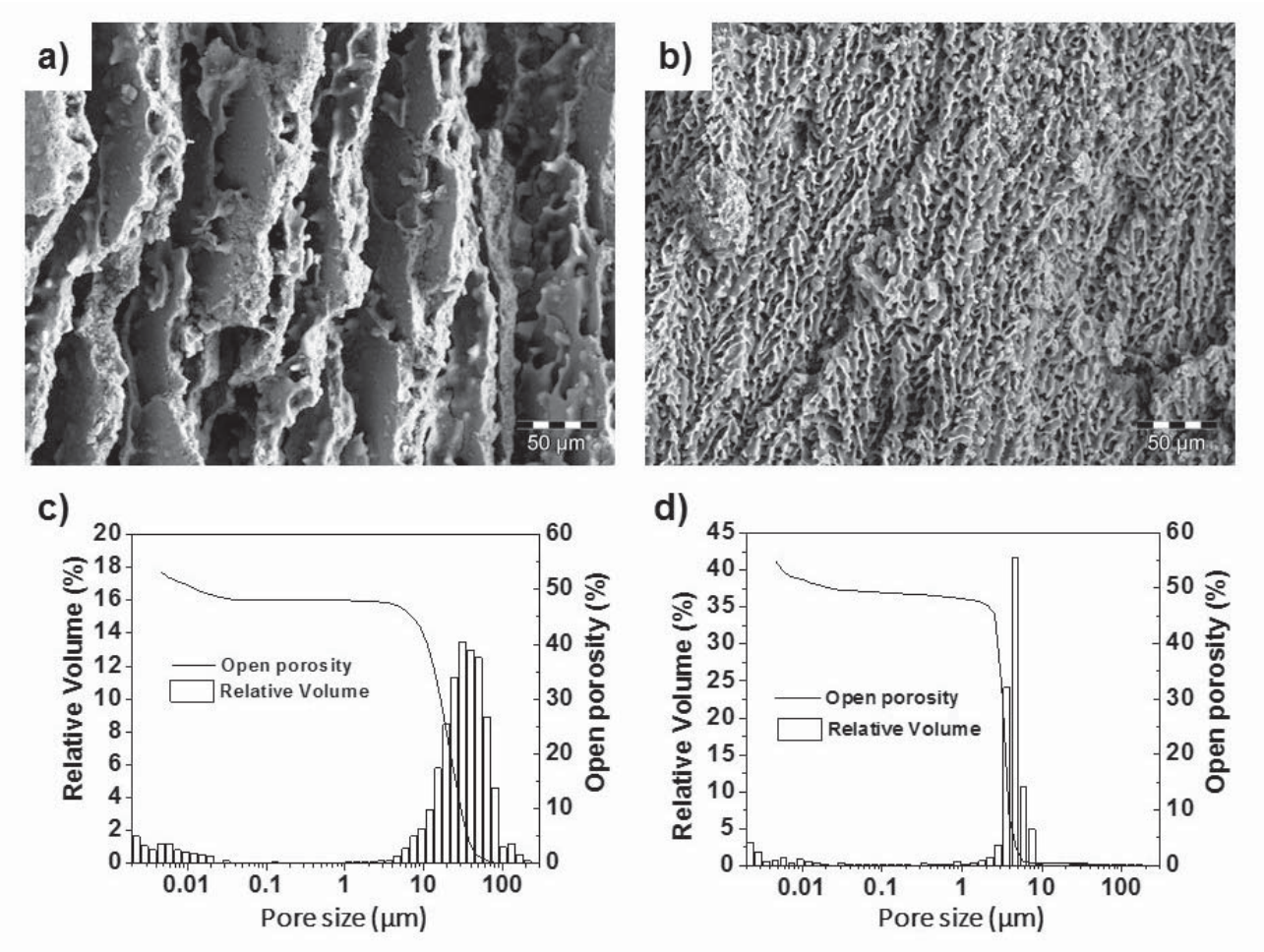

Figure 6.3: SEM images of pyrolyzed monoliths with the cross-section perpendicular to the monolith axis a-b) frozen at -80 °C and -150 °C, respectively. c-d) Pore size distribution versus relative pore volume and open porosity curves obtained from the mercury intrusion porosimetry of pyrolyzed samples.

monolith. In the middle part of the monolith, only radial lamellar pores were formed. The top and bottom were partially removed to get a cylindrical symmetric monolith. The upward lamellar structure at the bottom was preserved and the diameter of this area is d, which can be altered by cutting, see Table 6.1. As seen from Fig. 6.2(a), the parallel lines indicate the lamellar pores parallel to the radial direction, which can be partly seen in Fig. 6.2(d).

From the SEM, the lamellar pores, defined as the distances between the lamellae, were along radial direction (x axis in Fig. 6.2(a)) and show distances of around $20{\cdot}10^{-6}$ m to $50{\cdot}10^{-6}$ m and less than $1{\cdot}10^{-5}$ m for the samples frozen at -80 °C and -150 °C, respectively. The bridges between two adjacent lamellae were created by dendrites growth of ice. Depending on the freeze rate, the lamellar aspect ratios can be manipulated, as can be seen from Fig.

6.3(a-b). The mercury intrusion porosimetry in Fig. 6.3(c-d) showed that the monolith frozen at -80 °C had a porosity of 53.2% and pore size range of mainly $1{\cdot}10^{-5}$ m to $1{\cdot}10^{-4}$ m with relatively wide pore size distribution. The monolith frozen at -150 °C has an open porosity of 54.8%, a pore size of mainly $3{\cdot}10^{-6}$ m to $8{\cdot}10^{-6}$ m with a narrow pore size distribution. Samples prepared at two different freezing temperatures have similar cylindrical symmetric structures, which were formed by the similar temperature gradient direction, controlled by the mold. However, lower freeze temperature resulted in smaller pore sizes, which could influence the wicking performance.

6.2 Wicking experiment

Fig. 6.4 shows a schematic image of the setup for the wicking experiments. The weight of a porous sample was measured using an electronic high precision balance (LA 310S-0CE, Sartorius) with an accuracy of ±0.0001 g. The balance was fixed on a height-adjustable platform driven by two stepper motors (VRDM566/50, Berger Lahr/ Schneider Electric) with a velocity of 0.38 mm/s. The sample was placed in a closed vessel of 0.095 m diameter partly filled with FC-72 liquid supplied by 3M Fluorinet™. Some thermophysical properties of FC-72 liquid are listed in Table 4.3. The FC-72 test liquid showed perfect wetting characteristics with a variety

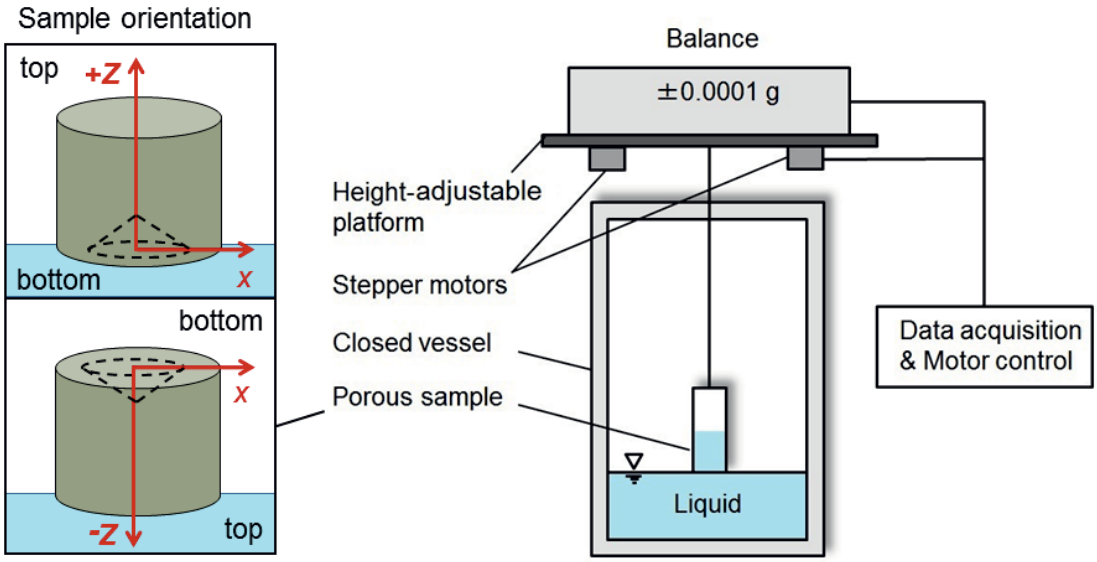

Figure 6.4: The schematic image of the setup for wicking experiments. Each sample was tested using "bottom to top" and "top to bottom" orientation to the liquid surface. These orientations are referred as to $+z$ and $-z$, respectively. Figure modified from [34].

of materials [36, 126, 38, 39, 40]. The contact angle with regard to the experimental samples was assumed to be zero. The tests were performed at room temperature and normal pressure. In order to initiate the wicking, a vertically oriented porous sample was submerged into the bulk liquid by a depth of approximately 3 mm. The liquid imbibed into the unsaturated (not submerged) part of the sample. The imbibition caused a sample weight increase that was recorded with a sampling rate of 20 Hz. A constant sample weight at the end of the imbibition indicated complete saturation of the sample. To finish the experiment the sample was driven approximately 6 mm upwards and, thus, detached from the liquid surface.

To study the impact of the anisotropy on the wicking process each sample was tested using "bottom to top" and "top to bottom" orientation to the liquid surface, see Fig. 6.4. In the following, we refer to these orientations as to $+z$ and $-z$, respectively. Four test runs were performed for each sample and each sample orientation.

Some corrections of the weight measurements were required to account for buoyancy, the Wilhelmy effect and the liquid level decrease due to the imbibition of the liquid into the samples. The sample weight changes caused by the liquid level decrease due to wicking could be eliminated using geometrical characteristics of the samples and of the experimental vessel. However, the buoyancy force could not be calculated accurately due to the uncertainty in the determination of the submersion depth (± 1 mm). The Wilhelmy force estimates a contribution of the outer meniscus, formed at the sample perimeter, upon contact of the sample with the liquid surface [16, 140]. Nevertheless, for porous media the accurate determination of this force was not possible. Moreover, the sample weight changes due to buoyancy and the Wilhelmy effect are difficult to separate from the early wicking process. Therefore, the correction of the sample weight measurements was performed following an approach proposed by Grebenyuk and Dreyer [34]. The total contribution of buoyancy and the Wilhelmy effect could be estimated if the liquid level decrease was corrected or negligible. The final weight of the completely saturated but still partly submerged sample has been subtracted from the actual weight of the saturated sample. The total correction of the sample weight measurements for experimental samples was found to be up to 12%.

6.3 Results

6.3.1 Macroscopic parameters

The characterization of the capillary transport abilities of porous media required a knowledge of macroscopic parameters, such as the open porosity, the characteristic pore radius, and the permeability.

The open porosity of the structures was determined using the mercury intrusion porosimetry ϕ_{merc}, see section 6.1.2 and Table 6.2. Nevertheless, hardware limitations of the setup for the mercury intrusion porosimetry allowed to test only some sample cuts to obtain ϕ_{merc}. Therefore, this macroscopic parameter was also computed using the results of the weight measurements of dry samples and samples completely saturated with FC-72 liquid. Thus, the open porosity ϕ could be calculated using

$$\phi = \frac{V_{\text{void}}}{V_{\text{total}}} = \frac{m_{\text{L}}/\rho_{\text{L}}}{V_{\text{total}}}, \tag{6.1}$$

where V_{total} is the total volume of a sample, V_{void} is the void volume of a sample that includes only the volume of interconnected pores, and ρ_{L} is the density of the liquid. The results for each sample are summarized in Table 6.2. The values of ϕ_{merc} and ϕ obtained using two different methods are in good agreement. However, for further calculations we used ϕ, which is a volume-averaged value of the open porosity determined for the whole structure. This is of importance for the macroscopic modeling of the wicking process.

In order to estimate the characteristic pore size of the structures we used the results of the mercury intrusion porosimetry, see section 6.1.2. The average pore size was calculated in an interval with the largest volume of pores. The pore diameters of $16.7{\cdot}10^{-6}$ m and $3.14{\cdot}10^{-6}$ m were obtained for the structures prepared at the freezing temperature of -80 °C and -150 °C, respectively. The corresponding values of the average pore radii are summarized in Table 6.2.

The characterization of the ability of a porous structure to conduct a flow through it is of importance for capillary transport processes. A macroscopic parameter that quantifies such a property of a porous media is the permeability K that is commonly defined via Darcy's law [159, 158], see section 2.5.5. Due to the anisotropy of our samples with respect to vertical wicking, this parameter was examined for both sample orientation, $+z$ and $-z$. In order to determine the permeability, wicking experiments were performed and the method proposed by Fries and Dreyer [126] was applied. The flow through porous media was implied analogous to the flow through a bundle of capillary tubes and the macroscopic approach was employed for the description of the imbibition, see 2.6.1. For smaller times the capillary rise is dominated

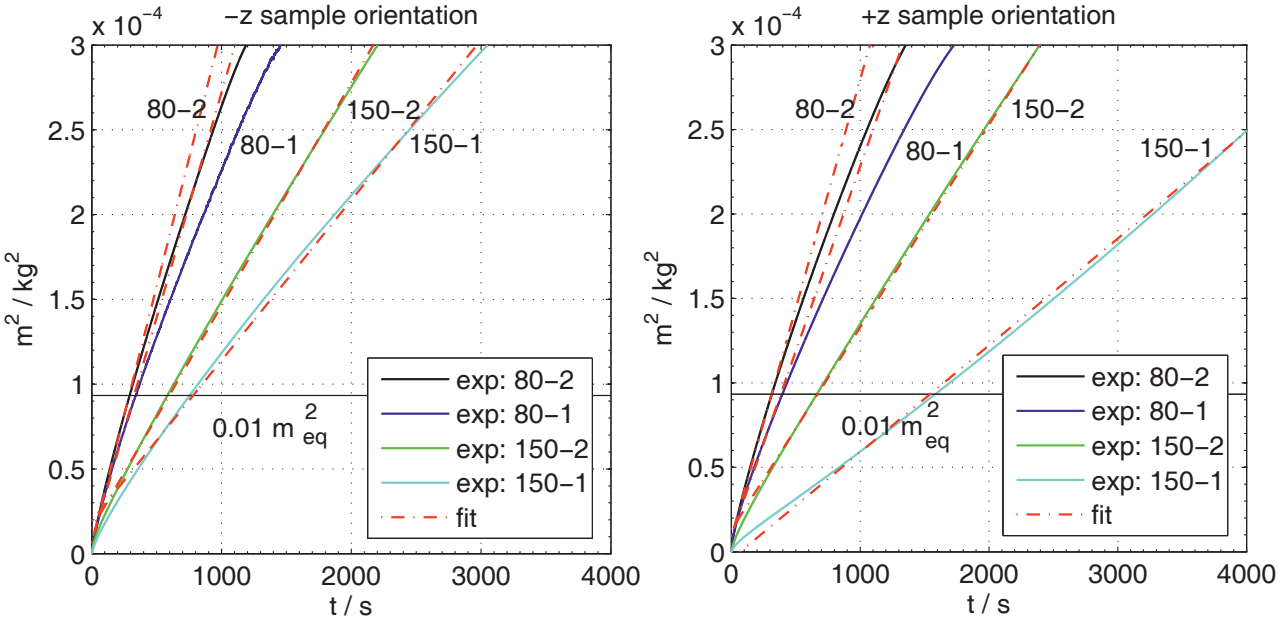

Figure 6.5: The squared mass of the imbibed FC-72 liquid into the samples 80-1, 80-2, 150-1 and 150-2 versus time. The imbibition rates differs for the samples and for $+z$ and $-z$ orientations of each sample. Eq. 6.4 was fitted to experimental data up 10% of the equilibrium wicking height for each sample. The equilibrium wicking height corresponds to the equilibrium wicking mass. The horizontal solid line with the inscription 0.01 m_{eq}^2 is referred to the squared value of 10 % of the equilibrium wicking mass for the samples 80-1 and 80-2. For the samples 150-1 and 150-2 the equilibrium wicking height exceeded the sample height, therefore, Eq. 6.4 was fitted to the whole range of the experimental data.

by inertia and viscous forces [115]. However, for porous media the inertia impact is negligible [93, 117, 101]. A viscous-dominated stage of the imbibition into porous media is described by the Lucas-Washburn equation [93, 94] (see Eq. 2.96)

$$\frac{2\sigma\cos\theta}{R_{\mathrm{s}}} = \frac{\phi\mu_{\mathrm{L}}\dot{h}h}{K}, \tag{6.2}$$

where h is the wicking height, σ and μ_{L} are the surface tension and the dynamic viscosity of liquid, respectively, θ is the contact angle and R_{s} is the static pore radius of a porous structure. The wicking height h can be recalculated into the mass of imbibed liquid using

$$m(t) = \rho_{\mathrm{L}}\phi A h(t), \tag{6.3}$$

where A is the cross-section area of a sample. Rearranging Eq. 6.2 and 6.3, one obtains

$$\frac{m^2}{t} = \frac{4\sigma\cos\theta\rho_{\mathrm{L}}^2 A^2\phi}{\mu_{\mathrm{L}}}\frac{K}{R_{\mathrm{s}}}. \tag{6.4}$$

The static pore radius R_s in Eq. 6.2 and 6.4 indicates the characteristic pore size of porous media determined using the wicking height h_{eq} at the equilibrium between the capillary and hydrostatic pressures [34, 126, 100]

$$\frac{2\sigma \cos\theta}{R_s} = \rho_L g h_{eq}, \tag{6.5}$$

where g is the gravity acceleration. The equilibrium height for the imbibition with the FC-72 liquid was estimated to be approximately 0.174 m and 0.923 m for the samples prepared at the freezing temperature of -80 °C and -150 °C, respectively. Due to the sample size limitation it was not possible to achieve such wicking heights experimentally. For further calculations we used the volume-weighted characteristic pore size R_{av} obtained via the mercury intrusion porosimetry.

Fig. 6.5 shows wicking results for the sample 80-1, 80-2, 150-1 and 150-2 in terms of the squared mass of the imbibed FC-72 liquid plotted versus time. The mass of the imbibed liquid was computed using the sample weight measurements during the imbibition and the dry sample weight measurements, and corrected in accordance with the argumentation provided in section 6.2. The samples demonstrated various imbibition rates, see Fig. 6.5. Moreover, the imbibition rates differed for -z and +z orientations of each sample that reflected the samples anisotropy in the axial direction.

According to Fries and Dreyer [126, 97], the influence of the hydrostatic pressure on wicking is negligible up to 10 % of the equilibrium wicking height. In this domain when accepting an error of 3.7 %, one might apply the Lucas-Washburn equation. This fraction of the equilibrium wicking height for the samples prepared at the freezing temperature of -80 °C was estimated to be 0.0174 m and recalculated into the equilibrium wicking mass m_{eq} using Eq. 6.3. The black horizontal solid line with the inscription 0.01 m_{eq}^2 is assigned to the squared value of 10 % of the equilibrium wicking mass on Fig. 6.5. Below this line the linear regression of the experimental data for the samples 80-1 and 80-2 had a constant slope and was fitted via Eq. 6.4. For the samples prepared at the freezing temperature of -150 °C the value related to 10 % of the equilibrium wicking height was estimated to be 0.0923 m. This exceeds the sample height on approximately 120 %, see Table 6.1. Hence, for these samples Eq. 6.4 was fitted to the whole range of the experimental data, see Fig. 6.5.

Using fitting via Eq. 6.4, the macroscopic parameters and geometrical characteristics from Tables 6.1 and 6.2, and the thermophysical properties of FC-72 liquid from Table 4.3, the permeabilities K_{-z} and K_{+z} for -z and +z sample orientations, respectively, were computed. The results are summarized in Table 6.2. The samples demonstrated lower permeability in

$+z$ direction, i.e. when they were oriented to the liquid surface with the cone structure of the upward oriented lamellar pores. This implies that the upward orientation of the lamellae contributed to forming porous structures of lower ability to conduct the liquid than the radial orientation. The decrease of the permeability here might be also stipulated by the influence of two temperature gradients at once at the bottom of the monolith during the fabrication process, resulting in smaller pore size. As shown in Table 6.2, the deviations between $K_{\text{-z}}$ and $K_{\text{+z}}$ were found to be from 10 % to 49 %. These values quantify the impact of the porous structure anisotropy on the capillary transport characteristics of the samples. Higher permeability was revealed for the samples prepared at the freezing temperature of -80 °C. The bigger pore size of these samples could stipulate such a result, see section 6.1.2.

6.3.2 Imbibition at different sample orientation

The measurements of the dry sample weight and the sample weight during the imbibition were used to calculate the mass of the imbibed liquid. Fig. 6.6 displays the increase of the imbibed mass of the FC-72 liquid in time for the samples 80-1, 80-2, 150-1 and 150-2 at -z and $+z$ orientations.

Fig. 6.6 shows that the smaller is the ratio d/D of the diameter of the upward oriented pores section to the overall diameter of a cylindrical sample, the smaller are the differences in wicking at -z and $+z$ sample orientations. That is in accordance with our expectations. The samples with smaller d/D are less anisotropic in the axial direction and have smaller differences in permeabilities for -z and $+z$ orientations, i.e. minimum $K_{\text{+z}}/K_{\text{-z}}$, see Table 6.2. Hence, for these samples we observed a minimum discrepancy of wicking results for -z and $+z$ sample orientations.

A comparison of wicking results for the samples prepared at two freezing temperatures reveals significant differences in imbibition rates. The samples prepared at the freezing temperature of -80 °C demonstrated faster wicking compared to the samples prepared at the freezing temperature of -150 °C, see Fig. 6.6. For these samples, a time approximately twice as large was required for complete saturation with FC-72 liquid. Meanwhile, the open porosity of the samples varied only slightly, see Table 6.2. That is in conformity with the results of the permeability determination, see section 6.3.1. The samples 80-1 and 80-2 demonstrated higher permeability compared to 150-1 and 150-2 for both sample orientations, see Table 6.2.

In addition, we observed larger differences in wicking at -z and $+z$ orientations for the samples prepared at the freezing temperature of -150 °C than for the samples prepared at -80 °C. That

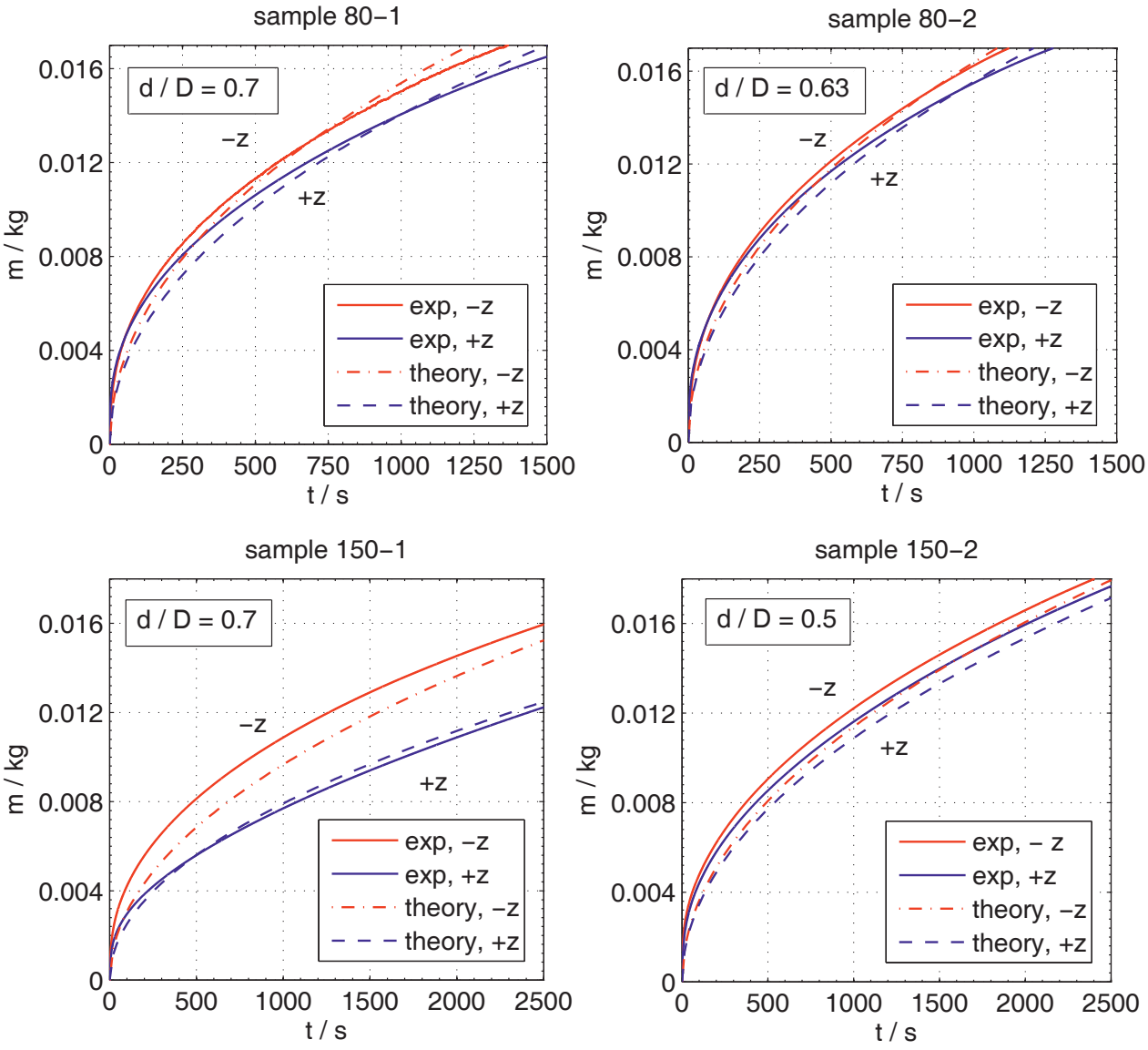

Figure 6.6: The mass of the imbibed FC-72 liquid into the samples 80-1, 80-2, 150-1 and 150-2 versus time. The theoretical prediction was computed using the Lucas-Washburn equation with gravity effects (Eq. 6.6) and the parameters from Table 6.3. The samples 80-1 and 80-2 demonstrate faster wicking compared to the samples 150-1 and 150-2. Meanwhile, the latter show the larger differences in the wicking rates at -z and +z sample orientations. The differences, however, become insignificant with the decrease of d/D.

was most pronounced for the samples 80-1 and 150-1 that were of the same value of d/D, see Fig. 6.6. This could not be compared directly for the samples 80-2 and 150-2 due to the inequality of the d/D parameter. Nevertheless, the sample 150-2 that was of a smaller d/D

demonstrated a slightly larger ratio K_{+z}/K_{-z} of the permeabilities at -z and +z orientations compared to the sample 80-2, see Table 6.2.

6.3.3 Theoretical prediction of wicking

In this section some theoretical prediction of wicking results is given. We continue using the analogy of the flow through porous media to the flow through a bundle of capillary tubes, and the macroscopic approach to the description of imbibition as in section 6.3.1. However, here we focus on the viscous-gravitational stage of the process.

In this domain the momentum balance for the imbibition of liquid into porous media reads as the interaction of the capillary pressure, viscous forces and hydrostatic pressure [93, 117, 101]

$$\frac{2\sigma\cos\theta}{R_{\mathrm{s}}} = \frac{\phi\mu_{\mathrm{L}}\dot{h}h}{K} + \rho_{\mathrm{L}}gh. \tag{6.6}$$

Eq. 6.6 is the Lucas-Washburn equation with gravity effects (also given as Eq. 2.95). The solution of Eq.3.1.1 was given as Eq. 3.12. In order to compare the impact of the viscous force and the hydrostatic pressure on the imbibition for each sample, we introduced the parameters listed in Table 3.1. Such a parameterization has been also applied in section 3.1.1. Substituting the parameters from Table 3.1 into Eq. 6.6, one obtains

$$1 = b\dot{h}h + ch. \tag{6.7}$$

The theoretical model prediction was computed for wicking into each sample at -z and +z orientations using Eq. 6.7 with the parameters from Table 3.1, the thermophysical properties of FC-72 liquid from Table 4.3 and the geometrical characteristics and macroscopic parameters of the samples from Tables 6.1 and 6.2. The calculated parameters of Eq. 6.7 are summarized in Table 6.3.

According to the definition of the parameter c given in Table 3.1, it indicates a relative influence of gravity on the imbibition that is stipulated by capillary pressure. Table 6.3 demonstrates that c is larger for the samples prepared at the freezing temperature of -80 °C than for the samples prepared at -150 °C. Such a result is due to a smaller pore size of the latter that ensures a higher capillary pressure. A different sample orientation does not influence the hydrostatic or capillary pressure, therefore, the parameter c varies only for different porous structures. Meanwhile, for each sample the parameter b is larger at +z orientation than at -z, see Table 6.3. This parameter indicates the relative influence of the viscous force on the imbibition. Such a result implies that the viscous force has a stronger influence on the imbibition at +z sample

Table 6.3: List of the parameters of Eq. 6.7.

Sample	b ($\mathrm{s\,m^{-2}}$) 10^6	c ($\mathrm{m^{-1}}$)
$-z$ orientation		
80-1	2.34	5.76
80-2	2.09	5.76
150-1	8.04	1.07
150-2	5.78	1.07
$+z$ orientation		
80-1	2.86	5.76
80-2	2.34	5.76
150-1	12.0	1.07
150-2	6.33	1.07

orientation. This is in conformity with the permeability results that showed higher values for the samples at -z orientation. The parameter b contains a combination of the macroscopic parameters unique for each porous structure. Due to that b also varies for each sample.

The results of the theoretical model prediction were plotted on Fig. 6.6. The theoretical prediction is in good agreement with the experiment data. That indicated that the macroscopic model that has been primarily developed for the description of the imbibition in a homogeneous porous structure could also serve as a simple tool to predict it for some anisotropic structures. Nevertheless, in this case the preliminary characterization of the anisotropy and directional determination of the macroscopic parameters are necessary.

6.4 Summary

The capillary transport abilities of anisotropic porous ceramic monoliths fabricated via the freeze-casting method were characterized. The lamellar pore structures with an axial anisotropy prepared at two different freezing temperatures (-80 °C and -150 °C) revealed similar porosity but different pore size distribution. Vertical wicking experiments were performed. Using sample weight measurement during imbibition, the increase of the mass of the imbibed liquid was

evaluated. The permeability was determined using results at the viscous-dominated stage of wicking. The deviations of permeability at two different sample orientations were found to vary from 10% to 49%. They are larger for the samples prepared at the freezing temperature of -150 °C that revealed smaller average pore size. These values quantified the impact of the axial anisotropy on the capillary transport abilities of the porous structures. Correspondingly, the larger differences in wicking at two sample orientations were also observed for these sample. However, the complete saturation with the experimental liquid occurred approximately twice as fast as for the samples prepared at the freezing temperature of -80 °C. Such a result is due to the higher permeability of the samples that could be stipulated by bigger pores. In addition, the experiment data was compared with a theoretical prediction performed using the Lucas-Washburn equation with gravity effects. The wicking results for each sample at both sample orientation demonstrated a good agreement with the theoretical prediction. This implies applicability of macroscopic modelling as a simple tool to predict wicking in some anisotropic porous structures. It requires, however, preliminary characterization and directional determination of macroscopic parameters of a porous medium.

Chapter 7

Numerical simulations of wicking

This chapter provides the results of the benchmark microscopic and macroscopic simulations of a fluid flow in porous media using the computational fluid dynamics software FLOW-3D.

7.1 3D image of porous media

X-ray tomography is a non-destructive technique that can be applied for the acquisition of three-dimensional (3D) information on internal structures of porous materials [161, 162, 164]. It is based on X-ray radiography. An X-ray beam is sent on a sample and the transmitted beam is recorded by a detector [164]. A two-dimensional projection of the absorption coefficients of the structure (radiograph) is formed using the ratio of the number of transmitted to incident photons [164, 163]. The sample is rotated between 0° and 180° about an axis perpendicular to the incident beam [163]. A large number of radiographs is taken. From the radiographs a 3D image of the sample is reconstructed using visualization software. 3D images can be exported as stereolithography files (STL). In such files the surface of a solid object is represented by a number of triangles that form an enclosed volume. The vertex coordinates of the triangles and the facet unit normals are used to create a geometry. For flow simulations it is of importance that the generated geometry object would have a closed surface. A special software (e.g. MiniMagics, AdMesh) can be used to identify errors in STL-files.

For this study the X-ray tomography was performed for a porous medium made of sintered glass frits (ROBU Glasfilter-Geraete, Germany). The solid material of the medium was specified as boroslicate glass 3.3. Similar structures of different pore size distribution and porosities were used for the wicking experiments with liquid nitrogen and the FC-72 liquid, see chapters 4 and 5. In order to capture a pore morphology with available resolution (approximately $10{\cdot}10^{-6}$

Table 7.1: Macroscopic parameters of the porous structure used for the X-ray tomography [127]. The porous structure was commercially obtained from ROBU Glasfilter-Geraete, Germany. ϕ, R_s and K are referred to as the porosity, the static pore radius and the permeability, respectively. For the flow simulations performed in this work the 3D-image of the structure was reduced in size.

ROBU class	ϕ	R_s	K
	(-)	(m)	(m^2)
		10^{-6}	10^{-12}
P1	0.35	119.8 ± 10.8	20.20 ± 5.00

m), the X-ray tomography was performed for a structure of larger pore size. Zhang [127] performed wicking experiments with a range of storable liquids to determine the macroscopic parameters of this structure. The values obtained by Zhang [127] are summarized in Table 7.1. The acquisition of the tomography data and its reconstruction as the stereolithography file (STL) was performed by Viscom AG, Germany. 720 images were obtained for the tomography reconstruction. The porosity value was used to define the outline of the solid edge of the structure via the reconstruction software. Using magnification options in computational fluid dynamics software FLOW-3D, the 3D-image of the scanned sample was reduced in size in order to get a structure with a pore size comparable to a pore size of the experimental samples used in this work, see Table 4.4. The magnification factor of $1.727 \cdot 10^{-1}$ was applied in x-, y- and z-directions. This 3D-image was used for microscopic flow simulations with FLOW-3D.

7.2 Computational fluid dynamics software FLOW-3D

FLOW-3D is a commercial computational fluid dynamics software that uses numerical techniques to solve equations for fluid flow and heat transfer problems. In this study an isothermal incompressible one-fluid flow was computed. The fluid is assumed to be Newtonian and the flow regime is to be laminar. The computations were performed using FLOW-3D Version 10.0. In this section the overview of the computation approach, relevant equations and numerical approximations is given. The detailed description can be found in the FLOW-3D user manual [165].

7.2.1 Control volume, meshing and geometry

To solve the conservation equations using a computational fluid dynamics software, one should first define the computational mesh. The latter consists of a number of interconnected elements, or cells that subdivide the space into small volumes (control volumes). Several nodes are associated with each cell in order to store the values of the flow parameters, such as pressure, temperature and velocity. The computational mesh serves to define the flow parameters at discrete locations, to set boundary conditions and to develop numerical approximations of the conservation equations.

The computational mesh in FLOW-3D is an orthogonal mesh defined in Cartesian or cylindrical coordinates. The mesh characteristics are assigned independently for each coordinate. FLOW-3D features uniform and non-uniform meshes. The uniform mesh is defined as the mesh with a uniform cell size in each direction. The non-uniform meshes can be generated using the mesh planes at fixed locations with the predefined cell size or the number of cells. The cells of a non-uniform mesh vary in a size for each direction. Using the multiple mesh blocks, one might increase the simulation resolution in the area of interest and decrease it where no flow is expected.

Solid objects in FLOW-3D are represented as the components with specific properties (e.g. thermophysical properties or roughness). Each component consists of one or a group of sub-components that might be defined, for example, by the primitive shapes generated by FLOW-3D (spheres, cylinders, boxes, etc.) or by the stereolithography files (STL).

The construction of the geometry of solid objects and the definition of the flow region is performed using the FAVOR$^{\mathrm{TM}}$ method (Fractional Area/Volume Obstacle Representation). The FAVOR$^{\mathrm{TM}}$ method embeds the geometry into a computational mesh using the area fractions A on the cell faces and the volume fractions V_{F} open to a fluid flow. For a cell within a solid object $V_{\mathrm{F}} = 0$. A cell is considered to be open to a fluid flow if $0 < V_{\mathrm{F}} \leq 1$.

7.2.2 Mass conservation

For the incompressible fluid flow with no turbulent diffusion terms and no mass sources the mass conservation equation in Cartesian coordinates (x, y, z) is given as

$$\frac{\partial}{\partial x}(uA_x) + \frac{\partial}{\partial y}(vA_y) + \frac{\partial}{\partial z}(wA_z) = 0, \tag{7.1}$$

where u, v and w are the velocity components x-,y- and z-directions, respectively, and A_x, A_y and A_z are the fractions of the cell areas open to the flow in x-,y- and z-directions, respectively.

7.2.3 Linear momentum conservation

The linear momentum conservation equations solved in FLOW-3D evolve from the Navier-Stokes equations. For an incompressible fluid in Cartesian coordinates they are given as

$$\frac{\partial u}{\partial t} + \frac{1}{V_{\mathrm{F}}}\left(uA_x\frac{\partial u}{\partial x} + vA_y\frac{\partial u}{\partial y} + wA_z\frac{\partial u}{\partial z}\right) = -\frac{1}{\rho}\frac{\partial p}{\partial x} + G_x + f_x, \tag{7.2}$$

$$\frac{\partial v}{\partial t} + \frac{1}{V_{\mathrm{F}}}\left(uA_x\frac{\partial v}{\partial x} + vA_y\frac{\partial v}{\partial y} + wA_z\frac{\partial v}{\partial z}\right) = -\frac{1}{\rho}\frac{\partial p}{\partial y} + G_y + f_y, \tag{7.3}$$

$$\frac{\partial w}{\partial t} + \frac{1}{V_{\mathrm{F}}}\left(uA_x\frac{\partial w}{\partial x} + vA_y\frac{\partial w}{\partial y} + wA_z\frac{\partial w}{\partial z}\right) = -\frac{1}{\rho}\frac{\partial p}{\partial z} + G_z + f_z. \tag{7.4}$$

In Eqs. 7.2, 7.3 and 7.4 the components (f_x, f_y, f_z) and (G_x, G_y, G_z) are the viscous and the body accelerations, respectively, in x-,y- and z-directions. Here no mass sources are considered. Eqs. 7.2, 7.3 and 7.4 are valid for the cells fully open to the fluid ($V_{\mathrm{F}} = 1$) and the cells intersecting with solid bodies ($0 < V_{\mathrm{F}} < 1$). If the cell is completely located in a solid object ($V_{\mathrm{F}} = 0$), these equations are not computed.

The viscous acceleration for a Newtonian fluid are calculated as

$$\rho V_{\mathrm{F}} f_x = wsx - \left(\frac{\partial}{\partial x}(A_x\tau_{xx}) + \frac{\partial}{\partial y}(A_y\tau_{yx}) + \frac{\partial}{\partial z}(A_z\tau_{zx})\right), \tag{7.5}$$

$$\rho V_{\mathrm{F}} f_y = wsy - \left(\frac{\partial}{\partial x}(A_x\tau_{xy}) + \frac{\partial}{\partial y}(A_y\tau_{yy}) + \frac{\partial}{\partial z}(A_z\tau_{zy})\right), \tag{7.6}$$

$$\rho V_{\mathrm{F}} f_z = wsz - \left(\frac{\partial}{\partial x}(A_x\tau_{xz}) + \frac{\partial}{\partial y}(A_y\tau_{yz}) + \frac{\partial}{\partial z}(A_z\tau_{zz})\right), \tag{7.7}$$

where τ_{xy}, τ_{xz}, τ_{yz}, τ_{xx}, τ_{yy} and τ_{zz} are the shear stresses given as Eqs. 2.22, 2.23, 2.24, 2.25, 2.26 and 2.27, respectively. The components wsx, wsy and wsz in Eqs. 7.5, 7.6 and 7.7 are the wall shear stress gradients. The approach to compute the wall shear stress is as follows. For the velocity component w in z-direction the wall shears arise from the solid areas on x- and y-faces of a cell. If the fractional flow area A of these cell faces is less than 1, the remaining area $(1 - A)$ is considered to be a wall. For a laminar flow the wall shear stress gradient on one of the x-faces is calculated as

$$wsz = -\frac{2\mu}{A_z\delta x^2}(1 - A_x)(w - w_0), \tag{7.8}$$

where δx is the cell size in the x-direction. In such a way the wall stress is evaluated at each of the four walls on the x- and y-faces. The total wall shear stress for the w-velocity is taken as a sum of these stresses. Analogically the wall shear stress gradients wsx and wsy are computed for the u- and v-velocities, respectively. If no moving solid components are considered and the no-slip condition is assumed, the velocity w_0 in Eq. 7.8 is taken as zero.

7.2.4 Free surface

In order to define the fluid configuration the approach developed by Hirt and Nichols [167] is used. The Volume of Fluid (VOF) function $F(x, y, z, t)$ is introduced so that it satisfies the following equation

$$\frac{\partial F}{\partial t} + \frac{1}{V_{\mathrm{F}}}\left(\frac{\partial}{\partial x}(FA_{\mathrm{x}}u) + \frac{\partial}{\partial y}(FA_{\mathrm{y}}v) + \frac{\partial}{\partial z}(FA_{\mathrm{z}}w)\right) = 0. \tag{7.9}$$

In case of a single fluid flow F is the volume fraction of the fluid. If $F = 1$, the cell is located fully in the fluid. If $F = 0$, the cell is located in the region with no fluid mass, i.e. in the void region. The free surface boundary condition is described in section 7.2.5. The free surface movement due to the pressure gradients can be computed with a standard method available in FLOW-3D "One fluid, free surface". This method is in detail described by Barkhudarov [168].

7.2.5 Numerical approximations

The mesh of rectangular cells of a width δx, depth δy and height δz is used for numerical computations. The indexes i, j and k serve to label the cells in x-, y- and z-directions, respectively. In addition, a fictitious layer of boundary cells is created to set mesh boundaries. The time discretization is given as $t^{n+1} = t^n + \delta t$, where n is the time level and δt is the time increment. Fluid fractions F, pressures p, fractional volumes V_{F}, densities ρ and viscosities μ are located at cell centers. Thus, $F^n_{i,j,k}$ and $p^n_{i,j,k}$ are, respectively, the fluid fraction and the pressure at the center of the cell (i, j, k) at the time level n, and $V_{\mathrm{F}_{i,j,k}}$ is the fractional volume for the flow at the center of the cell (i, j, k). In this study the density and viscosity are constant.

The velocities are located at cell-faces. The index $i + \frac{1}{2}$, for example, is denoted to the cell-face between the cells (i, j, k) and $(i + 1, j, k)$. Thus, $u^n_{i,j,k}$ is the x-direction velocity at the middle of the $i + \frac{1}{2}$ cell-face, $v^n_{i,j,k}$ is the y-direction velocity at the middle of the $j + \frac{1}{2}$ cell-face, and $w^n_{i,j,k}$ is the z-direction velocity at the middle of the $k + \frac{1}{2}$ cell-face at the time level n.

If the cell (i, j, k) contains the fluid and has at least one adjacent empty cell $(i \pm 1, j \pm 1, k \pm 1)$, the cell (i, j, k) is defined as the surface cell. The flag $N_{\mathrm{F}_{i,j,k}}$ serves to label cells in order to distinguish the empty cells, the surface cells and the cells fully filled with the fluid. For a cell fully filled with the fluid as well as for an obstacle cell $N_{\mathrm{F}_{i,j,k}} = 0$. An empty cell is labeled with $N_{\mathrm{F}_{i,j,k}} = 8$. The surface cells take values from 1 to 6 depending on which neighboring cell is located in the direction of the inward normal to the surface. Thus, the orientation of the free surface is indicated.

The equations are solved applying the finite-difference solution method. The following three-steps computation procedure is used for one increment in time δt:

1. A first guess for new time-level velocities is computed using the explicit approximations of the momentum equations (Eqs. 7.2, 7.3 and 7.4) with the initial conditions or previous time-level values.

2. The pressure is iteratively adjusted in each cell to satisfy the mass continuity equation (Eq. 7.1). The corresponding velocity changes are added to the velocities computed in step 1.

3. The free surface is updated using Eq. 7.9 to provide a new fluid configuration.

The finite-difference approximation of a first-order accurate in space and time increments is applied in this study. The advective and viscous terms are evaluated with an old-time level n for velocities. Wall shear stresses are evaluated implicitly. The computation of the fluid fraction F in the cell and the fluxes of F across the cell-faces is performed using the Volume of Fluid (VOF) method with a donor-acceptor flux approximation. This approximation evaluates the amount of F to be fluxed during one time step from the donor cell, i.e. the cell losing the fluid volume, to the acceptor cell, i.e. the cell gaining the fluid volume. The details are given in [165] chapter 3.

Momentum equation approximation

The finite-difference approximation of the momentum equations (Eqs. 7.2, 7.3 and 7.4) is given as

$$u_{i,j,k}^{n+1} = u_{i,j,k}^{n} + \delta t^{n+1}\left[-\frac{p_{i+1,j,k}^{n+1} - p_{i,j,k}^{n+1}}{(\rho\delta x)_{i+\frac{1}{2},j,k}^{n}} + G_x - FUX - FUY - FUZ + f_x - wsx\right], \quad (7.10)$$

$$v_{i,j,k}^{n+1} = v_{i,j,k}^{n} + \delta t^{n+1}\left[-\frac{p_{i,j+1,k}^{n+1} - p_{i,j,k}^{n+1}}{(\rho\delta y)_{i,j+\frac{1}{2},k}^{n}} + G_y - FVX - FVY - FVZ + f_y - wsy\right], \quad (7.11)$$

$$w_{i,j,k}^{n+1} = w_{i,j,k}^{n} + \delta t^{n+1}\left[-\frac{p_{i,j,k+1}^{n+1} - p_{i,j,k}^{n+1}}{(\rho\delta z)_{i,j,k+\frac{1}{2}}^{n}} + G_z - FWX - FWY - FWZ + f_z - wsz\right], \quad (7.12)$$

where (G_x, G_y, G_z) and (f_x, f_y, f_z) are the body and the viscous accelerations in x-,y- and z-directions, respectively. The components wsx, wsy and wsz in Eqs. 7.10, 7.11 and 7.12 are the wall shear stress accelerations in x-,y- and z-directions, respectively. The computation of the viscous and the wall shear stress accelerations is discussed in section 7.2.3. The components

FUX, FUY and FUZ in Eq. 7.10 are the advective fluxes of the velocity u in the x, y and z-directions, respectively. The advective fluxes of the velocities v and w are given in Eqs. 7.11 and 7.12, respectively. The advective flux of the velocity u in the x-direction is calculated as

$$\begin{aligned} FUX =& \frac{1}{2}\frac{\delta x_i V_{\mathrm{F}_{i,j,k}} + \delta x_{i+1} V_{\mathrm{F}_{i+1,j,k}}}{\delta x_i + \delta x_{i+1}} \\ & \left(\frac{1-\alpha}{2} \left(u_{i+1,j,k} A_{x_{i+1,j,k}} + u_{i,j,k} A_{x_{i,j,k}} \right) \frac{u_{i+1,j,k} - u_{i,j,k}}{\delta x_{i+1}} \right. \\ & \left. + \frac{1+\alpha}{2} \left(u_{i,j,k} A_{x_{i,j,k}} + u_{i-1,j,k} A_{x_{i-1,j,k}} \right) \frac{u_{i,j,k} - u_{i-1,j,k}}{\delta x_i} \right), \end{aligned} \tag{7.13}$$

where $\alpha = 0$ for the uniform size cells and $\alpha = 1$ for the cells of a different size in the x-direction. Analogically the advective fluxes are computed for each velocity in each direction. The details of the approximation method are provided in [165] chapter 3.

Pressure solution algorithm

The mass continuity equation is used for the iterative adjustment of the pressure in each cell (step 2). In case of an incompressible fluid the pressure correction can be performed applying the GMRES (Generalized Minimum RESidiual) method. The detailed description of this implicit pressure-velocity solver is given in [166] section 6.5.

Boundary conditions

In order to set the mesh boundaries, an additional layer of cells is created at each boundary. The specified pressure and the specified velocity conditions can be defined in these cells. The pressure boundary condition can be set using the static or the stagnation pressure. The static pressure is a specified pressure p continuous across the boundary. In this case a zero normal-derivative condition across the boundary is applied to the velocity. The stagnation pressure condition implies a stagnant fluid at the specified pressure that represent a large reservoir outside the mesh domain. The stagnation pressure is specified as $p + \rho u^2/2$ with u being the normal velocity component of the incoming flow. The hydrostatic pressure boundary condition can be applied for incompressible flows.

The volume of flow rate boundary condition is a modification of the specified velocity condition. In this case the velocity to achieve the specified flow rate is computed using the open area on the boundary.

The symmetry boundary condition implies the same values of the parameters on both sides of the symmetry plane.

The continuative boundary condition is an outflow condition that represents a smooth continuation of the flow through the boundary. For that the normal derivatives of all the parameters at the boundary are set to zero.

The internal obstacles can be represented as the free-slip, partial slip and no-slip boundaries. If the no-slip condition is chosen (as in this study), the influence of the internal obstacles is accounted using the wall shear stress algorithm, see section 7.2.3.

Free surface boundary condition

In order to apply a free-surface boundary condition, an approximate normal direction to the surface shall be assigned. This is represented by an integer value N_{F}, which identifies the neighboring cell closest to the direction of the inward normal to the surface. The latter shall point away from an empty neighbor cell. The boundary is assumed to be represented in each surface cell as a single-valued function $X(y,z)$, or $Y(x,z)$, or $Z(x,y)$ depending on the direction of the approximate normal to the surface. In case of the normal oriented in the z-direction the boundary is represented by $Z(x,y)$. The functions $X(y,z)$, or $Y(x,z)$, or $Z(x,y)$ are computed using the F values of the cells (see section 7.2.4) with the approach described in [165] chapter 3. The surface location in a cell is then defined by a flat surface normal to the direction of the inward normal to the surface.

The boundary condition for a free surface is defined as the specified pressure applied to the surface cells. This pressure is equal to the sum of the neighboring void region pressure and the surface tension pressure. The latter is an equivalent pressure that replaces the surface tension forces acting on a free-surface in a cell divided by the projected surface area. The surface tension forces act tangent to the surface and can be resolved into components directed along two principal tangent directions. If the inward surface normal is in the negative z-directions, then the surface tension force perpendicular to the x-axis can be calculated as given in [165] chapter 3 by

$$S_z = \frac{\sigma \delta y \left(\dfrac{\partial Z}{\partial x}\right)}{\left[1 + \left(\dfrac{\partial Z}{\partial x}\right)^2 + \left(\dfrac{\partial Z}{\partial y}\right)^2\right]^{1/2}}, \tag{7.14}$$

where σ is the predefined surface tension coefficient.

The wall adhesion condition is applied to the surface cells intersecting a wall or an obstacle. In that case S_z shall be multiplied by the fraction of the face open to flow. For the remaining

(closed) area fraction, the fluid is assumed to adhere to the wall with the predefined contact angle θ, which is the angle between the wall tangent and the fluid surface tangent.

7.3 Benchmark microscopic simulation (pore level)

7.3.1 Steady fluid flow through porous media

Sample volume

The STL-file with the 3D image of the porous structure made of the sintered glass frits (see section 7.1) was imported into FLOW-3D as a solid geometry component. First, the representative equivalent volume (REV) of the porous medium should be determined. REV is a minimum volume of a porous sample, from which macroscopic parameters become independent from the size of the sample [162]. In this case such macroscopic parameters are the porosity and permeability. In order to determine REV, several sample volumes of a cubic shape were chosen for simulations, see Table 7.2.

Table 7.2: The characteristics of the sample volumes and the mesh chosen for simulations. a is the length of the side of a cubic sample and V is the sample volume. N_{cell} is referred to as the number of the mesh cells of a size of $3.33{\cdot}10^{-6}$ m in x-, y- and z-directions snapped to each sample volume. N_{c} is referred to as the number of equivalent parallel cylindrical capillaries assigned to each sample volume, see Eq. 7.17.

a	V	N_{cell}	N_{c}
(m)	(m^3)	(-)	(-)
10^{-3}	10^{-12}	10^4	
0.15	3.375	9.1125	12
0.25	15.625	42.1875	32
0.35	42.875	115.7625	63
0.45	91.125	246.0375	104

Mesh

The Cartesian mesh with a cell size of $3.33{\cdot}10^{-6}$ m in x-, y- and z-directions was snapped to each sample volume. Due to a varied size of the sample volumes, a different number of the

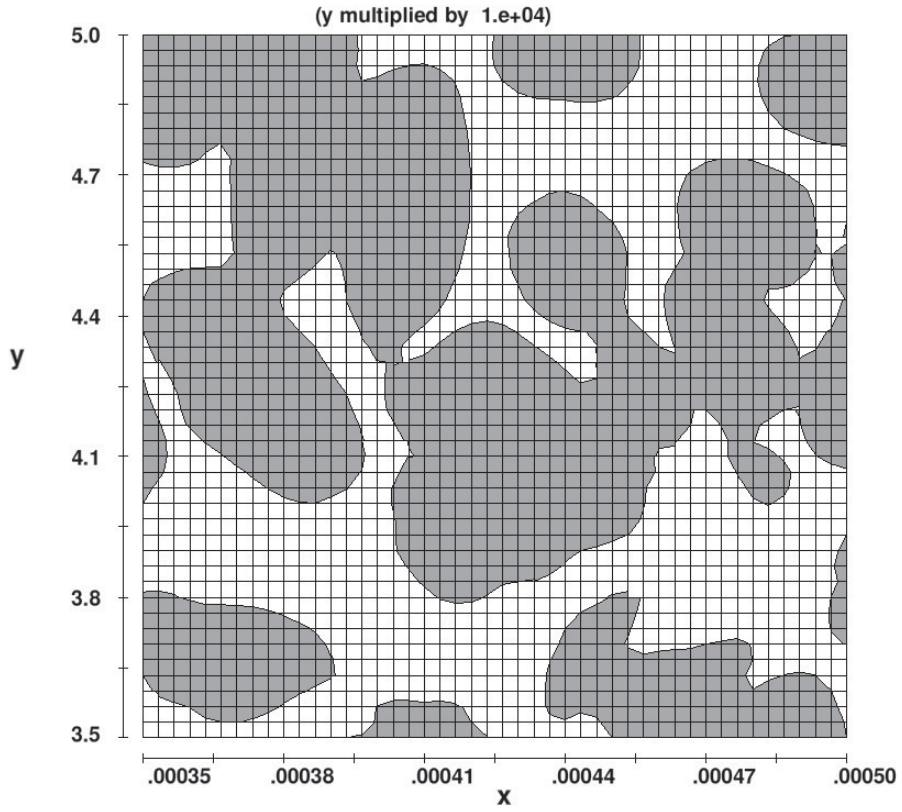

Figure 7.1: The Cartesian mesh with a cell size of $3.33{\cdot}10^{-6}$ m in x-, y- and z-directions snapped to the cubic sample volume with a length of the side $a = 0.15 \cdot 10^{-3}$ m. The sample volume is assigned to $N_\mathrm{c} = 12$ of equivalent parallel cylindrical capillaries, see Eq. 7.17 and Table 7.2. The solid structure is shown in gray color.

mesh cells N_cell was required, see Table 7.2. On Fig. 7.1 the mesh is shown on the cubic sample volume with a length of the side $a = 0.15 \cdot 10^{-3}$ m.

Equivalent cylindrical capillaries

In order to provide an analogy to the bundle of capillaries approach (see section 2.6.1), a number N_c of equivalent parallel cylindrical capillaries was assigned to each sample volume. If A is the area of the sample cross-section perpendicular to the fluid flow, the part of A open for the flow is given as ϕA, where ϕ is the porosity. On the other hand, ϕA can be expressed as the total cross-section area of N_c equivalent parallel cylindrical capillaries

$$\phi A = N_\mathrm{c} \frac{\pi D^2}{4}, \tag{7.15}$$

where D is the diameter of a cylindrical capillary. The cross-section area of a sample is calculated as

$$A = a^2, \tag{7.16}$$

where a is the length of a side of the cubic sample.
Rearranging Eq. 7.15 and substituting Eq. 7.16 into it, one obtains

$$N_\mathrm{c} = \frac{4\phi a^2}{\pi D^2}. \tag{7.17}$$

Substituting into Eq. 7.17 the subsequently determined values of the porosity ($\phi = 0.33$) and the static pore radius ($D = 2R_\mathrm{s} = 28.6{\cdot}10^{-6}$ m), N_c was calculated for each sample volume, see Table 7.2. The value of the static pore radius was obtained from the results of the wicking simulation. This is discussed in section 7.3.2.

Simulation settings

A simulation of a steady flow of an incompressible fluid through the porous medium was performed for each sample volume. The flow was specified as laminar with no-slip condition at the walls. At the boundary z_min the constant volume flow rate $Q = 10^{-12}$ m^{3}s^{-1} was applied. The boundary z_max served as the outflow with a specified pressure $p = 0$. All the other boundaries were set to symmetry. The fluid initialization was activated using the initial fluid elevation of $5{\cdot}10^{-6}$ m from the boundary z_min. The thermophysical properties of a fluid were taken as for water at 101 325 Pa and 293.15 K [141], see Table 7.3. The main settings of the simulations are summarized in Table 7.4. The details of the computation approach are given in section 7.2.

Table 7.3: The fluid properties set for the simulations. ρ_L and μ_L are referred to as the density and dynamic viscosity, respectively. The properties are taken as for water at 101 325 Pa and 293.15 K [141].

ρ_L ($\mathrm{kg\,m^{-3}}$)	μ_L ($\mathrm{Pa\,s}$) 10^{-3}
998.2	1.002

Table 7.4: The main settings of the simulation of a steady flow of an incompressible fluid through the porous medium.

General	
Interface tracking	No sharp interface
Number of fluids	One
Flow mode	Incompressible
Physics	
Viscosity and turbulence	Viscous laminar flow
	Wall shear boundary condition: no slip
Numerics	
Pressure solver	GMRES (implicit)
Viscous stress solver	Explicit
VOF advection	One fluid, no free surface
Momentum advection	First order
Fluid flow solver options	Solve momentum and continuity equations
Boundaries	
$z_{\min}$	specified volume flow rate $Q = 10^{-12}$ m^{3}s^{-1}
$z_{\max}$	specified pressure $p = 0$
Other boundaries	symmetry (default)
Initial conditions	
Pressure	Uniform
Void pressure	0
Fluid initialization (elevation)	$5{\cdot}10^{-6}$ m from $z_{\min}$

Results

For each sample volume the distributions of pressure and interstitial velocity of the fluid were obtained. Fig. 7.2 demonstrates the interstitial velocity distribution in a cross-section of the cubic sample volume with a length of the side $a = 0.45 \cdot 10^{-3}$ m, see Table 7.2. The sample volume is assigned to $N_c = 104$ of equivalent parallel cylindrical capillaries, see Eq. 7.17. The cross-section is perpendicular to the direction of the bulk flow (z) and taken in the middle part of the sample. As shown on Fig. 7.2, the interstitial velocity tends to approach its maximum values in the central parts of the pores and decreases at the pore walls. Similar results were

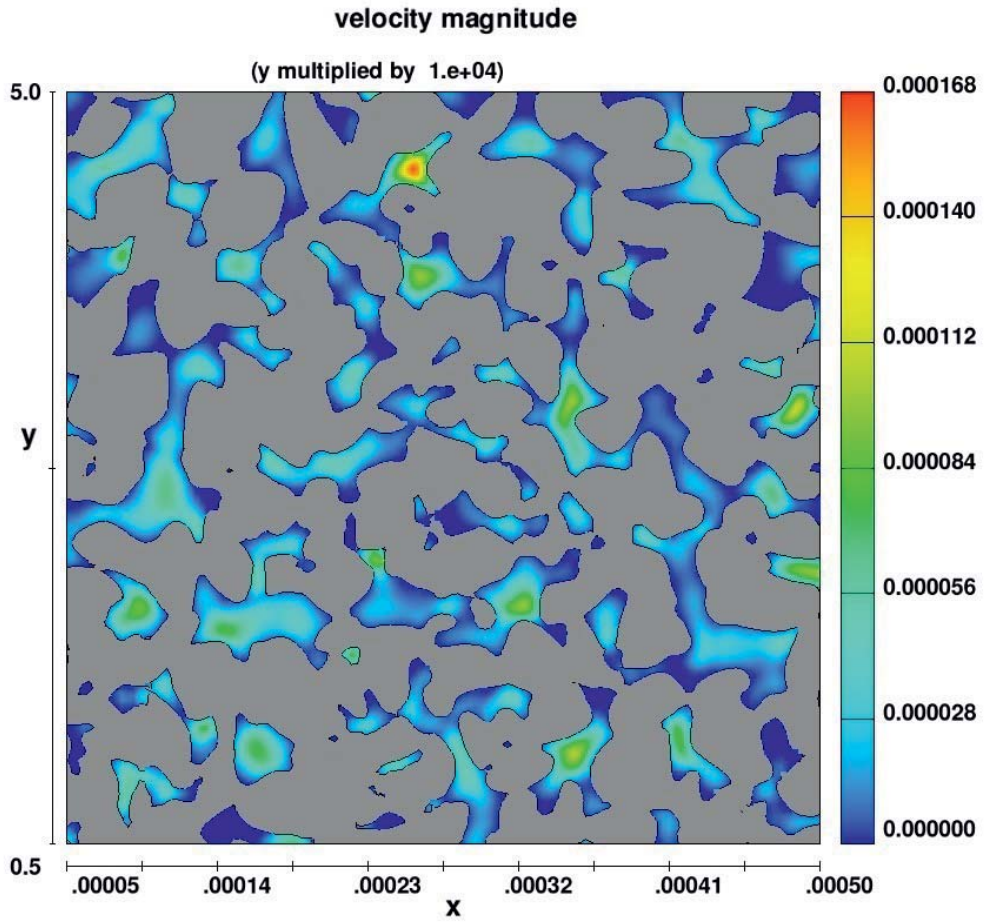

Figure 7.2: The distribution of the interstitial velocity of fluid (see the color bar) in the cross-section of the cubic porous sample with a length of the side $a = 0.45 \cdot 10^{-3}$ m (see Table 7.2). The solid structure is shown in gray color. The cross-section is perpendicular to the direction of the bulk flow (z) and taken in the middle part of the sample. The interstitial velocity tends to approach its maximum values in the central parts of the pores and decreases at the pore walls.

obtained for all the cross-sections of each sample volume from Table 7.2. Fig. 7.3 depicts the pressure distribution in a cross-section of the cubic sample volume with a length of the side $a = 0.45 \cdot 10^{-3}$ m, see Table 7.2. The cross-section is parallel to the direction of the bulk flow (z) and taken in the middle part of the sample. The pressure decreases from the boundary $z_{\min}$ (inflow) to the boundary $z_{\max}$ (outflow), where it was set as $p = 0$. Similar results were obtained for all the cross-sections parallel to z for each sample volume from Table 7.2.

The average pressure in the cross-sections perpendicular to the direction of the bulk flow (z) was calculated for each sample volume and plotted against z-coordinate, see Fig. 7.3. From the slope of the linear regression to the simulation data the pressure gradient $\mathrm{d}p/\mathrm{d}z$ was determined,

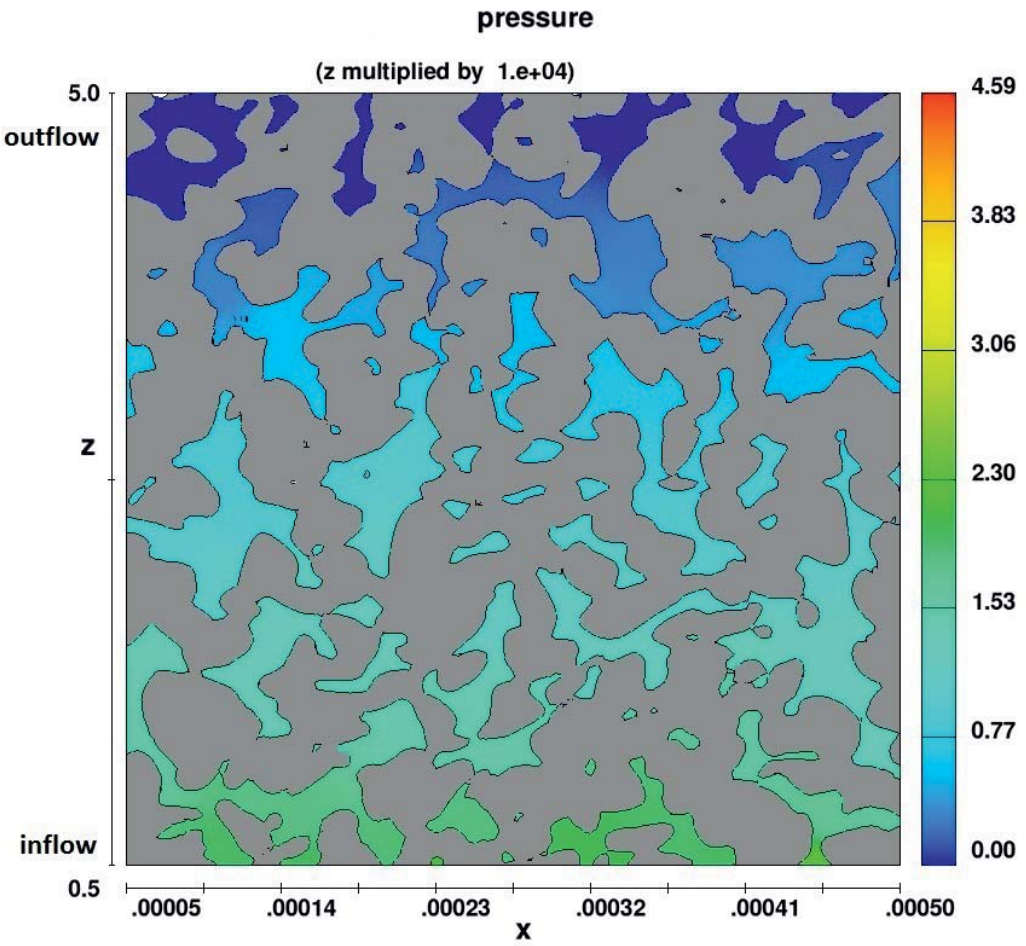

Figure 7.3: The pressure distribution (see the color bar) in the cross-section of the cubic porous sample with a length of the side $a = 0.45 \cdot 10^{-3}$ m (see Table 7.2). The solid structure is shown in gray color. The cross-section is parallel to the direction of the bulk flow (z) and taken in the middle part of the sample. The pressure decreases from the boundary $z_{\min}$ (inflow) to the boundary $z_{\max}$ (outflow), where it was set as $p = 0$.

see Table 7.5. Using $\mathrm{d}p/\mathrm{d}z$ and the one-dimensional Darcy's equation expressed as

$$-\frac{\mathrm{d}p}{\mathrm{d}z} = \frac{\mu_{\mathrm{L}}}{K}\frac{Q}{A}, \tag{7.18}$$

the permeability K was computed, see Table 7.5. In Eq. 7.18 the volume flow rate Q corresponds to the superficial (or filter) velocity. Using the Dupuit-Forchheimer assumption (Eq. 2.93), the interstitial velocity u_{L} can be computed via the volume flow rate Q, the porosity ϕ, and the cross-section area of a sample A as

$$u_{\mathrm{L}} = \frac{Q}{\phi A}. \tag{7.19}$$

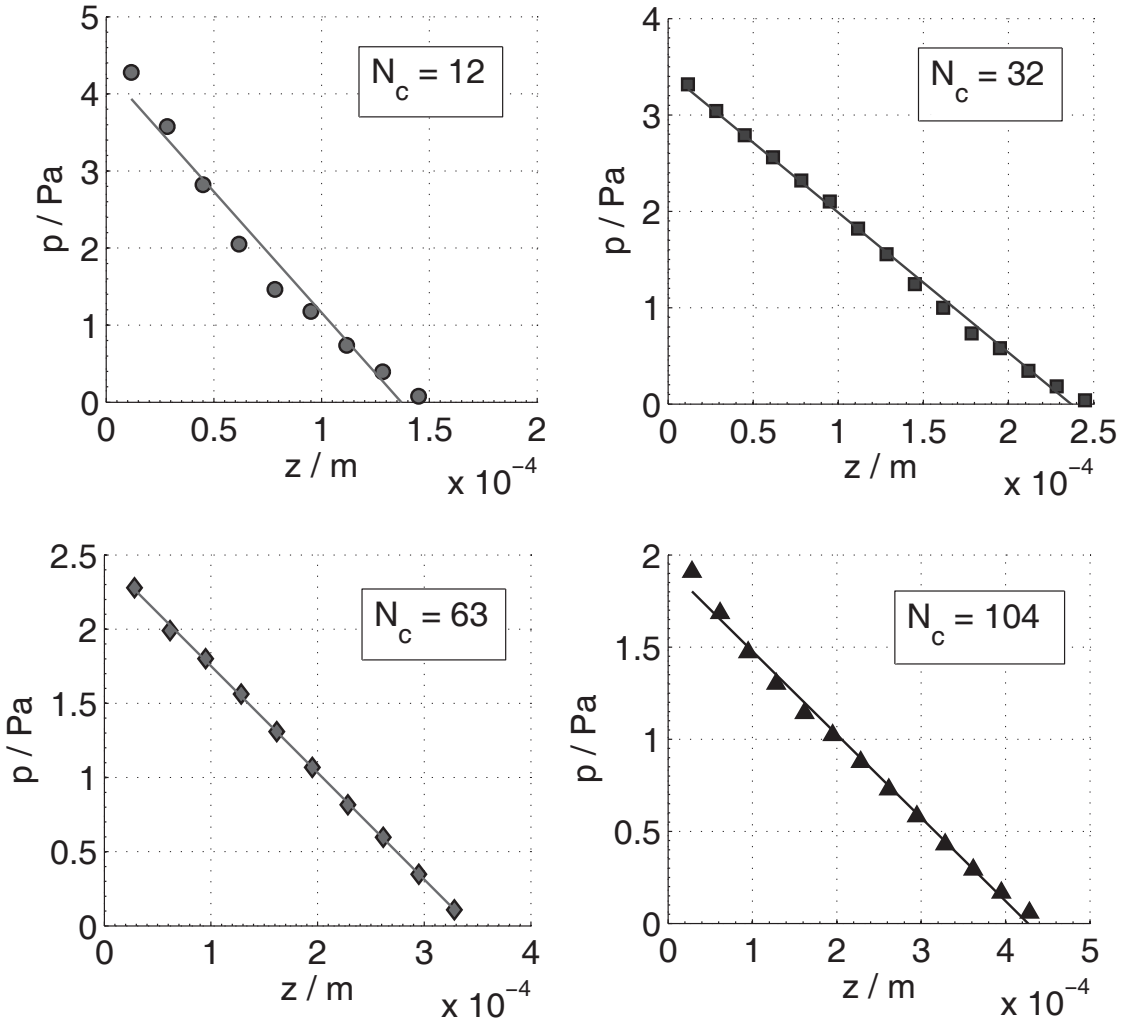

Figure 7.4: The average pressure in the cross-sections of porous samples perpendicular to the direction of the bulk water flow (z). The sample volumes assigned to the numbers $N_c = 12$, 32, 63 and 104 of equivalent parallel cylindrical capillaries were taken for computations, see Eq. 7.17 and Tables 7.2 and 7.5.

The porosity ϕ was determined using the calculated volume of the fluid V_L contained in a saturated porous sample and the total volume of each sample V (see Table 7.2) as

$$\phi = \frac{V_L}{V}. \tag{7.20}$$

The porosity values for each sample volume are summarized in Table 7.5. The analysis of the cross-sections of the sample volumes revealed no closed pores.

Table 7.5: The simulation inputs and results. N_c is referred to as the number of equivalent parallel cylindrical capillaries assigned to each sample volume, see Eq. 7.17. Q is the volume flow rate (superficial) in z-direction, A is the cross-section area of a sample, $\mathrm{d}p/\mathrm{d}z$ is the pressure gradient, K is the permeability, and ϕ is the porosity. Re, Eu, and Hg are referred to as the Reynolds, Euler, and Hagen number, respectively.

N_c	Q	A	$-\mathrm{d}p/\mathrm{d}z$	K	ϕ	Re	Eu	Hg
(-)	($\mathrm{m^3 s^{-1}}$)	($\mathrm{m^2}$)	($\mathrm{Pa\ m^{-1}}$)	($\mathrm{m^2}$)	(-)	(-)	(-)	(-)
10^6	10^{-12}	10^{-8}	10^3	10^{-12}		10^{-3}	10^6	
12	1	2.25	31.38	1.419	0.356	3.56	0.276	0.730
32	1	6.25	14.52	1.104	0.333	1.37	1.493	0.338
63	1	12.25	7.19	1.138	0.329	0.707	4.017	0.167
104	1	20.25	4.52	1.094	0.323	0.436	8.244	0.105

The simulation results can be presented using the dimensionless numbers. The Euler number characterizes the ratio of the pressure forces to the inertia forces and is given as

$$\mathrm{Eu} = \frac{\triangle p}{\rho_\mathrm{L} u_\mathrm{L}^2}, \tag{7.21}$$

where $\triangle p$ is the pressure drop through the porous medium and u_L is the interstitial velocity of liquid computed via Eq. 7.19.

The Hagen number represents the dimensionless pressure drop and is given as

$$\mathrm{Hg} = -\frac{\mathrm{d}p}{\mathrm{d}z}\frac{\rho_\mathrm{L} D^3}{\mu_\mathrm{L}^2}. \tag{7.22}$$

The characteristic length D in Eq. 7.22 is taken as $D = 2R_\mathrm{s} = 28.6{\cdot}10^{-6}$ m, where R_s is the subsequently determined value of the static pore radius, see section 7.3.2. The Reynolds number characterizes the ratio of the inertia forces to viscous forces and can be expressed as

$$\mathrm{Re} = \frac{\rho_\mathrm{L} u_\mathrm{L} D}{\mu_\mathrm{L}}, \tag{7.23}$$

where the characteristic length D is also taken as $D = 2R_\mathrm{s}$. The calculated values of the Euler, Hagen, and Reynolds numbers for each sample volume are summarized in Table 7.5. The Euler and Hagen numbers are plotted versus the Reynolds number on Fig. 7.5. The low values of the Reynolds number confirm the applicability of Darcy's law for the determination of the permeability K.

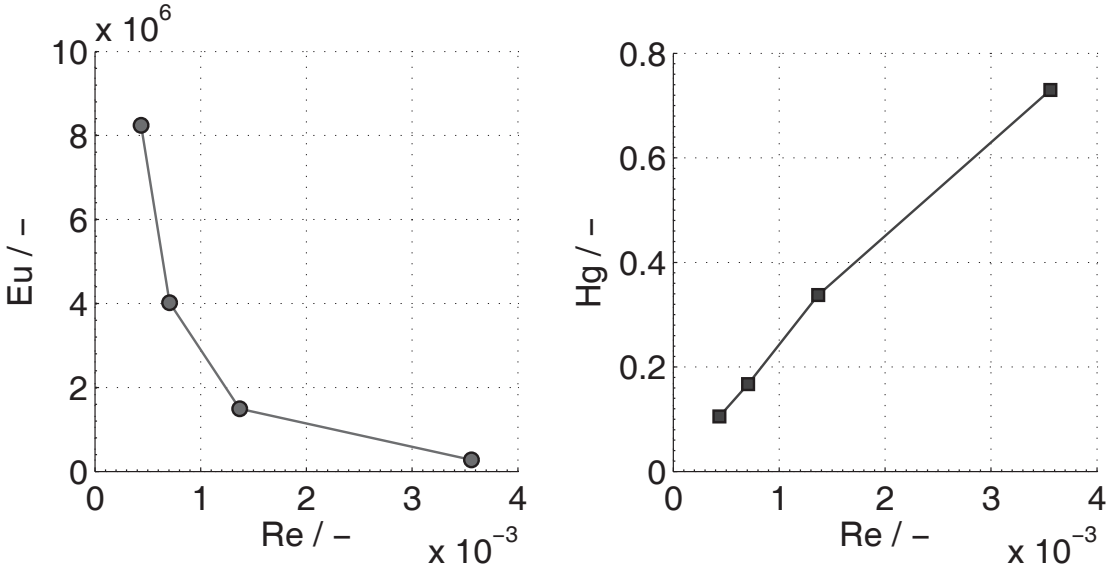

Figure 7.5: The Euler (Eu) and Hagen (Hg) numbers vs. the Reynolds (Re) number from the simulation results for different sample volumes, see Table 7.5. The low values of the Reynolds number confirm the applicability of Darcy's law for the determination of the permeability K.

Table 7.5 shows that for the sample volumes assigned to $N_c = 104$, 63 and 32 the permeability K deviates at less than 4%. However, K determined for the sample volume assigned to $N_c = 12$ is at approximately 29.7 % higher than K obtained for the largest sample volume assigned to $N_c = 104$. The porosity values ϕ varies from each other at approximately 3.1 % for the sample volumes assigned to $N_c = 104$, 63 and 32, see Table 7.5. Meanwhile, the deviation of ϕ computed for the sample volumes assigned to $N_c = 104$ and $N_c = 32$ was found to be approximately 10.2 %. The dependence of the calculated permeability and porosity values on the size of the chosen sample volume is depicted on Fig. 7.6. Taking into account these results, the representative equivalent volume (REV) for the porous media was defined as the sample volume assigned to $N_c = 32$ (the length of the side $a = 0.25 \cdot 10^{-3}$ m), see Table 7.5. This is a minimum computed sample volume, from which the macroscopic parameters K and ϕ change only slightly.

Using the chosen REV of the porous medium, the simulations with a smaller mesh size were performed. Two cell sizes of the Cartesian mesh were chosen: $2.27 \cdot 10^{-6}$ m and $1.67 \cdot 10^{-6}$ m in x-, y- and z-directions. The required number of the mesh cells N_{cell} for the sample volume was found to be equal to $1.331 \cdot 10^6$ and $3.375 \cdot 10^6$, respectively. The simulation results are summarized in Table 7.6.

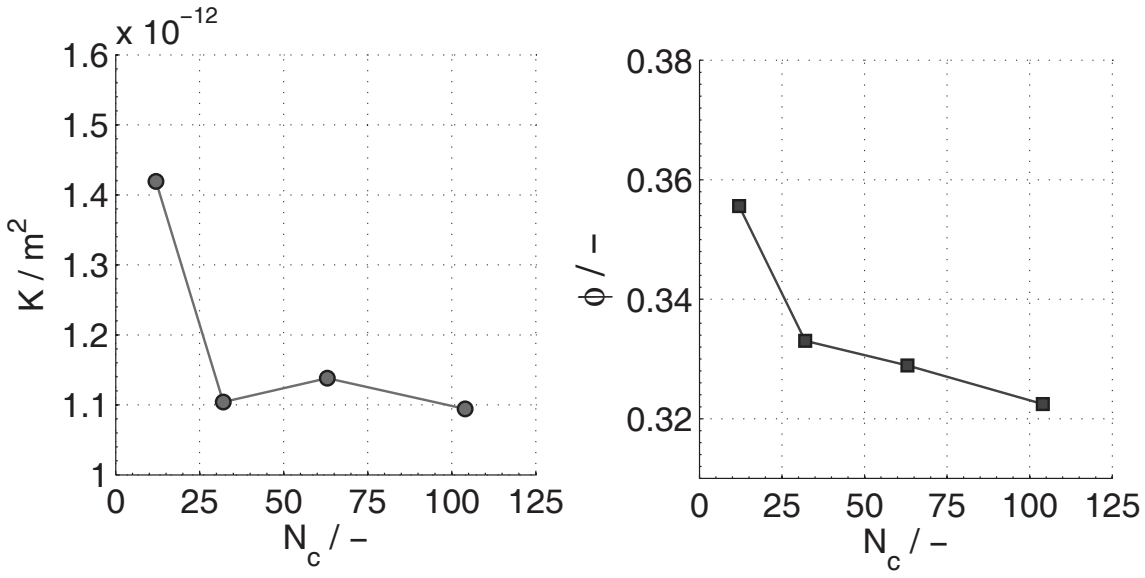

Figure 7.6: The computed permeability K and porosity ϕ for different sample volumes. The sample volumes were assigned to numbers N_c of equivalent parallel cylindrical capillaries, see Eq. 7.17 and Tables 7.2 and 7.5. The sample volume assigned to $N_c = 32$ is a minimum calculated sample volume, from which the macroscopic parameters K and ϕ change only slightly.

Table 7.6: The simulation inputs and results for the cubic sample volume with a length of the side $a = 0.25 \cdot 10^{-3}$ m. N_{cell} is referred to as the number of the mesh cells. Q is the volume flow rate in z-direction, A is the cross-section area of the sample, $\mathrm{d}p/\mathrm{d}z$ is the pressure gradient, K is the permeability, and ϕ is the porosity. Re, Eu, and Hg are referred to as the Reynolds, Euler, and Hagen number, respectively.

N_{cell}	Q	A	$-\mathrm{d}p/\mathrm{d}z$	K	ϕ	Re	Eu	Hg
(-)	m^3s^{-1}	m^2	(Pa m^{-1})	(m^2)	(-)	(-)	(-)	(-)
10^4	10^{-12}	10^{-8}	10^3	10^{-12}		10^{-3}	10^6	
42.1875	1	6.25	14.52	1.104	0.333	1.37	1.493	0.338
133.1	1	6.25	15.81	1.014	0.333	1.37	1.623	0.368
337.5	1	6.25	16.63	0.964	0.332	1.37	1.699	0.387

Fig. 7.7 shows the computed permeability K and porosity ϕ versus the number of the mesh cells N_{cell} used for the simulations. Fig. 7.7 and Table 7.6 demonstrate that the increase of the number of the mesh cells N_{cell} (i.e. the decrease of the mesh cell size) resulted in only a slight

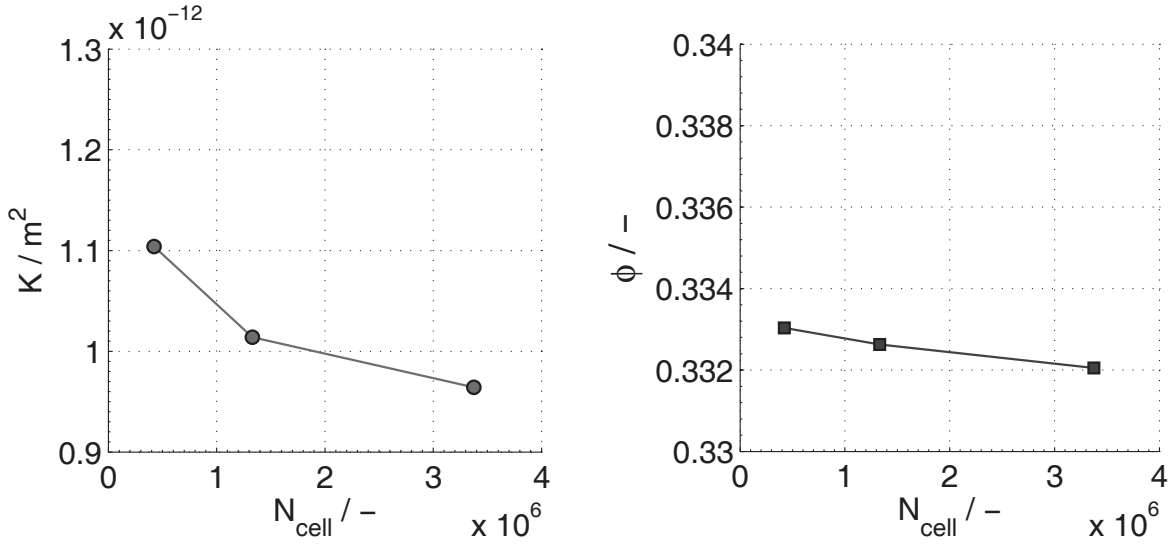

Figure 7.7: The computed permeability K and porosity ϕ for the cubic sample volume with a length of the side $a = 0.25 \cdot 10^{-3}$ m versus the number of the mesh cells N_{cell} used for the simulations. The increase of N_{cell} (i.e. the decrease of the mesh cell size) results in only a slight change of the calculated values of K and ϕ.

change of the calculated values of K and ϕ. Therefore, for further simulations the Cartesian mesh with a cell size of $3.33 \cdot 10^{-6}$ m was used in x, y and z - directions. It corresponds to $N_{\text{cell}} = 4.21875 \cdot 10^5$.

7.3.2 Wicking simulation

Sample volume

The same STL-file with the 3D image of the porous structure was imported into FLOW-3D as it was done for the simulations of the steady fluid flow through porous media, see section 7.3.1. For that simulations the representative equivalent volume (REV) was defined as the cubic sample volume assigned to the number $N_{\text{c}} = 32$ of equivalent parallel cylindrical capillaries, see Table 7.5. For the wicking simulation the height of the imbibed fluid is of interest. Therefore, the sample volume with the same square base ($N_{\text{c}} = 32$) but a longer height was chosen. The geometry of the sample volume is given in Table 7.7.

Table 7.7: The characteristics of the sample volume and the mesh chosen for simulations. a is the length of a side of the square base of the sample, H is the sample height and V is the sample volume. N_{cell} is referred to as the number of the Cartesian mesh cells snapped to the sample volume (the cell size is $3.33{\cdot}10^{-6}$ m in x- and y-directions and $3{\cdot}10^{-6}$ m in z - direction). N_{c} is referred to as the assigned number of equivalent parallel cylindrical capillaries, see Eq. 7.17.

a	H	V	N_{cell}	N_{c}
(m)	(m)	(m^3)	(-)	(-)
10^{-3}	10^{-3}	10^{-12}	10^4	
0.25	0.45	31.875	84.375	32

Mesh

The Cartesian mesh with a cell size of $3.33{\cdot}10^{-6}$ m in x- and y-directions and $3{\cdot}10^{-6}$ m in z - direction was snapped to the sample volume. As shown in section 7.3.1, the cell size smaller than $3.33{\cdot}10^{-6}$ m in x-, y- and z-directions does not cause a significant change of the permeability and porosity values. The required number of the mesh cells N_{cell} for the sample volume is given in Table 7.7.

Equivalent cylindrical capillaries

The sample volume was assigned to the number $N_{\text{c}} = 32$ of equivalent parallel cylindrical capillaries, see Eq. 7.17.

Simulation settings

An incompressible one-fluid free-surface flow through the porous medium was computed for the sample volume. The flow was specified as laminar with no-slip condition at the walls. The gravity component in z-direction was set to -9.8 m s^{-2}. The surface tension model was activated with the surface tension coefficient σ set to $6{\cdot}10^{-5}$ Pa s and the contact angle θ set to 0. At the boundary $z_{\min}$ the stagnation pressure was specified as $p = 1.013 \cdot 10^5$ Pa. The boundary $z_{\max}$ was set to be continuative. All the other boundaries were set to symmetry. The fluid initialization was activated using the initial fluid elevation of $5{\cdot}10^{-6}$ m from the boundary $z_{\min}$.

The thermophysical properties of a fluid were chosen in order to obtain the equilibrium wicking height h_{eq} within the given sample volume. The equilibrium wicking height can be estimated as

$$h_{\mathrm{eq}} = \frac{2\sigma \cos\theta}{\rho_{\mathrm{L}} g R_{\mathrm{s}}}, \tag{7.24}$$

where σ is the surface tension of the fluid, θ is the contact angle, g is the gravity acceleration and R_{s} is the static pore radius.

The properties do not refer to any real fluid. The density ρ_{L} and the surface tension σ were set in order to get h_{eq} smaller than the sample height H. The dynamic viscosity μ_{L} was chosen to ensure that h_{eq} is approached slowly, which is of importance for the simulation stability. The properties are summarized in Table 7.8.

The main settings of the simulations are summarized in Table 7.9. The details of the computation approach are given in section 7.2.

Simulation results

Fig. 7.8 demonstrates the open volume of the sample in the end of the wicking simulation. The pores are partly filled with the fluid. The simulation was stopped when in the smallest pore the fluid reached the boundary $z_{\max} = H$.

The increase of the volume of the imbibed fluid in time $V_{\mathrm{L}}(t)$ was obtained from the simulations. The mass of the imbibed fluid $m(t)$ was computed, see Fig. 7.9. The increase of m is fast in the beginning of the process and slows down to the end of the simulation. It is expected that when the capillary pressure is balanced by the gravity, the equilibrium wicking height h_{eq} is achieved and the wicking process stops. However, the pores enclosed in the sample volume are of different sizes and have irregular shapes. Thus, h_{eq} varies for the pores and might not

Table 7.8: The fluid properties set for the simulation. ρ_{L} and μ_{L} are referred to as the density and dynamic viscosity of the fluid, respectively. σ is the surface tension of the fluid and θ is the contact angle. The properties do not refer to any real fluid and were chosen in order to obtain the equilibrium wicking height for the given sample volume.

ρ_{L}	μ_{L}	σ	θ
$(\mathrm{kg\,m^{-3}})$	$(\mathrm{Pa\,s})$	$(\mathrm{N\,m^{-1}})$	(-)
	10^{-3}	10^{-5}	
2500	0.1	6	0

Table 7.9: The main settings of the wicking simulation in the porous medium.

General	
Interface tracking	Free surface or sharp interface
Number of fluids	One
Flow mode	Incompressible
Physics	
Viscosity and turbulence	Viscous laminar flow
	Wall shear boundary condition: no slip
Gravity	-9.8 m s^{-2} in z-direction
Surface tension	surface tension $\sigma = 6 \cdot 10^{-5}$ Pa s, contact angle $\theta = 0$
Numerics	
Pressure solver	GMRES (implicit)
Viscous stress solver	Explicit
Surface tension pressure	Explicit
VOF advection	One fluid, free surface
Momentum advection	First order
Fluid flow solver options	Solve momentum and continuity equations
Boundaries	
$z_{\min}$	specified stagnation pressure $p = 1.013 \cdot 10^5$ Pa
$z_{\max}$	continuative
Other boundaries	symmetry (default)
Initial conditions	
Pressure	Hydrostatic pressure in z-direction
Void pressure	$1.013 \cdot 10^5$ Pa
Fluid initialization (elevation)	$5{\cdot}10^{-6}$ m from $z_{\min}$

be reached simultaneously. Nevertheless, in the end of the simulation h_{eq} was achieved for the majority of the pores. As shown on Fig. 7.9, for the times from 2.5 s to 3.7 s the mass of the imbibed fluid increases from $1.708{\cdot}10^{-8}$ kg to $1.772{\cdot}10^{-8}$ kg that corresponds to the relative increase of 3.75 %. For these times Fig. 7.10 presents the pressure distribution in x-z cross-section of the sample volume. The cross-section was taken in the middle part of the sample. Fig. 7.10 shows that the bulk fluid does not rise significantly from 2.5 s to 3.7 s. This

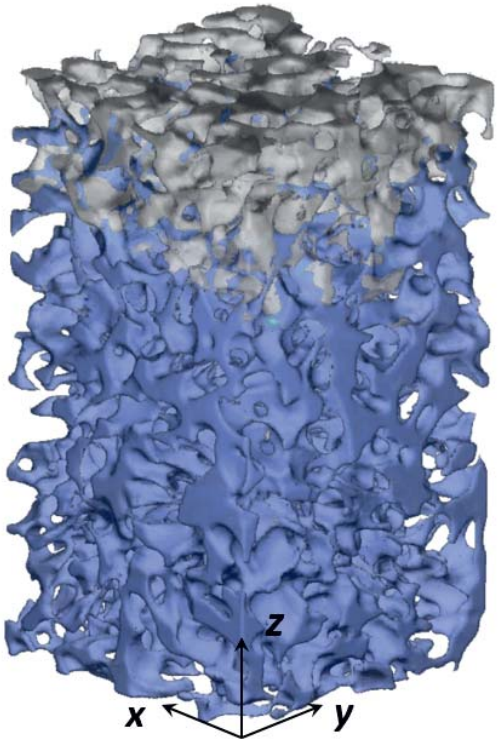

Figure 7.8: The open volume of the porous sample in the end of the wicking simulation. The pores are partly filled with the imbibed fluid (shown in purple color).

indicates that for the most of the pores in this cross-section the equilibrium wicking height h_{eq} was achieved. However, for some smaller pores in the upper area the fluid kept rising with the time, see Fig. 7.10. Similar results were obtained for the other cross-sections of the sample. The filling of such pores above the main wicking front contributes to the mass increase in the end of the simulation, see Fig. 7.9.

Fig. 7.11 demonstrates the results of the wicking simulation in terms of the wicking height h calculated as

$$h(t) = \frac{V_{\mathrm{L}}(t)}{\phi A}, \tag{7.25}$$

where the porosity was taken as $\phi = 0.33$, see section 7.3.1. The analysis of the sample cross-sections revealed no closed pores in the structure. Thus, the wicking height $h(t)$ is a volume-averaged value that characterizes the fluid rise in the network of the interconnected pores. Meanwhile, as mentioned before, the actual wicking height varies for the pores. Using the x-y cross-sections of the sample volume, the minimum and maximum wicking heights were estimated at $t = 0.5$ s, 1.5 s, 2.5 s and 3.7 s. The minimum wicking height corresponds to the height (z-coordinate) of the uppermost x-y-cross section completely filled with the fluid. The maximum wicking height corresponds to the height (z-coordinate) of the uppermost x-

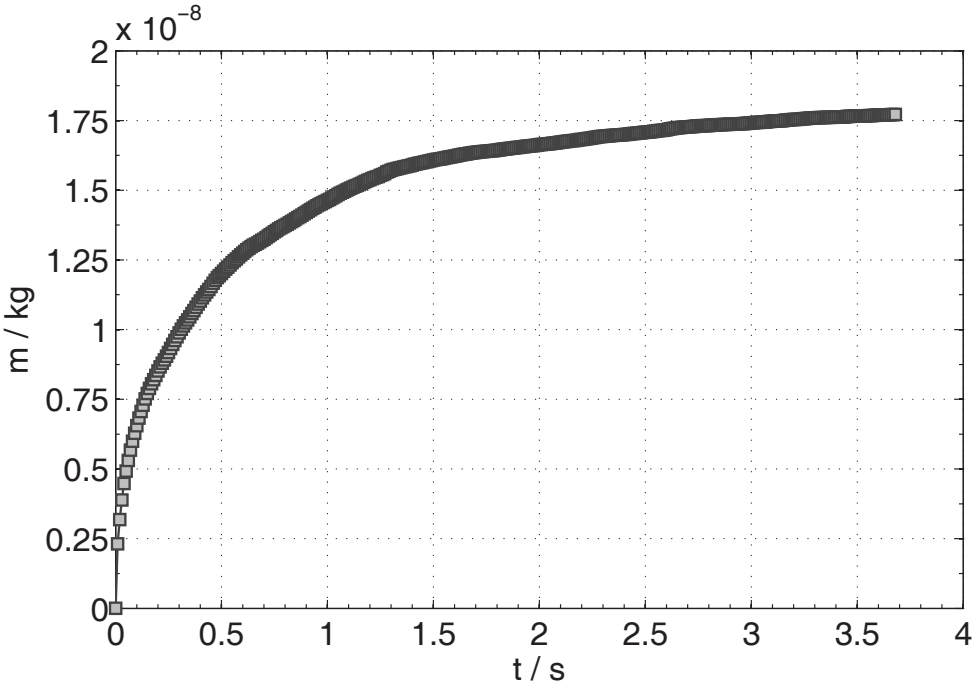

Figure 7.9: The mass increase of the liquid imbibed into the sample volume obtained from the wicking simulation.

y-cross section partly filled the fluid. The obtained values were plotted as the error bars to the corresponding volume-averaged values of h. Fig. 7.11 shows that the actual minimum and maximum wicking heights significantly deviate from the volume-averaged wicking heights at given times. This means that the chosen sample volume might not be considered as a representative elementary volume (REV) for the wicking simulation in such a porous structure.

The equilibrium wicking height h_{eq} was calculated as the volume-averaged h reached in the end of the simulation. It was found to be of approximately $3.44{\cdot}10^{-4}$ m. Using Eq. 7.24, the static pore radius $R_{\mathrm{s}} = 14.3 \cdot 10^{-6}$ m was computed. Nevertheless, the actual h_{eq} varied for the pores from approximately $2.8{\cdot}10^{-4}$ m to $4.5{\cdot}10^{-4}$ m, see Fig. 7.12. Such equilibrium wicking heights correspond to $17.5{\cdot}10^{-6}$ m and $10.9{\cdot}10^{-6}$ m, respectively.

The 3D-image of the porous structure was reduced in size using the magnification factor of $1.727{\cdot}10^{-1}$ applied in x-, y- and z-directions, see section 7.1. Meanwhile, the macroscopic parameters for this structure were experimentally determined, see Table 7.1. Applying the magnification factor to the value of the experimentally determined static pore radius, one obtains $R_{\mathrm{s}} = 20.7 \cdot 10^{-6}$ m. This value is comparable with the value of the static pore radius calculated from the simulation results ($R_{\mathrm{s}} = 14.3 \cdot 10^{-6}$ m).

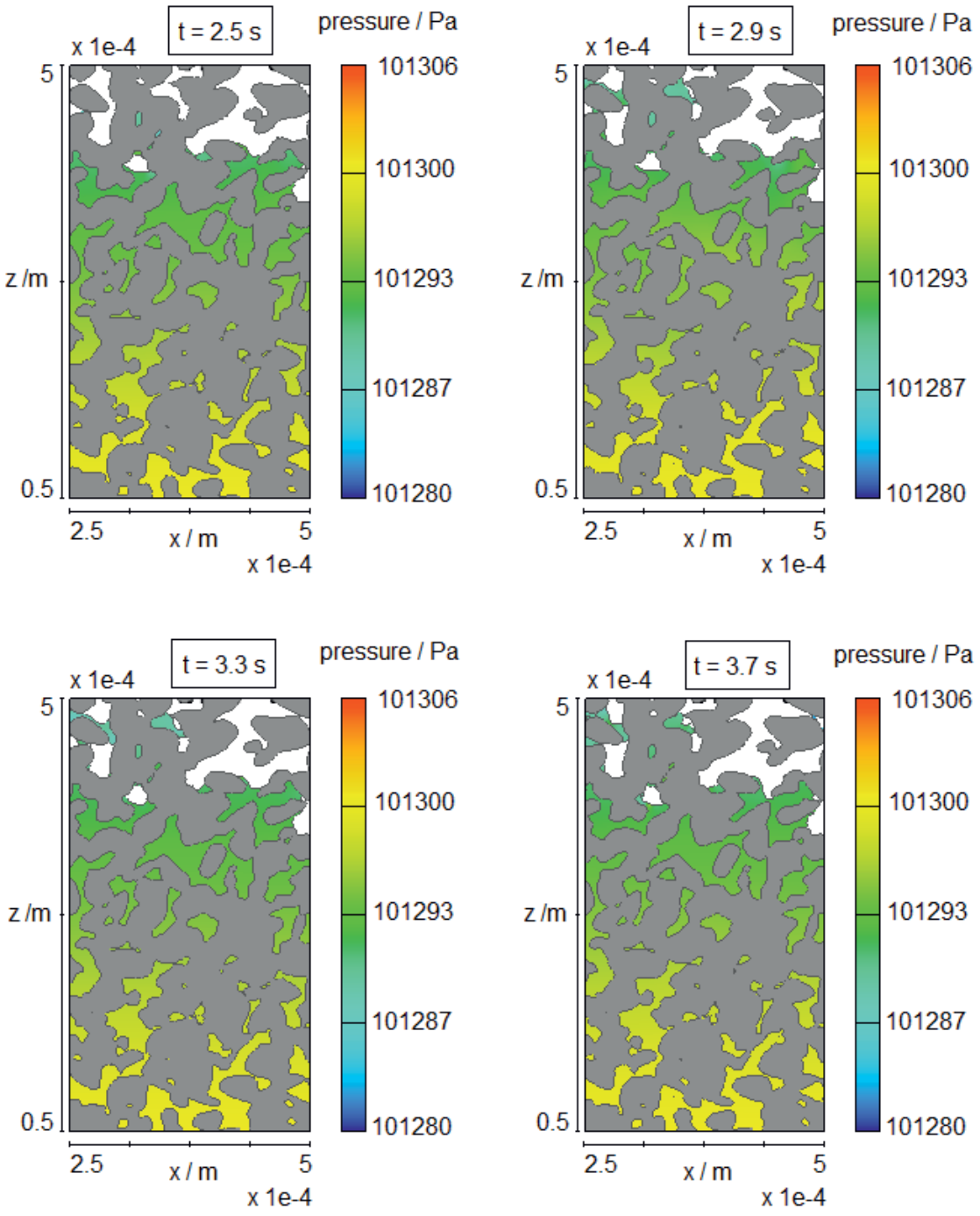

Figure 7.10: The pressure distribution (see the color bar) in the x-z cross-section of the sample at $t = 2.5$ s, 2.9 s, 3.3 s and 3.7 s of the wicking simulations. The solid structure is shown in gray color. The cross-section is taken in the middle of the sample. The level of the bulk fluid stays approximately constant, only for some smaller pores in the upper area of the sample the fluid keeps rising with the time.

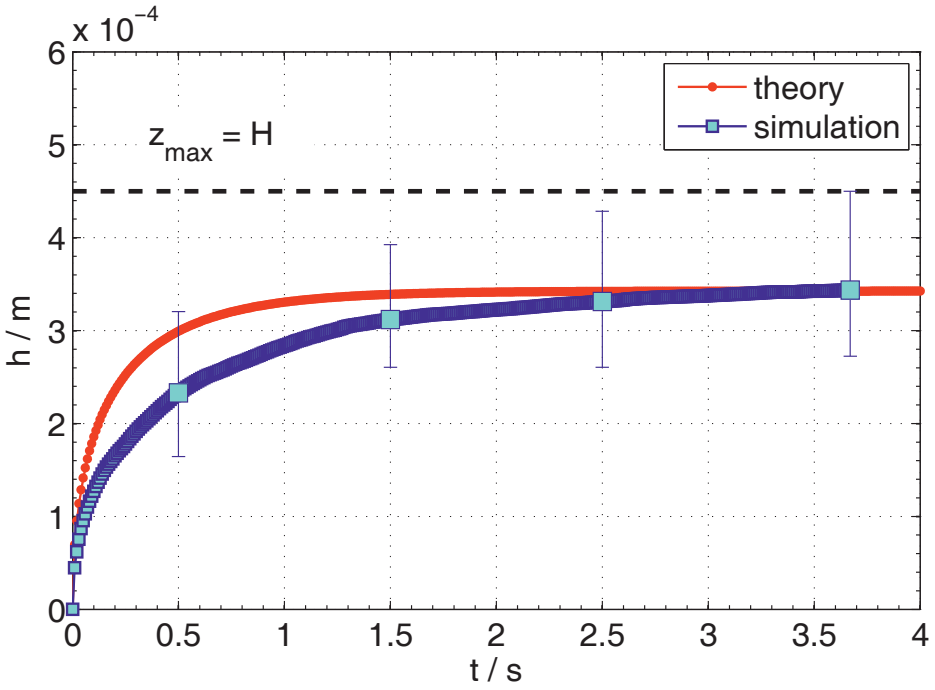

Figure 7.11: The wicking height vs. time. The simulation results correspond to the volume-averaged values computed via Eq. 7.25. The error bars are referred to as the minimum and maximum values of the actual wicking height at given times. The theoretical prediction was performed via the Lucas-Washburn equation with gravity effects (Eq. 2.95). The macroscopic parameters for Eq. 2.95 (the permeability K, the porosity ϕ and the static pore radius R_s) were taken as determined in the simulations. The predicted wicking height is within the actual minimum and maximum values (error bars) determined from the simulations.

A theoretical prediction of the wicking height in time was performed via the Lucas-Washburn equation with gravity effects (Eq. 2.95) using the macroscopic parameters determined from the simulations, see section 7.3.1. The permeability K, the porosity ϕ and the static pore radius R_s were taken as $1.104 \cdot 10^{-12}$ m^2, 0.33 and $14.3 \cdot 10^{-6}$ m, respectively. The computed values of K, ϕ and R_s are comparable to the experimentally determined for similar porous structures, see Table 4.4. The predicted wicking height is within the actual minimum and maximum values (error bars) of $h(t)$ determined from the simulations, see Fig. 7.11. The volume-averaged wicking height obtained from the simulations deviates from the predicted via the Lucas-Washburn model. On the one hand, this is due to the averaging of the volume of fluid used for the calculation of $h(t)$ via Eq. 7.25. On the other hand, for the Lucas-Washburn model the wicking height h at a given t is assumed to be the same for all the pores. However, this does not hold for the computed sample volume. In addition, the macroscopic parameters used for the Lucas-Washburn model are the volume-averaged values.

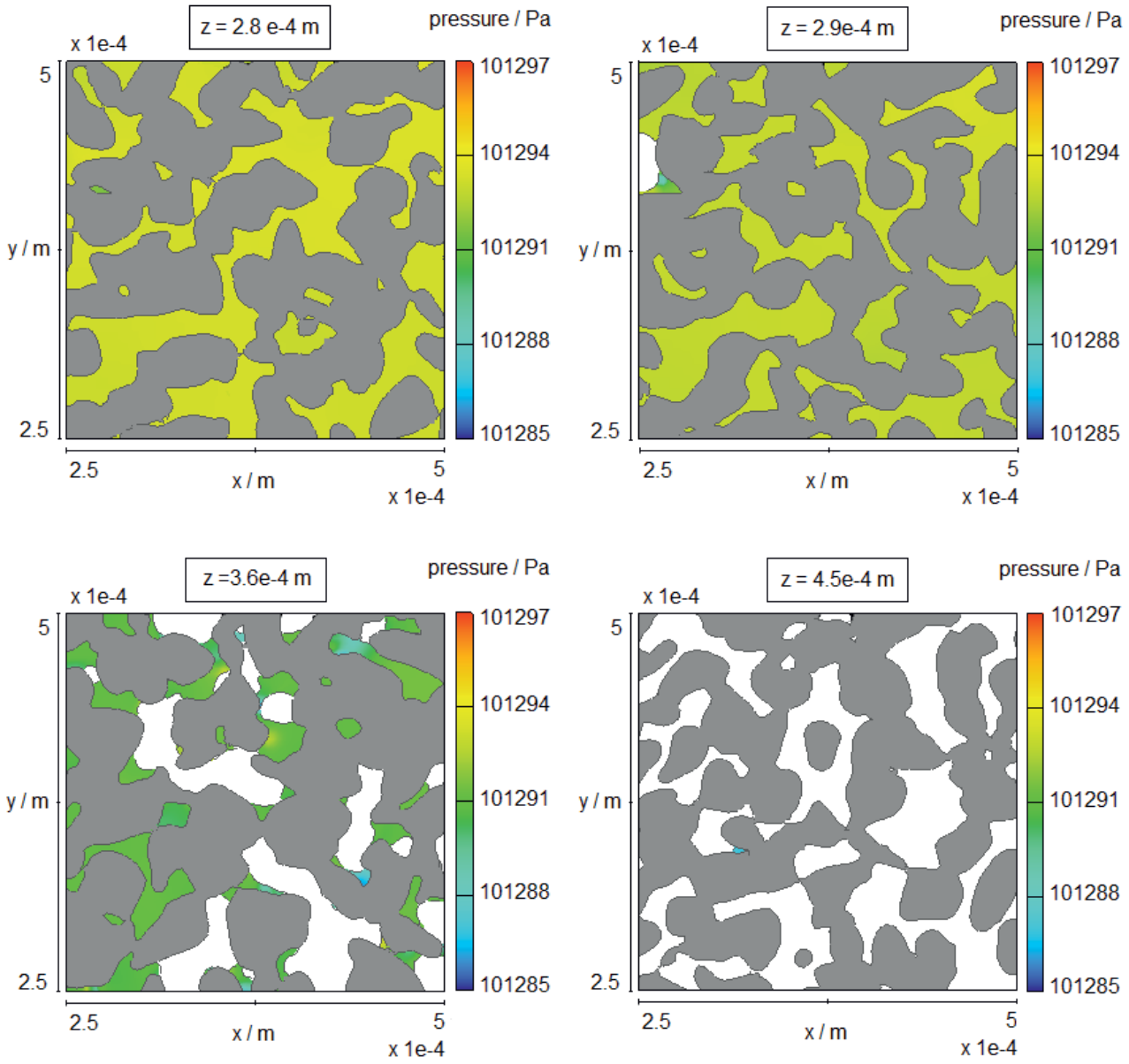

Figure 7.12: The pressure distribution (see the color bar) in x-y cross-sections of the sample in the end of the wicking simulation ($t = 3.7$ s). The solid structure is shown in gray color. The x-y cross-sections were taken at different z-coordinates between the minimum and maximum values of the equilibrium wicking height h_{eq}. The absence of fluid in the cross-section indicates that h_{eq} for the corresponding pores has been already reached at lower z.

7.4 Benchmark macroscopic simulation

7.4.1 Porous media model

FLOW-3D features a porous media model that is applicable to compute flows in structures with a pore size much smaller than a computational cell. This model is based on the use of the volume-averaged parameters of porous media and the modification of the Navier-Stokes equations.

In case of saturated flows in porous media a sharp interface is assumed between fully saturated and fully unsaturated regions. The capillary pressure p_c is a user-defined value that is subtracted from the void pressure at the sharp interface. The porosity ϕ of a medium in FLOW-3D is identical to the volume fraction V_F. The viscous pressure losses are taken into account using a porous media drag b. The porous media drag b_x in x-direction is calculated as

$$b_x = F_d u, \tag{7.26}$$

where u is the x-component of the fluid velocity and F_d is the drag coefficient. The porous media drag b_x is subtracted from the right side of the momentum equation for x-direction given as Eq. 7.2. Analogically the porous media drags b_y and b_z are computed and subtracted from the right sides of Eqs. 7.3 and 7.4, respectively. For low-velocity flows in porous media the drag coefficient F_d is calculated as

$$F_d = a_F V_F^{-b}. \tag{7.27}$$

In Eq. 7.27 the constant b is taken as zero and the constant a_F is expressed as

$$a_F = \frac{V_F}{K}\frac{\mu}{\rho}, \tag{7.28}$$

where ρ and μ are the fluid density and dynamic viscosity, respectively, and K is the permeability of porous media. The value of a_F should be preliminary defined by user. In fact, such an approach is a modification of the Navier-Stokes equations using Darcy's law. In order to perform computations using this approach, the porous media model with a Darcian saturated drag should be activated (as it was done for this study).

In addition, FLOW-3D is able to calculate drags that are dependent on the Reynolds number and the saturation of a porous medium. These features are not studied in this work.

7.4.2 Wicking simulation

Sample volume

Using the primitive shapes generated by FLOW-3D, two rectangular and two cylindrical geometry components were created. The sizes of the experimental samples R19, R12, C19 and C12 were applied, see Table 4.2.

Mesh

The uniform Cartesian meshes were used for the rectangular samples R19 and R12. For each of the samples C19 and C12 a cylindrical sector of 45° was chosen and the cylindrical mesh was snapped to this sector. For each sample the number of the mesh cells N_{cell} was set to 10^3.

Simulation settings

An incompressible one-fluid free-surface flow through the porous medium was computed for each sample volume. The gravity component in z-direction was set to -9.8 m s^{-2}. The porous media model with a Darcian saturated drag was activated. For each sample the porosity ϕ, the capillary pressure $\triangle p$ and the constant a_{F} of the drag coefficient were specified. The latter was computed via Eq. 7.28. The capillary pressure was calculated using the Young-Laplace equation for a circular capillary given as

$$\triangle p = \frac{2\sigma \cos\theta}{R_{\text{s}}}, \tag{7.29}$$

where σ is the surface tension of the fluid, θ is the contact angle, and R_{s} is the static pore radius. The experimentally obtained values of the porosity ϕ, static pore radius R_{s} and permeability K were used for the computations, see Table 4.4. For each sample the simulations were performed using the thermophysical properties of the FC-72 liquid at 101325 Pa and 298.15 K and the liquid nitrogen at 101325 Pa and 77.355 K (saturation). The surface tension σ, density ρ_{L} and dynamic viscosity μ_{L} of the FC-72 liquid and liquid nitrogen were given in Tables 4.3 and 4.6, respectively. For both liquids the contact angle θ was taken as zero. The computed input characteristics for the porous media model are summarized in Table 7.10.

At the boundary $z_{\min}$ the stagnation pressure condition was applied and the fluid fraction F was set to 1 to simulate the contact with a liquid reservoir. All the other boundaries were set to symmetry.

The main settings of the simulations are summarized in Table 7.11. The details of the computation approach are given in sections 7.2 and 7.4.1.

Table 7.10: The input characteristics for the porous media model. ϕ is referred to the porosity, $\triangle p$ is the capillary pressure and a_{F} is the constant for the Darcian drag coefficient calculated via Eq. 7.28.

		FC-72		Liquid nitrogen	
Sample	ϕ	$\triangle p$	a_{F}	$\triangle p$	a_{F}
	(-)	(Pa)	(s^{-1})	(Pa)	(s^{-1})
		10^2	10^4	10^2	10^4
R19	0.40	12.183	9.941	9.015	5.256
R12	0.44	19.512	18.265	14.439	9.657
C19	0.35	12.183	9.794	9.015	5.178
C12	0.31	19.512	34.442	14.439	18.211

Simulation results

An increase of the volume of the imbibed fluid in time $V_{\mathrm{L}}(t)$ was obtained from the simulations for each sample and each fluid. The mass of the imbibed fluid $m(t)$ was computed using the corresponding densities. The simulation results are presented on Fig. 7.13.

The wicking experiments have been performed with the samples R19, R12, C19 and C12 and the FC-72 liquid, see section 4.2. The results were plotted correspondingly on Fig. 7.13. The theoretical prediction was performed for both liquids and each sample using the Lucas-Washburn equation with gravity effects given as Eq. 2.95. The thermophysical properties of the FC-72 liquid and liquid nitrogen as well as the macroscopic parameters required for the computation via Eq. 2.95 were taken from Tables 4.3, 4.6 and 4.4, respectively. The simulation and the Lucas-Washburn equation with gravity effects provide similar results for the corresponding samples and fluids. This due to the similar computation approaches based on the combination of the momentum equation with Darcy's law. The experiment results for the FC-72 liquid are in a good agreement with the simulation data and theoretical prediction. The wicking experiments with liquid nitrogen were performed only with superheated samples. Therefore, for this case no experiment data is presented on Fig. 7.13. The wicking results with superheated samples are discussed in chapter 4.

Table 7.11: The main settings of the wicking simulation in the porous medium.

General	
Interface tracking	Free surface or sharp interface
Number of fluids	One
Flow mode	Incompressible
Physics	
Porous media	Darcian saturated drag
Gravity	-9.8 m s^{-2} in z-direction
Numerics	
Pressure solver	GMRES (implicit)
VOF advection	Automatic
Momentum advection	First order
Fluid flow solver options	Solve momentum and continuity equations
Boundaries	
$z_{\min}$	stagnation pressure with the fluid fraction $F = 1$
Other boundaries	symmetry (default)
Initial conditions	
Pressure	Uniform pressure
Void pressure	0

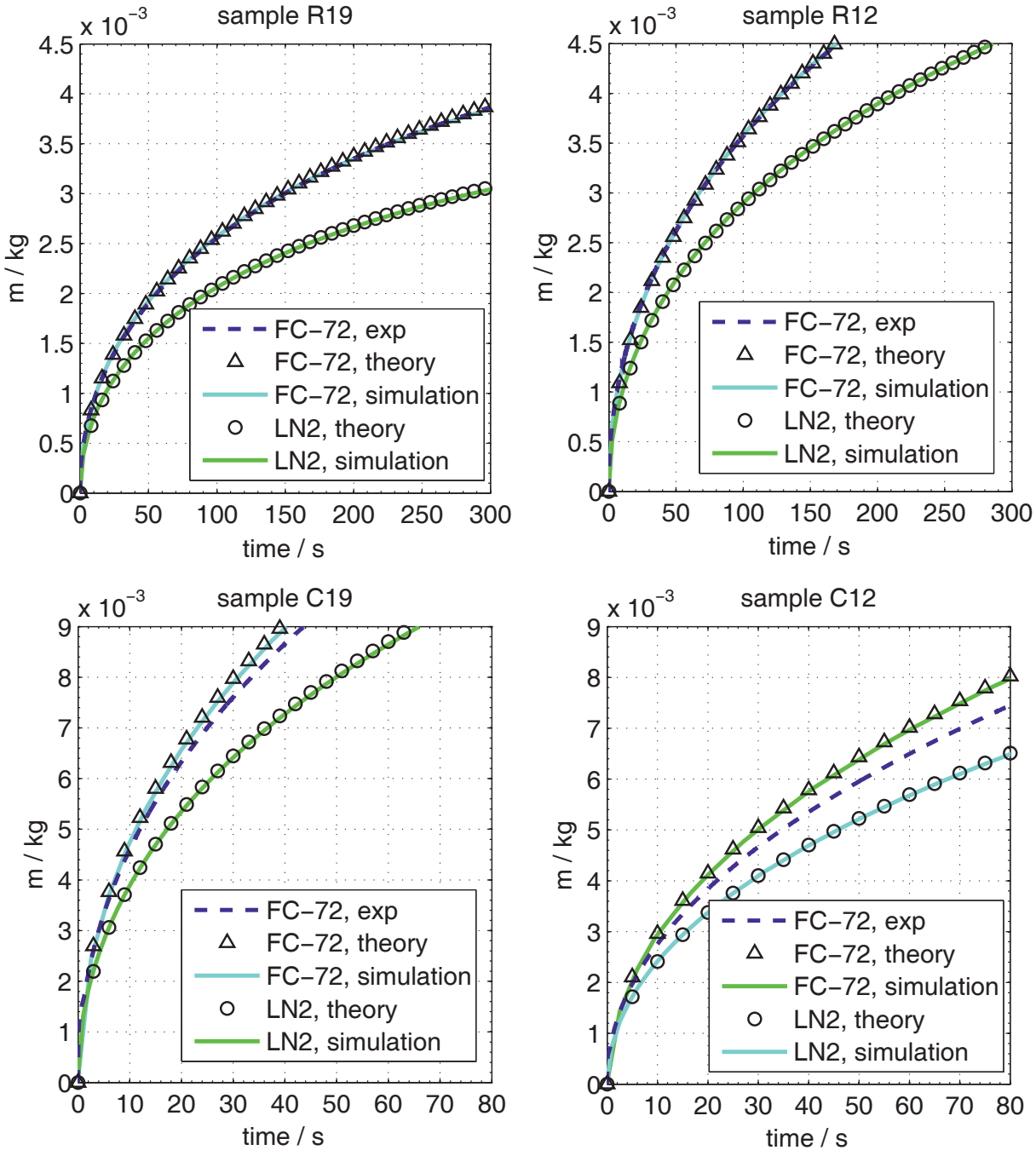

Figure 7.13: The mass of the imbibed FC-72 liquid and liquid nitrogen (LN2) into the samples R19, R12, C19 and C12 during the wicking process. The simulation results correspond to the results of the wicking simulation using the porous media model in FLOW-3D. The theoretical prediction was performed using the Lucas-Washburn equation with gravity effects (Eq. 2.95). The wicking experiments with the FC-72 liquid are described in section 4.2.

7.5 Summary

Benchmark microscopic and macroscopic simulations were performed using the computational fluid dynamics software FLOW-3D. Numerical calculation of the momentum and continuity equations was conducted for the isothermal incompressible one-fluid flow problems.

The microscopic simulations were performed using the 3D-image obtained via the X-ray tomography of a porous structure. From the steady fluid flow simulation the pressure drop through a porous medium was calculated. Using the pressure gradient and applying Darcy's law the permeability was determined. The porosity was calculated using the volume of the fluid contained in a completely saturated porous sample. From the simulations with different sample volumes the representative elementary volume (REV) was determined. It corresponds to the minimum sample volume, from which macroscopic parameters become independent of size. For the investigated structure the REV was defined as the sample volume assigned to the number $N_c = 32$ of equivalent parallel cylindrical capillaries (the length of the sample side $a = 0.25 \cdot 10^{-3}$ m), see section 7.3.1. For this sample volume the permeability $K = 1.104 \cdot 10^{-12}$ m^2 and the porosity $\phi = 0.33$ were computed. The mesh study revealed a Cartesian mesh with a cell size of $3.33 \cdot 10^{-6}$ m in x-, y- and z-directions being sufficient for the simulations.

The microscopic simulation of the wicking process allowed to obtain the increase of the volume of the imbibed fluid in time. The equilibrium wicking height h_{eq} was calculated as the volume-averaged height reached in the end of the simulation. The equilibrium wicking height h_{eq} of approximately $3.44 \cdot 10^{-4}$ m was obtained. Using the volume-averaged h_{eq}, the static pore radius $R_s = 14.3 \cdot 10^{-6}$ m was computed. The calculated values of K, ϕ and R_s were found to be comparable to the experimentally determined for similar porous structures, see Table 4.4. Nevertheless, the actual h_{eq} varied for the pores of the structure from approximately $2.8 \cdot 10^{-4}$ m to $4.5 \cdot 10^{-4}$ m. The deviations of the actual wicking heights in the pores from the volume-averaged values were also observed during the imbibition time. Such a result indicates that the chosen sample volume might not be considered as a representative elementary volume (REV) for the wicking simulation. The wicking height was predicted via the Lucas-Washburn model with gravity effects and using the calculated values of the macroscopic parameters K, ϕ and R_s. The predicted $h(t)$ was found to be within the actual minimum and maximum values of the wicking height determined from the simulations. However, it significantly deviated from the volume-averaged $h(t)$ obtained from the simulations. The Lucas-Washburn model is based on the volume averaging of the macroscopic parameters of the structure and implies the same wicking height in each pore. The considerable deviation of the actual $h(t)$ between the pores

was observed from the simulation results. Therefore, in this case the model can not provide a good prediction of the wicking results.

The macroscopic wicking simulations were performed using the porous media model available in FLOW-3D. The model is based on the computation of the Navier-Stokes equations and Darcy's law for flow in porous media. The simulations were conducted for the sample of geometries, sizes and macroscopic parameters corresponding to the samples used in the wicking experiments with liquid nitrogen and the FC-72 liquid. The theoretical prediction was performed via the Lucas-Washburn model with gravity effects. Due to the similar computation approaches the simulation and theoretical prediction provide similar results. Both were found to be in a good agreement with the experiment data.

Chapter 8

Conclusion and Outlook

8.1 Conclusion

The aim of this work was to advance the knowledge on the behavior of fluids in porous materials. The main focus was on the investigation of wicking of cryogenic liquids (cryo-wicking). The results are intended to contribute to the understanding of the wicking of a cryogenic liquid subjected to evaporation and become a foundation for further research in this field. In the second part of the work, the analysis of the capillary transport abilities of porous polymer-derived ceramic samples is presented. It provides an input for characterization of the porous media fabricated via the freeze-casting method. The study may be used to state a relation between processing parameters, microstructure and mass transport characteristics of this type of porous ceramics. In the third part, benchmark microscopic and macroscopic simulations performed via the computational fluid dynamics FLOW-3D are discussed. The results validate the applicability of the software to solve fluid flow problems in porous media. They may serve as a basis for further numerical investigations aimed to predict the wicking process, for example, under non-isothermal conditions or with a phase change.

8.1.1 Wicking of a cryogenic liquid

Wicking of a cryogenic liquid subjected to evaporation was studied. Two one-dimensional macroscopic models were proposed for the prediction of vertical wicking of a cryogenic liquid at saturation temperature into superheated porous media. The models are based on averaging of porous media via the introduction of macroscopic parameters (porosity, static pore radius, and permeability). The prediction is given in terms of the wicking height increase in time.

The models account for evaporation occurring at the wicking front due to the heat transfer between the superheated porous media and cryogenic liquid. The influence of the vapor flow created due to evaporation at the wicking front is particularly taken into consideration in the second model. For both models the dimensionless form was deduced applying the Buckingham π theorem. This allowed to find relations between the parameters and variables of the models and some dimensionless numbers (Bond, capillary and Jakob numbers).

Wicking experiments with liquid nitrogen were performed in a one-species system under predefined non-isothermal conditions using a novel test facility. The test facility enabled the determination of the mass of the imbibed liquid nitrogen measuring the weight increase of a porous sample during the imbibition. To the author's extent of knowledge these are the first wicking experiments performed with cryogenic fluids using the weight-time measurement technique. Prior to cryo-wicking experiments the test samples were characterized in vertical wicking experiments with the FC-72-liquid at room temperature. The samples were sintered glassfilter elements (borosilicate glass 3.3) of different characteristic pore sizes ($R_s = 19.7 \cdot 10^{-6}$ m and $R_s = 12.3 \cdot 10^{-6}$ m) and geometries (rectangular and cylindrical). A sample superheat in the test facility for cryo-wicking experiments was defined by the initial position of a sample in a stratified vapor environment inside the cryostat. The establishment of linear temperature gradients in nitrogen vapor was observed in the initial and the wicking sample locations. The wicking front propagation was detected using simultaneous sample weight and temperature measurements. Both method showed a good agreement with each other. The wicking height of 0.08 m was achieved in the experiments. Along with the results of Zhang et al. [127], these are the first reported values of the wicking height of liquid nitrogen. The mass of the imbibed liquid nitrogen was determined varying the sample superheat, geometry and porous structure. The experiment data was found to be in a qualitative agreement with the prediction given by the proposed theoretical model. The results revealed that the liquid loss at the wicking front due to evaporation caused by the heat transfer between liquid nitrogen and superheated sample does not lead to a significant decrease of the imbibition rate. This was particularly observed for the samples of smaller cross-sections (rectangular). For these samples a good quantitative agreement between the experiment and prediction data was found for the relative decrease of the imbibition rate at two sample superheats. However, the samples of larger cross-sections (cylindrical) revealed a significant deviation from the theoretical prediction in case of high sample superheat. A lower imbibition rate was observed. That was explained by the influence of the vapor created due to the heat transfer at the wicking front. The vapor counteracted the wicking front propagation. This effect was most pronounced for highly superheated samples of

large cross-sections due to a larger amount of the created vapor and a more complex trajectory for it to escape of the porous structure at the sample sides. The error analysis was given for the proposed model. The relative errors were estimated and found to be up to 12.7 % for rectangular and up to 16.5 % for cylindrical samples. The results were presented in dimensionless form. The study of the model parameters was conducted. It was shown that the capillary and Reynolds numbers decrease when the wicking front approaches the equilibrium wicking height.

In order to investigate the impact of the created vapor flow on the imbibition, cryo-wicking experiments were performed with sealed samples. The sealing was applied at lateral sides of the samples. Thus, the vapor created at the wicking front was partly blocked and could only escape through the sample top. The sealing showed no influence on the wicking rates in the experiments with the FC-72 liquid (no sample superheat). Cryo-wicking experiments were performed with liquid nitrogen using the same test facility as it was done for the tests with the not-sealed samples. For each experiment case similar sample superheat was ensured. The results of simultaneous sample weight and temperature measurements revealed that the local temperature of solid structure decreased to the saturation temperature of nitrogen before it got saturated with the liquid. Such a temperature decrease could be stipulated by the impact of the cold vapor created above the wicking front and pushed along the sample height due to the sample sealing. A significant decrease of the imbibition rates was observed for the sealed samples compared to the same samples with no sealing. That was explained by the impact of the additional pressure created by the vapor partly blocked in the structure. It was also observed that higher sample superheat might not cause a stronger reduction of the wicking rate. In case of high sample superheat a large amount of vapor is created in the beginning of the wicking process. This vapor is pushed along the sample height and might significantly cool down the solid structure above the wicking front. That leads to the production of the reduced amount of vapor, which resists the wicking front propagation, and thus, results in the increase of the imbibition rate. This is in conformity with experiment results. A qualitative agreement was observed between the experiment data and the prediction via the proposed wicking model in case of a low sample superheat. The model describes the results better than the Lucas-Washburn model performed for the isothermal case (no sample superheat). However, for high sample superheat the proposed model significantly underestimates the data. That is explained by the fact that the model does not account for such a great sample temperature decrease during the imbibition. The results were also discussed in dimensionless form. The influence of the model parameters on the prediction was studied.

8.1.2 Wicking into porous ceramic monoliths

Wicking experiments were performed to investigate the capillary transport abilities of anisotropic porous polymer-derived ceramic monoliths. The silicon oxycarbide (SiOC) cylindrical samples were fabricated via the freeze-casting method in the Advanced Ceramic Group of the University of Bremen. Two different freezing temperatures (-80 °C and -150 °C) were applied to produce lamellar pore structures of similar porosity ($\phi = 47$ % and $\phi = 52$ %, respectively) but different pore size ($R_{\text{av}} = 8.35{\cdot}10^{-6}$ m and $R_{\text{av}} = 1.57{\cdot}10^{-6}$ m, respectively). The monoliths revealed an axial anisotropy. The sample weight measurements were conducted during the vertical wicking of the FC-72 liquid into the test samples. The increase of the mass of the imbibed liquid was evaluated. In order to study the impact of the anisotropy, the experiments were performed at different sample orientations. The permeability of the structures was determined using results at the viscous-dominated stage of wicking. The obtained values varied at different sample orientations. The deviations were found to be from 10% to 49% that quantified the impact of the axial anisotropy on the capillary transport abilities of the porous structures. Also the deviations were found to be larger for the samples prepared at the freezing temperature of -150 °C that revealed smaller average pore size. Meanwhile, the samples prepared at the freezing temperature of -80 °C demonstrated higher permeability values that could be stipulated by their bigger average pore size. Accordingly, the complete saturation of such samples with the experimental liquid occurred approximately two times faster. A theoretical prediction of the wicking results were performed using the Lucas-Washburn model with gravity effects. For the computation of this macroscopic model the directionally dependent values of the permeability were applied. The theoretical prediction revealed a good agreement with experiment data. Such a result implies applicability of macroscopic modeling as a simple tool to predict wicking in some anisotropic porous structures. However, in this case a preliminary characterization and directional determination of macroscopic parameters of a porous medium are of importance.

8.1.3 Numerical simulations

The capillary transport properties of porous media and the wicking process were studied using the computational fluid dynamic software FLOW-3D Version 10.0. The overview of the computation approach, relevant equations and numerical approximations was given. Benchmark microscopic (pore level) and macroscopic simulations were performed for the isothermal incompressible one-fluid flow problems. The fluid was assumed to be Newtonian and the flow regime was laminar.

The software showed to be a good tool to provide the information on macroscopic parameters of real porous structures using their 3D-images. A 3D-image of the porous structure was reconstructed as the stereolithography (STL) file from the radiographs obtained via X-ray tomography. The STL file was imported in FLOW-3D as a solid geometry object. The steady fluid flow simulation allowed to determine a pressure drop through the porous medium and to calculate the permeability ($K = 1.104 \cdot 10^{-12}$ m^2) via Darcy's law. The porosity of the structure ($\phi = 0.33$) was evaluated from the volume of the fluid in a completely saturated structure. From the analysis of the permeability and porosity values obtained at different sample volumes the representative elementary volume (REV) was estimated. This is a minimum sample volume, from which macroscopic parameters become independent of size. The mesh study was performed.

FLOW-3D enabled to simulate the wicking process on a pore level. The simulation results were obtained in terms of the increase of the volume of the imbibed fluid in time. The equilibrium wicking height ($h_{\mathrm{eq}} = 3.44{\cdot}10^{-4}$ m) was calculated as the volume-averaged height reached in the end of the simulation. Using this value, the static pore radius ($R_{\mathrm{s}} = 14.3{\cdot}10^{-6}$ m) was estimated. The values of the permeability, porosity and the static pore radius obtained from the simulations were found to be comparable to the experimentally determined for similar porous structures. However, the image analysis of the simulation results showed that the actual wicking heights in pores significantly varied from the volume-averaged value. Thus, the chosen sample volume could not be considered as a REV for the wicking simulation. The simulation results were compared to the theoretical prediction given by the Lucas-Washburn model with gravity effects. For the model computations the macroscopic parameters obtained from the simulation were used. The predicted wicking height was found to be within the actual minimum and maximum values of the wicking height determined from the image analysis. Nevertheless, it significantly deviated from the volume-averaged value. As discussed above, the assumption of the uniform wicking height was violated for the chosen sample volume. Meanwhile, such an assumption is of importance when applying the Lucas-Washburn model. This explains the obtained deviations.

The porous media model available in FLOW-3D was applied to perform macroscopic wicking simulations. This model combines numerical computations of the Navier-Stokes equations and Darcy's law for flow in porous media. The porous media model allows to predict wicking results for lab-scale samples with pre-defined macroscopic parameters. The simulations were conducted for the sample of geometries, sizes and macroscopic parameters corresponding to the samples used in the wicking experiments with liquid nitrogen and the FC-72 liquid. The results were

found to be in a good agreement with the theoretical prediction via the Lucas-Washburn model with gravity effects. This is stipulated by the similar computation approaches. The results were also validated by the experiment data.

8.2 Outlook

This section summarizes the ideas for further experimental and theoretical research of the wicking phenomenon.

This work presents new experiment data for wicking of a cryogenic liquid (nitrogen) into porous media. The test facility built for these experiments enabled the superheat of the samples with regard to the liquid at saturation temperature. This allowed to study the effects of the evaporation and the influence of the newly created vapor on the wicking process. Nonetheless, no wicking experiments were performed with liquid nitrogen under isothermal conditions. The comparison of the isothermal wicking results with the results obtained in this work can provided an important input for the characterization of the process. Such results could also serve for the determination of the equilibrium wicking height for liquid nitrogen, see section 4.4.4. In experiments with some volatile liquids Fries et al. [126, 38] showed that the evaporation from a porous surface into surrounding environment can significantly reduce the equilibrium wicking height. This can be then proved also for a cryogenic liquid. Due to the hardware limitations it was not possible to achieve the equilibrium wicking height for the test samples. To overcome this, the samples of a larger pore size can be tested. Alternatively, the existing setup can be modified by arranging the protection baffle higher in the direction of the lid of the cryostat (see Fig. 4.5), or a larger setup can be built. In addition, it is of interest to perform cryo-wicking experiments with samples of different geometries, porous structures and thermophysical properties. For example, the samples tested in this work were of low thermal conductivity (1.13 $\mathrm{W\,m^{-1}\,K^{-1}}$ at 300 K). To study the influence of heat conduction in the solid structure of a porous sample on the wicking process, one might also perform experiments with structures of high thermal conductivity. The use of porous ceramics as the test samples for cryo-wicking experiments might be of interest for possible application of such materials for the transport of cryogenic propellants. Anisotropic porous samples can be tested too. The radial wicking of a cryogenic liquid might be studied. Moreover, there is still a gap in the existing knowledge for the wicking behavior of other cryogenic liquids, such as hydrogen, oxygen, methane, etc.

Some improvements of the proposed theoretical model for cryo-wicking can be done. More accurate results might be obtained if one accounts for heat conduction in the solid structure

of a porous sample. This was discussed in section 3.1.1. The experiment results showed that the vapor flow created due to the heat transfer of a cryogenic liquid with a superheated porous structure might significantly cool down the dry solid structure above the wicking front. Therefore, one should also account for the heat transfer between the created vapor and the dry solid structure. In addition, the evaporation from a porous surface of the sample saturated with a cryogenic liquid into surrounding environment can be studied. For that one might consider an approach proposed in [126, 38].

There is still a lack of data on the capillary transport abilities of porous ceramics fabricated using different techniques, such as sacrificial templating, direct foaming, etc. Moreover, the processing parameters of the freeze-casting method applied to produce porous samples for this work might be varied in a wider range to control pore size, porosity, and porous structure anisotropy. Thus, the wicking behavior can be adjusted. In particular, the effect of anisotropy on wicking should be also studied by comparing the obtained results with the wicking results for samples of homogeneous structures of similar pore size and porosity. More information on this account might be of interest for both, fluid dynamics and ceramics research communities.

For further numerical investigations the feasibility of the computational fluid dynamics software (CFD) FLOW-3D to simulate the wicking process under non-isothermal conditions and with a phase change might be studied at both, macroscopic and microscopic (pore size) scales. A possibility of the implementation of the heat transfer by conduction and convection for wicking simulations should be investigated. At a microscopic scale one might first consider to perform simulations using simplified geometries produced by the computer aided design tools. Other CFD software products can be validated to conduct wicking simulations. Herewith it is of major importance to provide reliable simulation results at reduced computational costs.

Appendix A

Appendix

A.1 The derivation of the solution for the equation for wicking of a cryogenic liquid into superheated porous structures with evaporation at the wicking front

This section is based on the publication "Wicking of liquid nitrogen into superheated porous structures"[1] by Y. Grebenyuk and M.E. Dreyer [34].
The equation is given in section 3.1.1 as

$$1 = ch + bh\dot{h}(1 + \epsilon(n_1 + n_2 h)). \tag{A.1}$$

Integrating Eq. A.1, one obtains

$$\begin{aligned} t(h) &= \int \frac{b(1+\epsilon(n_1+n_2h))h}{1-ch}\mathrm{d}h = \\ &= b(1+\epsilon n_1)\underbrace{\int \frac{h\mathrm{d}h}{1-ch}}_{1} + b\epsilon n_2 \underbrace{\int \frac{h^2}{1-ch}\mathrm{d}h}_{2}. \end{aligned} \tag{A.2}$$

Solving the integral 1 of Eq. A.2

$$\begin{aligned} \int \frac{h\mathrm{d}h}{1-ch} &= -\frac{1}{c}\int \frac{-ch\mathrm{d}h}{1-ch} = -\frac{1}{c}\int \frac{1-ch-1}{1-ch}\mathrm{d}h = \\ &= -\frac{1}{c}\int \left(1 - \frac{1}{1-ch}\right)\mathrm{d}h = -\frac{1}{c}\left[h + \frac{1}{c}\ln(1-ch)\right], \end{aligned} \tag{A.3}$$

[1] Reprinted from Cryogenics, Vol. 78, Y. Grebenyuk, M.E. Dreyer, Wicking of liquid nitrogen into superheated porous structures, Pages No. 27-39, Copyright (2017), with permission from Elsevier.

and the integral 2 of Eq. A.2

$$\begin{aligned}\int \frac{h^2}{1-ch}\mathrm{d}h &= -\frac{1}{c^2}\int \frac{-c^2h^2}{1-ch}\mathrm{d}h = -\frac{1}{c^2}\int \frac{1-c^2h^2-1}{1-ch}\mathrm{d}h = \\ &= -\frac{1}{c^2}\int \left[\frac{(1-ch)(1+ch)}{1-ch} - \frac{1}{1-ch}\right]\mathrm{d}h = \\ &= -\frac{1}{c^2}\int \left(1+ch-\frac{1}{1-ch}\right)\mathrm{d}h = \\ &= -\frac{1}{c^2}\left[h+\frac{ch^2}{2}+\frac{1}{c}\ln(1-ch)\right],\end{aligned} \tag{A.4}$$

and substituting the solutions to Eq. A.2, one obtains

$$\begin{aligned}t(h) &= -\frac{1}{c}\left[h+\frac{1}{c}\ln(1-ch)\right]b(1+\epsilon n_1) - \\ &\quad -\frac{b\epsilon n_2}{c^2}\left[h+\frac{ch^2}{2}+\frac{1}{c}\ln(1-ch)\right] = \\ &= -\frac{b}{c}\left[(1+\epsilon n_1)h+\frac{1}{c}(1+\epsilon n_1)\ln(1-ch)\right] - \\ &\quad -\frac{b}{c}\left[\frac{\epsilon n_2}{c}h+\frac{\epsilon n_2 h^2}{2}+\frac{\epsilon n_2}{c^2}\ln(1-ch)\right] = \\ &= -\frac{b}{c}\left[\left(1+\epsilon\left(n_1+\frac{n_2}{c}\right)\right)h\right] - \\ &\quad -\frac{b}{c}\left[\left(1+\epsilon\left(n_1+\frac{n_2}{c}\right)\right)\frac{1}{c}\ln(1-ch)\right] - \frac{b}{c}\frac{\epsilon n_2 h^2}{2} = \\ &= -\frac{b\epsilon n_2}{2c}h^2 - \frac{b}{c}\left(1+\epsilon\left(n_1+\frac{n_2}{c}\right)\right)\left(h+\frac{1}{c}\ln(1-ch)\right).\end{aligned} \tag{A.5}$$

A.2 The derivation of the solution for the equation for wicking of a cryogenic liquid into superheated porous structures with evaporation at the wicking front and the influence of the created vapor on the wicking front propagation

The equation is given in section 3.2.1 as

$$1 = ch + bh\dot{h}(1+\epsilon(n_1+n_2h)) + \mu_{\mathrm{F}}^* b\dot{h}(L-h)\left(1+\frac{\epsilon}{\rho_{\mathrm{F}}^*}(n_1+n_2h)\right). \tag{A.6}$$

Integrating Eq. A.6, one obtains

$$t(h) = \underbrace{\int \frac{bh(1+\epsilon(n_1+n_2h))}{1-ch}\mathrm{d}h}_{1} + \underbrace{\int \frac{\mu_\mathrm{F}^* b(L-h)\left(1+\frac{\epsilon}{\rho_\mathrm{F}^*}(n_1+n_2)\right)}{1-ch}\mathrm{d}h}_{2}. \tag{A.7}$$

The solution of the integral 1 of Eq. A.7 is given in Appendix A.1 and yields

$$\int \frac{bh(1+\epsilon(n_1+n_2h))}{1-ch}\mathrm{d}h = -\frac{b\epsilon n_2}{2c}h^2 - \frac{b}{c}\left(1+\epsilon\left(n_1+\frac{n_2}{c}\right)\right)\left(h+\frac{1}{c}\ln(1-ch)\right). \tag{A.8}$$

The integral 2 of Eq. A.7 reads as

$$\begin{aligned}\int \frac{\mu_\mathrm{F}^* b(L-h)\left(1+\frac{\epsilon}{\rho_\mathrm{F}^*}(n_1+n_2h)\right)}{1-ch}\mathrm{d}h = \mu_\mathrm{F}^* b \underbrace{\int \frac{L\left(1+\frac{\epsilon}{\rho_\mathrm{F}^*}(n_1+n_2h)\right)}{1-ch}\mathrm{d}h}_{2.1} - \\ -\mu_\mathrm{F}^* b \underbrace{\int \frac{h\left(1+\frac{\epsilon}{\rho_\mathrm{F}^*}(n_1+n_2h)\right)}{1-ch}\mathrm{d}h}_{2.2}.\end{aligned} \tag{A.9}$$

Solving the integral 2.1 of Eq. A.9

$$\begin{aligned}\int \frac{L\left(1+\frac{\epsilon}{\rho_\mathrm{F}^*}(n_1+n_2h)\right)}{1-ch}\mathrm{d}h &= L\left(\left(1+\frac{n_1}{\rho_\mathrm{F}^*}\right)\int\frac{1}{1-ch}\mathrm{d}h + \frac{n_2}{\rho_\mathrm{F}^*}\int\frac{h}{1-ch}\mathrm{d}h\right) = \\ &= L\left[-\frac{\left(1+\frac{\epsilon n_1}{\rho_\mathrm{F}^*}\right)}{c}\ln(1-ch) - \frac{\epsilon n_2}{\rho_\mathrm{F}^* c}\int\left(1-\frac{1}{1-ch}\right)\mathrm{d}h\right] = \\ &= L\left[-\frac{\left(1+\frac{\epsilon n_1}{\rho_\mathrm{F}^*}\right)}{c}\ln(1-ch) - \frac{\epsilon n_2}{\rho_\mathrm{F}^* c}\left(h+\frac{1}{c}\ln(1-ch)\right)\right] = \\ &= -\frac{L}{c}\left(1+\frac{\epsilon}{\rho_\mathrm{F}^*}\left(n_1+\frac{n_2}{c}\right)\right)\ln(1-ch) - \frac{\epsilon n_2}{\rho_\mathrm{F}^* c}Lh,\end{aligned} \tag{A.10}$$

and the integral 2.2 of Eq. A.9

$$\int \frac{h\left(1+\frac{\epsilon}{\rho_\mathrm{F}^*}(n_1+n_2h)\right)}{1-ch}\mathrm{d}h = -\frac{\epsilon n_2}{2\rho_\mathrm{F}^* c}h^2 - \frac{1}{c}\left(1+\frac{\epsilon}{\rho_\mathrm{F}^*}\left(n_1+\frac{n_2}{c}\right)\right)\left(h+\frac{1}{c}\ln(1-ch)\right), \tag{A.11}$$

and substituting the solutions to Eq. A.9, one obtains

$$\begin{aligned}\int \frac{\mu_{\mathrm{F}}^* b(L-h)\left(1+\frac{\epsilon}{\rho_{\mathrm{F}}^*}\left(n_1+n_2 h\right)\right)}{1-ch}\mathrm{d}h &= \mu_{\mathrm{F}}^* b\left[-\frac{L}{c}\left(1+\frac{\epsilon}{\rho_{\mathrm{F}}^*}\left(n_1+\frac{n_2}{c}\right)\right)\ln(1-ch)-\frac{\epsilon n_2}{\rho_{\mathrm{F}}^* c}Lh\right]+\\ &+\mu_{\mathrm{F}}^* b\left[\frac{\epsilon n_2}{2\rho_{\mathrm{F}}^* c}h^2+\frac{1}{c}\left(1+\frac{\epsilon}{\rho_{\mathrm{F}}^*}\left(n_1+\frac{n_2}{c}\right)\right)\left(h+\frac{1}{c}\ln(1-ch)\right)\right]=\\ &=\mu_{\mathrm{F}}^* b\left[-\frac{\epsilon n_2}{\rho_{\mathrm{F}}^* c}\left(Lh-\frac{h^2}{2}\right)+\frac{1}{c}\left(1+\frac{\epsilon}{\rho_{\mathrm{F}}^*}\left(n_1+\frac{n_2}{c}\right)\right)\left(h+\left(\frac{1}{c}-L\right)\ln(1-ch)\right)\right].\end{aligned} \tag{A.12}$$

Substituting Eq. A.8 and Eq. A.12 to Eq. A.7, one obtains

$$\begin{aligned}t(h) &= -\frac{b\epsilon n_2}{2c}h^2-\frac{b}{c}\left(1+\epsilon\left(n_1+\frac{n_2}{c}\right)\right)\left(h+\frac{1}{c}\ln(1-ch)\right)+\\ &+\mu_{\mathrm{F}}^* b\left[-\frac{\epsilon n_2}{\rho_{\mathrm{F}}^* c}\left(Lh-\frac{h^2}{2}\right)+\frac{1}{c}\left(1+\frac{\epsilon}{\rho_{\mathrm{F}}^*}\left(n_1+\frac{n_2}{c}\right)\right)\left(h+\left(\frac{1}{c}-L\right)\ln(1-ch)\right)\right]=\\ &=-\frac{b\epsilon n_2}{c}\left[\frac{\mu_{\mathrm{F}}^*}{\rho_{\mathrm{F}}^*}Lh+\left(1-\frac{\mu_{\mathrm{F}}^*}{\rho_{\mathrm{F}}^*}\right)\frac{h^2}{2}\right]-\frac{b}{c}\left[1+\epsilon\left(n_1+\frac{n_2}{c}\right)\right]\left(h+\frac{1}{c}\ln(1-ch)\right)+\\ &+\frac{\mu_{\mathrm{F}}^* b}{c}\left[1+\frac{\epsilon}{\rho_{\mathrm{F}}^*}\left(n_1+\frac{n_2}{c}\right)\right]\left(h+\left(\frac{1}{c}-L\right)\ln(1-ch)\right)=\\ &=-\frac{b\epsilon n_2}{c}\left[\frac{\mu_{\mathrm{F}}^*}{\rho_{\mathrm{F}}^*}Lh+\left(1-\frac{\mu_{\mathrm{F}}^*}{\rho_{\mathrm{F}}^*}\right)\frac{h^2}{2}\right]-\mu_{\mathrm{F}}^* L\frac{b}{c}\left[1+\frac{\epsilon}{\rho_{\mathrm{F}}^*}\left(n_1+\frac{n_2}{c}\right)\right]\ln(1-ch)-\\ &-\frac{b}{c}\left[1-\mu_{\mathrm{F}}^*+\epsilon\left(1-\frac{\mu_{\mathrm{F}}^*}{\rho_{\mathrm{F}}^*}\right)\left(n_1+\frac{n_2}{c}\right)\right]\left(h+\frac{1}{c}\ln(1-ch)\right).\end{aligned} \tag{A.13}$$

List of Figures

List of Tables

Bibliography

[1] F.A.L. Dullien. Porous media: fluid transport and porous structure, 2nd edition. Academic Press Inc., 1992.

[2] A.E. Scheidegger. The physics of flow through porous media, 3rd edition. University of Toronto Press, 1974.

[3] H. Darcy. Les Fontaines Publiques de la ville de Dijon. Dalmont, 1856.

[4] F.M. White. Fluid Mechanics, 6th edition. McGraw Hill, New York, 2008.

[5] J.P. Burelbach, S.G. Bankoff, S.H. Davis. Nonlinear stability of evaporating/ condensing liquid films. Journal of Fluid Mechanics, 195: 463-494, 1988.

[6] V.P. Isachenko, V.A. Osipova, A.S. Sukomel. Fundamentals of heat transfer, 3rd edition. Mir Publishers, 1980.

[7] S.S. Kutateladze. Fundamentals of heat transfer, 2nd edition. Academic Press, New York, 1963.

[8] K. Lunkenheimer, K.D. Wantke. Determination of the surface tension of surfactant solutions applying the method of Lecomte du Noiiy (ring tensiometer). Colloid and Polymer Science, 259: 354-366, 1981.

[9] H.H. Zuidema, G.W. Waters. Ring method for determination of interfacial tension. Industrial and Engineeering Chemistry, 13(5): 312-313, 1941.

[10] V.B. Fainerman, R. Miller, P. Joos. The measurement of dynamic surface tension by the maximum bubble pressure method. Colloid and Polymer Science, 272: 731-739, 1994.

[11] K.J. Mysels. Improvements in the maximum-bubble-pressure method of measuring surface tension. Langmuir, 2: 428-432, 1986.

[12] B.B. Lee, P. Ravindra, E.S. Chan. New drop weight analysis for surface tension determination of liquids. Colloids and Surfaces A: Physicochemical and Engineering Aspects, 332: 112-120, 2009.

[13] R.N. McNally, H.C. Yeh, N. Balasubramanian. Surface tension measurements of refractory liquids using the modified drop weight method. Journal of Material Science, 3: 136-138, 1968.

[14] X. Wang, T. Ederth, O. Inganas. In situ Wilhelmy balance surface energy determination of poly(3-hexylthiophene) and poly(3,4-ethylenedioxythiophene) during electrochemical doping-dedoping. Langmuir, 22: 9287-9294, 2006.

[15] D.E. Curtin, R.D. Lousenberg, T.J. Henry, P.C. Tangeman, M.E. Tisack. Advanced materials for improved PEMFC performance and life. Journal of Power Sources, 131: 41-48, 2004.

[16] A. Al-Shareef, P. Neogi, B. Bai. Force based dynamic contact angles and wetting kinetics on a Wilhelmy plate. Chemical Engineering Science, 99: 113-117, 2013.

[17] S. Schmitt. Experimental and numerical investigations of two-phase flow with non-isothermal boundary conditions under microgravity conditions. Cuvillier Verlag, Göttingen, 2016.

[18] L.L. Vasiliev. Heat pipes in modern heat exchangers. Applied Thermal Engineering, 25: 1-19, 2005.

[19] A. Sommers, Q. Wang, X.Han, C. T'Joen, Y. Park, A. Jacobi. Ceramics and ceramic matrix composites for heat exchangers in advanced thermal systems - a review. Applied Thermal Engineering, 30: 1277-1291, 2010.

[20] A. Julbe, D. Farrusseng, C. Guizard. Porous ceramic membranes for catalytic reactors - overview and new ideas. Journal of Membrane Science, 181: 3-20, 2001.

[21] M. Nacken, G.V. Baron, S. Heidenreich, S. Rapagna, A. D'Orazio, K. Gallucci, J.F.M. Denayer, P.U. Foscolo. New DeTar catalytic filter with integrated catalytic ceramic foam: Catalytic activity under model and real bio syngas conditions. Fuel Processing Technology, 134: 98-106, 2015.

[22] N. Gao, A. Li, C. Quan, F. Gao. Hydrogen-rich gas production from biomass steam gasification in an updraft fixed-bed gasifier combined with a porous ceramic reformer. International Journal of Hydrogen Energy, 33: 5430-5438, 2008.

[23] J. Adler. Ceramic diesel particulate filters. International Journal of Applied Ceramic Technology, 2(6): 429-439, 2005.

[24] S. Sarkar, S. Bandyopadhyay, A. Larbot, S. Cerneaux. New clay-alumina porous capillary supports for filtration application. Journal of Membrane Science, 392-393: 130-136, 2012.

[25] E.C. Hammel, O.L.R. Ighodaro, O.I.Okoli. Processing and properties of advanced porous ceramics: an application based review. Ceramics International, 40: 15351-15370, 2014.

[26] J. Li, Y. Zou, L. Cheng. Experimental study on capillary pumping performance of porous wicks for loop heat pipe. Experimental Thermal and Fluid Science, 34: 1403-1408, 2010.

[27] P. Singh, A. Chatterjee, S. Ghosh. Vertical wicking tester for monitoring water transportation behavior in fibrous assembly. Review of Scientific Instruments, 87: 105114, 2016.

[28] P. van der Meeren, J. Cocquyt, S. Flore. Quantifying wetting and wicking phenomena in cotton terry as affected by fabric conditioner treatment. Textile Research Journal, 72(5): 423-428, 2002.

[29] J.K. Spelt and A.W. Neumann. Solid Surface Tension: The Equation of State Approach and the Theory of Surface Tension Components. Theoretical and Conceptual Considerations. Langmuir, 3: 588-591, 1987.

[30] U.O.M. Vazquez, W. Shinoda, P.B. Moore, C. Chiu, S.O: Nielsen. Calculating the surface tension between a flat solid and a liquid: a theoretical and computer simulation study of three topologically different methods. Journal of Mathematical Chemistry, 45: 161-174, 2009.

[31] N. Kulev, S. Basting, E. Baensch, M.E. Dreyer. Interface reorientation of cryogenic liquids under non-isothermal boundary conditions. Cryogenics, 62: 48-59, 2014.

[32] N. Kulev, M.E. Dreyer. Drop tower experiments on non-isothermal reorientation of cryogenic liquids. Microgravity Science and Technology, 22: 463-474, 2010.

[33] S. Schmitt, M.E. Dreyer. Free surface oscillations of liquid hydrogen in microgravity conditions. Cryogenics, 72: 22-35, 2015.

[34] Y. Grebenyuk, M.E. Dreyer. Wicking of liquid nitrogen into superheated porous structures. Cryogenics, 78: 27-39, 2016.

[35] M. Ramiasa, J. Ralston, R. Fetzer, R. Sedev. The influence of topography on dynamic wetting. Advances in Colloid and Interface Science, 206: 275-293, 2014.

[36] N. Fries, K.Odic, M. Dreyer. Wicking of Perfectly Wetting Liquids into a Metallic Mesh. Proceedings of the 2nd International Conference on Porous Media and its Applications in Science and Engineering ICPM2, Kauai, Hawaii, USA, 2007.

[37] N. Fries, K. Odic, M. Conrath, M. Dreyer. The effect of evaporation on the wicking of liquids into a metallic weave. Journal of Colloid and Interface Science, 321: 118-129, 2008.

[38] N. Fries, K. Odic, M. Conrath, M. Dreyer. The capillary rise of liquids in a metallic weave - evaporation effects. Proceedings of the Sixth International ASME Conference on Nanochannels, Microchannels and Minichannels ICNMM2008, Darmstadt, Germany, 2008.

[39] R. Raj, C. Kunkelmann, P. Stephan, J. Plawsky, J. Kim. Contact line behavior for a highly wetting fluid under superheated conditions. International Journal of Heat and Mass Transfer, 55: 2664-2675, 2012.

[40] C. Buffone, V. Grishaev, A. Glushchuk. Experimental investigation of liquid retention in a cyclone evaporator under variable gravity conditions. Applied Thermal Engineering, 99: 235-243, 2016.

[41] S. Sikalo, H.D. Wilhelm, I. V. Roisman, S. Jakirlic, C. Tropea. Dynamic contact angle of spreading droplets: Experiments and simulations. Physics of Fluids, 17: 062103, 2005.

[42] T.S. Jiang, S.G. Oh, I. V. Roisman, J.C. Slaterry. Correlation for dynamic contact angle. Journal of Colloid and Interface Science, 69: 74-77, 1994.

[43] M. Bracke, F. De Voeght, P. Joos. The kinetics of wetting: the dynamic contact angle. Progress in Colloid and Polymer Science, 79: 142-149, 1989.

[44] S.F. Kistler, P.M. Schweizer. Liquid film coating. Chapman Hall, London, 1997.

[45] D. Gaulke. Capillary driven transport of liquid between parallel perforated plates. Cuvillier Verlag, Göttingen, 2016.

[46] N. Fries. Capillary transport processes in porous materials - experiment and model. Cuvillier Verlag, Göttingen, 2010.

[47] K.P. Hallinan, H.C. Chebaro, S.J. Kim, W.S. Chang. Evaporation from an extended meniscus for non-isothermal interfacial conditions. Journal of Thermophysics and Heat Transfer, 8(4): 709-716, 1994.

[48] Z.K. Tu, W. Liu, Z.C. Liu, X.M. Huang. Interface stability in a capillary loop undergoing phase changes in non-gravitational conditions. Chinese Science Bulletin, 55(35): 4069-4073, 2010.

[49] M.M. Labani, R. Rezaee, A. Saeedi, A. Al Hinai. Evaluation of pore size spectrum of gas shale reservoirs using low pressure nitrogen adsorption, gas expansion and mercury porosimetry: A case study from the Perth and Canning Basins, Western Australia. Journal of Petroleum Science and Engineering, 113: 7-16, 2013.

[50] S. Westermarck, A.M. Juppo, L. Kervinen, J. Yliruusi. Pore structure and surface area of mannitol powder, granules and tablets determined with mercury porosimetry and nitrogen adsorption. European Journal of Pharmaceutics and Biopharmaceutics, 46: 61-68, 1998.

[51] U. Kuila, M. Prasad. Specific surface area and pore-size distribution in clays and shales. Geophysical Prospecting, 61: 341-362, 2013.

[52] M. Plötze, P. Niemz. Porosity and pore size distribution of different wood types as determined by mercury intrusion porosimetry. European Journal of Wood and Wood Products, 69: 649-657, 2011.

[53] J. Ilavsky, C.C. Berndt, J. Karthikeyan. Mercury intrusion porosimetry of plasma-sprayed ceramic. Journal of Materials Science, 32: 3925-3932, 1997.

[54] M.J. Moura, P.J. Ferreira, M.M. Figueiredo. Mercury intrusion porosimetry in pulp and paper technology. Powder Technology, 160: 61-66, 2005.

[55] A. Hernandez, J.I. Calvo, P. Pradanos, F. Tejerina. Pore size distributions in microporous membranes. A critical analysis of the bubble point extended method. Journal of Membrane Science, 112: 1-12, 1996.

[56] J. Hartwig, J.A. Mann Jr., S.R. Darr. Parametric analysis of the liquid hydrogen and nitrogen bubble point pressure for cryogenic liquid acquisition devices. Cryogenics, 63: 25-36, 2014.

[57] W.B. Lindquist, A. Venkatarangan, J. Dunsmuir, T. Wong. Pore and throat size distributions measured from synchrotron X-ray tomographic images of Fontainebleau sandstones. Journal of Geophysical Research, 105(B9): 21509-21527, 2000.

[58] R.C. Atwood, J.R. Jones, P.D. Lee, L.L. Hench. Analysis of pore interconnectivity in bioactive glass foams using X-ray microtomography. Scripta Materialia, 51: 1029-1033, 2004.

[59] L. Farber, G. Tardos, J.N. Michaels. Use of X-ray tomography to study the porosity and morphology of granules. Powder Technology, 132: 57-63, 2003.

[60] N. Epstein. On tortuosity and the tortuosity factor in flow and diffusion through porous media. Chemical Engineering Science, 44(3): 777-779, 1989.

[61] A. Koponen, M. Kataja, J. Timonen. Tortuous flow in porous media. Physical Review Letters E, 54(1): 406-410, 1996.

[62] M. Matyka, A. Khalili, Z. Koza. Tortuosity-porosity relation in porous media flow. Physical Review Letters E, 78(026306): 1-8, 2008.

[63] A. Duda, Z. Koza, M. Matyka. Hydraulic tortuosity in arbitrary porous media flow. Physical Review Letters E, 84(036319): 1-8, 2011.

[64] B.-M. Yu, J.-H. Li. A geometry model for tortuosity of flow path in porous media. Chinese Physics Letters, 21(8): 1568-1571, 2011.

[65] P.-Y. Lanfrey, Z.V. Kuzeljevic, M.P. Dudukovic. Tortuosity model for fixed beds randomly packed with identical particles. Chemical Engineering Science, 65: 1891-1896, 2010.

[66] L. Pisani. Simple expression for the tortuosity of porous media. Transport in Porous Media, 88: 193-203, 2011.

[67] A.C. Liakopoulos. Darcy's coefficient of permeability as symmetric tensor of second rank. International Association of Scientific Hydrology. Bulletin, 10(3): 41-48, 1965.

[68] G. Lei, P.C. Dong, S.Y. Mo, S. Yang, Z.S. Wu, S.H. Gai. Calculation of full permeability tensor for fractured anisotropic media. Journal of Petroleum Exploration and Production Technology, 5: 167-176, 2015.

[69] A. Koponen, M. Kataja, and J. Timonen. Permeability and effective porosity of porous media. Physical Review E, 56(3): 3319-3325, 1997.

[70] P. Xu, B. Yu. Developing a new form of permeability and Kozeny-Carman constant for homogeneous porous media by means of fractal geometry. Advances in Water Resources, 31: 74-81, 2008.

[71] H.A. Nooruddin, M.E. Hossain. Modified Kozeny-Carmen correlation for enhanced hydraulic flow unit characterization. Journal of Petroleum Science and Engineering, 80: 107-115, 2012.

[72] M. Conrath, N. Fries, M. Zhang, M.E. Dreyer. Radial capillary transport from an infinite reservoir. Transport in Porous Media, 84: 109-132, 2010.

[73] R. Morent, N. De Geyter, C. Leys, E. Vansteenkiste, J. De Bock, W. Philips. Measuring the wicking behavior of textiles by the combination of a horizontal wicking experiment and image processing. Review of Scientific Instrument, 77 (093502), 2006.

[74] M. Lago, M. Araujo. Capillary rise in porous media. Physica A, 289: 1-17, 2001.

[75] L. Galet, S. Patry, J. Dodds. Determination of the wettability of powders by the Washburn capillary rise method with bed preparation by a centrifugal packing technique. Journal of Colloid and Interface Science, 346: 470-475, 2010.

[76] Z. Liu, Y. Hu, J. Zhao, Z. Qu, F. Xu. Experimental and numerical studies on liquid wicking into filter papers for paper-based diagnostics. Applied Thermal Engineering, 88: 280-287, 2015.

[77] M.F. Pucci, P.J. Liotier, S. Drapier. Capillary wicking in flax fabrics. Effects of swelling in water. Colloids and Surfaces A: Physicochemical and Engineering Aspects, 498: 176-184, 2016.

[78] C.J. Hong, J.B. Kim. A study of comfort performance in cotton and polyester blended Fabrics. I. Vertical wicking behavior. Fibers and Polymers 8(2): 218-224, 2007.

[79] T. Stuart, R.D. McCall, H.S.S. Sharma, G. Lyons. Modelling of wicking and moisture interactions of flax and viscose fibres. Carbohydrate Polymers, 123: 359-368, 2015.

[80] R. Masoodi, K.M. Pillai. Darcy-s law-based model for wicking in paper-like swelling porous media. AIChE Journal, 56(9): 2257-2267, 2010.

[81] R. Masoodi, H. Tan, K.M. Pillai. Numerical simulation of liquid absorption in paper-like swelling porous media. AIChE Journal, 58(8): 2536-2544, 2012.

[82] M.A. Hanlon, H.B. Ma. Evaporation heat transfer in sintered porous media. Journal of Heat Transfer, 125: 644-652, 2003.

[83] C. Li, G.P. Peterson, Y. Wang. Evaporation/boiling in thin capillary wicks (I) - Wick thickness effects. Journal of Heat Transfer, 128: 1312-1319, 2006.

[84] C. Li, G.P. Peterson. Evaporation/boiling in thin capillary wicks (II) - Effects of volumetric porosity and mesh size. Journal of Heat Transfer, 128: 1320-1328, 2006.

[85] A. Brautsch, P.A. Kew. Examination and visualisation of heat transfer processes during evaporation in capillary porous structures. Applied Thermal Engineering, 22: 815-824, 2002.

[86] M.J. Blunt. Flow in porous media - pore-network models and multiphase flow. Current Opinion in Colloid and Interface Science, 6: 197-207, 2001.

[87] A. Joekar-Niasar, M. Prodanovic, D. Wildenschild, S. M. Hassanizadeh. Network model investigation of interfacial area, capillary pressure and saturation relationships in granular porous media. Water Resources Research, 46(W06526), 2010.

[88] M. Prat. Discrete models of liquid-vapour phase change phenomena in porous media. Revue Générale de Thermique, 37: 954-961, 1998.

[89] C. Figus, Y. Le Bray, S. Bories, M. Prat. Heat and mass transfer with phase change in a porous structure partially heated - continuum model and pore network simulations. International Journal of Heat and Mass Transfer, 49: 2557-2569, 1999.

[90] L.A. Segura. Modeling at pore-scale isothermal drying of porous materials: liquid and vapor diffusivity. Drying Technology, 25: 1677-1686, 2007.

[91] A.G. Yiotis, A.G. Boudouvis, A.K. Stubos, I. N. Tsimpanogiannis, Y. C. Yortsos. Effect of liquid films on the drying of porous media. AIChE Journal, 50(11): 2721-2737, 2004.

[92] A.G. Yiotis, A.K. Stubos, A.G. Boudouvis, Y. C. Yortsos. A 2-D pore-network model of the drying of single-component liquids in porous media. Advances in Water Resources, 24: 439-460, 2001.

[93] E.W. Washburn. The dynamics of capillary flow. Physical Review, 17(3): 273-283, 1921.

[94] R. Lucas. Ueber das Zeitgesetz des kapillaren Aufstiegs von Fluessigkeiten. Kolloid-Z., 23: 15-22, 1918.

[95] D. Lukas, V. Soukupova. Recent studies of fibrous materials wetting dynamics. INDEX 99 Congress, Geneva, Switzerland, 1999.

[96] E.W. Zhmund, F. Tiberg, and K. Hallstensson. Dynamics of capillary rise. Journal of Colloid and Interface Science, 228: 263-269, 2000.

[97] N. Fries, M. Dreyer. An analytic solution of capillary rise restrained by gravity. Journal of Colloid and Interface Science, 320: 259-263, 2008.

[98] A. Hamraoui, T. Nylander. Analytical Approach for the Lucas-Washburn Equation. Journal of Colloid and Interface Science, 250: 415-421, 2002.

[99] G. Martic, J. De Coninck, and T.D. Blake. Influence of the dynamic contact angle on the characterization of porous media. Journal of Colloid and Interface Science, 263: 213-216, 2003.

[100] R. Masoodi, K.M. Pillai, P.P. Varanasi. Role of hydraulic and capillary radii in improving the effectiveness of capillary model in wicking. Proceedings of FEDSM2008 2008 ASME Fluids Engineering Conference. Jacksonville, Florida, USA, 2008.

[101] R. Masoodi, K.M. Pillai, P.P. Varanasi. Darcy's law based models for liquid absorption in polymer wicks. AIChE J, 53(11): 2769-2782, 2007.

[102] R. Masoodi, K.M. Pillai, P.P. Varanasi. Darcy's law-based numerical simulation for modelling 3D liquid absorbtion into porous wicks. AIChE J, 53(11): 2769-2782, 2007.

[103] E.P. Symons. Wicking of liquids in screens. NASA TN D-7657, 1974.

[104] R. Masoodi, K.M. Pillai. Wicking in porous materials. Taylor and Fransis Group, New York, 2013.

[105] P. Ranut, E. Nobile, L. Mancini. High resolution microtomography-based CFD simulation of flow and heat transfer in aluminum metal foams. Applied Thermal Engineering, 69: 230-240, 2014.

[106] H. Li., F. Wang, C. Wang, X. Gao, X. Li. Liquid flow behavior study in SiC foam corrugated sheet using a novel ultraviolet fluorescence technique coupled with CFD simulation. Chemical Engineering Science, 123: 341-349, 2015.

[107] X. Li, G. Gao, L. Zhang, H. Sui, H. Li, X. Gao, Z. Yang, C. Tian, J. Zhang. Multiscale simulation and experimental study of novel SiC structured packings. Industrial and Engineering Chemistry Research, 51: 915-924, 2012.

[108] G. Boccardo, L. del Plato, D. Marchisio, F. Augier, Y. Haroun, D. Ferre, M. Icardi. Porescale simulation of fluid flow in packed-bed reactors via rigid-body simulations and CFD. Proceedings of the 10th International Conference on CFD in Oil and Gas, Metallurgical and Process Industries, Trondheim, Norway, 2014.

[109] S. Meinicke, C.O. Moeller, B. Dietrich, M. Schlüter, T. Wetzel. Experimental and numerical investigation of single-phase hydrodynamics in glass sponges by means of combined µPIV measurements and CFD simulation. Chemical Engineering Science, 160: 131-143, 2017.

[110] S. Meinicke, T. Wetzel, B. Dietrich. Scale-resolved CFD modelling of single-phase hydrodynamics and conjugate heat transfer in solid sponges. International Journal of Heat and Mass Transfer, 108: 1207-1219, 2017.

[111] G.A. Narsilio, O. Buzzi, S. Fityus, T.S. Yun, D.W. Smith. Upscaling of Navier-Stokes equations in porous media: Theoretical, numerical and experimental approach. Computers and Geotechnics, 36: 1200-1206, 2009.

[112] W. Fourie, R. Said, P. Young, D.L. Barnes. The simulation of pore scale fluid flow with real world geometries obtained from X-ray computed tomography. Proceedings of the COMSOL Conference, Boston, USA, 2007.

[113] M. Zhang. Capillary transport of cryogenic liquids in porous structures. Cuvillier Verlag, Göttingen, 2013.

[114] N. Fries, M. Dreyer. Dimensionless scaling methods for capillary rise. Journal of Colloid and Interface Science, 338: 514-518, 2009.

[115] M. Stange, M. Dreyer, H. Rath. Capillary driven flow in circular cylindrical tubes. Physics of Fluids, 15: 2587-2601, 2003.

[116] N. Fries, M. Dreyer. The transition from inertial to viscous flow in capillary rise. Journal of Colloid and Interface Science, 327: 125-128, 2008.

[117] M. Lago, M. Araujo. Capillary rise in porous media. Physica A, 289: 1-17, 2001.

[118] D.E. Jaekle. Propellant Management Device Conceptual Design and Analysis: Galleries. AIAA-97-2811, 1997.

[119] M. Wollen, F. Merino, J. Schuster, C. Newton. Cryogenic Propellant Management Device: Conceptual Design Study. NASA/CR-010-216777, 2010.

[120] S. Darr, J. Hartwig. Optimal liquid acquisition device screen weave for a liquid hydrogen fuel depot. International Journal of Hydrogen Energy, 39: 4356-4366, 2014.

[121] J. Hartwig, S. Darr. Influential factors for liquid acquisition device screen selection for cryogenic propulsion systems. Applied Thermal Engineering, 66: 548-562, 2014.

[122] J. M. Jurns, J. W. Hartwig. Liquid oxygen liquid acquisition device bubble point tests with high pressure liquid oxygen at elevated temperatures. Cryogenics, 52: 283-289, 2012.

[123] P. Behruzi, J. Klatte, G. Netter. Passive Phase Separation in Cryogenic Upper Stage Tanks. Proceeding of 49th AIAA/ASME/SAE/ASEE Joint Propulsion Conference, San Jose, USA, 2013.

[124] M. Conrath, Y. Smiyukha, E. Fuhrmann, M. Dreyer. Double porous screen element for gas-liquid phase separation. International Journal of Multiphase Flow, 50: 1-15, 2013.

[125] E.P. Symons. Wicking of liquids in screens. NASA TN D-7657, 1974.

[126] N. Fries, K. Odic, M. Conrath, M. Dreyer. The effect of evaporation on the wicking of liquids into a metallic weave. Journal of Colloid and Interface Science, 321: 118-129, 2008.

[127] T. Zhang, P. deBock, E. W. Stautner, T. Deng, C. Immer. Demonstration of liquid nitrogen wicking using a multi-layer metallic wire cloth laminate. Cryogenics, 52: 301-305, 2012.

[128] S.W. Choi, W.I. Lee, H.S. Kim. Analysis of flow characteristics of cryogenic liquid in porous media. International Journal of Heat and Mass Transfer, 87: 161-183, 2015.

[129] J. Hartwig, D. Chato, J. McQuillen. Screen channel LAD bubble point tests in liquid hydrogen. International Journal of Hydrogen Energy, 39(2): 853-861, 2013.

[130] J. Hartwig, J. McQuillen, J. Jurns. Screen channel liquid-acquisition-device bubble point tests in liquid oxygen. Journal of Thermophysics and Heat Transfer, 29(2): 353-363, 2015.

[131] R. Ranjan, J.Y. Murthy, S.V. Garimella. A microscale model for thin-film evaporation in capillary wick structures. International Journal of Heat and Mass Transfer, 54: 169-179, 2011.

[132] K.K. Bodla, J.Y. Murthy, S.V. Garimella. Evaporation analysis in sintered wick microstructures. International Journal of Heat and Mass Transfer, 61: 729-741, 2013.

[133] Y. Xuan, K. Zhao, Q. Li. Investigation on heat and mass transfer in a evaporator of a capillary-pumped loop with the lattice Boltzmann method: pore scale simulation. Transport in Porous Media, 89(3): 337-355, 2011.

[134] M. Prat. Pore network models for the study of transfers in the porous wick of loop heat pipes. Heat Pipe Science and Technology, 1(2): 129-149, 2010.

[135] L. Mottet, T. Coquard, M. Prat. Three dimensional liquid and vapour distribution in the wick of capillary evaporators. International Journal of Heat and Mass Transfer, 83: 636-651, 2015.

[136] G. Ramon, A. Oron. Capillary rise of a meniscus with phase change. Journal of Colloid and Interface Science, 327: 145-151, 2008.

[137] J. Polansky, T. Kaya. An experimental and numerical study of capillary rise with evaporation. International Journal of Thermal Sciences, 91: 25-33, 2015.

[138] M. Quintard, S. Whitaker. Two-phase flow in heterogeneous porous media: the method of large-scale averaging. Transport in Porous Media, 3: 357-413, 1988.

[139] D. Lasseux, M. Quintard, S. Whitaker. Determination of permeability tensors for two-phase flow in homogeneous porous media: theory. Transport in Porous Media, 24: 107-137, 1996.

[140] E. Rame. The interpretation of dynamic contact angles measured by the Wilhelmy plate method. Journal of Colloid and Interface Science, 185: 245-251, 1997.

[141] E. Lemmon, M. Huber, M. McLinden. REFPROP: Reference fluid thermodynamic and transport properties. NIST Standard reference database 23, Version 9.0, 2010.

[142] Eckels Engineering Inc. CryoComp, Version 5.1, 2010.

[143] W. Schnelle, J. Engelhardt, E. Gmelin. Specific heat capacity of Apiezon N high vacuum grease and of Duran borosilicate glass. Cryogenics, 39(3): 271-275, 1999.

[144] J.W. Hartwig. Screen channel liquid acquisition device bubble point test in liquid nitrogen. Cryogenics, 74: 95-105, 2016.

[145] J. Hartwig, J. McQuillen. Analysis of screen channel LAD bubble point tests in liquid methane at elevated temperature. AIAA-2012-0759, 2012.

[146] D.J. Chato, M.T. Kudlac. Screen Channel Liquid Acquisition Devices for Cryogenic Propellants. AIAA-2002-3983, 2002.

[147] M. Ulbricht, O. Schuster, W. Ansorge, M. Ruetering, P. Steiger. Influence of the strongly anisotropic cross-section morphology of a novel polyethersulfone microfiltration membrane on filtration performance. Separation and Purification Technology, 57: 63-73, 2007.

[148] T. Liu, M. Huang, X. Li, C. Wang, C.X. Gui, Z.Z. Yu. Highly compressible anisotropic graphene aerogels fabricated by directional freezing for efficient absorption of organic liquids. Carbon, 100: 456-464, 2016.

[149] S.Y. Chung, M.A. Elrahman, D. Stephan. Investigation of the effects of anisotropic pores on material properties of insulating concrete using computed tomography and probabilistic methods. Energy and Buildings, 125: 122-129, 2016.

[150] P. Colombo. Engineering porosity in polymer-derived ceramics. Journal of the European Ceramic Society, 28(7): 1389-1395, 2008.

[151] A. Studart, U.T. Gonzenbach, E. Tervoort, L.J. Gauckler. Processing routes to macroporous ceramics: a review. Journal of the American Ceramic Society, 89(6): 1771-1789, 2016.

[152] E.O. Einset. Capillary infiltration rates into porous media with application to Silcomp processing. Journal of the American Ceramic Society, 79(2): 333-338, 1996.

[153] S. Kumar, A. Kumar, A. Shukla, A.K. Gupta, R. Devi. Capillary infiltration studies of liquids into 3D-stitched C-C preforms Part A: Internal pore characterization by solvent infiltration, mercury porosimetry, and permeability studies. Journal of the European Ceramic Society, 29: 2643-2650, 2009.

[154] S. Kumar, A. Kumar, R. Devi, A. Shukla, A.K. Gupta. Capillary infiltration studies of liquids into 3D-stitched C-C preforms Part B: Kinetics of silicon infiltration. Journal of the European Ceramic Society, 29: 2651-2657, 2009.

[155] K. Okada, S. Uchiyama, T. Isobe, Y. Kameshima, A. Nakajima, T. Kurata. Capillary rise properties of porous mullite ceramics prepared by an extrusion method using organic fibers as the pore former. Journal of the European Ceramic Society, 29: 2491-2497, 2009.

[156] K. Okada, A. Imase, T. Isobe, A. Nakajima. Capillary rise properties of porous geopolymers prepared by an extrusion method using polylactic acid (PLA) fibers as the pore formers. Journal of the European Ceramic Society, 31: 461-467, 2011.

[157] H. Zhang, P. D'Angelo Nunes, M. Wilhelm, K. Rezwan. Hierarchically ordered micro/meso/macroporous polymer-derived ceramic monoliths fabricated by freeze-casting. Journal of the European Ceramic Society, 36: 51-58, 2016.

[158] S. Whitaker. Flow in porous media I: a theoretical derivation of Darcy's law. Transport in Porous Media, 1: 3-25, 1986.

[159] W.G. Gray, K. O'Neill. On general equations for flow in porous media and their reduction to Darcy's law. Water Resources Research, 12(2): 148-154, 1976.

[160] Y. Grebenyuk, H.X. Zhang, M. Wilhelm, K. Rezwan, M.E. Dreyer. Wicking into porous polymer-derived ceramic monoliths fabricated by freeze-casting. Journal of the European Ceramic Society, 37(5): 1993-2000, 2017.

[161] D. Wildenschild, A.P. Sheppard. X-ray imaging and analysis techniques for quantifying pore-scale structure and processes in subsurface porous medium systems. Advances in Water Resources, 51: 217-246, 2013.

[162] R. Al-Raoush, A. Papadopoulos. Representative elementary volume analysis of porous media using X-ray computed tomography. Powder Technology, 200: 69-77, 2010.

[163] E. Maire, P. Colombo, J. Adrien, L. Babout, L. Biasetto. Characterization of the morphology of cellular ceramics by 3D image processing of X-ray tomography. Journal of the European Ceramic Society, 27: 1973-1981, 2007.

[164] L. Salvo, P. Cloetens, E. Maire, S. Zabler, J.J. Blandin, J.Y. Buffiere, W. Ludwig, E. Boller, D. Bellet, C. Josserond. X-ray micro-tomography an attractive characterization

technique in materials science. Nuclear Instruments and Methods in Physics Research B, 200: 273-286, 2003.

[165] FLOW-3D User Manual, Version 10.0.

[166] Y. Saad. Iterative methods for sparse linear systems, 2nd edition. SIAM, 2003.

[167] C.W. Hirt, B.D. Nichols. Volume of fluid method for the dynamics of free boundaries. Journal of Computational Physics, 1(39): 201-225, 1981.

[168] M.R. Barkhudarov. Lagrangian VOF advection method for FLOW-3D. Technical Report FSI-03-TN63-R, Flow Science, Inc., July 2004.

[169] W.B. Young. Analysis of capillary flows in non-uniform cross-sectional capillaries. Colloids and Surfaces A: Physicochemical and Engineering Aspects, 321: 123-128, 2004.

[170] M. Hemmat, A. Borhan. Creeping flow through sinusoidally constricted capillaries. Physics of Fluids 7 (9): 2111-2121, 1995.

[171] T.L. Staples, D.G. Shaffer. Wicking flow in irregular capillaries. Colloids and Surfaces A: Physicochemical and Engineering Aspects, 204: 239-250, 2002.

[172] D. Patro, S. Bhattacharyya, V. Jayaram. Flow kinetics in porous ceramics: understanding with non-uniform capillary models. Journal of the American Ceramic Society, 90(10): 3040-3046, 2007.

[173] A. Marmur. Kinetics of penetration into uniform porous media: testing the equivalent-capillary concept. Langmuir, 19: 5956-5959, 2003.